

Study and Characterization of Magnetic Materials for Beam Intensity Monitors at CERN

THÈSE N° 8272 (2018)

PRÉSENTÉE LE 26 JANVIER 2018

À LA FACULTÉ DES SCIENCES ET TECHNIQUES DE L'INGÉNIEUR
LABORATOIRE DE TECHNOLOGIE DES POUDRES
PROGRAMME DOCTORAL EN SCIENCE ET GÉNIE DES MATÉRIAUX

ÉCOLE POLYTECHNIQUE FÉDÉRALE DE LAUSANNE

POUR L'OBTENTION DU GRADE DE DOCTEUR ÈS SCIENCES

PAR

Silvia AGUILERA MURCIANO

acceptée sur proposition du jury:

Prof. D. Damjanovic, président du jury
Prof. H. Hofmann, Dr O. R. Jones, directeurs de thèse
Prof. A. M. Hirt, rapporteuse
Dr A. Jeff, rapporteur
Prof. P. Mural, rapporteur



ÉCOLE POLYTECHNIQUE
FÉDÉRALE DE LAUSANNE

Suisse
2018

"Sé breve en tus razonamientos, que ninguno hay gustoso si es largo."
Miguel de Cervantes, Don Quijote de la Mancha.

A mi familia.

Acknowledgements

I feel my thesis is special because it is not only the combination of a lot of hard work from a lot of different people, but also the product of acts of kindness and friendship. I have to start thanking my thesis directors, who both agreed to help me start this adventure, Prof. Heinrich Hofmann from the LTP lab in EPFL and Dr. Rhodri Jones, BI group leader at CERN. I am grateful for their help during all these years, and also for their trust when I reached out to them to start the PhD. I hope it was as interesting as as fun as it was for me. I can't forget Patrick Odier who introduced me and patiently guided me through the world of transformers and has even managed to make me understand some electronics. Thank you Patrick for being my mentor throughout this journey. I can't forget Lars Soby who has been my section leader during all these years for his support. I would also like to thank the Jury of my thesis, Prof. Damjanovic, Prof. Hirt, Dr. Jeff and Prof. Muralt for taking the time in reading and helping make my thesis better.

During my PhD I have been helped by many people which I have to thank for sharing their expertise and teaching me about their field. The following people from EPFL have been an important part of this thesis as they have helped me to obtain all of the results: Cindy Känel and Jacques Morisod from MHMC, Hamed Kazemi and Cyril Cattin (LMM), Xavier Jeanbourquin (LIMNO), Sylvain Coudret (CEL), Pierre Mettraux and Stefano Mischler (SM), Duncan Alexander, Cécile Hébert, Barbora Bártoová and Emad Oveisi (CIME), Benjamin Dwir (LPN), Ping Huan (LQM), Dirk Grundler (ENS).

I also have to thank Alla Arakcheeva (EO Phase Solution), Martin Robyr (UNIL), Jeremy Tillier, Olha Sereda and Saba Zabihzadeh (CSEM), Jeffrey McCord and Matic Klug (Christian-Albrechts-Universität zu Kiel), Remo Müller (PerkinElmer), Ana Arauzo (Universidad de Zaragoza), Ann Hirt and Hans-Peter Haechler (ETHZ) for helping me with measurements and even opening the doors of their labs for me.

I have received a lot of help from my colleagues at CERN as well. I have to thank Stefano Sgobba, Michał Czapski, Ana Teresa Pérez, Floriane Leaux, Maud Scheubel, Holger Neupert, Josep Busom, Mauro Taborrelli, Benoit Teissandier, Marius Lungulescu, Wilhelmus Vollenberg, Fritz Motschmann and Mateusz Bednarek.

I have to thank my section at CERN and all the people that have been a part of it during all these years. Merci Seb, Romain, Franck et Jacques pour leur aide et soutien.

Acknowledgements

I have to thank David, Jeroen, Franco, Jiri, Jocelyn, Ole and Michele for their support and kindness. Gracias al equipo español que ha pasado por la sección, Ricardo, Ángel, Juanjo, Alfonso y Daniel por siempre tener jamón y una sonrisa en casos de emergencia.

I can't forget about my second family in Lausanne, where I have felt welcomed and supported from the beginning. Thanks to Sandra, Abhishek T., Lionel, Gabi, Abhisek K., Azade, Aslam, David, Weitian, Debora, Sophie, Milica, Irena, Mariana, Jirawan, Amar, João and Sami. I have to give special thanks to Carlos, Paul, Jacques, Shawn Anne and Rosana for helping me in the lab and with all the crazy paperwork that a PhD entails.

My mental health would be much more deteriorated if it wasn't for the help of the great professionals I have met in the secretariats at CERN and EPFL. Thanks Erika, Anne, Chrystelle and Madeleine for making my life easier and for being such wonderful women.

I can't forget the crazy o'clock lunch team and the chocolate club for their good spirits and for the laughs. Thank you Tom, Miguel, Jack, Thomas, Kacper, Frankie, Apostolos and the many more that have made lunch fun. My time here would have been very boring if it wasn't for all the people in the diving, sailing and skiing club that have always asked me about my thesis and with whom I've enjoyed endless hours of sharing our hobbies. Debo agradecer también a la Asociación, y en especial a Cris, Gema y Mari Carmen todo el apoyo que me han dado desde que nos conocimos. Gracias a todos por estar ahí cuando más se necesita. Merci aux filles TDAC, spécialement a Chris et Jenni pour toutes les heures de danses et rigolades, vous-etes cool! Gracias a todos los amigos que a pesar de la distancia han seguido ahí a pie del cañon, especialmente a Jordi, con el que después de tantos años, nada ha cambiado.

Thanks to all the wonderful people I have met during this adventure for being there in the good and not so good times: Lorraine, Mario, Javi and Vijay. Gracias Juan por los cafés en momentos de crisis y por el apoyo incondicional que tanta falta me ha hecho, sobre todo al final. I have to also thank Michał K. for his help with the thesis and in the lab and for his patience with my lack of understading with all the electricrky I've needed.

Je dois aussi remercier ma nouvelle famille suisse pour m'avoir accueilli les bras ouverts et pour leur soutien. Thanks especially to Mic for sticking through with this not-so-fun time and always being there.

Y finalmente, gracias a mi familia, en especial a mi madre, mi padre y mi hermana por su apoyo y cariño que nunca me ha faltado aunque estemos a veces un poco lejos. Os quiero.

Geneva, December 2017

S. A.

Abstract

The number of particles in the beams used at CERN is measured by a family of devices called the Beam Current Transformers (BCTs). One of such devices is the DC Current Transformer (DCCT) measuring the total number of particles in an accelerator. The DCCT is built around a magnetic core made of a soft magnetic material. Currently, the DCCT cores are purchased from one of a few industrial partners. This situation might result in some significant issues with development of the DCCTs. Firstly, the choice of the core can be made only among the already developed and manufactured cores. Secondly, the industrial partners do not normally guarantee long-term availability of their products which could manifest itself as future maintenance problems. Thirdly, the cores available on the market have not been developed with CERN's intended application in mind and, hence, might be non-optimal for the DCCTs. These three factors, among others, led to a decision to investigate a possibility of in-house core manufacturing.

BCT cores are made up of a soft magnetic material in ribbon-form between 20 and 30 microns thick, wound into a toroidal shape. They are amorphous or nanocrystalline cobalt and iron-based alloys that show high permeabilities and low coercivities. Several commercial alloys in their amorphous as-cast state were purchased after identifying the key parameters of the materials for the application, contacting suppliers and studying the available materials to find the most suitable ones. This choice was made by confronting the as-cast properties of the alloys with the needs of the instruments which would house the magnetic cores.

The materials were then characterised to determine how to thermally treat them in order to obtain a range of different final magnetic properties. This study also resulted in establishing the best candidates to fabricate the sample cores. After this, three alloys were selected (iron-based alloy Finemet FT-3 from Metglas and two-cobalt based materials, 6025 G40 from Vacuumschmelze and 2705 M from Metglas) based on their as-cast properties. The cores and ribbons of the selected materials were then annealed at different temperatures and durations to study the effect of the treatment in both. Three treatments were done on the selected samples, below the Curie temperature, between the Curie and the crystallisation temperature and above the crystallisation temperature. Measurements of the samples were taken after the thermal treatment and compared to the results of the as-cast materials to see the effects of the annealing. This gave a range of different final materials with various permeability vs frequency behaviours, BH-curves and Barkhausen Noise. These new materials, in addition to the untreated as-cast ones,

Acknowledgements

provide a good range of samples to choose from for applications with different needs. Based on the results presented in this thesis, one can suggest that the best material to build DCCT cores would be the iron-based nanocrystallised Metglas Finemet FT-3 material. It shows a high permeability up to 10 kHz and a low coercivity of about 3.5 A m^{-1} , with a rounded BH-curve and saturation over 1 T. Regarding FBCTs, the cores need a very flat BH-curve with high permeability and minimum coercivity. From all the materials presented, Vacuumschmelze's cobalt-based Vitrovac 6025 G40 is the material that would be the most suitable. It has the lowest coercivity (0.84 A m^{-1}) and saturation of 0.5 T. However, the perfect material would need magnetic thermal annealing to create a high magnetic anisotropy in the material for a flat curve.

Keywords: soft magnetic materials, amorphous alloys, nanocrystalline alloys, DC Current Transformers, beam intensity measurements

Résumé

Dans les faisceaux utilisés au CERN, le nombre de particules est mesuré par une famille de dispositifs appelés BCT (Beam Current Transformers). Un de ces dispositifs est le transformateur de courant continu (DCCT) qui mesure le nombre total de particules dans les différents accélérateurs. Le DCCT est construit autour d'un cœur magnétique constitué de trois tores. Actuellement, les tores DCCT sont achetés auprès de quelques partenaires industriels. Cette situation pourrait entraîner des complications importantes pour le développement des DCCT. Premièrement parce que le choix de tore ne peut être fait que parmi ceux déjà développés et fabriqués. Deuxièmement, que les partenaires industriels généralement ne garantissent pas la disponibilité à long terme de leurs produits, ce qui pourrait se traduire aussi par des difficultés de maintenance futures. Troisièmement, les tores disponibles sur le marché n'ont pas été développés en fonction des applications envisagées par le CERN et pourraient donc ne pas être idéaux pour les DCCT. Ces trois facteurs, entre autres, ont mené à la décision d'étudier la possibilité d'une fabrication des tores en interne au CERN.

Les tores des transformateurs DCCT sont constitués d'un matériau magnétique doux en forme de ruban entre 20 et 30 microns d'épaisseur, enroulé en une forme toroïdale. Ce sont des alliages amorphes ou nanocristallins à base de cobalt et de fer qui présentent des perméabilités élevées et de faibles coercivités. Plusieurs alliages commerciaux dans leur état de fabrication amorphe ont été achetés après avoir premièrement identifié les paramètres clés des matériaux pour l'application, et après avoir contacté les fournisseurs et étudié les matériaux disponibles pour trouver les plus appropriés ; le choix a été fait en comparant les propriétés de base des alliages avec les besoins des instruments qui abriteront les tores magnétiques.

Ces matériaux ont ensuite été caractérisés pour déterminer comment les traiter thermiquement afin d'obtenir une gamme de différentes propriétés magnétiques finales. Cette étude a également permis d'établir les meilleurs candidats pour fabriquer les échantillons. Après cela, trois alliages ont été sélectionnés (un alliage à base de fer Finemet FT-3 de Metglas et deux matériaux à base de cobalt, 6025 G40 de Vacuumschmelze et 2705 M de Metglas) sur la base de leurs propriétés sans traitement thermique. Les tores et les rubans des matériaux sélectionnés ont ensuite été recuits à différentes températures et durées pour étudier l'effet des traitements. Trois traitements thermiques ont été effectués sur les échantillons sélectionnés, d'abord en dessous de la température de Curie, puis entre le point de Curie et la température de cristallisation et enfin au-dessus de la température de

Acknowledgements

cristallisation. Les mesures de ces échantillons ont été faites après le traitement thermique et comparées aux résultats des matériaux amorphes pour mesurer les effets du recuit. Cela a donné à la fin une gamme de matériaux finaux aux comportements de perméabilité, de fréquence, des courbes BH et de bruit Barkhausen différents. Ces matériaux traités ainsi que les matériaux amorphes fournissent une bonne gamme d'échantillons à choisir pour des applications et des besoins différents.

Sur la base des résultats présentés dans cette thèse, on peut suggérer que le meilleur matériau pour construire des tores DCCT serait le matériau Metglas FT-3 nanocristallisé à base de fer. Il montre une perméabilité élevée jusqu'à 10 kHz et une faible coercivité d'environ 3.5 A m^{-1} , avec une courbe BH arrondie et une saturation sur 1 T. En ce qui concerne les transformateurs rapides (FBCTs), les tores ont besoin d'une courbe BH très plate avec une perméabilité élevée et une coercivité minimale. De tous ces matériaux étudiés, le Vitrovac 6025 G40 à base de cobalt de Vacuumschmelze est le matériau qui conviendrait le mieux. Il a la plus faible coercivité (0.84 A m^{-1}) et une saturation de 0.5 T. Cependant, le matériau parfait nécessiterait un recuit thermique avec un champ magnétique pour créer une forte anisotropie magnétique dans le matériau et ainsi obtenir une courbe plate.

Mots clefs : matériaux magnétiques doux, alliages amorphes, alliages nanocristallins, transformateurs de courant continu, mesures d'intensité de faisceau

Contents

Acknowledgements	i
Abstract (English/Français)	iii
List of figures	xi
List of tables	xvii
Introduction	1
1 State of the art	5
1.1 History of current transformers at CERN	5
1.2 Principle of operation of DCCTs	6
1.3 Materials for beam instrumentation	8
1.3.1 Soft magnetic materials	9
1.3.2 Amorphous alloys	12
1.3.3 Nanocrystalline alloys	14
1.3.4 Thermal treatments	17
1.3.5 Material characterisation for transformer cores	18
1.4 Objectives of the thesis	22
2 Materials and Methods	23
2.1 Materials	23
2.2 Methods: Composition	23
2.2.1 Inductive Coupled Plasma - Optical Emission Spectrometry (ICP-OES)	23
2.2.2 X-ray Photoelectron Spectroscopy (XPS)	24
2.2.3 Scanning Electron Microscopy- Energy-Dispersive X-ray spectroscopy (SEM-EDX)	24
2.2.4 Electron Micro Probe Analyser (EMPA)	25
2.3 Methods: Crystallinity	25
2.3.1 X-ray Diffraction (XRD)	25
2.3.2 High Energy X-ray Diffraction (HE-XRD)	25
2.3.3 Transmission Electron Microscopy (TEM)	25

Contents

2.4	Methods: Phase transformation	26
2.4.1	Differential Scanning Calorimetry (DSC)	26
2.4.2	High Temperature in-situ XRD (HT-XRD)	26
2.5	Methods: Magnetic properties	27
2.5.1	Impedance analyses	27
2.5.2	BH-curve measurement	28
2.5.3	Curie temperature measurements	29
2.5.4	Magnetic domain imaging	31
2.5.5	Barkhausen Noise (BN)	32
2.5.6	Other physical properties	32
3	Iron-based alloys results	35
3.1	Composition	35
3.1.1	XPS	35
3.1.2	SEM-EDX	36
3.1.3	EMPA	37
3.1.4	Assessment	37
3.2	Crystallinity	38
3.2.1	XRD	38
3.2.2	HE-XRD	39
3.2.3	TEM	42
3.2.4	Assessment	48
3.3	Phase transformation	48
3.3.1	DSC	48
3.3.2	High Temperature in-situ XRD (HT-XRD)	51
3.3.3	Assessment	54
3.4	Magnetic properties	56
3.4.1	Impedance analyses	56
3.4.2	BH-curve measurements	58
3.4.3	Curie temperature measurements	60
3.4.4	VSM and AGM	64
3.4.5	Magnetic domain imaging	67
3.4.6	Barkhausen Noise	74
3.5	Other physical properties	75
3.5.1	Thickness	75
3.5.2	Density	76
3.6	Results discussion	76
4	Cobalt-based alloy results	77
4.1	Composition	77
4.1.1	XPS	77
4.1.2	SEM-EDX	78
4.1.3	EMPA	79

4.1.4	Assessment	79
4.2	Crystallinity	79
4.2.1	XRD	79
4.2.2	HE-XRD	79
4.2.3	TEM	81
4.2.4	Assessment	86
4.3	Phase transformation	86
4.3.1	DSC	86
4.3.2	High Temperature in-situ XRD (HT-XRD)	88
4.3.3	Assessment	91
4.4	Magnetic Properties	93
4.4.1	Impedance analyses	93
4.4.2	BH-curve measurements	93
4.4.3	Curie temperature measurements	95
4.4.4	VSM	97
4.4.5	Magnetic domain imaging	99
4.4.6	Barkhausen Noise (BN)	104
4.5	Thickness	105
4.6	Density	105
4.7	Results discussion	106
5	Results of thermal treatments	107
5.1	Choice of materials	107
5.1.1	Thermal treatments	108
5.2	Annealing results	109
5.2.1	F samples ($T_C = 327^\circ\text{C}$, $T_x = 511^\circ\text{C}$)	109
5.2.2	V samples ($T_C = 222^\circ\text{C}$, $T_x = 550^\circ\text{C}$)	114
5.2.3	M samples ($T_C = 361^\circ\text{C}$, $T_x = 513^\circ\text{C}$)	118
5.2.4	Summary of results	122
6	Conclusions and outlook	125
6.1	Conclusions	125
6.1.1	Iron-based alloys	125
6.1.2	Cobalt-based alloys	128
6.1.3	Thermally treated cores	130
6.1.4	Proposed materials for transformer cores	133
6.2	Outlook	133
A	Iron-based alloys results	135
A.1	Composition: XPS	135
A.2	Crystallinity: TEM of sample MA	135
A.3	Phase transformation: DSC	136
A.4	Magnetic properties: Magnetic domain imaging	137

Contents

A.4.1	Sample C1	137
A.4.2	Sample C6	137
B	Cobalt-based alloy results	141
B.1	Composition: XPS	141
B.2	Crystallinity: HE-XRD	141
B.3	Phase transformation	142
B.3.1	DSC	142
B.3.2	TEM	143
B.4	Magnetic properties	143
B.4.1	Curie Temperature: Kappabridge	143
B.4.2	Magnetic domain imaging: MOKE	144
C	Magnetism basics [1], [2]	145
C.0.1	Types of magnetic materials	147
	Bibliography	159
	Curriculum Vitae	161

List of Figures

1	Overview of the CERN accelerator complex [3].	2
1.1	Production of even harmonics [4].	7
1.2	Principle of the two-core magnetic modulator, adapted from [5].	7
1.3	DCCT cores response only with the modulation signal (left) and with beam and modulation signal (right). Adapted from [6].	8
1.4	Coercivity and saturation induction for different types of materials [1]. . .	10
1.5	Coercivity vs. grain size for soft magnetic materials [7]	10
1.6	Magnetic domain formation. Adapted from [8].	12
1.7	Crysallisation schematic of Finemet [41].	15
1.8	TEM images of standard Finemet ($\text{Fe}_{73.5}\text{Cu}_1\text{Nb}_3\text{Si}_{13.5}\text{B}_9$): (a) as-cast, (b) 2 minutes at 550 °C, (c) 2 hours at 550 °C. Finemet without Nb ($\text{Fe}_{76.5}\text{Cu}_1\text{Si}_{13.5}\text{B}_9$): (d) 8 seconds at 550 °C, (e) 120 seconds at 550 °C, (f) 1 hour at 550 °C [9].	16
1.9	BH-curves of Metglas (Fe-Ni base), as cast, longitudinally and transversely-field annealed. Adapted from [10].	19
1.10	BH-curves (at 0.1 Hz) and permeability (at 50 Hz) of Finemet annealed for 1 h at 540 °C without (R) and with a magnetic field applied parallel (Z) and transversely (F2) to the magnetic path. Sample F1 was first crystallized at 540 °C and subsequently transverse field annealed at 350 °C [7].	20
1.11	High resolution distortion-free Kerr microscope [11].	21
2.1	Second BH-curve setup.	29
2.2	Barkhausen noise setup.	32
2.3	Barkhausen noise setup.	33
3.1	XPS surface results for samples C1 (a) and MA (b).	36
3.2	XPS in-depth results for sample F.	37
3.3	XRD diffraction patterns for C1 (a), C6 (b), F (c) and MA (d).	38
3.4	Superimposed diffraction patterns of samples C1 and C6.	39
3.5	MA crystallographic structure refinement.	40
3.6	Fe_3Si -type structure simulation for sample MA.	40
3.7	DP refinement for sample MA with Fe_3Si -type structure.	41

List of Figures

3.8	TEM images for sample C1: bright field (a), dark field (b,c), high-resolution (d). The arrow in the insert shows the selected ring in the DP.	42
3.9	DP of sample C1 with the theoretical rings of $\text{Fe}_{0.91}\text{Si}_{0.09}$ superimposed. .	43
3.10	TEM images for sample C6: bright field (a) and dark field (b,c).	44
3.11	DP of sample C6 with the theoretical rings of $\text{Fe}_{0.91}\text{Si}_{0.09}$ superimposed. .	44
3.12	TEM images for sample F: bright field (a) and dark field (b,c,d).	45
3.13	DP of sample F with the theoretical rings of $\text{Fe}_{0.91}\text{Si}_{0.09}$ superimposed. .	46
3.14	TEM images for sample MA: bright field (a), dark field (b,c) and high-resolution (d).	47
3.15	DP of sample MA with the theoretical rings of $\text{Fe}_{0.91}\text{Si}_{0.09}$ superimposed.	47
3.16	Heating rate dependence of crystallisation onset and peak temperatures for iron-based samples.	49
3.17	HT-XRD analysis for sample C1.	51
3.18	Phase analysis for sample C1.	52
3.19	Grain size study for sample C1.	52
3.20	HT-XRD analysis for sample C6.	53
3.21	Phase analysis for sample C6.	53
3.22	HT-XRD analysis for sample F.	53
3.23	Phase analysis for sample F.	54
3.24	Relative complex permeability for three F cores.	57
3.25	Relative complex permeability for iron-based cores.	57
3.26	Comparison of BH-curve setups: first setup (F-1) and new setup (F-2 and F-3).	58
3.27	Comparison of BH-curves of iron-based alloys with the first setup.	59
3.28	Curie Temperatures using VSM for samples C1 (a) and C6 (b).	60
3.29	Curie Temperature hysteresis curve for sample C6 at $20^\circ\text{C min}^{-1}$	61
3.30	Kappabridge measurements of sample C1.	62
3.31	Kappabridge measurements of sample MA.	63
3.32	VSM magnetisation curves for sample C1 (a) and a close-up of the central part (b).	65
3.33	VSM magnetisation curves for sample C6 (a) and a close-up of the central part (b).	65
3.34	VSM magnetisation curves for sample MA (a) and a close-up of the central part (b).	66
3.35	Fresnel mode images for sample MA analysed with TEM, over-focused (a) and under-focused (b). Arrows indicate a domain wall.	67
3.36	Domain image with superimposed TIE calculation. Arrow indicates a domain wall.	68
3.37	BH-loop (a) and MOKE-loop (b) of sample C1.	69
3.38	Magnetic domain observation for sample C1: whole sample (a), non-stressed (b), semi-stressed (c) and stressed (d).	70
3.39	BH-loop (a) and MOKE-loop (b) of sample C6.	71

3.40	Magnetic domain observation for sample C6: whole sample (a), non-stressed (b), semi-stressed (c) and stressed (d).	71
3.41	Details of the circular-structured domains for sample C6.	72
3.42	BH-loop (a) and MOKE-loop (b) of sample F.	73
3.43	Magnetic domain observation for sample F: whole sample (a), non-stressed (b), semi-stressed (c) and stressed (d).	74
3.44	Barkhausen Noise comparison for iron-based alloys.	75
4.1	XPS surface results for samples V (a) and N (b).	78
4.2	XPS in-depth results for sample V.	78
4.3	XRD diffraction patterns for V (a), N (b), M (c).	80
4.4	Diffraction Pattern of sample V.	81
4.5	TEM images for sample V: bright field (a), dark field (b,c), high resolution (d). The arrow in the insert shows the selected ring in the DP.	82
4.6	DP of sample V with the theoretical rings of hexagonal cobalt (a) and Co ₂ Si (b) superimposed.	82
4.7	TEM images for sample N: bright field (a,b), dark field (c,d).	84
4.8	DP of sample N with the theoretical rings of hexagonal cobalt superimposed.	84
4.9	TEM images for sample M: bright field (a), dark field (b,c), high resolution (d).	85
4.10	DP of sample M with the theoretical rings of hexagonal cobalt (a) and Co ₂ Si (b) superimposed.	85
4.11	Heating rate dependence of crystallisation onset and peak temperatures for cobalt-based samples.	87
4.12	HT-XRD analysis for sample V.	89
4.13	Phase analysis for sample V after annealing.	89
4.14	HT-XRD analysis for sample N.	90
4.15	Phase analysis for sample N after annealing.	90
4.16	HT-XRD analysis for sample M.	91
4.17	Diffraction pattern of sample M after annealing.	91
4.18	Relative complex permeability for three V cores.	94
4.19	Relative complex permeability for the cobalt-based materials.	94
4.20	Comparison of BH-curves for the cobalt-based alloys.	95
4.21	Curie Temperature hysteresis curve for sample N at 20 °C min ⁻¹	96
4.22	Kappabridge measurement for sample V.	97
4.23	VSM magnetisation curves for sample C1 (a) and a close-up of the central part (b).	98
4.24	VSM magnetisation curves for sample N (a) and a close-up of the central part (b).	98
4.25	VSM magnetisation curves for sample M (a) and a close-up of the central part (b).	99
4.26	MFPM measurement for sample V.	100

List of Figures

4.27	BH-loop (a) and MOKE-loop (b) of sample V.	100
4.28	Magnetic domain observation for sample V: whole sample (a), non-stressed (b), semi-stressed (c) and stressed (d).	101
4.29	BH-loop (a), MOKE-loop (b), and MOKE-loop of the whole sample (c) of material N.	102
4.30	Magnetic domain observation for sample N: whole sample (a), non-stressed (b), c) and semi-stressed (d).	102
4.31	BH-loop (a), and MOKE-loop (b) and whole-sample MOKE loop (c) of sample M.	103
4.32	Magnetic domain observation for sample M: whole sample (a), non-stressed (b) and semi-stressed (c, d).	104
4.33	Barkhausen Noise comparison for cobalt-based alloys.	105
5.1	Open oven with core and ribbons inside.	108
5.2	Permeability analysis of sample F before and after annealing below T_C . . .	109
5.3	BH-curve of sample F before and after annealing below T_C	110
5.4	BN of sample F before and after annealing below T_C	110
5.5	Permeability analysis of sample F before and after annealing between T_C and T_x	111
5.6	BH-curve of sample F before and after annealing between T_C and T_x . . .	112
5.7	BN of sample F before and after annealing between T_C and T_x	112
5.8	Permeability analysis of sample F before and after annealing above T_x . . .	113
5.9	BH-curve of sample F before and above T_x	113
5.10	BN of sample F before and after annealing above T_x	114
5.11	Permeability analysis of sample V before and after annealing below T_C . .	115
5.12	BH-curve of sample V before and after annealing below T_x	115
5.13	Permeability analysis of sample V before and after annealing between T_C and T_x	116
5.14	BH curve of sample V before and after annealing between T_C and T_x . . .	116
5.15	BN of sample V before and after annealing below T_C (V-C) and between T_C and T_x (V-S).	117
5.16	Permeability of samples V-X1 and V-X2 annealed above T_x	117
5.17	Permeability analysis of sample M before and after annealing below T_C . .	118
5.18	Explanation of the Perminvar-type loop, adapted from [12].	119
5.19	BH curve of sample M before and after annealing below T_C	119
5.20	Permeability analysis of sample M before and after annealing between T_C and T_x	120
5.21	BH curve of sample M before and after annealing between T_C and T_x . . .	121
5.22	BN of sample M before and after annealing below T_C (M-C) and between T_C and T_x (M-S).	121
5.23	Permeability analysis of sample M after annealing above T_x	122
A.1	XPS surface results for samples C6 (a) and F (b).	135

A.2	High resolution TEM images for sample MA.	135
A.3	Magnetic domains of sample C1.	137
A.4	Magnetic domains of sample C6.	137
A.5	Magnetic domains of sample C6.	138
A.6	Magnetic domains of sample C6.	139
A.7	Magnetic domains of sample F.	139
A.8	Magnetic domains of sample F in the stressed area.	140
B.1	XPS surface results for sample M.	141
B.2	HE-XRD Diffraction Patterns of sample N (a) and sample M (b).	141
B.3	High-Resolution TEM of sample M	143
B.4	Magnetic domains of sample V.	144
B.5	Magnetic domains of sample N.	144
C.1	Relationship between magnetic field (H) and inductance (B) [1].	145

List of Tables

1.1	Summary of main families of nanocrystalline alloys [13].	17
3.1	Carbon and oxygen surface content [at. %].	36
3.2	SEM-EDX results for iron-based materials.	36
3.3	EMPA results for iron-based materials [at. %].	37
3.4	HE-XRD results for iron-based alloys.	39
3.5	C1 DP rings vs $\text{Fe}_{0.91}\text{Si}_{0.09}$ DP.	43
3.6	C6 DP rings vs $\text{Fe}_{0.91}\text{Si}_{0.09}$ DP.	44
3.7	F DP rings vs $\text{Fe}_{0.91}\text{Si}_{0.09}$ DP.	45
3.8	MA DP rings vs $\text{Fe}_{0.91}\text{Si}_{0.09}$ DP.	46
3.9	PerkinElmer DSC 8000 T_x results for iron-based alloys at $10^\circ\text{C min}^{-1}$. . .	48
3.10	Netzsch DSC 404 C T_x results for iron-based alloys at $10^\circ\text{C min}^{-1}$	50
3.11	Netzsch DSC 404 C melting temperature results for iron-based alloys at $10^\circ\text{C min}^{-1}$	50
3.12	HT-XRD results for iron-based alloys.	54
3.13	Relative difference between both DSC measurements.	55
3.14	Comparison of onset of crystallisation temperatures for iron-based alloys. .	55
3.15	Absolute relative difference between the onset crystallisation temperature measured by both DSC's and HT-XRD.	56
3.16	Impedance results for iron-based alloys.	56
3.17	Comparison of both BH curve setups for sample F.	58
3.18	BH curve results for iron-based alloys	59
3.19	Curie temperature at $10^\circ\text{C min}^{-1}$ for iron-based alloys with TGA.	62
3.20	Curie temperature at $11^\circ\text{C min}^{-1}$ for iron-based alloys with Kappabridge. .	63
3.21	Curie temperature comparison for TGA, Kappabridge, VSM and literature values [$^\circ\text{C}$].	63
3.22	Difference between first crystallisation temperature and T_C [$^\circ\text{C}$].	65
3.23	VSM saturation summary for iron-based alloys.	66
3.24	Thickness results of iron-based alloys.	75
3.25	Density results of iron-based alloys in g cm^{-3}	76
4.1	Carbon and oxygen surface content.	77
4.2	SEM-EDX results for cobalt-based alloys.	78

List of Tables

4.3	EMPA results for cobalt-based alloys.	79
4.4	HE-XRD results for cobalt-based alloys.	80
4.5	V DP rings vs Co_2Si and Co DP rings.	81
4.6	N DP rings vs hexagonal cobalt's DP.	83
4.7	M DP rings vs Co_2Si and Co DP rings.	83
4.8	PerkinElmer DSC 8000 results for cobalt-based alloys at $10^\circ\text{C min}^{-1}$	86
4.9	Netzsch DSC 404 C results for cobalt-based alloys at $10^\circ\text{C min}^{-1}$	88
4.10	Melting temperatures for cobalt-based alloys.	88
4.11	HT-XRD results for iron-based alloys.	90
4.12	Relative difference between both DSC measurements.	92
4.13	Onset of crystallisation temperatures comparison for cobalt-based alloys.	92
4.14	Absolute relative difference between the onset crystallisation temperature measured by both DSC's and HT-XRD.	92
4.15	Impedance results for cobalt-based alloys.	93
4.16	BH curve results for cobalt-based alloys.	95
4.17	Curie temperature at $10^\circ\text{C min}^{-1}$ for cobalt-based alloys with TGA.	96
4.18	Curie temperature at $11^\circ\text{C min}^{-1}$ for cobalt-based alloys with Kappabridge.	96
4.19	T_C comparison for TGA, Kappabridge, VSM and literature values [$^\circ\text{C}$].	97
4.20	Difference between first crystallisation temperature and T_C [$^\circ\text{C}$].	97
4.21	VSM saturation summary for cobalt-based alloys.	99
4.22	Thickness results of cobalt-based alloys.	105
4.23	Density results of cobalt-based alloys in g cm^{-3}	106
5.1	Summary of materials to be annealed.	107
5.2	Comparison of parameters before and after annealing.	122
5.3	Comparison of parameters before and after annealing.	124
A.1	Iron-based alloys results at 5°C min^{-1}	136
A.2	Iron-based alloys results at $20^\circ\text{C min}^{-1}$	136
A.3	Iron-based alloys results at $50^\circ\text{C min}^{-1}$	136
B.1	Cobalt-based alloy results at 5°C min^{-1}	142
B.2	Cobalt-based alloy results at $20^\circ\text{C min}^{-1}$	142
B.3	Cobalt-based alloy results at $50^\circ\text{C min}^{-1}$	142

Introduction

The European Organization for Nuclear Research (CERN in its original French acronym) is situated in Geneva, Switzerland and houses a series of machines that accelerate particles successively increasing their energies. The Large Hadron Collider (LHC) is the largest accelerator in the complex, where two counterrotating proton beams travelling inside two separate beam pipes are accelerated up to the energy of 6.5 TeV per proton. The beams can collide at four different points around the LHC, where large particle detectors are located: ALICE (A Large Ion Collider Experiment), ATLAS (A Toroidal LHC ApparatuS), CMS (Compact Muon Solenoid) and LHCb (Large Hadron Collider beauty). Other facilities at CERN include the Antiproton Decelerator (AD), the Online Isotope Mass Separator (ISOLDE) and the neutron Time-Of-Flight facility (nTOF). Figure 1 shows an overview of the whole complex, with the dates when the different accelerators were built and their circumferences.

In order to operate the complex safely and efficiently, different properties of the beam are continuously measured with techniques collectively referred to as Beam Instrumentation. The basic beam parameters which are observed in most accelerators include the transverse position of the beam inside the beam pipe, transverse and longitudinal distribution of particles (commonly called beam profiles) as well as beam intensity, which denotes the number of electric charges forming the beam.

The beams used at CERN are not a continuous string of particles, but a continuous succession of packets called bunches, that make up a bunch train. The presence of such a temporal structure has significant consequences for designers of instruments that observe the beam parameters, as different measurement techniques present different sensitivities to fast and slow signals.

The instruments of interest for this dissertation are referred to as Beam Current Transformers (BCTs). These devices are capable of measuring the beam intensity by measuring the electric current created by the motion of electric charges forming the beam. In general, all the BCTs use cores made of magnetic materials where the beam acts as the primary winding. An in-depth explanation of the principle of operation of BCTs is available in [14].

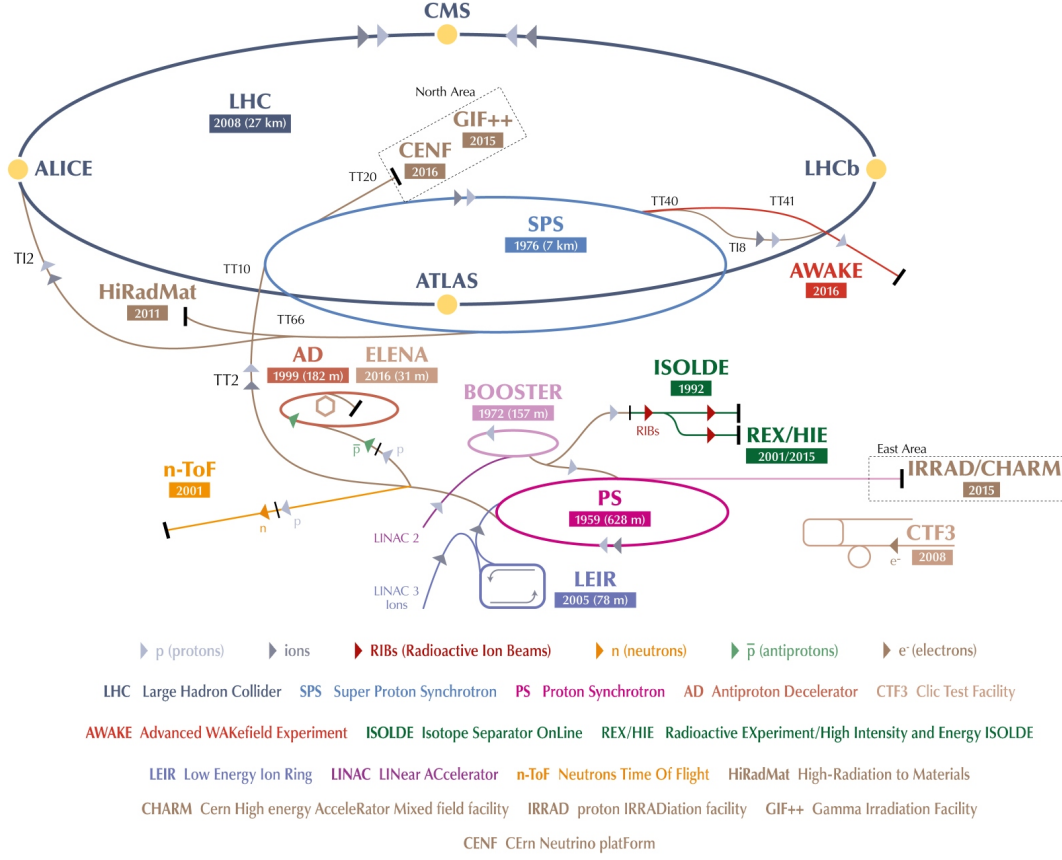


Figure 1 – Overview of the CERN accelerator complex [3].

The BCTs used at CERN can be divided into three distinct categories:

- Direct Current Transformers: DC Current Transformers (DCCTs) are the only instruments that measure the DC (or 0 Hz) component of the beam intensity which is equivalent to measuring the total beam current.
- Alternating Current Transformers: at CERN, more commonly called Fast Beam Current Transformers (FBCTs), give a high quality image of the bunches forming the beam.
- Other transformer-like devices: other devices such as the Integrating Current Transformer (ICT) or the Wall Current Transformer (WCT).

In an ideal accelerator, where all the particles are contained within well-defined bunches, the information provided by the DCCTs would be redundant to the FBCT measurements. In reality, however, some of the particles escape the main bunches and flow freely around the machine or might form micro-bunches. Both of these phenomena are undetectable for the FBCTs. Moreover, accurate absolute calibration of the DCCTs is significantly easier than calibration of the FBCTs [15]. Therefore, most of CERN accelerators use both the

DCCTs and FBCTs to provide complementary measurements of the beam intensity.

As the scientific goals set for CERN are becoming more challenging, the increasing requirements placed on beam instrumentation need continuous research into the most fundamental limitations of all measurement techniques. In the case of the BCTs, the magnetic cores which are used to build them are the most crucial component and, ultimately, can limit the performance reach of the instrument.

As of today, the magnetic cores used in CERN BCTs are purchased from industry. This clearly limits the choice of available cores and could also lead to core shortage should a supplier stop providing a certain product. The primary objective of this thesis is to explore the possibility of replacing the off-the-shelf cores used in DCCTs by ones manufactured in-house. This is achieved by performing an in-depth analysis of the available magnetic materials, identifying and purchasing the best candidates, characterising the raw materials and finally constructing and measuring of small sample cores.

The structure of the thesis is as follows:

- **Chapter 1: State of the art**, where the context of the work is introduced and the important scientific concepts are described;
- **Chapter 2: Materials and methods**, where the relevant methods and characterisation techniques are described;
- **Chapter 3: Iron-based alloys results**, where the results of characterisation tests performed on iron-based alloys are presented;
- **Chapter 4: Cobalt-based alloys results**, where the results of characterisation tests performed on cobalt-based alloys are presented;
- **Chapter 5: Results of thermal treatments**, where the effects of different thermal treatments on raw materials and assembled test cores are shown;
- **Chapter 6: Conclusions and outlook**, where the results are summarised and discussed and an outlook for the future is provided.

1 State of the art

1.1 History of current transformers at CERN

Beam Current Transformers have been used at CERN since the 1960s to measure the number of particles in the beam [16]. The first beams in the Proton Synchrotron (PS) were measured using this method, where the reading of the output voltage of the transformer was proportional to the beam's intensity. However, regular current transformers are unable to measure Direct Current (DC), which became a problem when beam storage rings started being used. Due to this, the first DC Current Transformers (DCCTs) were developed at CERN in 1969 to measure the DC beam current in the Intersecting Storage Rings (ISR), located after the PS.

One of the limitations that the DCCT presents is its sensitivity. For some applications that require measurement of currents smaller than $1\text{ }\mu\text{A}$, the Cryogenic Current Comparator (CCC) was developed by I.K. Harvey in 1972 [17]. The CCC was developed to compare DC current ratios. Nowadays it is used in combination with Superconducting Quantum Interference Devices (SQUIDS) to measure the azimuthal component of the beam's magnetic field, which is proportional to the current. CCCs require cores that are able to work in cryogenic conditions, maintaining a certain permeability at these very low temperatures. Only recently, have studies been done in order to compare the performance of different materials in cryogenic environment [18].

Due to the fact that the DCCT cannot measure the intensity of individual bunches or bunch trains, Alternating Current (AC) transformers are used. For this purpose, the Bergoz Instrumentation S.A.R.L. Fast Beam Current Transformer is used at CERN. The FBCT core is reported to be made of cobalt-based amorphous and/or nanocrystalline materials, depending on the specifications of the instrument. This AC Current Transformer has a bandwidth of up to 2 GHz [19].

In recent years, new beam monitors have been developed at CERN to improve intensity

measurements. One of them, The Integrating Current Transformer (ICT) is a monitor designed in collaboration with Bergoz Instrumentation S.A.R.L. for accurate measurements of the bunch intensity in the LHC. Two high-permeability nanocrystalline magnetic cores are enclosed in a capacitive box which limits the beam frequency spectrum seen by the transformer to minimise beam-position-dependency. The ICT principle of operation requires the cores to exhibit a small, but non-zero, coercivity [20], [21].

1.2 Principle of operation of DCCTs

The transformer is installed so that the beam passes through approximately the centre of the instrument, creating a single turn primary winding. The secondary winding is distributed around the transformer's core and picks up the induced beam signal. The basic principle of operation is thoroughly explained in reference [6]. It is based on the non-linear relationship of the core's magnetic material between the applied magnetic field (H) and the magnetic induction (B), the BH-curve. If a core is wound and fed a modulation current, it will create magnetic induction in the material, which in turn creates a magnetic field in the coil. This signal can be either a voltage or a current, producing a triangular, sinusoidal or rectangular waveform, depending on the magnetic properties of the material [4]. For such signals, the created waveform $H(t)$ will contain only odd harmonics when the B-H curve is perfectly symmetrical as can be seen in a simplified model in Figure 1.1, where hysteresis is not considered for simplification. However, if the beam is passing at the same time as the modulation current, an external field H_{ext} will be created in the core, making $H(t)$ asymmetrical. This will imply the apparition of even harmonics, especially the second harmonic of the modulation signal (at twice its frequency). The effect of adding hysteresis to all of these assumptions is mainly the shift in phase of the harmonics.

This external field, H_{ext} , cannot be measured directly from the second harmonic of $H(t)$ nor $B(t)$, as the mathematical relationship is difficult to express and is not linear [6]. An easier solution is to add an additional feedback winding to the core in order to compensate for the field created by the beam, suppressing the second harmonic created by it. The current needed to suppress the second harmonic will therefore be a direct measure of the beam current. This is the principle of a zero-flux detector.

To suppress the modulation frequency and therefore the first harmonic, a second core may be added to the setup. The modulation winding of this core is wound in the opposite direction to the first core's winding as can be seen in Figure 1.2. If the two cores are identical, with no beam the difference of the two $H(t)$ waveforms will be zero as shown in Figure 1.3. When the beam then passes through the two cores, even harmonics appear. An external feedback current winding around both cores can compensate for H_{ext} . This current can be varied automatically to keep the second harmonic at zero, which will therefore indicate the beam current which was causing it. This second harmonic technique

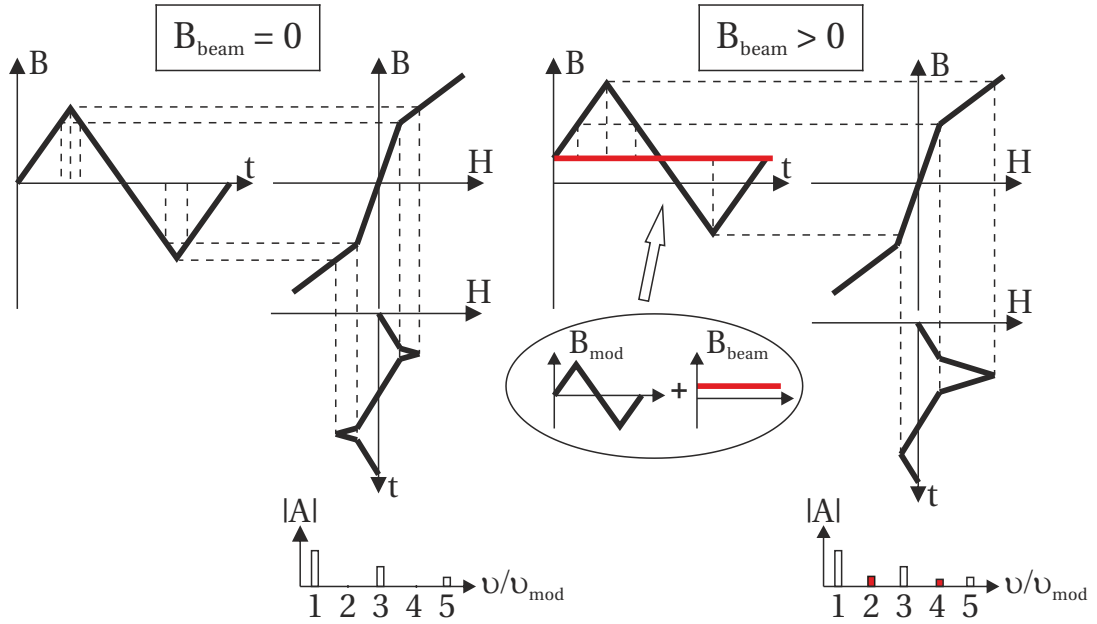


Figure 1.1 – Production of even harmonics [4].

results in a higher sensitivity and a better signal to noise ratio [5]. Figure 1.2 shows the basic principle of the two core configuration.

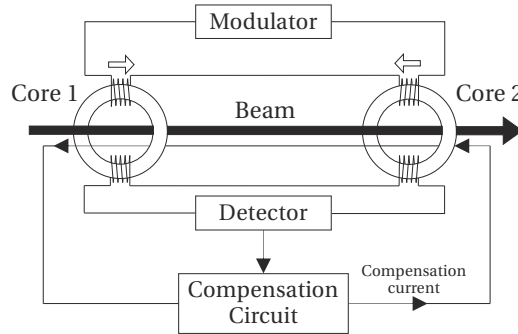


Figure 1.2 – Principle of the two-core magnetic modulator, adapted from [5].

This two-core configuration will be able to measure only the DC component of the beam's current. A third core is therefore needed in the transformer in order to measure the AC component. An additional improvement was achieved in 1989 by improving the excitation and demodulation circuits, which led to noise reduction. The DCCT was then renamed the Parametric Current Transformer [22].

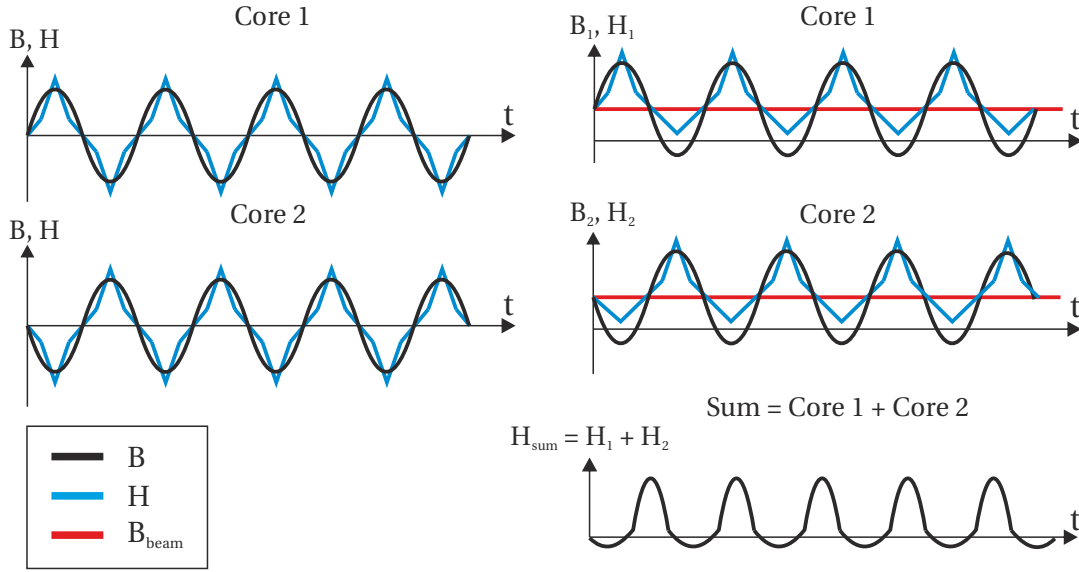


Figure 1.3 – DCCT cores response only with the modulation signal (left) and with beam and modulation signal (right). Adapted from [6].

1.3 Materials for beam instrumentation

Typically, transformer cores are made out of wound ribbon of thicknesses of about $30\text{ }\mu\text{m}$. For the first DCCTs built, a 70 % - 80 % iron-nickel alloy called Ultraperm 10, from Vacuumschmelze GmbH & Co was used [23]. The first studies compare this alloy with ferrites, stating that the higher permeability of this alloy leads to a faster response to a pulse. It was already seen at this time that a smaller ribbon thickness of $10\text{ }\mu\text{m}$ limited the losses by Eddy currents (induced electric currents in the magnetic material due to magnetisation) in the core compared to the $50\text{ }\mu\text{m}$ ribbon [24]. In 1989, the material of the cores was changed to a $25\text{ }\mu\text{m}$ thick amorphous cobalt-based ribbon manufactured by Vacuumschmelze GmbH & Co. KG., Vitrovac 6025, with composition $(\text{CoFe})_{70}(\text{MoSiB})_{30}$. A DupontTM Mylar[®] foil of between $1\text{ }\mu\text{m}$ and $2\text{ }\mu\text{m}$ was added between the ribbon layers as insulation [22] in order to reduce these Eddy current losses.

As has been seen before, one of the most important characteristics for the DCCT is the pairing of cores in order to minimise the apparition of odd harmonics. This was already stated by Unser in 1981 [25]. This was done by measuring the BH-curves and the permeabilities of a wide range of cores, and then choosing the ones that showed the most similar characteristics. A simulation study was performed by Kottman [26] in order to determine the effects of the difference of the cores in the transformer's response. The main conclusions of this study were:

- the higher the permeability, the higher is the amplitude of the second harmonic. To obtain a high permeability, the alloy's microstructure should allow easy domain wall

motion as well as domain rotation. This means that the material should have low magnetocrystalline anisotropy and magnetostriction [13].

- there is a strong dependence between the transformer's response and the flatness of the saturation region. The flatter it is, the further the core goes into saturation, producing larger amplitude in the second harmonic
- the dependence of the amplitude of the second harmonic is not affected much by the coercivity of the material. However, for AC applications, it should be kept low to avoid losses
- the rounding of the shape of the BH-curve is also seen to have an effect on the output of the transformer, again affecting the amplitude of the second harmonic

This gives an idea of the importance of the material selection and core pairing for the DC Current Transformers. It is a critical step in the fabrication of the instrument and can determine its final read-out. A good choice of material is also critical for other beam monitors, each having specific requirements.

For this application, especially for the AC component, the losses in the magnetic material (called hysteresis loss) should be minimised. This energy comes also from two main sources [13]:

- Eddy currents that translate into resistive losses. In order to minimise them, electrical conductivity of the cross-section of the cores is decreased, often by laminating the material and sometimes by insulating these layers.
- Anomalous losses that are attributed to the motion of domain walls. To reduce these losses the domain wall motion may be reduced by thermally treating the cores.

1.3.1 Soft magnetic materials

As has just been discussed, most of the beam instruments mentioned require materials that will give large magnetisation changes as a result of small applied magnetic fields which is the definition of soft magnetic materials. There are different types of these materials, such as bcc (body centred-cubed) α -iron, silicon-iron alloys, fcc (face centred-cubed) α -cobalt, nickel-iron alloys, cobalt-iron alloys, soft ferrites, amorphous alloys and nanocrystalline alloys [27]. However, the permeabilities of most of these alloys are small compared to the nanocrystalline and amorphous alloys, and therefore more research and development has been done in these materials [13]. Magnetic materials are considered hard if their coercivity is around or larger than 10 kA m^{-1} and soft if it is less than 1000 A m^{-1} . Soft magnetic materials are characterised as well for having a high saturation magnetisation (up to 2 T), high maximum relative permeability (up

to 600 000), small remanence and hysteresis loops, a rapid response to high-frequency magnetic fields, a high Curie temperature (due to the presence of iron, cobalt or nickel) and a high electrical resistivity [1], [28]. Figure 1.4 shows the coercivity and saturation induction (B_s) of different magnetic materials.

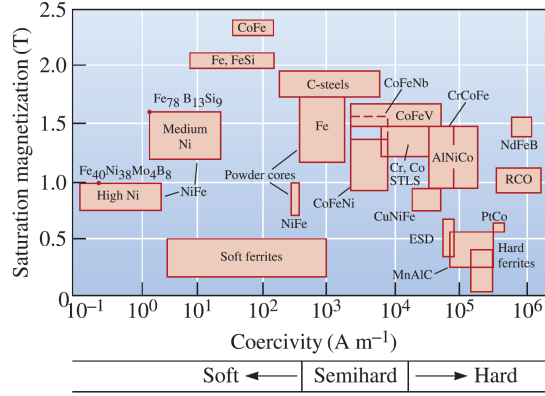


Figure 1.4 – Coercivity and saturation induction for different types of materials [1].

Microstructure, and especially the structural correlation length is directly related to the magnetic properties, as it has a direct influence on the coercivity of the material as can be seen on Figure 1.5. Starting from atomic distances in amorphous alloys up to millimetre grain sizes (D), coercivity steeply increases following a D^6 -power law reaching a maximum and then decreasing again for grain sizes above 150 nm according to the $1/D$ law for polycrystalline magnets [7]. Permeability shows a similar behaviour, being essentially inversely proportional to coercivity.

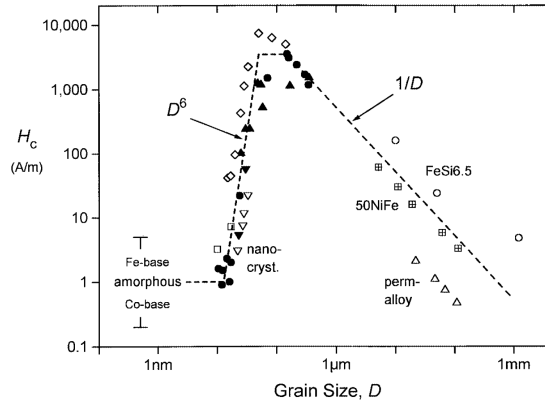


Figure 1.5 – Coercivity vs. grain size for soft magnetic materials [7]

The decrease of coercivity in nanocrystalline materials is not caused by the same mechanism as the superparamagnetic phenomena. Superparamagnetism is not interesting for soft magnetic applications since changes in magnetisation require large magnetic fields due to their low permeability. Magnetic softening occurs when the structural correlation length becomes smaller than the ferromagnetic exchange length, which is in the order of

nanometres. When this happens, the magnetic moment of adjacent grains align, which in turn makes the total anisotropy different than the easy magnetisation directions of the individual grains [29]. The local anisotropies are averaged out by the exchange interaction, and the net anisotropy effect on the magnetisation process is zero. The most important contributions to this anisotropy (from highest to lowest) are [30]:

- magneto-crystalline anisotropy, mainly caused by spin-orbit interactions, is the preference of magnetisation vector to align with the easy crystal axes [11]. The practical consequence is that more energy is required to magnetise the material in certain directions with respect to others.
- magneto-elastic anisotropy, also caused by spin-orbit interactions, but it affects the dimensions of the lattice when subjected to a magnetic field, inducing strains in the material. When the spins rotate due to the magnetic field, the electronic orbitals move causing a change in the electrostatic energy and therefore interfering with the lattice.
- anisotropies induced by annealing

The effective magneto-crystalline anisotropy needs to be low for good soft magnetic behaviour, which happens in both amorphous and nanocrystalline materials by the averaging effect of the exchange interaction. However, superior soft magnetic properties are achieved when magnetostriction (the spontaneous deformation of the crystal lattice due to magnetisation) is zero or low, as it reduces magneto-elastic anisotropy (from internal or external mechanical stress). Internal stresses can be introduced during the fabrication process or when winding the material into its final shape, degrading the magnetic properties. In the as-cast state, these stresses can go up to 100 MPa [30].

Iron, for example, has easy $\langle 100 \rangle$, hard $\langle 111 \rangle$ and medium $\langle 110 \rangle$ crystallographic directions. This gives a cubic symmetry anisotropy that in case of application of inhomogeneous stresses to the material, would give domains in more than one of the easy axes giving 90° domain walls (where magnetisation rotates 90° from one domain to another) [11].

In magnetic materials larger than nanometres, the magnetostatic self-interaction of the material leads to magnetisation inhomogeneities in order to decrease the stray field of the material. This leads to the formation of regions with different magnetised directions called magnetic domains. As shown in Figure 1.6, the stray field of the sample is reduced if the material is subdivided into smaller domains with opposing directions. Further reduction and even elimination can be achieved by the formation of "closure domains" near the edge of the sample.

This concept was first introduced by Weiss in 1907 and explains why ferromagnetic materials can be demagnetised below their Curie temperature. Domains are separated by comparatively thin domain walls, as the magnetisation inside the domains lies along easy

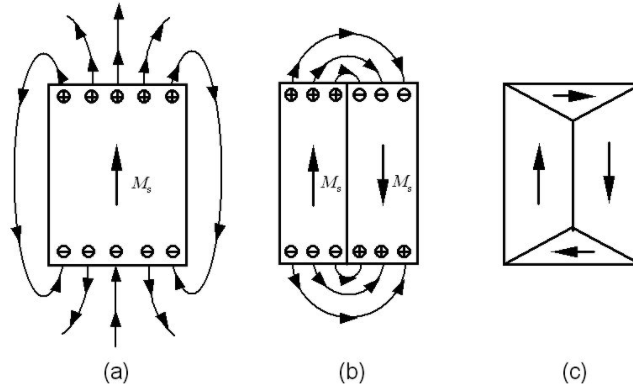


Figure 1.6 – Magnetic domain formation. Adapted from [8].

directions, whereas the transition between two easy magnetisation directions involves energetically unfavourable spin orientations. As a consequence, magneto-crystalline anisotropy favours narrow domain walls with thicknesses of hundreds or thousands of atomic distances [31], [8].

During magnetisation, magnetic domain walls move through the material sweeping from the maximum external field to the minimum. "Pinning" or hindrance of these walls leads to high-loss behaviour. One might think that nanocrystalline materials, having large amounts of grain boundaries and therefore potential pinning-centres, would have very high losses. However, it has been seen that if the grain diameter is below the magnetic exchange length, the magneto-crystalline anisotropy energy is averaged over the exchange volume and yields very small values. This allows the domain wall to pass without impediments through the material [32].

1.3.2 Amorphous alloys

Historically, the first report of amorphous metallic alloys (or bulk metallic glasses) was made by Kramer in the 1930's, produced by vapour deposition. In 1950, A. Brenner et al. [33] electrodeposited high nickel content phosphorus alloys that showed only one broad diffuse peak in the X-ray scattering pattern, indicating a large variation of the neighbouring atomic distances [8]. Such alloys have been in use for many years as hard, wear and corrosion resistant coatings. It was not until 1960 that Duwez and his team discovered a method of preparing amorphous alloys by direct quenching from the melt [34].

These alloys have only short range order, no symmetries nor internal structure and therefore no crystal grains nor boundaries. This leads to excellent soft magnetic properties [28]. The advantages of an amorphous local structure were primarily seen in the reduction of magnetic anisotropy and the improvement of related properties like

hysteresis and permeability. This random atomic structure also leads to greater values of electrical resistivity compared to common metallic alloys ($\rho \geq 100 \mu\Omega \text{ cm}$), enabling higher frequency operation [9]. Their density can also be up to a few percent lower compared to crystalline material with the same composition, associated with a higher amount of free volume in the structure.

Metallic glasses present disadvantages such as lower magnetisation (and saturation induction) relative to the pure alternatives, deriving from the necessity to include glass stabilising elements, and costly processing [9].

Magnetostriction of a completely saturated sample is typically 20 ppm to 40 ppm for iron-rich alloys and -5 ppm to -3 ppm for cobalt-rich. Addition of nickel to alloys decreases magnetostriction and is linked with the decrease of saturation magnetisation, as high nickel content makes the system paramagnetic [35].

There is a wide range of techniques for producing amorphous materials such as ball milling, electrodeposition, sputtering, hot pressing, warm extrusion, etc. To obtain an amorphous phase, it is necessary to suppress the nucleation and growth of a crystalline phase in the liquid region between the melting and glass transition temperature [36]. A metallic alloy that can easily be produced in its amorphous state is said to have a high Glass-Forming Ability (GFA). Three basic empirical rules were described by Inoue [36] in order to obtain alloys with good GFA:

- 1) the system must consist of more than three elements,
- 2) there must be a significant difference between the atomic size ratios of the main constituent elements (above 12 %),
- 3) negative enthalpy of mixing.

These rules have been revised to include newer amorphous materials that did not comply with these basic ones [37].

Melt spinning is one of the most widely used techniques for the synthesis of amorphous alloys. The molten metal is ejected through an orifice onto a rotating copper wheel, with a quench rate of $1 \times 10^5 \text{ }^\circ\text{C s}^{-1}$ to $1 \times 10^7 \text{ }^\circ\text{C s}^{-1}$ to "freeze" the alloy in a glassy state avoiding nucleation and growth of crystallites. This produces a thin ($\approx 30 \mu\text{m}$) ribbon that can be spun as a toroid. Only compositions that are close to their deep eutectic will allow the glass to form at these quench rates.

Typical composition of amorphous alloy systems is given by $(\text{T})_{70-90}(\text{X})_{10-30}$, where T is any combination of transition metals and X refers to additional elements like metalloids (silicon or boron) and/or refractory metals (like niobium, molybdenum, zirconium, hafnium, etc.) For magnetic applications, T is one of the ferromagnetic elements like

iron, cobalt and/or nickel [30], [9].

The aforementioned additional elements can be divided into two groups [8]:

- metalloids such as B, Si, P or C (metal-metalloid systems). They can be generically described as $(\text{FeCoNi})_{70-85}(\text{metalloid})_{15-30}$ in atomic percent, which is the norm as opposed to crystalline alloy compositions. Metalloids lower the melting temperature of the alloy and stabilise the amorphous phase [27].
- early transition metals such as zirconium, niobium, tantalum, titanium, etc. (metal-metal systems). These elements also help the glass-forming ability of the alloy with the added feature that they inhibit diffusion [9]. Due to high oxygen reactivity of early transition metals, casting is not possible for these alloys. Some also have the effect of increasing the crystallisation temperature [38].

1.3.3 Nanocrystalline alloys

Nanocrystalline alloys are very interesting as they can have good mechanical properties, can be soft or hard magnetically and have high catalytic properties that cannot otherwise be found in ordinary amorphous or crystalline alloys [36]. Nanocrystalline alloys have all been optimised to achieve small magnetostrictive coefficients and therefore large permeabilities [39]. The enhanced soft magnetic properties of nanocrystalline alloys are due to the synergy effect between the crystal grain size, the intergranular amorphous matrix and their compositions. The amorphous phase surrounding the nanocrystals facilitates the exchange interaction between them, leading to high saturation magnetisation [13].

$\text{T}_{1-x-y-z}\text{TE}_x\text{M}_y\text{NM}_z$ is the general formula that represents the composition of soft nanocrystalline magnetic alloys where:

- T is Co, Ni or Fe
- TE is an early transition metal like Zr, Nb, Hf, Ta, etc. They are added, like for amorphous metals, for their GFA as they provide a diffusion barrier and inhibit grain growth [9].
- M is a metalloid like B, P, Si, etc. Also added for GFA.
- NM is a noble metal, added to provide nucleation sites for the crystalline phase.

Their production started in 1988, when Y. Yoshizawa and his group, developed a nanocrystalline alloy with composition $\text{Fe}_{73.5}\text{Cu}_1\text{Nb}_3\text{Si}_{13.5}\text{B}_9$, by adding small amounts of Nb and Cu to the basic FeSiB alloy [38]. With this composition, copper enhances the nucleation of bcc FeSi crystallites while niobium inhibits crystallite growth and at the same time inhibits the formation of boride compounds [2], [7]. This alloy has since been

trademarked and is known as Finemet.

A crystallization heat treatment leads to a morphology of FeSi (DO_3) grains approximately 10 nm in diameter embedded in a residual amorphous matrix and 5 nm fcc Cu(Fe) grains in the amorphous matrix [40] that serve as nucleation sites for the FeSi crystals. This nanocrystalline composite structure is remarkably stable in temperature against grain growth allowing for design engineers to contemplate high temperature applications [9]. The mechanism of crystallisation was proposed in 1997 by Ayers [41] and can be seen in Figure 1.7. The heat treatment favours the creation of copper-rich fcc clusters first that serve as nucleation points for the FeSi crystals, and makes the amorphous matrix enriched in Nb and B. The next step is the nucleation of FeSi bcc crystals, which are the main crystalline phase in the alloy. As crystals grow the amorphous phase gets depleted in Fe and becomes richer in Nb. The Nb functions as a glass stabiliser and limits the growth of the crystallites. Nb may also play a role in limiting the solubility of Cu in the amorphous phase. To determine the optimal annealing temperature, the as-spun ribbon is examined by differential scanning calorimetry to identify the primary and secondary crystallisation temperatures, to avoid crossing the second crystallisation temperature that would precipitate the secondary unwanted phase [9].

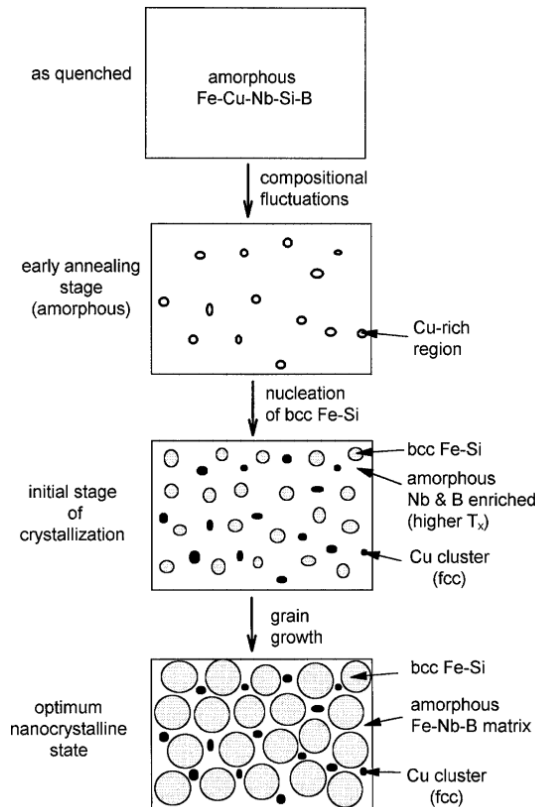


Figure 1.7 – Crystallisation schematic of Finemet [41].

This alloy proved to have excellent magnetic properties, with coercivity under 2 A m^{-1} , near zero magnetostriction and saturation up to 1.7 T [42]. Another advantage was the price, as it is much cheaper than the cobalt-based alloys alternatives [13].

The high relative permeability over 1×10^5 was obtained by annealing around 570°C for 1 hour. As it has been mentioned before, the microstructure (mainly the structural correlation length), determines the material behaviour. The induced magnetic anisotropy in Finemet comes from the ordering of the Fe and Si atoms in the bcc FeSi phase. The magnitude of the induced magnetic anisotropy is determined by the fraction and Si content in the grain and can explain the induced magnetic anisotropy of a conventional FeSi alloy [30]. Also, the highest permeability is obtained when the thermal treatment crystallises only the main bcc FeSi phase. On the other hand, when the annealing temperature is higher than the optimum annealing temperature, the formation of the compound phases such as Fe_2B with large magnetocrystalline anisotropy drastically decreases the permeability. The change in magnetisation can be attributed to the pinning of domain walls on the iron boride precipitates [40].

It has been seen that, after annealing at 550°C for as much as 2 hours, the grain size remains below 10 nm . If Nb is removed, the diffusion barrier is not there any more and grain growth occurs giving crystals up to 50 nm in just 1 hour. The Transmission Electron Microscopy (TEM) results can be seen in Figure 1.8 [9].

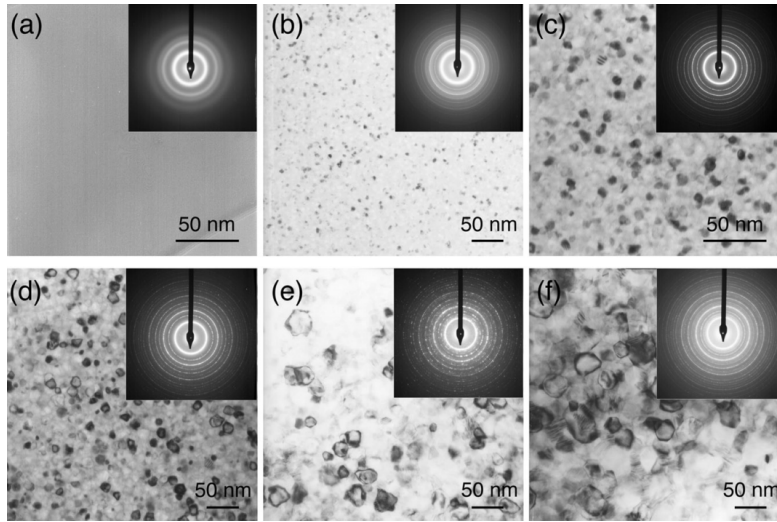


Figure 1.8 – TEM images of standard Finemet ($\text{Fe}_{73.5}\text{Cu}_1\text{Nb}_3\text{Si}_{13.5}\text{B}_9$): (a) as-cast, (b) 2 minutes at 550°C , (c) 2 hours at 550°C . Finemet without Nb ($\text{Fe}_{76.5}\text{Cu}_1\text{Si}_{13.5}\text{B}_9$): (d) 8 seconds at 550°C , (e) 120 seconds at 550°C , (f) 1 hour at 550°C [9].

In fact, the grain size in the Finemet alloy (or ones with similar compositions) is decisive for its soft magnetic behaviour, but ultimately is only a prerequisite. The key parameter of the nanocrystalline iron-based alloys is that the crystallised phases also lead to low or vanishing saturation magnetostriction (λ_s) as it is the ultimate responsible for the

simultaneous increase of the initial permeability upon nanocrystallisation. Otherwise, the soft magnetic properties would be only comparable to that of stress-relieved amorphous Fe-based alloys [30].

In 1989, Prof. Masumoto's laboratory developed a new alloy with an original composition of FeZrB. They first expected to have a nanoscale α -Fe/ZrB material, but were pleased to discover that the melt-spun amorphous alloy crystallized to two-phase α -Fe/amorphous materials similar to the microstructure previously observed in Finemet, with crystals of approximately 25 nm. Soft materials, based on Fe-M-B-Cu (M = Zr, Nb, Hf...), have been patented by Kojima et al. under the trade name Nanoperm [39]. They have a bigger concentration of iron (83 - 89 at. %) compared to Finemet \approx 74 at. % and a higher saturation magnetisation as a result.

More recently, in 1997, McHenry developed a family of nanocrystalline alloys with composition (Fe,Co)-M-B-Cu (M = Nb, Hf, or Zr), called Hitperm. These have shown to have a maximum saturation magnetisation between 1.6 T to 2.1 T combined with high permeabilities and high Curie temperatures. If Finemet has α -FeSi nanoparticles, Nanoperm shows α -Fe particles with a bcc structure. In Hitperm alloys, nanocrystalline bcc α -FeCo and B₂ α' -FeCo are formed with significantly improved high temperature magnetic properties compared to the latter. Hitperm materials were developed for applications with smaller permeability requirements but required large inductions at high temperatures [39], [43].

Table 1.1 – Summary of main families of nanocrystalline alloys [13].

	Finemet	Nanoperm	Hitperm
Composition	FeSiBNbCu	FeMBCu	FeCoMBCu
Crystalline phase	α -Fe α -FeSi (DO ₃)	α -Fe (bcc)	α -FeCo (bcc) α' -FeCo (B ₂)
Saturation magnetisation [T]	1.0 - 1.2	1.5 - 1.8	1.5 - 1.8
Curie temperature [°C]	< 700	770	> 965

1.3.4 Thermal treatments

Thermal treatments are necessary to transform amorphous materials into nanocrystalline ones. But thermal treatments are also used to change the magnetic properties of the alloys without changing their microstructure, either by only heating, or by also adding magnetic fields during the treatment to induce anisotropy in the material. It should be taken into account that after annealing, especially if the material has been transformed to nanocrystalline, it becomes brittle and difficult to manipulate. Elastic strain and plastic deformation can severely degrade the magnetic performance of the material once

it is in this state. It is therefore preferable to anneal the material in its final shape, to avoid unnecessary manipulation once the annealing has taken place.

Thermal treatments at temperatures lower than the Curie point are referred to as “ageing” and “annealing” if they are over [44], but the term “annealing” is commonly used for both. Low temperature treatments (300 °C to 400 °C) have been known to substantially improve soft magnetic properties. In both amorphous and nanocrystalline alloys, if the material is annealed over the Curie temperature in a magnetic field, a significant anisotropy can be induced [9]. This will mean that the magnetic polarisation inside the material will have a preferred direction and will therefore affect the final magnetic properties, such as the shape of its BH-curve. The external magnetic field aligns the local magnetisation inside the material, meaning that magnetic thermal treatments should therefore happen below the Curie temperature [8]. This can give excellent low-frequency soft magnetic properties equal or better to the best permalloys (Ni-Fe alloys) [2]. The magnetisation of amorphous alloys is ruled by nucleation and growth of magnetic domains. Nucleation already exists at the beginning of the demagnetisation stage. The remanent magnetic state can occur by distribution of domains in the absence of a field. When the material is annealed in such conditions, the internal spontaneous field can act similarly to an external magnetic field in each domain or wall, resulting in the creation of local magnetic anisotropies. Since the internal field is distributed according to the easy direction, anisotropies will also be this way, which means that domain walls are stabilised and fixed in the same position as they were during annealing. This increases coercivity due to the pinning of walls by the induced anisotropies [45].

Annealing can cause stress relaxation, controlled development of induced anisotropy, adjustment of a well-defined domain structure, controlled micro structural changes, and nanocrystallization, as has been seen before [28]. Figure 1.9 shows an example of Metglas material (Fe-Ni base), with the effect of longitudinal and transverse-field annealing compared to the as-cast magnetic curve.

1.3.5 Material characterisation for transformer cores

Once the target material has been selected, it is wound into a core for further thermal annealing or directly for its final use. Normally, cores are wound with squared-shaped cross-sections, or at least keeping the outside diameter/ inside diameter ratio lower than 1.1 to improve the homogeneity of the applied field and reduce the possibility of an inhomogeneous response [44]. Special attention has to be given to the ribbon tension when the core is wound. R. Hasegawa [46] states that tension control becomes necessary in core winding, especially for larger cores as the tension can vary greatly from the inside to the outside part. This, as well as magnetostriction, even if small, cannot be neglected and can have an effect on the core’s final performance.

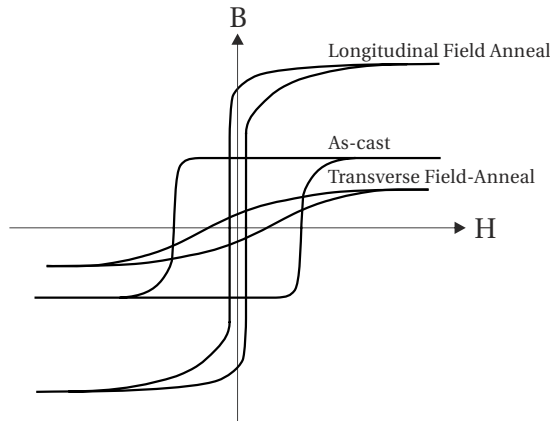


Figure 1.9 – BH-curves of Metglas (Fe-Ni base), as cast, longitudinally and transversely-field annealed. Adapted from [10].

When the core is properly wound, it can then be thermally treated and then measured in order to see its final properties. Following is a list of some of the parameters that can be measured in order to check the state of the core.

Barkhausen Noise (BN)

The Barkhausen effect is a physical phenomenon that manifests itself as a series of discrete jumps in the magnetisation of ferromagnetic material when exposed to a varying magnetic field due to magnetic domain shifts. Surrounding the sample by a secondary coil, the induced voltage can be transformed into acoustic noise, from which the term Barkhausen Noise (BN) derives [47]. This effect is often used as a non-destructive test to check changes in micro structure (grain boundaries, dislocations, inhomogeneities, etc.) and stress configurations of materials, and offers a good overview of changes in magnetic domains.

BH curve and permeability

Figure 1.10 is a good example of how the BH-curve can change the permeability vs amplitude response at a fixed frequency. In this case, Finemet was annealed without a magnetic field and then in presence of a parallel and transverse field. It can be seen how different BH-curves have a very different permeability behaviour, with the flat curves having also relatively flat permeability response vs field amplitude. This is due to the fact that the magnetisation process is determined mainly by rotation of the domains, which gives a constant permeability until saturation. The square loop (Z) is the result of longitudinal field anneal and the magnetisation process is dominated by 180° domain wall displacements. The round loop (R) is a result of annealing without a field. Magnetisation

is a mixture of rotation and domain wall displacement, and has characteristically high initial and maximum permeability. However, this is not always the case, as sometimes annealing without a magnetic field does not mean there are no induced anisotropies. The existence of magnetic domains in the sample is already a source of anisotropy under the Curie temperature. In this case, the anisotropy is magnetisation-induced and not field-induced like for the other cases. Zero-field annealing gives a distribution of uniaxial anisotropies that reflect the state of the domains during heat treatment [35].

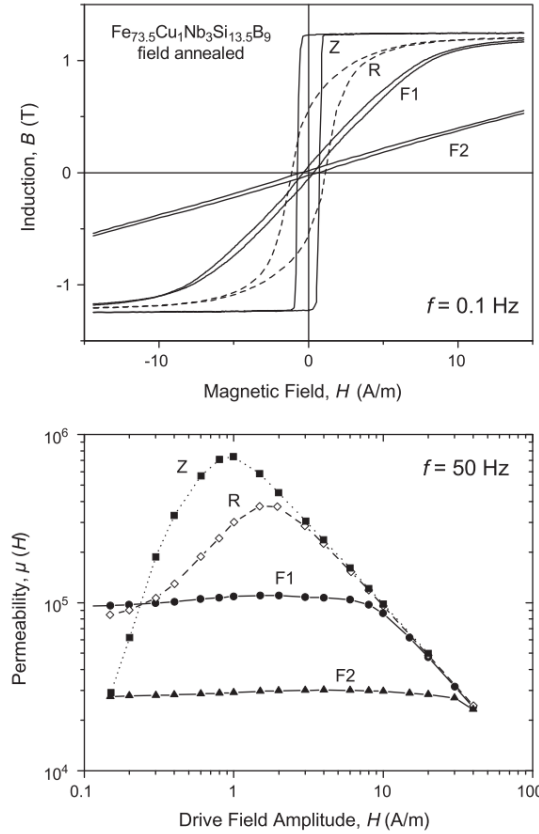


Figure 1.10 – BH-curves (at 0.1 Hz) and permeability (at 50 Hz) of Finemet annealed for 1 h at 540 °C without (R) and with a magnetic field applied parallel (Z) and transversely (F2) to the magnetic path. Sample F1 was first crystallized at 540 °C and subsequently transverse field annealed at 350 °C [7].

Field-annealed samples present a lower coercivity than those annealed without an external magnetic field. This can be explained by the less complex domain pattern caused by the induced anisotropy [35].

Magnetic domain imaging

There are several techniques that allow the observation of magnetic domains. The first technique developed for this purpose was used by Bitter in 1932 [48], where he used iron

oxide particles of $1\text{ }\mu\text{m}$ suspended in ethyl acetate (today commonly called ferrofluid). This method remains today widely used for its simplicity and sensitivity [11].

Since then, a variety of methods have been developed to visualise magnetic domains:

- Magneto-Optical (MO) methods: they can be of two types, based on reflection (using the Magneto Optical Kerr Effect, or MOKE) or in transmission, using the Faraday Effect. Because the Faraday effect is restricted to transparent media, the MOKE is more widely used. They use polarised light that rotates in the presence of a magnetic field that can be analysed with a polarised lens microscope. Depending on the orientation of the magnetisation in the sample and the plane of incidence of the polarised light (which depends on the latter), this effect is called polar, transverse or longitudinal. The light passes through a polariser, is then reflected from the sample with polar, longitudinal or transverse components excited depending on the magnetisation in the sample. The light then passes through the analyser.

If two domains have opposite magnetisation, the amplitudes will differ in sign. The analyser can be set up so that the light from one of the domains is extinguished, so that one will appear dark and the other one bright.

High resolution images can be achieved with the setup shown in Figure 1.11, which is based on a conventional polarising microscope. Using a blue light for its short wavelength a resolution of $0.3\text{ }\mu\text{m}$ can be achieved. Domain dynamics can be also observed with this technique. However, the samples should be reasonably flat and the penetration depth of the technique is of about 10 nm .

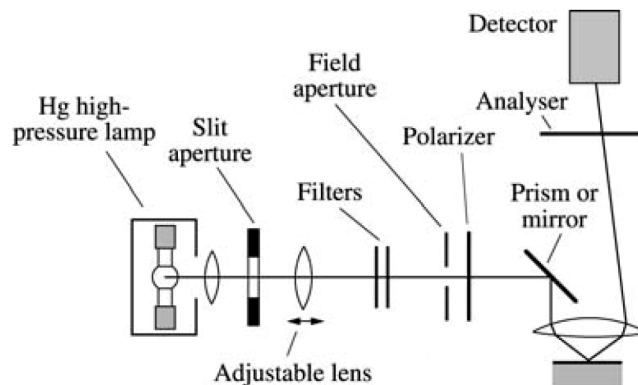


Figure 1.11 – High resolution distortion-free Kerr microscope [11].

- Transmission Electron Microscopy: in an electron microscope, accelerated electrons interact with the electron-transparent sample and are deflected by the Lorentz force caused by the perpendicular component of the magnetic induction of the sample. Different operating modes are used in order to obtain the domain information of the sample, either in-focus observation, differential phase contrast, or the more commonly used, the

defocused Fresnel mode. These techniques can have a resolution down to the nanometre level.

- Other techniques include Scanning Transmission Microscopy (STM), electron holography, mechanical microscanning techniques like Magnetic Force Microscopy (MFM), X-ray topography and neutron topography.

1.4 Objectives of the thesis

The objectives of the thesis can be summarised as follows:

- identify and purchase raw materials that would be suitable for building cores for beam instruments for CERN
- characterise these materials fully, including characteristic temperatures, composition, magnetic properties and microstructure
- select the best materials based on their as-cast properties to build test cores
- anneal sample ribbons and study the differences before and after the thermal treatment
- build test cores and anneal them with all the information obtained from the previous studies to see the differences before and after the thermal treatment

2 Materials and Methods

2.1 Materials

As it has been stated in the previous chapter, the most interesting soft magnetic alloys are iron-based and cobalt base, nanocrystalline and amorphous. A market research was done in order to contact a number of raw-material providers that would be able to produce and deliver these alloys in their amorphous state (as nanocrystallised they would be too brittle to handle), with a high permeability and a low coercivity as basic characteristics.

After this, the following materials were purchased from these companies:

- Qinhuangdao Yanqin Nano Science & Technology Co., Ltd.: iron-based amorphous and iron-based nanocrystalline alloys
- Metglas Inc.: iron-based amorphous Finemet FT-3 and cobalt-based alloy 2705 M
- Vacuumschmelze GmbH & Co. KG: cobalt-based amorphous Vitrovac 6025 G40
- Nanostructured & Amorphous Materials, Inc. (Nanoamor): cobalt-based amorphous

2.2 Methods: Composition

2.2.1 Inductive Coupled Plasma - Optical Emission Spectrometry (ICP-OES)

In order to analyse the samples by this technique, the alloys were dissolved in Aqua Regia (mixture of nitric acid and hydrochloric acid in a molar ratio of 1:3). An insoluble transparent residue was seen in all of the samples. A SEM-EDX analysis showed it was mainly composed of silicon and oxygen, which accounted for a final error from 4 % to 17 % in the composition analysis depending on the sample. The ICP-OES results are

therefore not representative for the samples.

The measurement was done with a Shimadzu ICP-OES 9000 and analysed with the ICPEsolution Launcher software at EPFL. The high-temperature argon plasma was generated using high frequency (27.12 MHz). The liquid samples were aspirated and atomized by a nebuliser and then supplied to the plasma to excite the elements in the sample, thus causing them to emit light.

2.2.2 X-ray Photoelectron Spectroscopy (XPS)

Measurements were carried out using a PHI VersaProbe II scanning XPS microprobe (Physical Instruments AG, Germany) at EPFL. Analyses were performed using a monochromatic aluminium K- α X-ray source of 24.8 W power with a beam size of 100 μm . The spherical capacitor analyser was set at 45° take-off angle with respect to the sample surface. The pass energy was 46.95 eV yielding a full width at half maximum of 0.91 eV for the silver 3d 5/2 peak. Curve fitting was performed using the PHI Multipak software. The uncertainty of the measurement is between 2 % and 3 %.

All samples were seen to present a carbon and oxygen contamination layer, making superficial analysis unusable for quantitative analysis. Samples showed an average of 45 % of carbon and 34 % of oxygen on the surface. Argon sputtering was then needed in order to study the samples at depth, but it was observed that preferential sputtering occurred in all samples, giving erroneous compositions (enriched in iron and impoverished in cobalt).

2.2.3 Scanning Electron Microscopy- Energy-Dispersive X-ray spectroscopy (SEM-EDX)

Analyses were performed with a Scanning Electron Microscope, field emission gun FEG Sigma (ZEISS) with InLens (Secondary Electron), Evan-Thornley Secondary Electron (SE2), and back-scattered electron (AsB) detectors for imaging at CERN. The chemical composition was measured with a 50 mm² X Max EDX detector (Oxford) and analysed with INCA software. The uncertainty of the measurement is 0.1 %.

Boron cannot be easily detected by SEM-EDX because of the relatively poor peak to background ratio. Moreover, in the specific case of the studied samples, a certain overlap between peaks of boron and carbon in the EDX spectrum can introduce significant errors in the calculations. Also, the technique's limitations make it impossible to detect elements below around 0.2 % of weight (exact value depending on the weight) and light elements with atomic number below 4. Elements with an atomic number between 4 and 11 can be detected only if present in a large amount.

2.2.4 Electron Micro Probe Analyser (EMPA)

A JEOL 8200 Superprobe with an Energy-dispersive X-ray spectroscopy e2v Silicon Drift Detector was used for the EMPA analysis, performed at UNIL in Lausanne. An acceleration voltage of 10 keV, a current of 20 nA and focused beam were used for the measurements, except for the Finemet sample which was measured at 15 keV, current 10 nA, beam size of 2 μm . The samples were encapsulated in resin and bombarded with the electron beam aiming at the centre of the ribbons, emitting X-rays.

Boron is also a complicated element to detect with EMPA, as it emits X-Rays at a high wavelengths and a special adapted diffraction crystal is needed. In optimal conditions, the instrument is capable of detecting trace elements down to hundreds of ppms.

2.3 Methods: Crystallinity

2.3.1 X-ray Diffraction (XRD)

XRD measurements were performed at CERN with a Siemens D5000 X-ray Diffractometer with a KRISTALLOFLEX 760 X-ray Generator and a copper source ($K\alpha = 1.54060 \text{ \AA}$). Measurements were taken with a coupled $\theta/2\theta$ scan, step size 0.02° and time per step of 0.3 s.

2.3.2 High Energy X-ray Diffraction (HE-XRD)

The Powder X-ray diffraction analyses were done by Phase Solutions Co. Ltd. in the Swiss-Norwegian beamline BM01A, which operates in the range of 8 keV to 22 keV [49] in the European Synchrotron Radiation Facility (ESRF) in Grenoble. The ESRF produces X-rays of high energy, called “hard” X-rays, which have wavelengths of 0.1 nm to 0.01 nm or energy in the range 10 keV to 120 keV [50]. The X-Ray beam cross-section was 0.3 mm x 0.3 mm with a wavelength of $\lambda = 0.6963 \text{ \AA}$. Data was recorded with a pixel detector PILATUS-2M.

2.3.3 Transmission Electron Microscopy (TEM)

TEM measurements were taken at EPFL with a TECNAI OSIRIS and an 11 Megapixel Gatan Orius CCD camera. Samples were analysed at 200 keV and a camera length of 968 mm for iron-based alloys and 1000 mm for the cobalt-based. The TECNAI OSIRIS has 0.24 nm point resolution (the minimum distance by which two point scatterers must be separated to be discernible for a given wavelength and aperture) and a 0.14 nm information limit (the highest resolution that it can achieve).

2.4 Methods: Phase transformation

2.4.1 Differential Scanning Calorimetry (DSC)

Several DSC's (Differential Scanning Calorimeters) were used to accurately determine the crystallization and melting points of the alloys:

- Crystallization temperatures at different heating rates were measured with a PerkinElmer DSC 8000 and analysed with PyrisTM software. All the materials were studied at heating rates of 5 °C/min, 10 °C/min, 20 °C/min and 50 °C/min. All the curves were started from room temperature, as this would be the case, should the material be annealed in an oven. The Magnetec sample is not listed, as the crystallization temperature is higher than 600 °C, which is the temperature limit for the aluminium sample pans used. The temperature measurements taken have an uncertainty of ± 0.058 °C [51].
- Crystallization and melting temperatures were measured with Netzsch DSC 404 C with a TASC 414/3A Controller and a power unit Pu 1.851.05 under argon atmosphere at 10 °C/min in alumina pans. Data was analysed with the NETZSCH Proteus[®] Software for Thermal Analysis. First, several scans were done up to 1200 °C to determine the melting temperatures. With the first scan, the crystallisation temperatures could also be determined.

2.4.2 High Temperature in-situ XRD (HT-XRD)

High-Temperature X-Ray Diffraction (HT-XRD) experiments were done at the The Swiss Center for Electronics and Microtechnology (CSEM) in Neuchatel. They were performed using a HTK 16N Anton Paar high-temperature chamber mounted in an X'Pert Pro-MPD PANalytical diffractometer. In order to ensure good temperature control of the samples, the regulation thermocouple was soldered on the bottom part of the platinum heating strip whereas the sample was located on the top part of the heating element, acting also as the sample-holder. The diffractometer was equipped with the copper K α radiation (1.541 874 Å) and the diffracted intensity was recorded using a PIXcel detector with its maximum active length of 3.347° in order to allow quick acquisition of each diffractogram. The diffraction patterns were acquired for 2θ angles ranging from 20° to 90° with a step size of 0.03°. The acquisition time of each diffractogram was 20 minutes under continuous nitrogen flow during the whole time.

Diffractograms were analysed with the X'Pert HighScore Plus 2.2e PANalytical software. The crystalline phases in the samples were found by comparing measured diffractograms and reference patterns of the Inorganic Crystal Structure Database (ICSD).

For the calculation of the grain size, the Debye-Scherrer equation is used:

$$\tau = \frac{\kappa \cdot \lambda}{\beta \cdot \cos \theta} \quad (2.1)$$

Where:

τ : the mean size of the crystals [nm]

κ : crystallite shape factor, depends on the crystal structure

λ : X-ray wavelength [nm]

β : width at the Full Width Half Maximum (FWHM) [rad]

θ : Bragg diffraction angle [rad]

2.5 Methods: Magnetic properties

2.5.1 Impedance analyses

The measurement of the relative complex permeability was done with an Agilent Impedance Analyser 4294 from 40 Hz to 110 MHz, using a probe adapter. The measurements were performed with no DC bias, oscillation level of 500 mV, precise bandwidth and oscillation frequency of 1 MHz. The effective in-series resistance and inductance were measured in order to calculate the imaginary and real part of the complex permeability. The uncertainty of the measured parameters were calculated according to the operation manual of the analyser [52]. In order to perform the measurement, the ribbons were wound into cores with an outside diameter of approximately 40 mm and with 20 turns for the measurement. At least two cores of each material were made.

The real part (μ') represents the energy storage of the core:

$$\mu'_e = \frac{l \cdot L_{eff}}{\mu_0 \cdot N^2 \cdot A} \quad (2.2)$$

Where:

l : Average magnetic path length of toroidal core [m]

L_{eff} : Inductance of toroidal coil [H]

$$\mu_0 = 4\pi \cdot 10^{-7} \text{ [H m}^{-1}\text{]}$$

N : Number of turns

A : Effective cross-sectional area of toroidal core [m^2]

The imaginary part (μ'') represents the energy loss in the core:

$$\mu_e'' = \frac{l \cdot (R_{\text{eff}} - R_w)}{\mu_0 \cdot N^2 \cdot \omega \cdot A} \quad (2.3)$$

Where:

R_{eff} : Equivalent resistance of magnetic core loss including wire resistance [Ω]

R_w : Resistance of wire only [Ω]

ω : angular frequency = $2\pi \cdot \text{frequency}$ [rad s^{-1}]

2.5.2 BH-curve measurement

Two purpose-built setups were used to measure the BH-curve. For both setups, the core-under-study was wound with two 8-turn windings formed by two custom-made PCBs. This solution was chosen to assure the same winding geometry for all the measurements.

The indirect BH-curve measurements were carried out by saturating the primary winding with a sinusoidal voltage at 212 Hz. The current flowing through the primary winding was continuously measured as a voltage across a small resistance of a precisely known value. From this, the H-field at any given time can be calculated as:

$$H(t) = \frac{I'(t) \cdot N_1}{l} \quad (2.4)$$

where I' is the current flowing through the primary winding, N_1 is the number of turns on the primary winding and l is the average magnetic path length within the core.

The voltage induced on the secondary winding of the core under study was continuously measured across a large resistance. From this, the B-field at any given time can be

calculated as:

$$B(t) = \frac{1}{(N_2 \cdot A)} \cdot \int_t^{t_2} V_{sec}(\tau) d\tau \quad (2.5)$$

Where V_{sec} is the voltage across the secondary winding, N_2 is the number of turns on the secondary winding and A is the effective cross-sectional area of the core.

The primary winding excitation generator of the first setup was found to introduce non-negligible non-linearities to the measurements. Furthermore, the analogue integrator used to obtain the induced magnetic field (B) by integrating the secondary winding voltage suffered from small drifts and additional non-linearities making data analysis prone to errors. These observations led to development of the second setup shown in Figure 2.1.

The primary winding excitation generator of the second setup was highly linear even with high excitation currents. The analogue integrator was replaced by digital integration conducted offline on raw data. Moreover, the second setup used a resistor for measurements of the primary winding current as well as cables of much better quality which did not introduce any significant error to the measurement process.

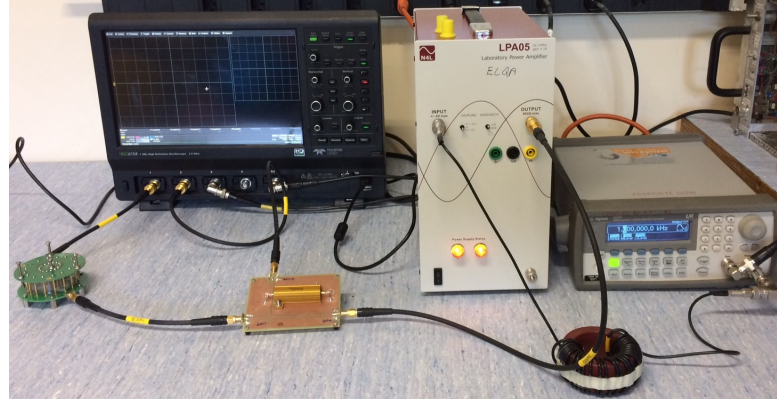


Figure 2.1 – Second BH-curve setup.

2.5.3 Curie temperature measurements

Vibrating Sample Magnetometry (VSM), University of Zaragoza

A first study with the Qinhuangdao material was done in the University of Zaragoza with a Quantum Design PPMS (Physical Properties Measurement System). Calibration was done with a standard palladium sample to ensure a minimum accuracy of 1 % of the magnetic moment. The oven temperature was calibrated using the magnetic transition

of nickel. Samples were analysed at 0.1 T, with the field parallel to the sample plate holder. Samples were cut into squares of 3 mm and glued to the sample holder. Samples were then covered with copper to optimise thermal contact and to minimise radiation. The heater and thermocouple are embedded in the holder and in direct contact with the sample. All measurements were done under vacuum.

Thermogravimetric Analyses (TGA)

A PerkinElmer 4000 TGA was used, where samples were placed in alumina pans, covered by alumina powder, under nitrogen at a flow of 20 mL/min. A magnet was placed above the sample outside of the oven. Below the Curie temperature, the sample is attracted to the magnet and the TGA detects a certain mass that is lower than the sample's real mass. Once the Curie temperature is crossed, the sample is not magnetic any more and therefore it is not attracted to the magnet, which is detected as a mass increase at a certain temperature. This will be therefore the Curie temperature of the sample.

Kappabridge analyses

A second measurement was performed at the Laboratory for Natural Magnetism in ETHZ. Measurements were done with an AGICO Kappabridge MFK1-FA and a CS4 High Temperature Furnace Apparatus (a non-magnetic furnace with a special platinum thermometer, CS4 temperature control unit, laboratory power supply EA-PS, cooling water reservoir with a pump, and an argon flow meter). The specimen was placed in a measuring vessel which was heated by a platinum wire. The temperature is measured by special platinum thermosensor. Measurements were done at $11\text{ }^{\circ}\text{C min}^{-1}$ under argon at a frequency of 976 Hz with the sample placed statically. The measurement had an uncertainty of $\pm 3.1\%$ [53]. The data was analysed with the Tauxe method [54], taking the Curie temperature as the point with maximum curvature in the susceptibility curve.

Vibrating Sample Magnetometry (VSM) and Alternating Gradient Magnetometry (AGM)

VSM measurements were performed in the Laboratory of Natural Magnetism in ETHZ with a Princeton Measurements Corp. (now Lake Shore Cryotronics, Inc.) model 3900 MicroMag Vibrating Sample Magnetometer. Samples were cut to 3 mm squares for the measurement.

A Vibrating Sample Magnetometer from Quantum Design was used to reach 1100 K. Samples of 3 mm x 3 mm were glued flat to the sample holder with special cement. The sample was covered with the cement and wrapped in copper foil to optimize thermal contact and minimize radiation. A heater and a thermometer are embedded in the holder

in direct contact with the sample. Measurements were performed in a high vacuum environment, at 1 kOe from 300 K to 1000 K.

The same set of measurements was performed with an Alternating Gradient Magnetometer Micromag 2900 from PCM in order to be compared with the VSM results. Both machines were calibrated with an Yttrium Iron garnet sphere standard from the National Institute of Standards and Technology (NIST), number 2853.

2.5.4 Magnetic domain imaging

Magnetic Force Microscopy (MFM)

A PSIA XE-100 from Park Systems in oscillating mode was used to study the samples with a NanosensorsTM tip type PPP-LM-MFMR, with enhanced lateral resolution and a minimum magnetic resolution of 35 nm.

TEM

The FEI Titan Themis with Lorentz microscopy in Fresnel mode was used for magnetic domain imaging of sample MA after preparation with Focused Ion Beam (FIB) in order to make them electron transparent. The image obtained from the Transport-of-Intensity Equation (TIE) using the over-focused and under-focused images from the Fresnel mode.

Magneto-Optical Kerr Effect (MOKE)

Samples were analysed by the University of Kiel in the laboratory of Nanoscale Magnetic Materials and Magnetic Domains of Prof. Jeffrey McCord. Images were taken with parallel sensitivity and parallel field to long axis (direction left-right based on image).

Two microscopes were used for the samples. One is the commercially available setup Axio Imager vario V2 from Zeiss. It has an adapted illumination system with LEDs. Two LED sources were used at the same time: a red (wavelength 630 nm) and a blue one (460 nm). An Optosplit device from Cairn research was used in order to take both images at the same time, with a Hamamatsu Orca r2 (C10600) camera.

The second setup is house-built and uses a green LED (wavelength 520 nm) and has a constant magnification of 0.35. The camera used was a Hamamatsu C4742-95.

The experimental determination of magnetization loops obtained by magneto-optics utilizes the fact that by varying the phase or the angle of incidence, the magnitude and even the sign of the MO signal from individual layers vary in a different way [55].

2.5.5 Barkhausen Noise (BN)

BN tests were performed with a purpose-built setup adapted from [47]. The samples were surrounded by two coils: the primary excitation coil consisting of a few hundred turns and the secondary pickup coil consisting of some tens of turns. The excitation coil was driven by a relatively high current symmetrical triangular wave at a frequency of 30 mHz. The BN was then measured as the signal induced on the pickup coil during the zero-crossing of the excitation wave. Figure 2.2 shows an example of the excitation current with the BN corresponding to a Finemet FT-3 sample.

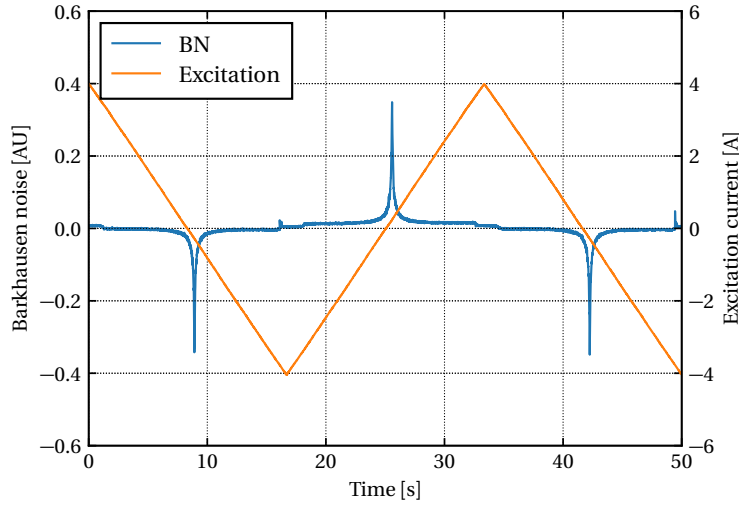


Figure 2.2 – Barkhausen noise setup.

Due to the extremely low frequency at which the measurements were taken, the setup was carefully optimised to reduce its susceptibility to any external electromagnetic fields, coming mostly from the 50 Hz electric power distribution network. The sample and both coils were shielded by an external metallic housing forming a simple Faraday cage. Moreover, the excitation signal was heavily filtered by an active low-pass filter with a cut-off frequency of 1 Hz. Finally, all the inter-connections were equipped with very high quality common-mode chokes in order to attenuate any stray signals induced on the cables. Figure 2.3 shows the setup used.

2.5.6 Other physical properties

Thickness

Thickness was measured with a TESAMASTER 25 mm to 50 mm micrometre (reference 00310002) with the help of a 30 mm Hoffmann Group steel gauge (reference 00045). The micrometre has an uncertainty of $\pm 2 \mu\text{m}$ [56] and the gauge has a tolerance class 0

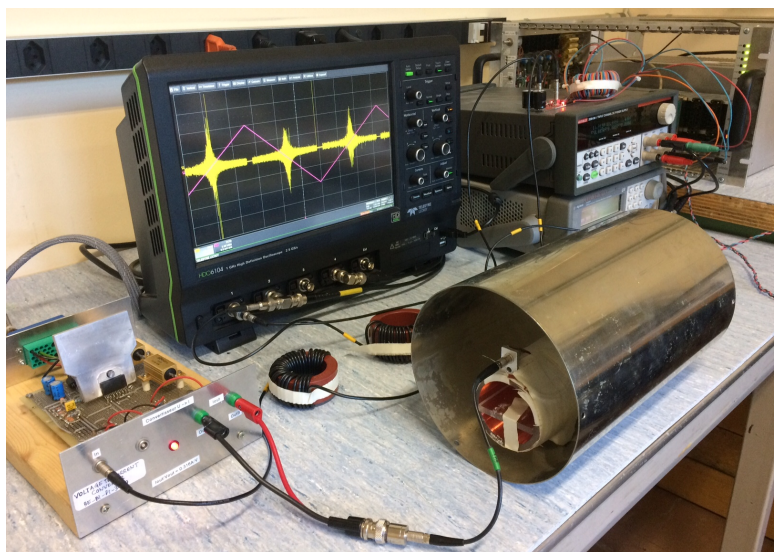


Figure 2.3 – Barkhausen noise setup.

according to the ISO 3650 and has therefore a length tolerance of $\pm 0.2 \mu\text{m}$ [57].

Density

Density measurements were performed using a Micrometrics Accupyc 1330 gas pycnometer with nitrogen, by averaging 10 measurements. The uncertainty of the density measurement was calculated taking into account that the mass measurement used for its calculation, taken with a Mettler-Toledo AB204-S analytic scale, with an uncertainty of 0.03 mg [58]. The Accupyc is accurate to within 0.03 % of reading plus 0.03 % of nominal full-scale cell chamber volume, which in this case was 10 cm^3 [59]. The uncertainty for the density was calculated taking into account the multiple uncertainty components principle by quadratic sum [60].

3 Iron-based alloys results

In order to make the reading of results easier, the materials will be referred to in the following way:

- Qinhuangdao Yanqin Nano Science & Technology Co., Ltd.: Fe-based amorphous alloy → (C1)
- Qinhuangdao Yanqin Nano Science & Technology Co., Ltd.: Fe-based nanocrystalline alloy → (C6)
- Metglas Inc.: Fe-based amorphous Finemet FT-3 → (F)
- Magnetec, GmbH: Fe-based nanocrystalline alloy → (MA). In order to have a commercial nanocrystalline iron-based alloy as a reference, several industrially-made ready to use Magnetec GmbH cores were purchased and opened to extract the internal material for the study.

3.1 Composition

3.1.1 XPS

As has been mentioned before, the surface analyses of samples showed a high percentage content of oxygen and carbon. Figure 3.1 shows the surface XPS results for samples C1 and MA. The carbon and oxygen peaks are clearly present in the sample. Results for samples C6 and F can be seen in Appendix A: Iron-based results.

Table 3.1 shows a summary of the carbon and oxygen content (in atomic %) on the surface of the materials analysed. All of the samples exhibit over 40 % of carbon content and over 35 % of oxygen content, rendering the quantification of the composition of the alloy impossible.

Chapter 3. Iron-based alloys results

Table 3.1 – Carbon and oxygen surface content [at. %].

Sample	Carbon content [at. %]	Oxygen content [at. %]
C1	46.12	37.60
C6	42.82	36.95
F	49.94	42.98
MA	44.70	38.38

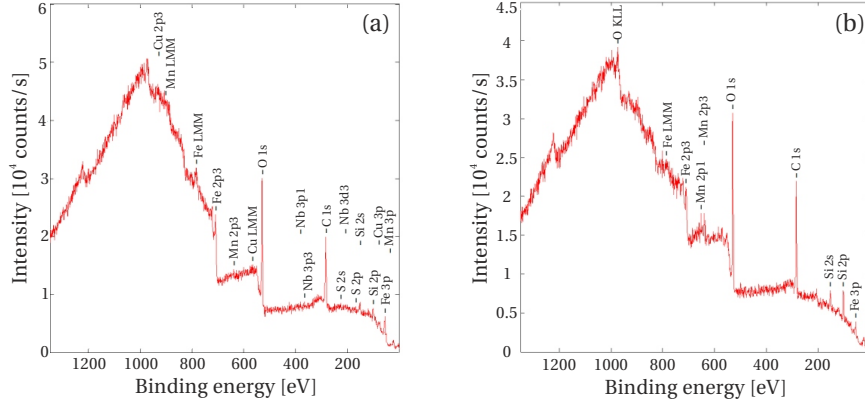


Figure 3.1 – XPS surface results for samples C1 (a) and MA (b).

An in-depth analysis of sample F showed that the oxygen and carbon layer are still present at a depth of 9 nm, where there is still a 12.14 % of carbon and a 10.82 % of oxygen. Figure 3.2 shows how the atomic percent composition of the sample changes with depth (each sputtered layer was 9 nm). However, comparing with the rest of the composition results, it was confirmed that preferential sputtering was occurring, giving a composition enriched in cobalt, and therefore incorrect. No more iron-based samples were analysed due to this.

3.1.2 SEM-EDX

The following table show the composition for the iron-based alloys in atomic percent.

Table 3.2 – SEM-EDX results for iron-based materials.

Sample	Composition [at. %]
C1	$\text{Fe}_{77.8}\text{Co}_{0.6}\text{Nb}_{3.1}\text{Si}_{17.5}\text{Cu}_1$
C6	$\text{Fe}_{88.4}\text{Si}_{11.6}$
F	$\text{Fe}_{77.3}\text{Si}_{17.6}\text{Nb}_{3.6}\text{Cu}_{1.5}$
MA	$\text{Fe}_{78.1}\text{Nb}_3\text{Si}_{18}\text{Cu}_1$

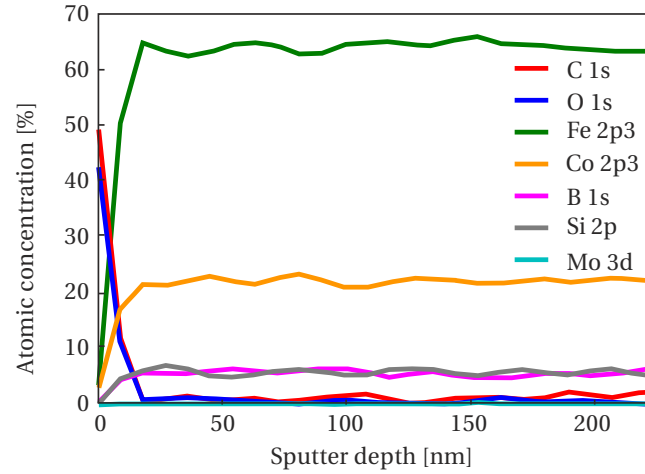


Figure 3.2 – XPS in-depth results for sample F.

3.1.3 EMPA

Table 3.3 shows the EMPA results for the iron-based materials in atomic percent.

Table 3.3 – EMPA results for iron-based materials [at. %].

Sample	Composition
C1	$\text{Fe}_{73.4}\text{Co}_{0.3}\text{Nb}_3\text{Si}_{14.4}\text{B}_8\text{Cu}_{0.9}$
C6	$\text{Fe}_{78}\text{B}_{12.9}\text{Si}_{8.9}\text{Cu}_{0.1}$
F	$\text{Fe}_{79.6}\text{Co}_{0.1}\text{Nb}_3\text{Si}_{16.1}\text{Cu}_1$
MA	$\text{Fe}_{73.6}\text{Nb}_3\text{Si}_{14.7}\text{B}_{7.6}\text{Cu}_{0.9}$

3.1.4 Assessment

The following compositions are known from literature:

- Magnetec (MA): $\text{Fe}_{73.5}\text{Nb}_3\text{Si}_{15.5}\text{B}_7\text{Cu}$ [61].
- Finemet (F) : Fe, Si, B and small amounts of Cu and Nb [62].

As has been stated before, boron cannot be detected by SEM-EDX and therefore, the results of the samples that contain boron can only be used qualitatively. Sample F, the only one without boron (even though the theoretical composition does have it), has a similar composition in both methods, although it can be seen that the EMPA technique shows traces of 0.1% of cobalt. For the rest of the samples, SEM-EDX and EMPA show the same elements present. Comparing both results by normalising the EMPA results without taking into account the boron content, the maximum difference in element composition is of 2.5%, found in the iron content of sample F. Moreover, the results are

in good agreement with the composition found in the literature for sample MA.

The XPS cannot be used because of the preferential sputtering in the in-depth results and the contamination in the surface results.

3.2 Crystallinity

3.2.1 XRD

All the samples show crystallinity compatible with α -iron as can be seen in Figure 3.3, with the α -iron peaks shown in red. With exception of sample MA, diffraction peaks are not very high with respect to the baseline noise, due to the low proportion of crystalline phase present, indicating that there is a majoritarian amorphous phase. The width of the peaks is inversely proportional to the crystallite size, again indicating that all samples except MA have very small crystallites embedded in the amorphous matrix.

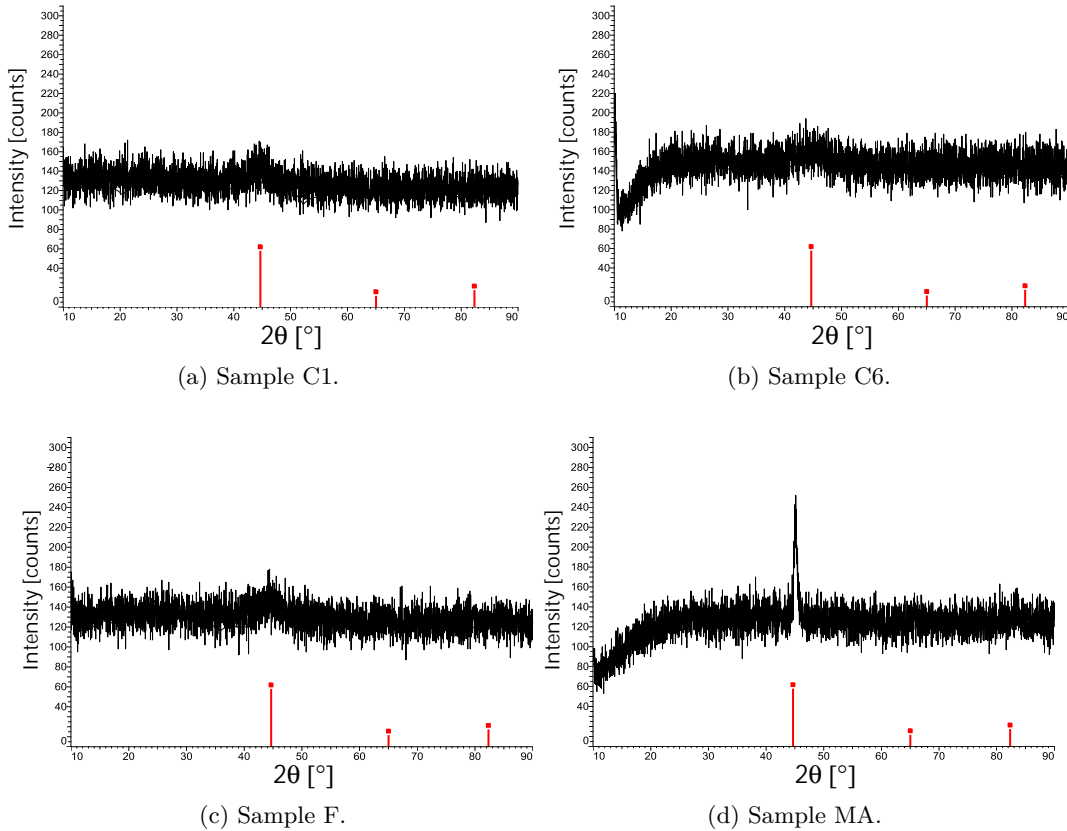


Figure 3.3 – XRD diffraction patterns for C1 (a), C6 (b), F (c) and MA (d).

3.2.2 HE-XRD

Table 3.4 shows the results for the HE-XRD for the iron-based alloys. When the test was performed, sample F had not been acquired yet and was therefore not analysed. The table shows the composition of the crystalline phase found in the alloys as well as the average size of the crystallites.

Table 3.4 – HE-XRD results for iron-based alloys.

Sample	Crystalline phase composition	Average size [nm]
C1	α -Fe	1.6 ± 0.2
C6	α -Fe	1.5 ± 0.2
MA	$\text{Fe}_{75}\text{CuNb}_{3.3}\text{Si}_{16.5}\text{B}_{4+x}$:	
	fraction I: 90.4 %	14.3 ± 0.2
	fraction II: 9.6 %	1.7 ± 0.2

The diffraction profiles of samples C1 and C6 are similar to each other and the average crystallite size is practically identical as can be seen on Figure 3.4, where the diffraction profiles for both samples have been superimposed. Both diffraction profiles can be fitted with an α -iron structure with an Im-3m space group and a cell parameter of $a \approx 2.9 \text{ \AA}$.

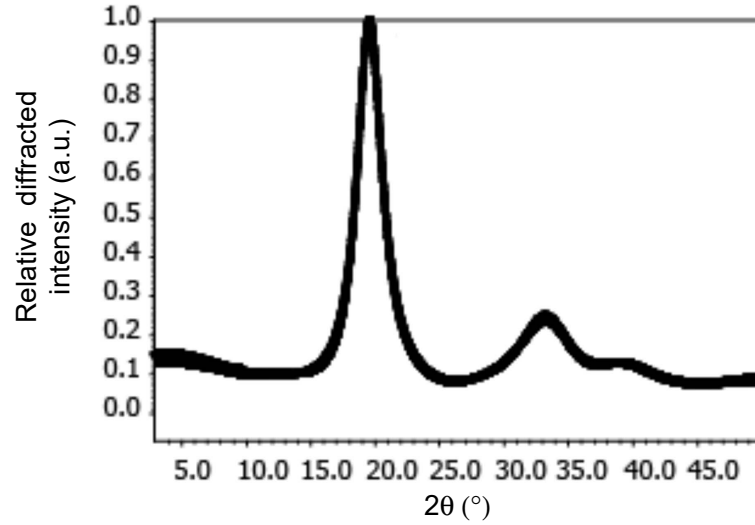


Figure 3.4 – Superimposed diffraction patterns of samples C1 and C6.

Figure 3.5 shows the structure refinement for sample MA and indicates it is compatible with a structure type Fe_3Si ; a cubic structure with a space group type Fm-3m and cell parameter $a = 5.66 \text{ \AA}$. The structure has three sites of atomic positions: Fe1 (4b), Fe2 (8c) and Si1 (4a) as can be seen on figure 3.5 (a). For a composition of $\text{Fe}_{75}\text{CuNb}_{3.3}\text{Si}_{16.7}\text{B}_4$, the iron atoms in the alloy would be found in the Fe1 and Fe2-sites, while the Si-site

would be occupied with a mixture of the rest of the atoms (66 % Si, 4 % Cu, 13 % Nb and 16 % B).

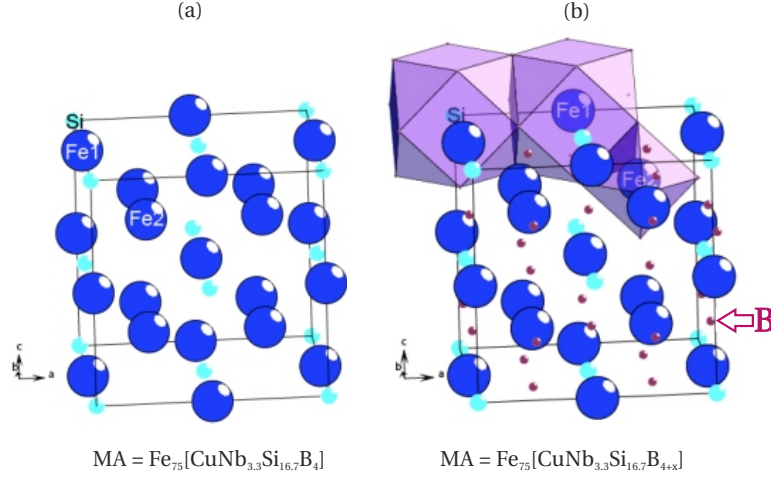


Figure 3.5 – MA crystallographic structure refinement.

However, as the known composition is $Fe_{75}CuNb_{3.3}Si_{16.7}B_7$, the only Wyckoff position which can be considered for these (marked as B2) is 24d with coordinate $(\frac{1}{4} \frac{1}{4} 0)$ as can be seen in the residual electron density map in Figure 3.6. This provides a comparison between the experimental Diffraction Pattern (DP) and the $Fe_{75}CuNb_{3.3}Si_{16.7}B_7$ model. The map will show positive density where there should be more electrons present and negative where there should be less.

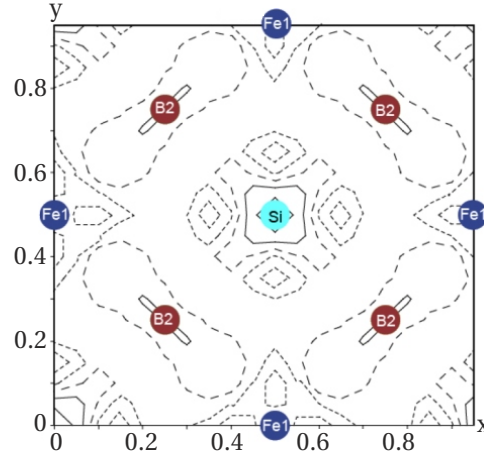
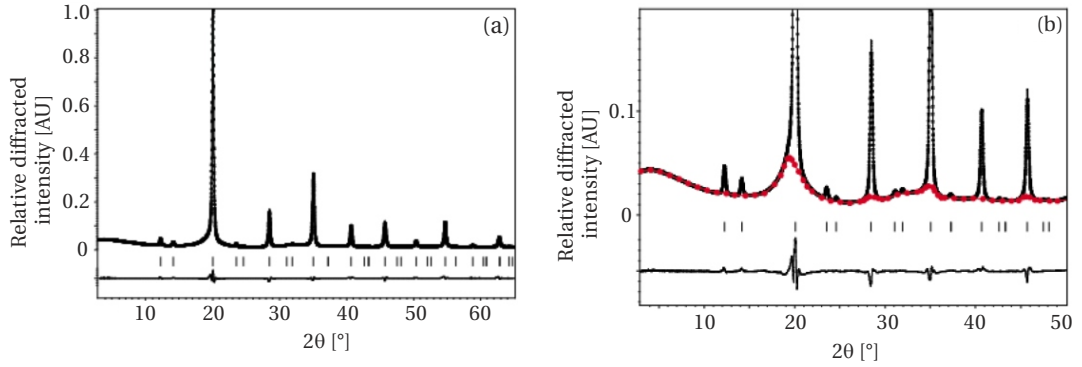


Figure 3.6 – Fe_3Si -type structure simulation for sample MA.

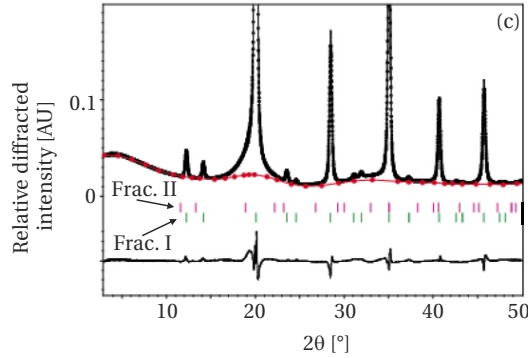
The dotted lines correspond to a negative density, dashed to zero and solid to positive density values, the step between them being $0.2 e \text{ \AA}^{-1}$. In this case, a very small electron density ($0.22 e \text{ \AA}^{-1}$) is observed in the vicinity of the B2 sites. The cubo-octahedron and

octahedral coordination of the main structural atoms seem very plausible, even if the refinement of the 24d site occupancy in the simulations shows a low probability for the presence of the boron atoms. The iron and silicon-sites would be occupied with the same atom distribution as for the first case.

Structure refinement for the DP was done with the $\text{Fe}_{75}\text{CuNb}_{3.3}\text{Si}_{16.7}\text{B}_4$ structure. Figure 3.7 (a) shows the DP profile, with the Bragg reflections of the Fe_3Si -type structure (shown as vertical lines underneath) and below them, the difference between both profiles. Figure 3.7 (b) shows a detail of the DP, with the resulting background after subtracting the Fe_3Si DP in red. The background is unusual and points out that there must be a second fraction with the same composition but with a smaller domain size. The refinement accounting for both fractions improves the background significantly. The unit cell parameter a and the contribution percentage were refined independently for each fraction.



(a) MA structure refinement with Fe_3Si -type structure. (b) Detail of refinement with Fe_3Si -type structure.



(c) Detail of refinement with two different fractions.

Figure 3.7 – DP refinement for sample MA with Fe_3Si -type structure.

Figure 3.7 (c) shows the resulting background after the refinement of the fractions, giving a predominant fraction ($90.4\% \pm 0.7\%$) of $14.3 \pm 0.2\text{ nm}$ and another one, $9.6\% \pm 0.6\%$

of 1.7 ± 0.2 nm. Fraction I was found to have $a = 5.6725 \text{ \AA} \pm 2 \times 10^{-4} \text{ \AA}$, while for fraction II $a = 5.99 \text{ \AA} \pm 2 \times 10^{-2} \text{ \AA}$. The rest of the atomic parameters (cubic cell type and Fm-3m space group), were set to be identical.

These results on the nanocrystalline phase of this alloy had never been studied before. The expected composition of the crystals in iron-based nanocrystallised alloys is normally α -iron. The refinement of the DP shows that the crystalline phase has a composition like the one of the alloy. However, it can be seen from the subtraction of the DP and the baseline that there are still some secondary unidentified phases that could contain α -iron, but the refinement clearly points to the crystals having a composition of $\text{Fe}_{79.6}\text{Si}_{16.1}\text{Nb}_3\text{Cu}_1\text{Co}_{0.1}$, with two fractions of different size.

3.2.3 TEM

Sample C1

C1's TEM DP images show rings indicating that the sample presents crystallinity.

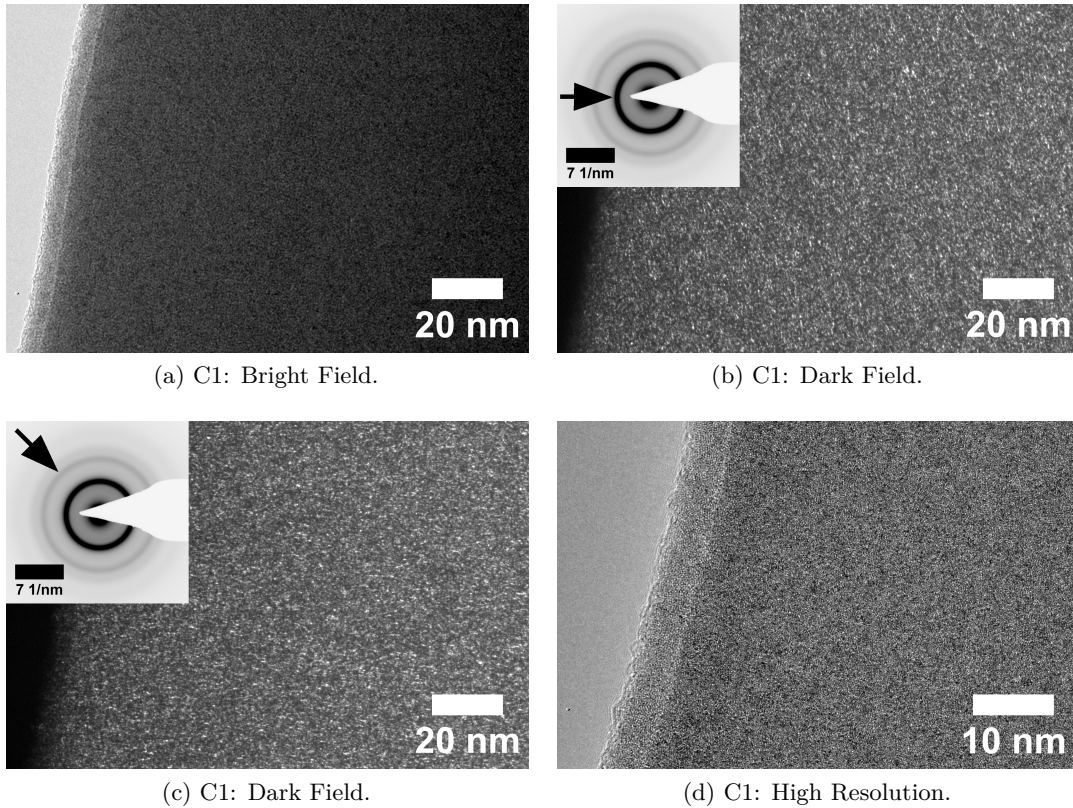


Figure 3.8 – TEM images for sample C1: bright field (a), dark field (b,c), high-resolution (d). The arrow in the insert shows the selected ring in the DP.

3.2. Crystallinity

Looking at the DP for C1 and checking in the Crystallographic Open Database (COD), it can be seen that the best fit is found for bcc $\text{Fe}_{0.91}\text{Si}_{0.09}$, with space group Im-3m and cell parameter $a \approx 2.9 \text{ \AA}$ (COD ID 9006607). Figure 3.9 shows the DP with the superimposed diffraction rings of the $\text{Fe}_{0.91}\text{Si}_{0.09}$ structure, with the Gaussian curves representing the intensity of each ring. Table 3.5 shows the radii measured experimentally for sample C1 and the database's ring diameter for the structure as well as the difference between them.

Table 3.5 – C1 DP rings vs $\text{Fe}_{0.91}\text{Si}_{0.09}$ DP.

	Radius 1 [nm^{-1}]	Radius 2 [nm^{-1}]	Radius 3 [nm^{-1}]	Radius 4 [nm^{-1}]
C1	4.89	6.66	8.16	9.55
$\text{Fe}_{0.91}\text{Si}_{0.09}$	4.97	7.04	8.62	9.95
Difference	1.7 %	5.3 %	5.3 %	4.0 %

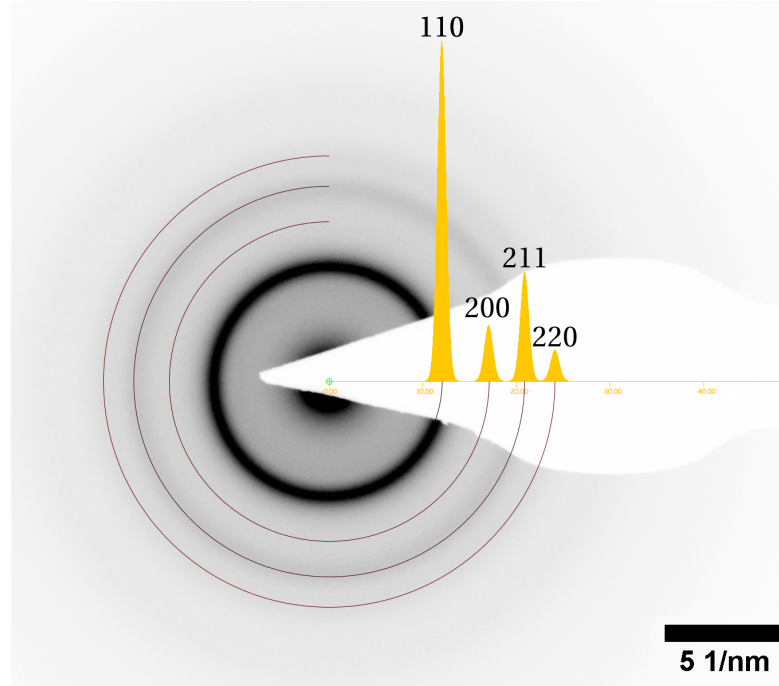


Figure 3.9 – DP of sample C1 with the theoretical rings of $\text{Fe}_{0.91}\text{Si}_{0.09}$ superimposed.

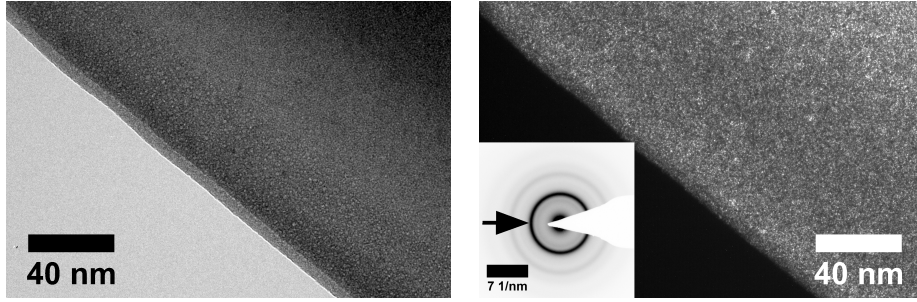
Sample C6

As with sample C1, C6's TEM DP images show rings indicating that the sample also presents crystallinity.

As observed in sample C1, sample C6 also presents the best fit for the same crystalline structure with composition $\text{Fe}_{0.91}\text{Si}_{0.09}$. Table 3.6 shows the radii for the measured sample and for the $\text{Fe}_{0.91}\text{Si}_{0.09}$ structure found in the COD.

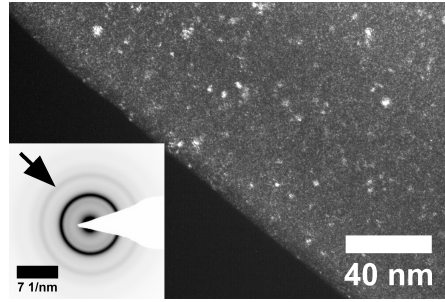
Table 3.6 – C6 DP rings vs $\text{Fe}_{0.91}\text{Si}_{0.09}$ DP.

	Radius 1 [nm^{-1}]	Radius 2 [nm^{-1}]	Radius 3 [nm^{-1}]	Radius 4 [nm^{-1}]
C6	4.97	6.97	8.40	10.08
$\text{Fe}_{0.91}\text{Si}_{0.09}$	4.97	7.04	8.62	9.95
Difference	0.1 %	0.9 %	2.5 %	1.3 %



(a) C6: Bright Field.

(b) C6: Dark Field.



(c) C6: Dark Field.

Figure 3.10 – TEM images for sample C6: bright field (a) and dark field (b,c).

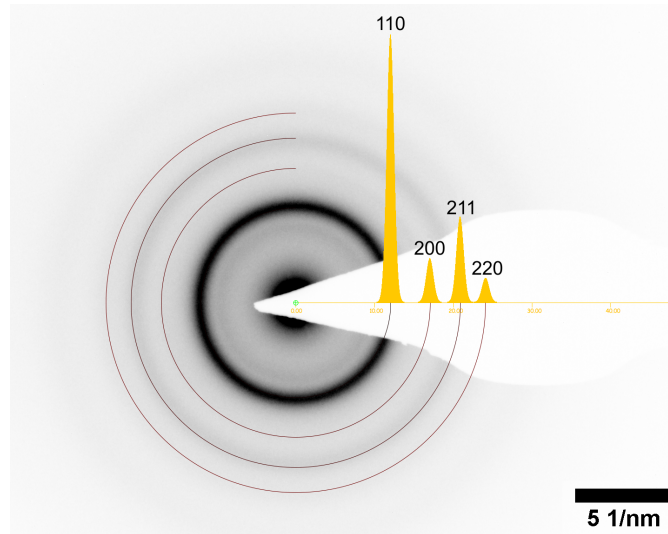


Figure 3.11 – DP of sample C6 with the theoretical rings of $\text{Fe}_{0.91}\text{Si}_{0.09}$ superimposed.

Sample F

Sample F proved to be especially susceptible to beam damage. Several exposure tests were performed in order to ensure that the final results would not be affected by the beam. It was found that an exposure of one minute or less did not affect the sample's microstructure. As with the samples before, the DP also indicates the presence of a crystalline phase.

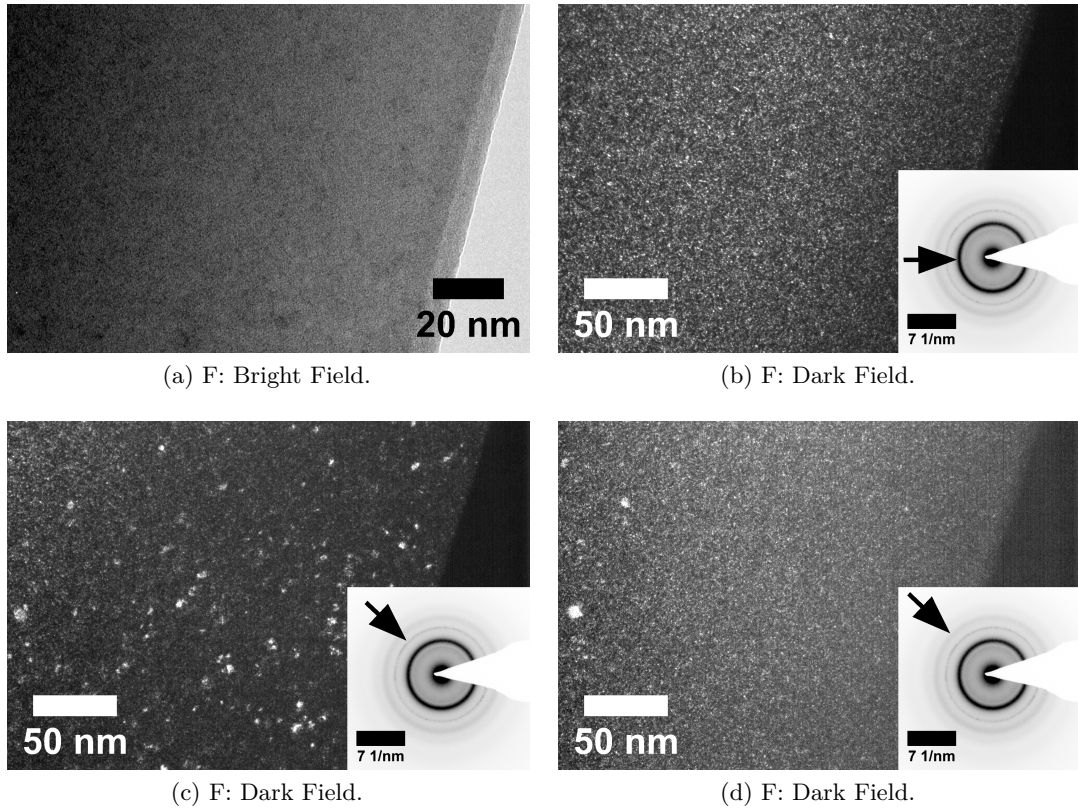


Figure 3.12 – TEM images for sample F: bright field (a) and dark field (b,c,d).

Sample F also shows the best fit for $\text{Fe}_{0.91}\text{Si}_{0.09}$, with the same crystal structure as C1 and C6 (space group Im-3m and $a \approx 2.9 \text{ \AA}$).

Table 3.7 – F DP rings vs $\text{Fe}_{0.91}\text{Si}_{0.09}$ DP.

	Radius 1 [nm^{-1}]	Radius 2 [nm^{-1}]	Radius 3 [nm^{-1}]	Radius 4 [nm^{-1}]
F	4.85	6.79	8.41	9.65
$\text{Fe}_{0.91}\text{Si}_{0.09}$	4.97	7.04	8.62	9.95
Difference	2.6 %	3.6 %	2.5 %	3.1 %

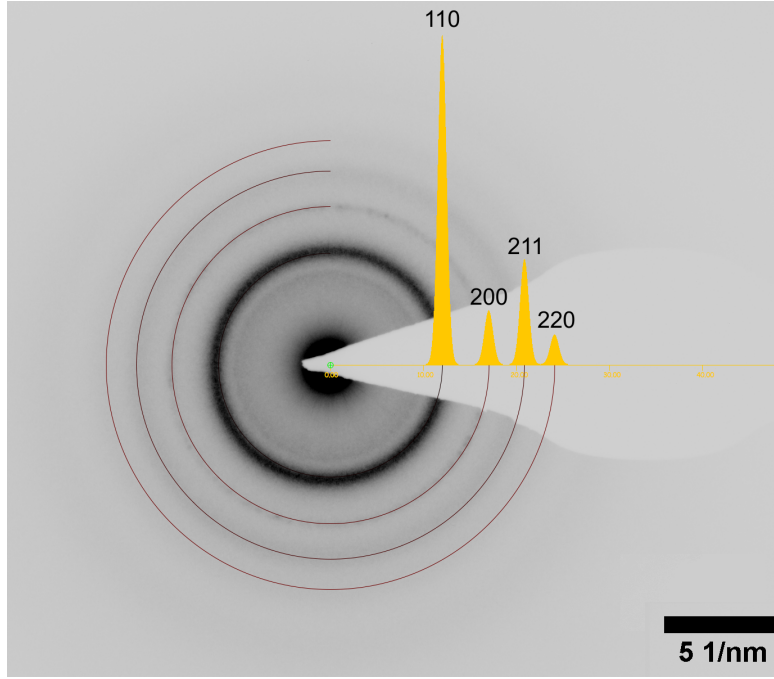


Figure 3.13 – DP of sample F with the theoretical rings of $\text{Fe}_{0.91}\text{Si}_{0.09}$ superimposed.

MA

Sample MA showed the largest crystals of all the iron-based samples. The average size of 14nm calculated by HE-XRD is consistent with the crystals visible below. More high-resolution images can be seen in Appendix A.

The particle analysis of Figure 3.14 (b) shows an average particle size of $10.9 \text{ nm} \pm 5.7 \text{ nm}$. The biggest particle in the image is 25.9 nm and the smallest one 4.4 nm.

The particle analysis on Figure 3.14 (c) shows an average particle size of $8.9 \text{ nm} \pm 4.7 \text{ nm}$. The biggest particle in the image is 22.2 nm and the smallest one 3.6 nm.

MA also shows the best fit for the $\text{Fe}_{0.91}\text{Si}_{0.09}$ structure. Table 3.8 shows the radii comparison and Figure 3.15 both DPs superimposed for comparison.

Table 3.8 – MA DP rings vs $\text{Fe}_{0.91}\text{Si}_{0.09}$ DP.

	Radius 1 [nm^{-1}]	Radius 2 [nm^{-1}]	Radius 3 [nm^{-1}]	Radius 4 [nm^{-1}]
MA	5.06	7.10	8.67	9.91
$\text{Fe}_{0.91}\text{Si}_{0.09}$	4.97	7.04	8.62	9.95
Difference	1.6 %	0.9 %	0.6 %	0.4 %

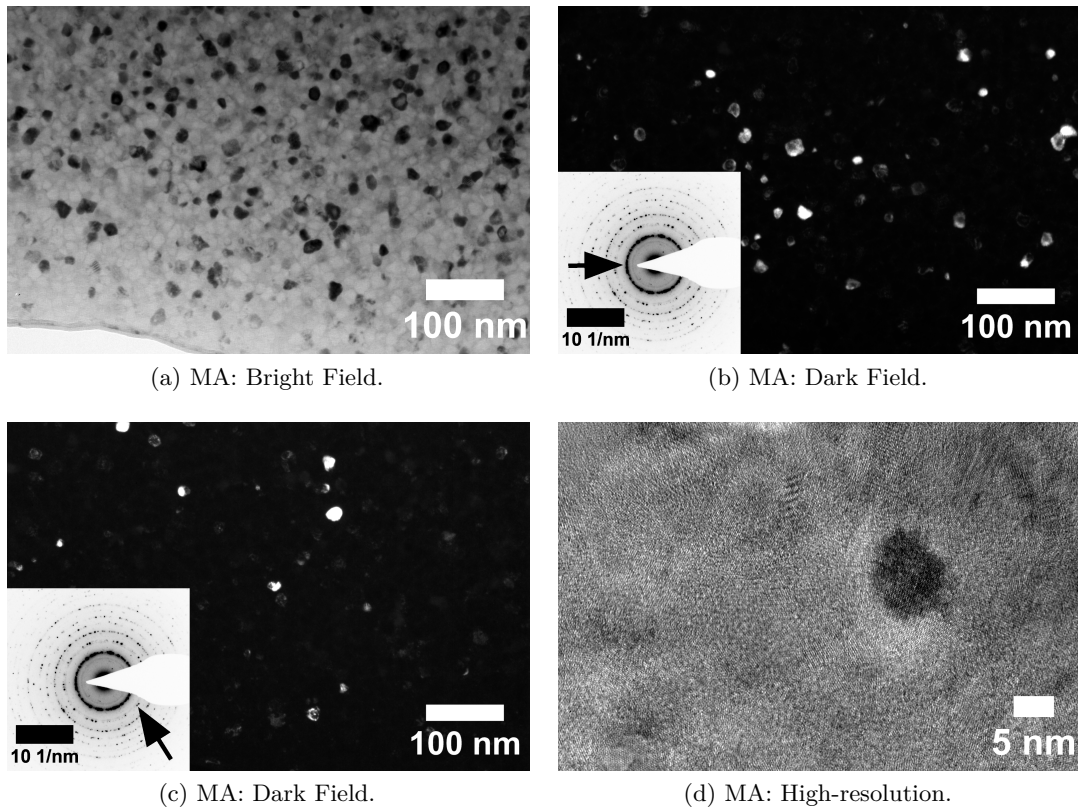


Figure 3.14 – TEM images for sample MA: bright field (a), dark field (b,c) and high-resolution (d).

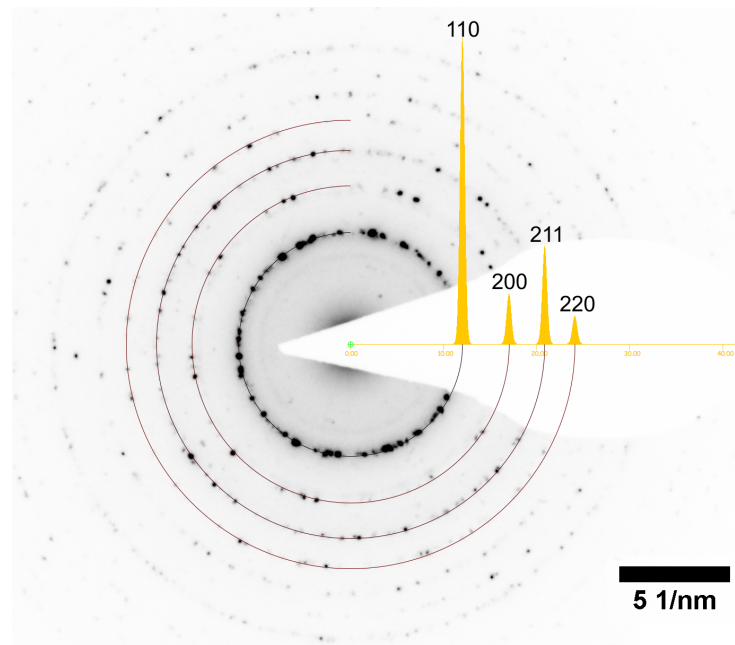


Figure 3.15 – DP of sample MA with the theoretical rings of $\text{Fe}_{0.91}\text{Si}_{0.09}$ superimposed.

3.2.4 Assessment

Regarding the average crystallite size, the three techniques (XRD, HE-XRD and TEM) are consistent and show that all samples present a certain amount of crystallinity, with sample MA having the largest crystals. HE-XRD shows crystal sizes of $14.3 \text{ nm} \pm 0.2 \text{ nm}$, while the crystals seen on TEM are $10.9 \text{ nm} \pm 5.7 \text{ nm}$.

Regarding the composition of the crystals, HE-XRD diffraction profiles fit an α -iron with space group Im-3m and cell parameter $a \approx 2.9$, whilst the TEM has a better fit for bcc $\text{Fe}_{0.91}\text{Si}_{0.09}$, with space group Im-3m and cell parameter $a \approx 2.9 \text{ \AA}$ (COD ID 9006607). It can be seen that both the space group and the cell parameter are the same for both fits, the difference in the composition of the structure can be attributed to the differences in the techniques, as it has been seen that the crystallite size is also different.

3.3 Phase transformation

3.3.1 DSC

PerkinElmer DSC 8000

Table 3.9 shows the onset and peak crystallisation temperatures for the iron-based samples at $10^\circ\text{C min}^{-1}$. Sample MA crystallises only over 680°C and can therefore only be seen on the Netzsch DSC results. Samples C1 and F presented a peak with a very similar onset at about 510°C , while C6 showed two crystallisation peaks with onset at 501.86°C and 544.01°C .

Table 3.9 – PerkinElmer DSC 8000 T_x results for iron-based alloys at $10^\circ\text{C min}^{-1}$.

Sample	Onset [$^\circ\text{C}$]	Peak [$^\circ\text{C}$]	Area [J g^{-1}]
C1	510.85	531.06	58.00
C6	501.86	510.19	45.34
	544.01	549.94	70.35
F	510.31	529.02	67.77

The rest of tables for the onset and peak temperatures for all of the samples at 5°C min^{-1} , $20^\circ\text{C min}^{-1}$ and $50^\circ\text{C min}^{-1}$ can be seen in Appendix A.

Figure 3.16 shows the plots with the onset and peak crystallisation temperatures for all the samples and peaks (as sample C6 presents two). It can be seen that both temperatures increase linearly with the heating rate. The temperatures measured at $20^\circ\text{C min}^{-1}$ look higher than what they were predicted to be. This can also be seen in

the cobalt-based alloys, suggesting that it might be a problem with the calibration at this particular heating rate. The worst fit is seen on the F sample for the crystallisation peak temperature, with an $R^2 = 0.893$.

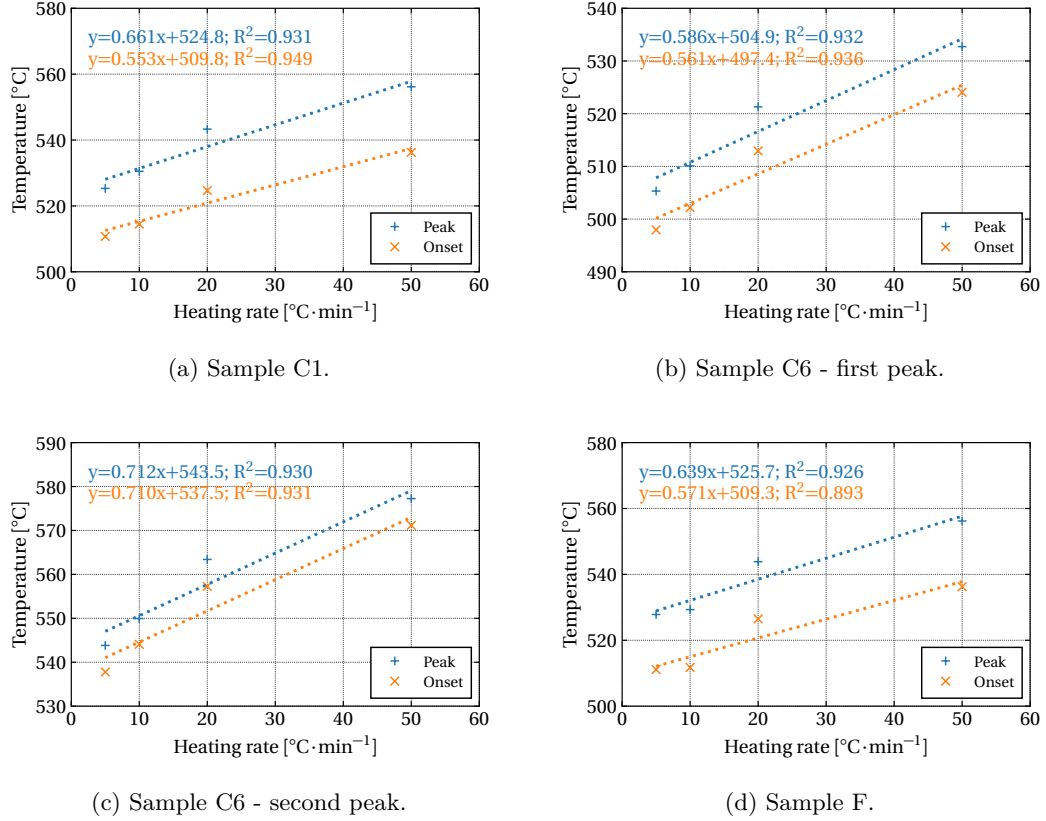


Figure 3.16 – Heating rate dependence of crystallisation onset and peak temperatures for iron-based samples.

The increase of the crystallisation temperature can be explained due to the fact that it is a solid state phase transformation usually dependent on atomic diffusion and often controlled by nucleation and growth kinetics. When the material is exposed to different heating rates, it will be at high temperatures during varying times, affecting diffusivity. Bigger elements present in the alloy have a slow diffusion velocities at low heating rates and therefore remain in the amorphous matrix, not being able to crystallise [63].

Netzsch DSC 404 C

Table 3.10 shows the crystallisation onset, peak and area for all samples as well as the difference between the onset crystallisation temperatures. The Netzsch DSC, being able to measure up to a higher temperature, shows peaks that could not be measured with the PerkinElmer DSC for samples C1 and F. Sample MA was measured and showed as well

Chapter 3. Iron-based alloys results

two crystallisation peaks like the rest of the samples, but in a higher temperature range, the first one at 681.4 °C and the second one at 718.1 °C. The onset and peak temperatures are comparable with the PerkinElmer measurements. The difference between the onset crystallisation temperatures is important to avoid the crystallisation of unwanted phases as described in [2], [7]. For this reason, it is desirable that the crystallisation temperatures are far apart to decrease the risk of this happening. Sample MA presents the lowest difference, with 36.7 °C and then sample C6, with 42.2 °C. Sample F has the highest difference of 210.6 °C, which allows for a comfortable operation margin over the first crystallisation temperature.

Table 3.10 – Netzsch DSC 404 C T_x results for iron-based alloys at 10 °C min⁻¹.

Sample	Onset [°C]	Peak [°C]	Area [J g ⁻¹]	$\Delta\text{Onset}(T_{x2} - T_x)$
C1	507.8	529.5	63.4	178.2
	686.0	700.0	19.3	
C6	498.1	507.7	43.1	42.2
	540.3	544.8	67.7	
F	507.5	527.4	61.8	210.6
	695.1	703.8	26.2	
MA	681.4	693.3	16.4	36.7
	718.1	730.0	3.3	

The melting temperatures for the alloys can be seen in Table 3.11. Four scans were performed in order to calculate the average of the melting temperature. It can be seen that C1, F and MA present a very similar result (around 1100 °C), while C6 has a slightly higher melting temperature, 1139.1 °C.

Table 3.11 – Netzsch DSC 404 C melting temperature results for iron-based alloys at 10 °C min⁻¹.

Sample	Onset [°C]	Std. Dev. [°C]
C1	1102.4	0.2
C6	1139.1	0.5
F	1102.6	0.5
MA	1104.2	0.0

The DSC curves of the samples show a lack of glass transition. This does not necessarily imply that the material is not really amorphous or is microcrystalline. Jin et al. [64] suggest that glass transition may be obscured by other exothermic reactions since the glass transition of a particular material partly depends on its thermal history. That is, a small exothermic peak due to the glass transition may be obscured when other heat

evolving reactions, such as structural relaxation, occur near the glass transition. These heat evolution reactions can be removed by pre-annealing the samples to reveal the glass transition temperature.

3.3.2 High Temperature in-situ XRD (HT-XRD)

Sample C1

Figure 3.17 shows the results for the HT-XRD for sample C1. It can be seen in Figure 3.17 (b) that C1 before annealing shows a broad peak in the range of 40° to 52° . Figure 3.17 (a) shows a crystallisation onset temperature of 540°C , with new diffraction peaks appearing at 550°C .

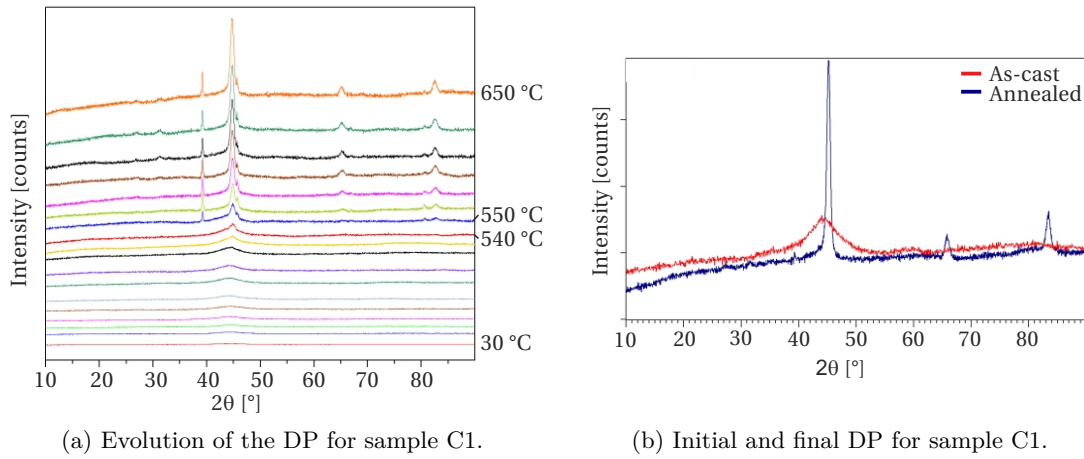


Figure 3.17 – HT-XRD analysis for sample C1.

The phase analysis in Figure 3.18 shows the peak in the range of 38° to 52° in the DP after annealing is consistent with a cubic Fe_3Si phase. The small peak at 39° (marked with an arrow) corresponds to the platinum substrate.

The variation of the grain size of Fe_3Si was calculated using the Scherrer equation as can be seen in Figure 3.19. An increase in grain size, from 11 nm to 22 nm is observed by rising the temperature from 550°C to 650°C . The grain size measured at room temperature after cooling was 22 nm.

Sample C6

The DP of the as-cast sample presents crystallinity as can be seen on Figure 3.20 (b). The alloy shows a crystallisation onset between 430°C and 450°C and another one between 500°C and 520°C .

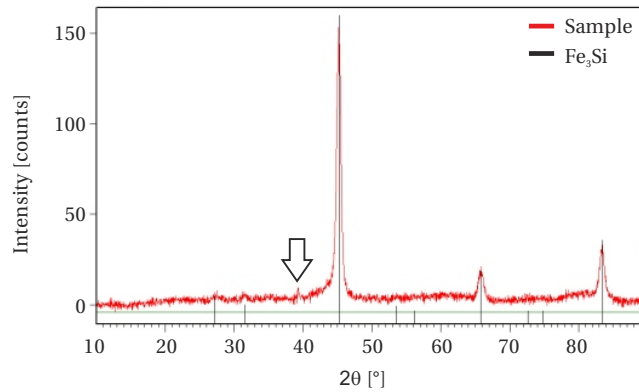


Figure 3.18 – Phase analysis for sample C1.

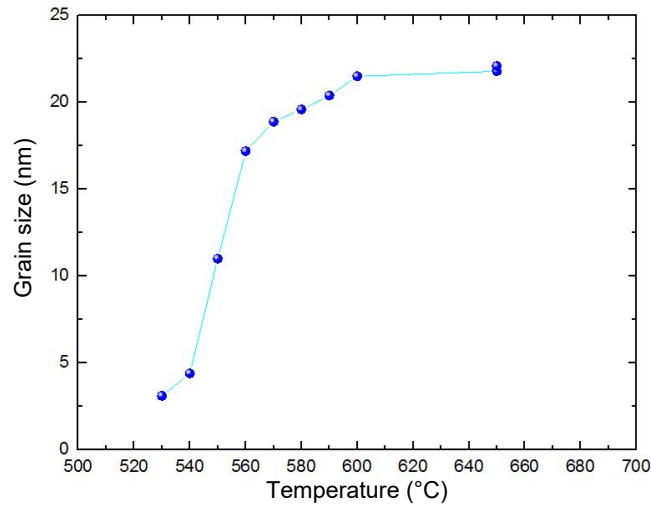


Figure 3.19 – Grain size study for sample C1.

The peak at 470 °C is consistent with a cubic $\text{Fe}_{1.9}\text{Si}_{0.1}$ phase, while the peak at 520 °C is consistent with a tetragonal Fe_2B phase. The diffraction pattern of the annealed sample shows that the $\text{Fe}_{1.9}\text{Si}_{0.1}$ phase represents 73 % of the total crystal concentration, while the Fe_2B represents 27 %.

Sample F

The DP of the as-cast sample presents crystallinity. Sample F shows that crystallisation starts between 550 °C and 575 °C.

The DP shows the crystals have a composition of Fe_3Si . However, it can be seen that the main peak is asymmetric and that some of the smaller peaks cannot be identified, suggesting there must be an underlying unidentified phase.

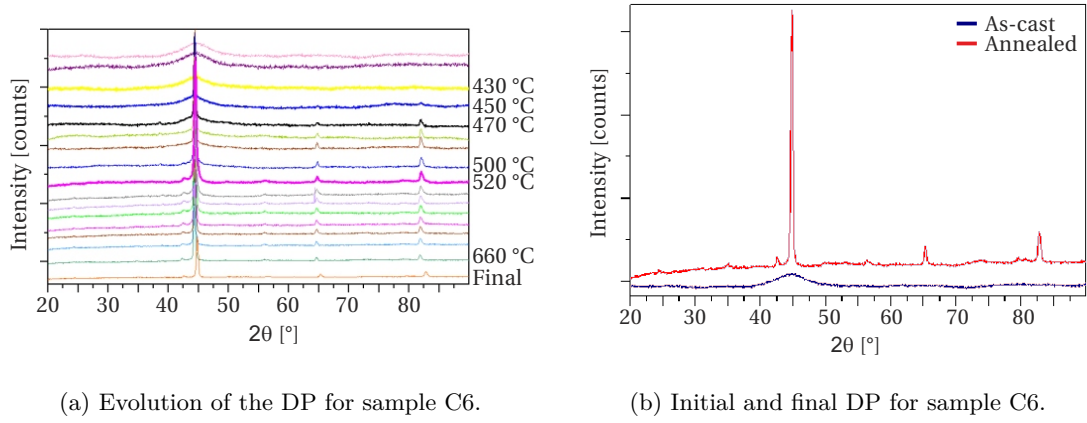


Figure 3.20 – HT-XRD analysis for sample C6.

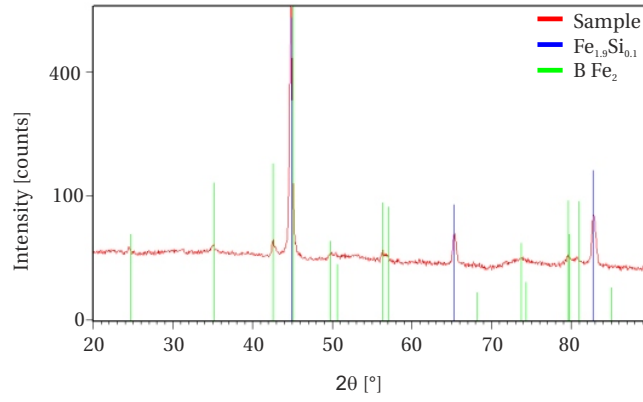


Figure 3.21 – Phase analysis for sample C6.

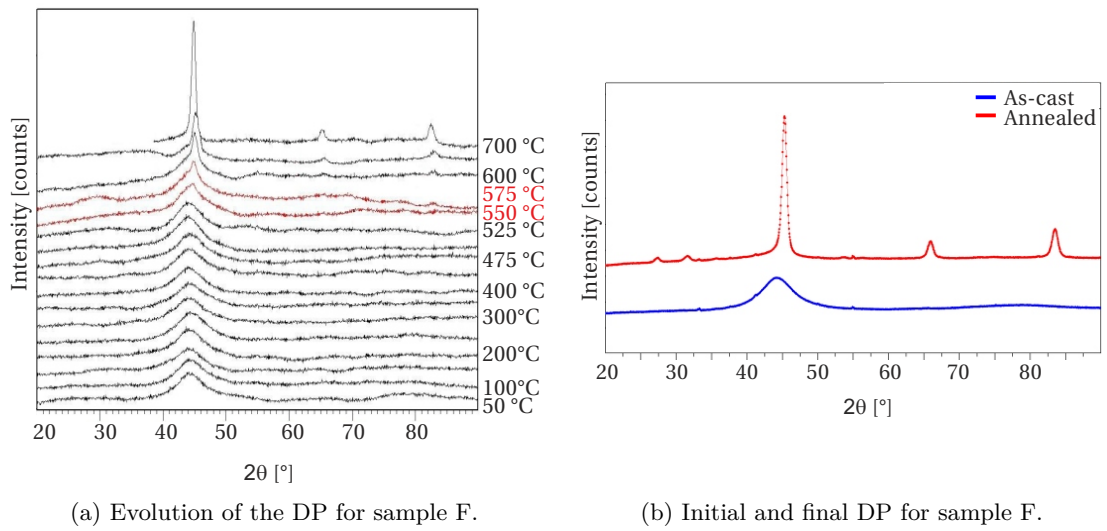


Figure 3.22 – HT-XRD analysis for sample F.

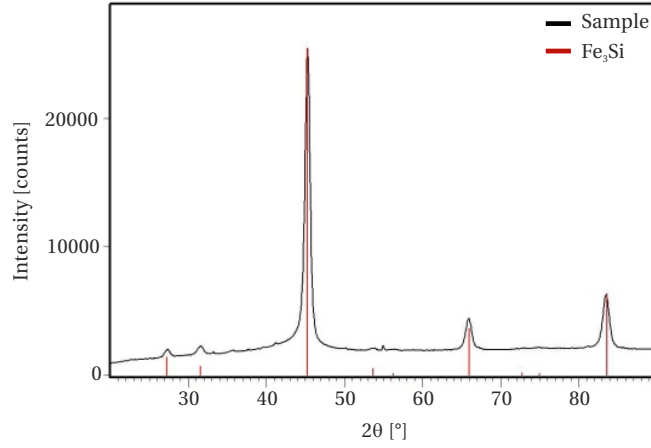


Figure 3.23 – Phase analysis for sample F.

Sample MA

Sample MA could not be measured due to the fragility caused by its nanocrystalline structure. Diffraction patterns showed mainly the platinum substrate peaks.

Table 3.12 shows a summary of the HT-XRD results.

Table 3.12 – HT-XRD results for iron-based alloys.

Sample	T_x [°C]	Composition
C1	540 - 550	Fe ₃ Si
C6	430 - 450 520	Fe _{1.9} Si _{0.1} Fe ₂ B
F	550 - 575	Fe ₃ Si

3.3.3 Assessment

Comparing the three techniques and the differences between their measurements, it can be seen that:

- The relative differences between both DSCs comparing the onset and the peak crystallisation temperatures is less than 1 % for all the samples. The biggest difference is the peak crystallisation temperature of C6, with a relative difference of 0.93 %. The highest relative area difference under the curves can be found in sample C1 at 9.3 %.
- Sample MA has a crystallisation point over 600 °C and could therefore be analysed only by the Netzsch DSC. The fragility of the sample made it impossible to measure it by

Table 3.13 – Relative difference between both DSC measurements.

Sample	Onset [%]	Peak [%]	Area [%]
C1	0.60	0.29	9.3
C6	0.75	0.49	4.86
	0.68	0.93	3.82
F	0.55	0.31	8.75

HT-XRD and only one measurement is available.

Table 3.14 shows a summary of the onset crystallisation temperatures measured by the three different techniques. In order to compare the three techniques, the onset crystallisation peak is taken as the reference parameter for Table 3.15. The relative differences show that the maximum divergence is found between the PerkinElmer DSC and the HT-XRD measurement, of 14.06 %. The rest of the relative differences are under this value and can be therefore considered as normal taking into account the precision of the instruments and the different measuring techniques. The value from the HT-XRD taken to calculate this is the average of the two temperatures between which the crystallisation is detected. It should be taken into account as well that the HT-XRD measurement was taken in steps and therefore the onset crystallisation temperature is less precise than with the other two techniques.

As it was seen in Table 3.10, all of the samples present a second crystallisation peak. The only sample where this is visible on the HT-XRD results is sample C6, as for samples C1 and F the final experimental temperature was lower than the second crystallisation peak, present at 686 °C for sample C1 (with the HT-XRD test finishing at 650 °C) and at 695 °C for sample F (with the HT-XRD finishing at 700 °C).

Table 3.14 – Comparison of onset of crystallisation temperatures for iron-based alloys.

Sample	PE DSC [°C]	Netzsch DSC [°C]	HT-XRD [°C]
C1	511	508	540 - 550
C6	502	498	430 - 450
	544	540	500 - 520
F	510	508	550 - 575
MA	-	681	-

Table 3.15 – Absolute relative difference between the onset crystallisation temperature measured by both DSC's and HT-XRD.

Sample	PerkinElmer vs HT-XRD [%]	Netzsch vs HT-XRD [%]
C1	6.27	6.83
C6	14.06	13.20
	6.67	5.94
F	9.28	9.78

3.4 Magnetic properties

3.4.1 Impedance analyses

Table 3.16 shows the maximum relative complex permeability measured for each set of cores, taking into account the uncertainty of the measurement (only values with less than 10 % uncertainty were kept). A total of five F cores were measured, the maximum relative difference being 22.9 % (representing a standard deviation of 143.2), even though the packing factor and mass are similar (difference is less than 2 %). This could be caused by inhomogeneities in the material or due the manipulation of the core, as external stresses can greatly affect the properties. Figure 3.24 shows the three F cores which present the most differences between them. It can be seen, despite the differences in permeability, that the shape of the curve is similar in all of them, with a cut-off frequency of around 10 kHz, where the permeability starts dropping significantly.

Table 3.16 – Impedance results for iron-based alloys.

Sample	Max. relative permeability	Max. Relative difference [%]
C1	2884 ± 24.1	4%
C6	3057 ± 39	7%
F	1250 ± 25	22.9%

Figure 3.25 shows a summary of the amorphous iron-based cores. It can be seen that sample C6 presents no plateau in the measurement frequency range and the permeability drops quickly from the beginning.

The maximum permeability according to the Magnetec datasheet is in the order of 200 000.

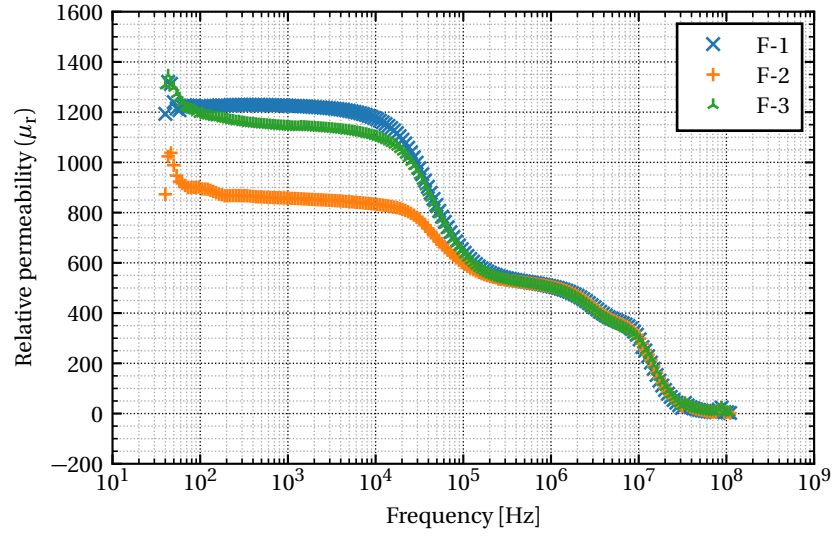


Figure 3.24 – Relative complex permeability for three F cores.

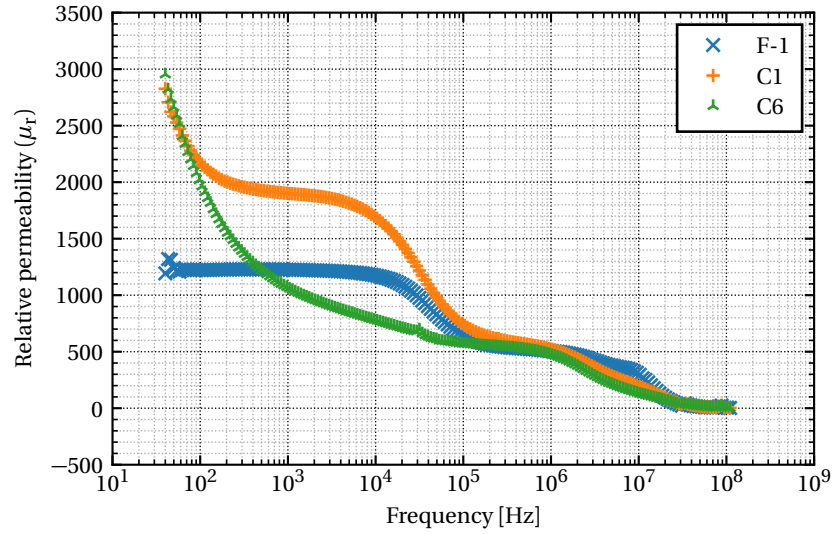


Figure 3.25 – Relative complex permeability for iron-based cores.

Assessment

The relative permeability vs frequency plot is one of the most interesting in order to pick the material for the cores and the instruments. It can be seen from Figure 3.25 that material C6 does not look like a good candidate if the working regime of the instrument should be above 10 kHz. Even though C1 and F look like better materials, it should also be taken into account that their permeabilities are very low, especially compared to the cobalt-based alloys studied in the next chapter. However, as it has already been stated,

iron-based nanocrystalline alloys present very interesting soft magnetic properties, and so thermally treating these materials can potentially improve their magnetic properties.

3.4.2 BH-curve measurements

As it was explained in the Materials and Methods Chapter, two BH curve setups were used during the study. Some of the F cores were measured with the old setup, and others with the new one, giving slightly different BH curves, due to the difference in the excitation. Out of the five F cores measured, the two with the old setup presented a relative difference of 0.69 % between them, while the new setup gave a maximum difference of 15.6 %. This difference comes from the core that showed the lower permeability in Figure 3.24. Table 3.17 summarises the coercivity and remanence values for sample F with both setups.

Table 3.17 – Comparison of both BH curve setups for sample F.

Setup	Coercivity average [A m^{-1}]	Remanence average [T]
Old	14.42 ± 1.44	0.16 ± 0.02
New	19.8 ± 0.20	0.25 ± 0.003

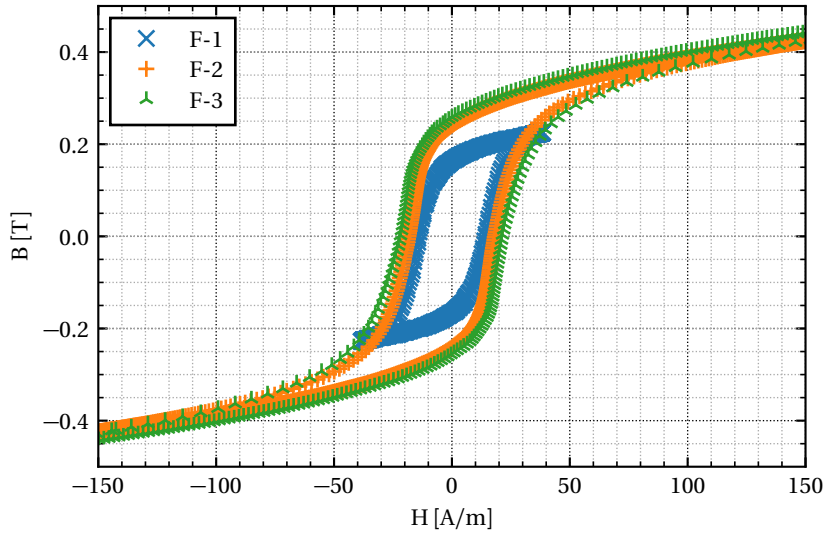


Figure 3.26 – Comparison of BH-curve setups: first setup (F-1) and new setup (F-2 and F-3).

Samples C1 and C6 were both measured with the old BH curve setup. Figure 3.27 shows a comparison of the three iron-based alloys measured with the old setup (for comparison purposes), while Table 3.18 presents the average coercivity and the remanence of the cores.

Table 3.18 – BH curve results for iron-based alloys

Sample	Coercivity [A m^{-1}]	Remanence [T]	Max. relative difference (Hc, Br)
C1	15.05	0.30	0.93%, 0%
C6	19.20	0.70	5.46%, 1.45%

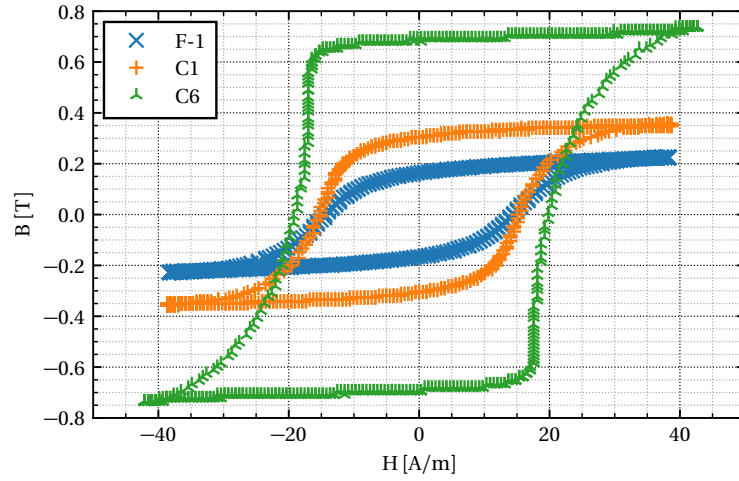


Figure 3.27 – Comparison of BH-curves of iron-based alloys with the first setup.

Assessment

The BH curve measurement is another critical point to take into account in order to choose a material for instrumentation. The saturation value, the losses (coercivity) and the shape of the curve can be key aspects for performance. In DCCTs, as it has been mentioned before, two identical cores are needed, the BH curve being the most critical point where the cores can differ.

Looking at the iron-based alloys BH-curves it can be seen that their coercivities are high. This in principle, makes the material less interesting as a candidate for cores. However, as it has been discussed in previous chapters, some methods for reducing losses can be applied in order to improve this aspect.

The remanence values of F and C1 are also quite low, whilst C6 has a higher value its coercivity is also really high at almost 20 A/m. All these parameters, taken together into account, make the amorphous-iron based materials less interesting for fabricating cores.

3.4.3 Curie temperature measurements

VSM

A first Curie temperature analysis was done by VSM in the University of Zaragoza only with samples C1 and C6. The results can be seen in Figure 3.28. The results have an uncertainty of 10 %.

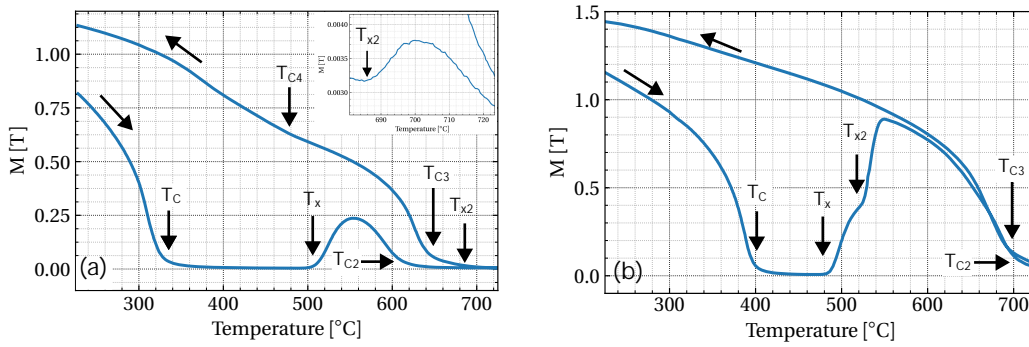


Figure 3.28 – Curie Temperatures using VSM for samples C1 (a) and C6 (b).

Figure 3.28 (a) shows the typical curve for a partially nanocrystallised sample, where the cooling curve shows the Curie temperatures of the two-phased system: the nanocrystalline phase and the residual amorphous phase. The difference in the Curie temperatures for the amorphous phase (T_C and T_{C4}) is explained by the progressive enrichment in metalloids, the interactions between the nanoparticles in the amorphous matrix and the influence of the nanostructure in the magnetisation process [65]. The sample shows a first T_C at 327°C and then the onset of crystallisation (T_X) is at 510°C. The third inflection point (T_{C2}) indicates the Curie temperature of the crystallised phase, seen at 606°C. A new onset crystallisation temperature (T_{X2}) (seen in the insert of the figure) is seen at 685°C, but the sample was not heated enough to see the Curie point of this new phase. Once the sample has reached 730°C, the magnetisation of the sample is recorded during the cooling ramp, giving the fourth inflection point (T_{C3}) for the crystallised phase at 643°C. The residual amorphous phase shows a Curie temperature (T_{C4}) at 478°C.

Sample C6 in Figure 3.28 (b) does not show a residual amorphous matrix T_C on the cooling curve, indicating that most of the sample has been crystallised. It shows a T_C at 407°C. Then, crystallisation takes place in two steps, at 487°C and 530°C. A Curie temperature is then seen at 710°C during heating and then at 692°C during the cooling ramp.

The crystallisation temperatures measured here correspond well to the ones measured by DSC, with onsets at 507.8°C and 686.0°C for C1 and at 498.1°C and 540.3°C for C6.

TGA

To study the rest of the samples, more measurements were done with the TGA. Data was recorded during the heating and cooling ramps, where the thermal hysteresis can be clearly seen in Figure 3.29. When the sample is heated over its Curie temperature, the sample becomes non-magnetic and therefore is not attracted to the magnet placed on top of it. This makes the TGA see an increase in mass of the sample and T_C is calculated to be at the inflection point of the curve. The temperature continues to increase until it reaches a plateau, and then cooling starts at the same rate as the heating. It can be seen in the figure that the sample becomes magnetic again, becomes attracted to the magnet, and the measured mass drops. This happens at a higher temperature for all of the studied samples.

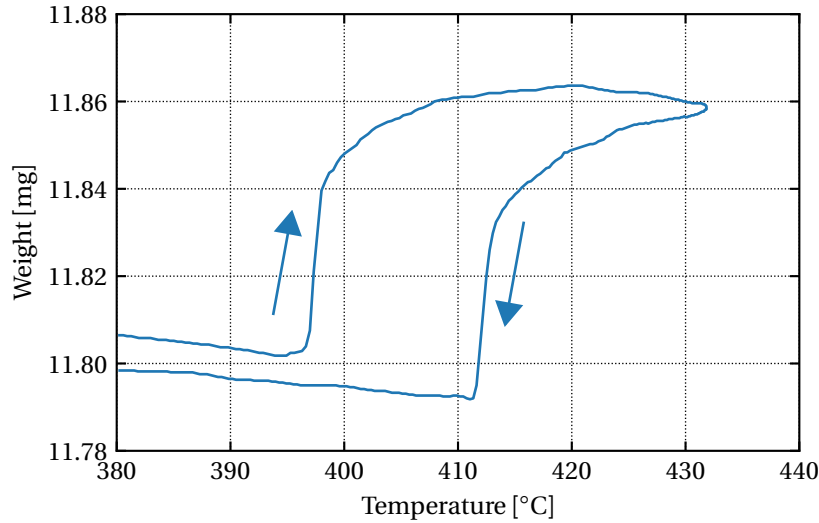


Figure 3.29 – Curie Temperature hysteresis curve for sample C6 at $20\text{ }^{\circ}\text{C min}^{-1}$.

For all of the samples measured, the Curie temperature during heating was always lower than the one during cooling. This phenomenon is called the magnetocaloric effect, which is the reversible temperature change of a magnetic material when a magnetic field is applied or removed, which has been used as a refrigeration technique since its discovery by Warburg in 1881. When the magnetic field is applied to the material, the magnetic moments of the material orient themselves parallel to the field, decreasing the entropy associated with the system. If this is done without any heat exchange (adiabatically), this decrease in magnetic entropy is compensated but the increase of entropy of the lattice, causing at the same time an increase of temperature in the sample. If an adiabatic demagnetisation occurs, the entropy of the sample increases and therefore the lattice entropy decreases, lowering the temperature. If this is done in cycles with a refrigerating fluid, it is the basis for a magnetic refrigerator [66]. If several heating cycles are done, the first heating ramp is different from the following ones, suggesting that there is a

Chapter 3. Iron-based alloys results

process of stress relaxation that changes the material's properties.

Table 3.19 shows the Curie temperature during the heating phase for a heating rate of $10\text{ }^{\circ}\text{C min}^{-1}$. The total uncertainty for the TGA measurement is $\pm 2.6\text{ }^{\circ}\text{C}$.

Table 3.19 – Curie temperature at $10\text{ }^{\circ}\text{C min}^{-1}$ for iron-based alloys with TGA.

Sample	Curie temperature at $10\text{ }^{\circ}\text{C min}^{-1}$ [$^{\circ}\text{C}$]
C1	319
C6	405
F	319
MA	565

Kappabridge

Thermal hysteresis was also seen in all of the samples. Figure 3.30 shows the measurement of sample C1, where the thermal hysteresis can be seen. As with the DSC measurements, all of the Curie temperatures during cooling were higher than during heating. Also, as with the DSC, some samples were measured twice in a row, showing that the initial Curie temperature changes possibly due to the effect of stress-relaxation, but the difference between the heating and the cooling curve can still be seen. The T_C measured during cooling does not change even after several heating cycles, as the stress relaxation mainly happens during the first heating stage.

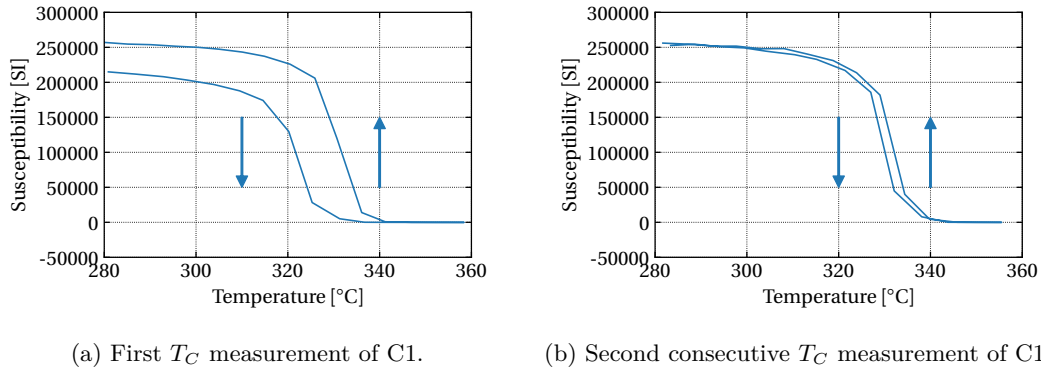


Figure 3.30 – Kappabridge measurements of sample C1.

All of the curves look the same except for sample MA that can be seen in Figure 3.31. The same sample was heated twice up to $700\text{ }^{\circ}\text{C}$. As was seen previously, sample MA has two crystallisation temperatures, with onsets at $682\text{ }^{\circ}\text{C}$ and $718\text{ }^{\circ}\text{C}$. As the measurement's final temperature is above the first crystallisation temperature, the sample will increase its crystallite size, as sample MA already had nanocrystals. This can be seen in Figure 3.31 (a), where the heating and cooling ramp behave differently.

The cooling ramp shows a peak at 259 °C that was not present during heating. Also, during the cooling ramp, the microstructural changes are already visible in the T_C step, that is much smaller than the one on the heating ramp. The second, shows that the sample has indeed changed with the first treatment, with the peak now appearing as well during the heating phase at 253 °C and at 256 °C during cooling.

Table 3.20 – Curie temperature at 11 °C min⁻¹ for iron-based alloys with Kappabridge.

Sample	Curie temperature at 11 °C min ⁻¹ [°C]
C1	325 ± 10
C6	402 ± 12
MA	569 ± 18

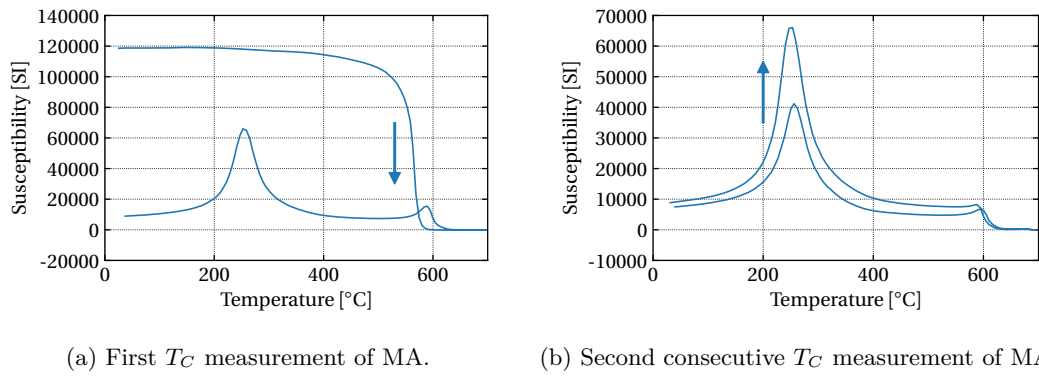


Figure 3.31 – Kappabridge measurements of sample MA.

Assessment

Table 3.21 shows a comparison between all the measurements for the iron-based samples.

Table 3.21 – Curie temperature comparison for TGA, Kappabridge, VSM and literature values [°C].

Sample	TGA	Kappabridge	VSM	Literature
C1	319 ± 2.6	325 ± 10	327 ± 3.3	
C6	405 ± 2.6	402 ± 12	407 ± 3.3	
F	319 ± 2.6			
MA	565 ± 2.6	569 ± 18		600 [61]

Even though all the measurements are in good agreement, some potential differences could be caused by the following:

- A thermal inertia in the measuring device: in the case of the TGA the sample is held

by an alumina pan and covered with alumina powder in order to weight it down against the force of the magnet. The thermocouple is situated under the pan. This might give a thermal lag between the oven and sample temperature which would be more critical the higher the heating and cooling ramps. This becomes apparent with the relative difference in the measured Curie temperature between the cooling and heating ramps, as it increases linearly with the heating rate. In the Kappabridge, this effect is given by the different heat capacities between the sample and the thermocouple.

- The effects of the thermal treatment on the sample: comparing heating and cooling curves within each method, for the TGA the biggest relative difference is seen in C1 (3.5 %), while for the Kappabridge it is seen in MA (6.2 %). During the heating process, the material suffers changes that affect the Curie temperature. This was confirmed in the TGA when the same sample was subjected to several heating and cooling curves, where it was seen that the first Curie temperature measured was different than the subsequent ones. After, all Curie temperatures in the heating curves were similar, as were the ones in the cooling curves. This indicates a possible stress relaxation during the annealing. The most representative example for this is shown in the next chapter.

In order to compare the TGA and the Kappabridge, it should also be taken into account that:

- the heating and cooling rates in the Kappabridge measurements were slightly higher than in the TGA measurements. The set rate for the Kappabridge was $11\text{ }^{\circ}\text{C min}^{-1}$ but measurements show an average heating rate of about $14\text{ }^{\circ}\text{C min}^{-1}$ and a cooling rate of about $12\text{ }^{\circ}\text{C min}^{-1}$.
- the final temperature of the heating ramp was not the same for both methods, so the thermal annealing effects were not the same for the samples.

As stated in [9], if the sample wants to be magnetically annealed, this should happen just below the Curie temperature. In order to ensure that the sample does not change micro-structurally during this process, the Curie temperature should be as far away as possible from the crystallisation temperature. For the iron-based alloys, the smallest difference between the two temperatures is seen in sample C6, $96\text{ }^{\circ}\text{C}$ and the largest one, $189\text{ }^{\circ}\text{C}$ for sample C1 as can be seen in Table 3.22. Taking into account the temperature-control mechanisms and precision of modern ovens, these temperature differences are more than enough to ensure that if the sample is not to be crystallised, there will be no risk if the target temperature is T_C .

3.4.4 VSM and AGM

VSM measurements were taken of all of the samples to study the induced magnetisation (M) and magnetic induction (B) of the samples. This was done for different excitation

Table 3.22 – Difference between first crystallisation temperature and T_C [°C].

Sample	$\Delta(T_x - T_C)$
C1	181
C6	91
F	189
MA	112

fields up to 200 kA m^{-1} . Below, two measurements for each sample are presented, the first one showing the sample saturated for a higher excitation field and the second one at a lower excitation field to see a close-up at coordinates (0,0).

Sample C1

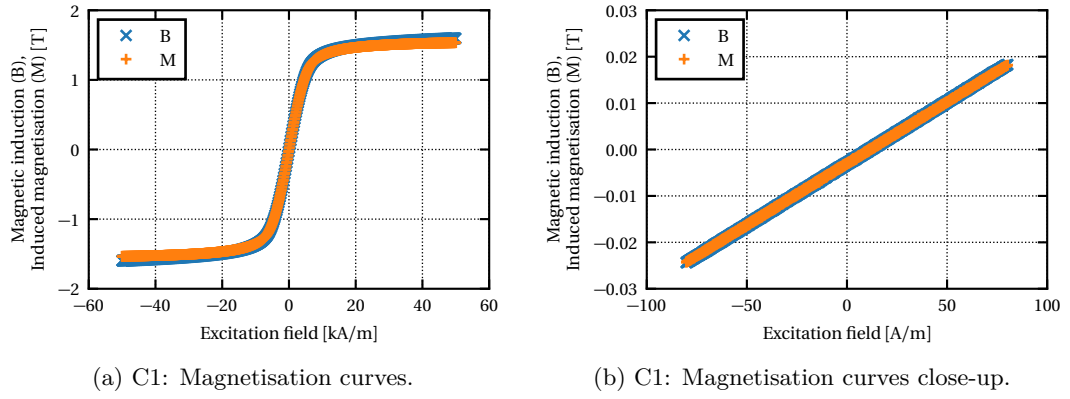


Figure 3.32 – VSM magnetisation curves for sample C1 (a) and a close-up of the central part (b).

Sample C6

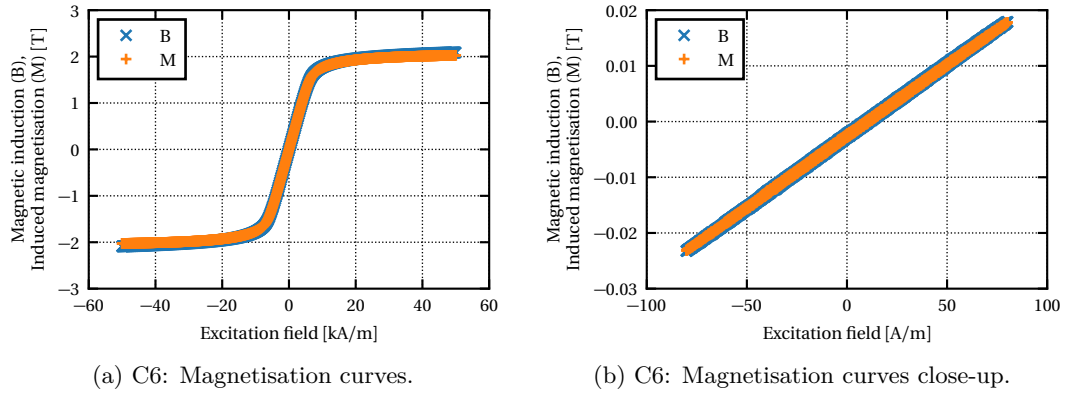


Figure 3.33 – VSM magnetisation curves for sample C6 (a) and a close-up of the central part (b).

Sample MA

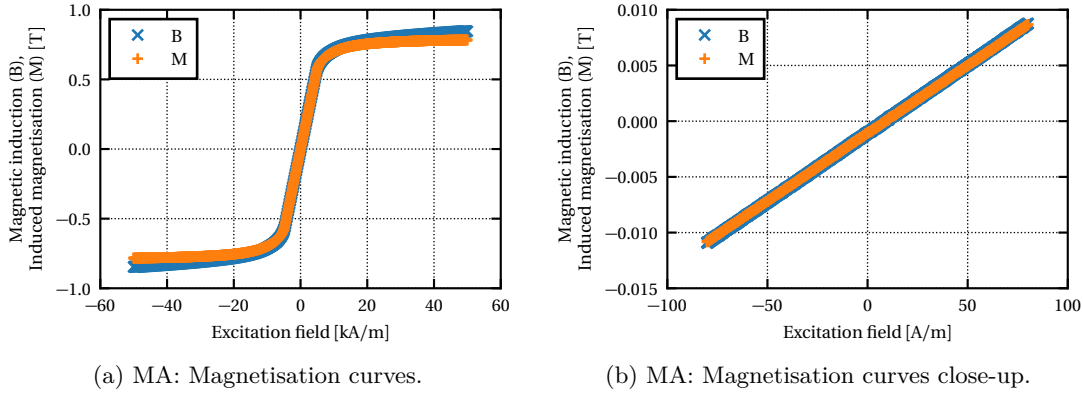


Figure 3.34 – VSM magnetisation curves for sample MA (a) and a close-up of the central part (b).

Sample F

Sample F was not analysed as it was purchased after these tests.

AGM

AGM measurements were done to cross-check the VSM results, using the same conditions. The AGM analyses gave the same saturation results (extracted from the M magnetisation curve) as the VSM, the relative differences for sample C1 being 5.5 %, 4.6 % for C6 and 2.5 % for MA.

Assessment

None of the samples present coercivity and remanence is practically zero. It can be seen in the close-up graphs that some samples are not centred, which is due to some residual magnetisation. Table 3.23 shows a summary of the saturation values of the induced magnetisation (M) measured.

Table 3.23 – VSM saturation summary for iron-based alloys.

Sample	Saturation [T]
C1	1.53 ± 0.05
C6	2.04 ± 0.02
MA	0.79 ± 0.01

The difference between the VSM and AGM curves and the BH-curve can be explained

by the difference inside of the material and therefore of domain walls present in the measured sample. When a core is measured, many domain walls that have to rotate or grow are present in the sample, which has more pinning points and therefore will present a response to an external field with losses (coercivity). However, a smaller sample, like the one used for VSM and AGM, will present less domains that, in the absence of pinning points, will give a magnetisation curve with no losses [67].

3.4.5 Magnetic domain imaging

TEM

A first test with sample MA was done to visualise the magnetic domains in the sample. Figure 3.35 (a) shows the over-focused image in Fresnel mode of the sample, while Figure 3.35 (b) shows the under-focused image. Figure 3.36 shows results from the calculations of the Transport-of-Intensity Equation (TIE) using the over-focused and under-focused images from the Fresnel mode. The TIE image is 1024 x 1024 pixels, each pixel having a size of 3.77 nm. The biggest visible domain dimension in the image is approximately 3 μm , marked with an arrow in the three images. The images do not show any enclosed region, which means that the whole domain could not be observed by this technique.

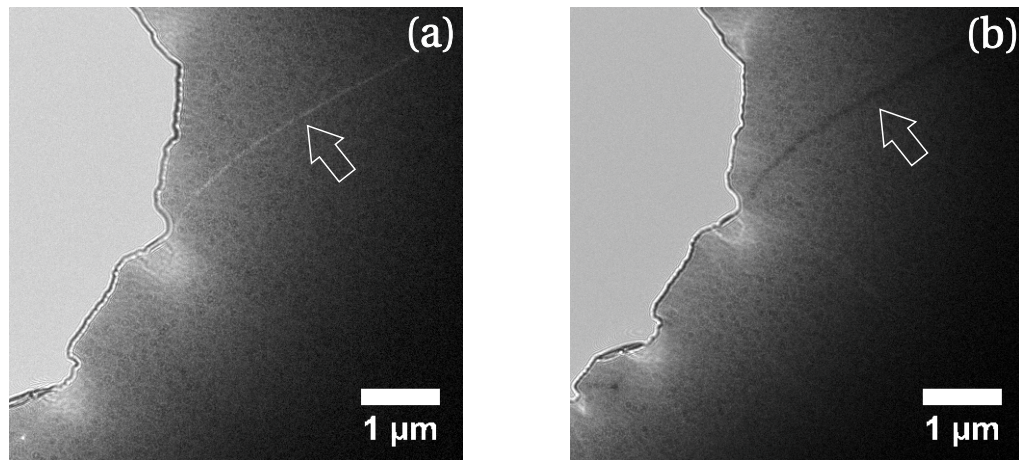


Figure 3.35 – Fresnel mode images for sample MA analysed with TEM, over-focused (a) and under-focused (b). Arrows indicate a domain wall.

MFMM

MFMM tests were performed on only some of the samples, as it became clear from the first results that the uneven surface was the main limitation factor in the area to visualise. In addition to this, the irregular topography interfered with the magnetic signal, making it

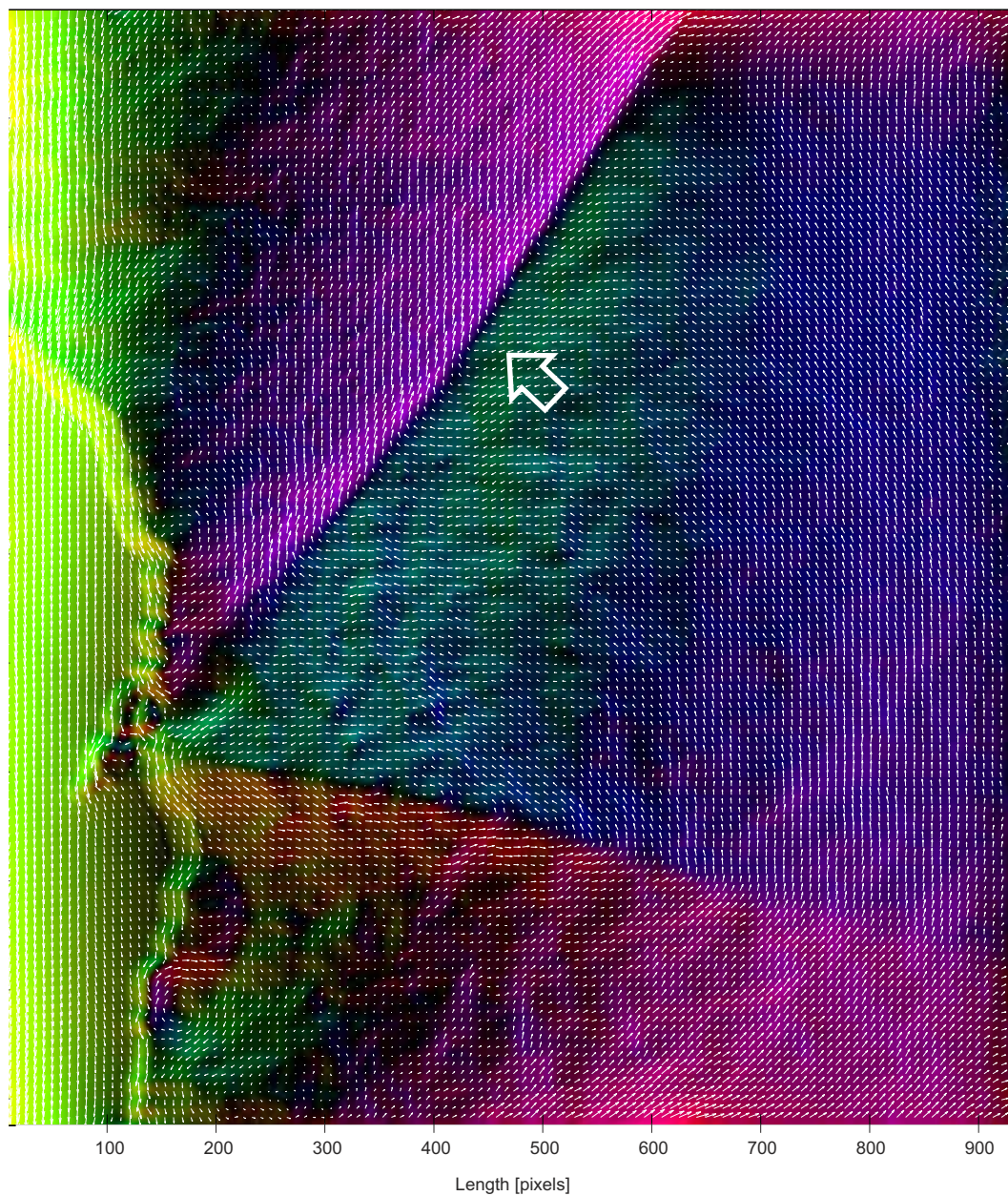


Figure 3.36 – Domain image with superimposed TIE calculation. Arrow indicates a domain wall.

hard to separate both in the post-processing stage. The best example of MFM domains can be seen in the next chapter.

MOKE

The BH-loop, MOKE-loop and magnetic domain imaging was performed for all the samples. The BH-loops were studied in two directions, parallel to the long axis of the ribbon (marked as long in the graphs), and transversally (marked as short). MOKE-loops were studied in areas of the ribbon that had different degrees of stress (present around the areas where the samples were held down). For the magnetic domain images, the magnetic field is always applied parallel in the left-right direction.

Sample C1

The BH-curve shows that the parallel and transverse magnetisation of the sample show no significant differences. This indicates that the sample has small domains that are distributed evenly along the ribbon. This can be seen in Figure 3.38 (a), where the whole sample looks homogeneous, and in Figure 3.38 (b) where a close-up of the non-stressed sample shows small patches of domains, indicated with white arrows on the image. Sample C1 shows local inhomogeneities, an example shown with the black arrow. It can be seen how the domain pattern is affected by these inhomogeneities.

The MOKE loops show that additional stresses from mechanically attaching the sample to the holder changes the material magnetically. Domain images show that this applied stress has a preferential orientation in the direction of the casting of the material that could be related to texture and structure deformation. Figure 3.38 (c) and (d) show a semi-stressed and stressed region of the sample respectively. The domains that appear in these areas are much bigger than the small patches of domains seen in the non-stressed sample. More images can be seen in Appendix A.

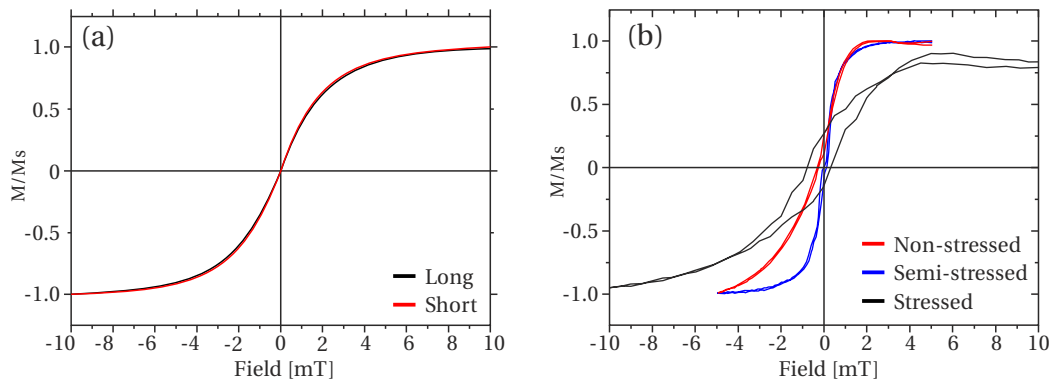


Figure 3.37 – BH-loop (a) and MOKE-loop (b) of sample C1.

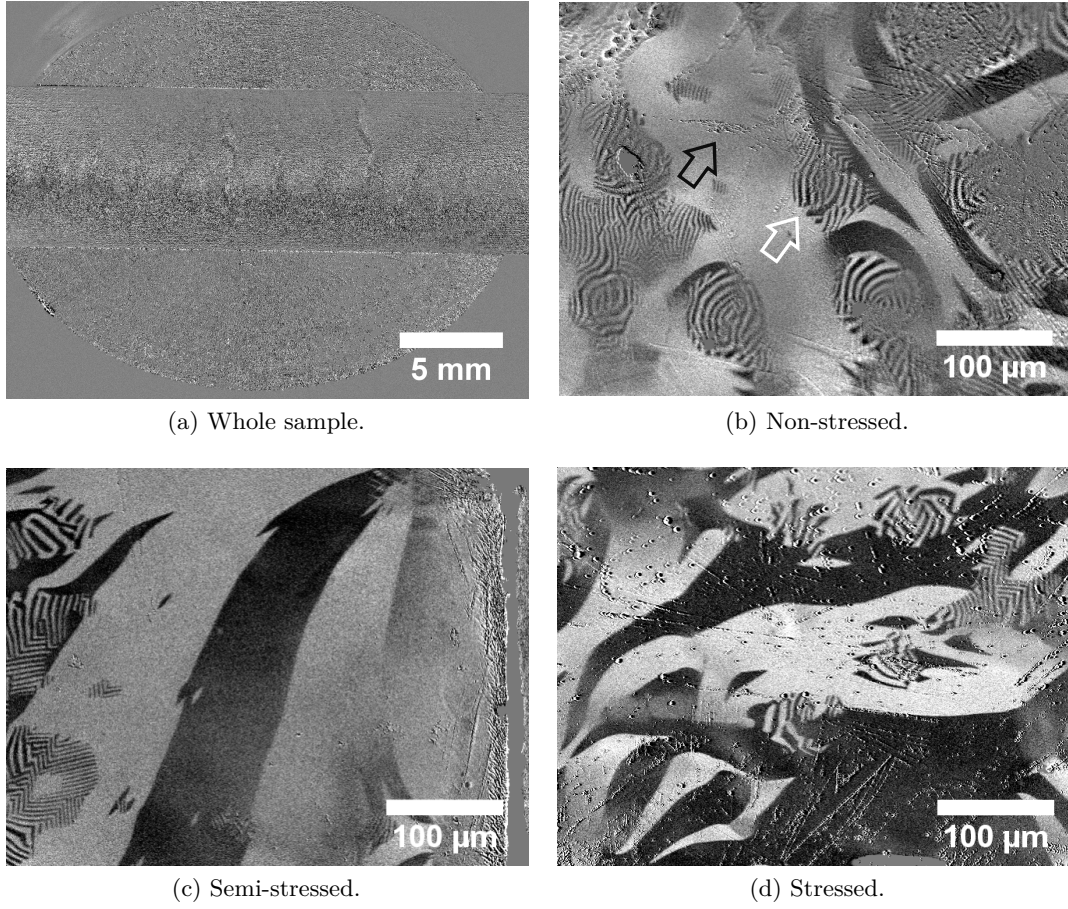


Figure 3.38 – Magnetic domain observation for sample C1: whole sample (a), non-stressed (b), semi-stressed (c) and stressed (d).

Sample C6

The BH-curve for sample C6 in Figure 3.39 (a) compared to sample C1 shows that it reaches the saturation plateau at a lower field than C1. The curve being less rounded than the C1 curve indicates the presence of bigger domains in the material, which is confirmed in Figure 3.40 (a) with the view of the whole sample, where longer domains in the longitudinal direction of the ribbon can be seen, mixed with regions of smaller domains, pointed out in the image. Figure 3.40 shows that the sample is highly inhomogeneous and presents several different magnetic states and behaviours, as well as high stress point defects on the sample. A particularly peculiar domain formation can be seen on Figure 3.40 (c), in a transition region of no-stress to semi-stress, where circular domains appear. More images for C6 domains can be found in Appendix A.

The MOKE-loops in Figure 3.39 show a different behaviour for the different magnetic regions. It can be seen that stress has a big effect on the magnetic response of the sample, although as opposed to sample C1, the applied stress forms non-directional domains, an

example of which can be seen in Figure 3.40 (d).

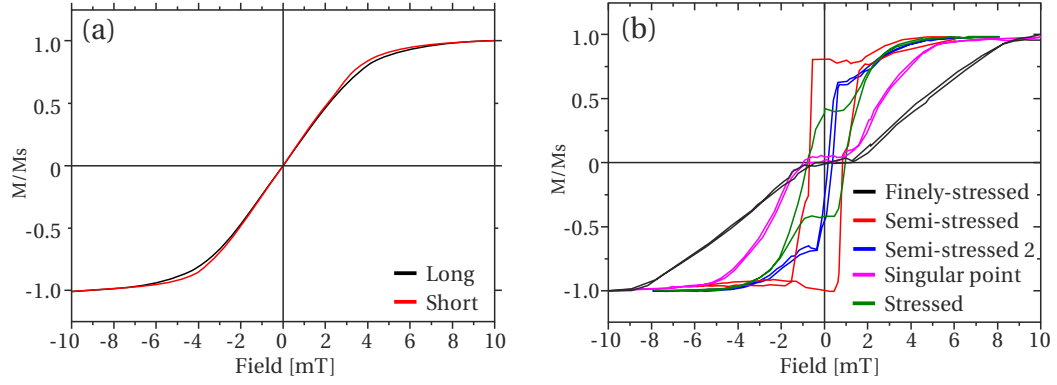


Figure 3.39 – BH-loop (a) and MOKE-loop (b) of sample C6.

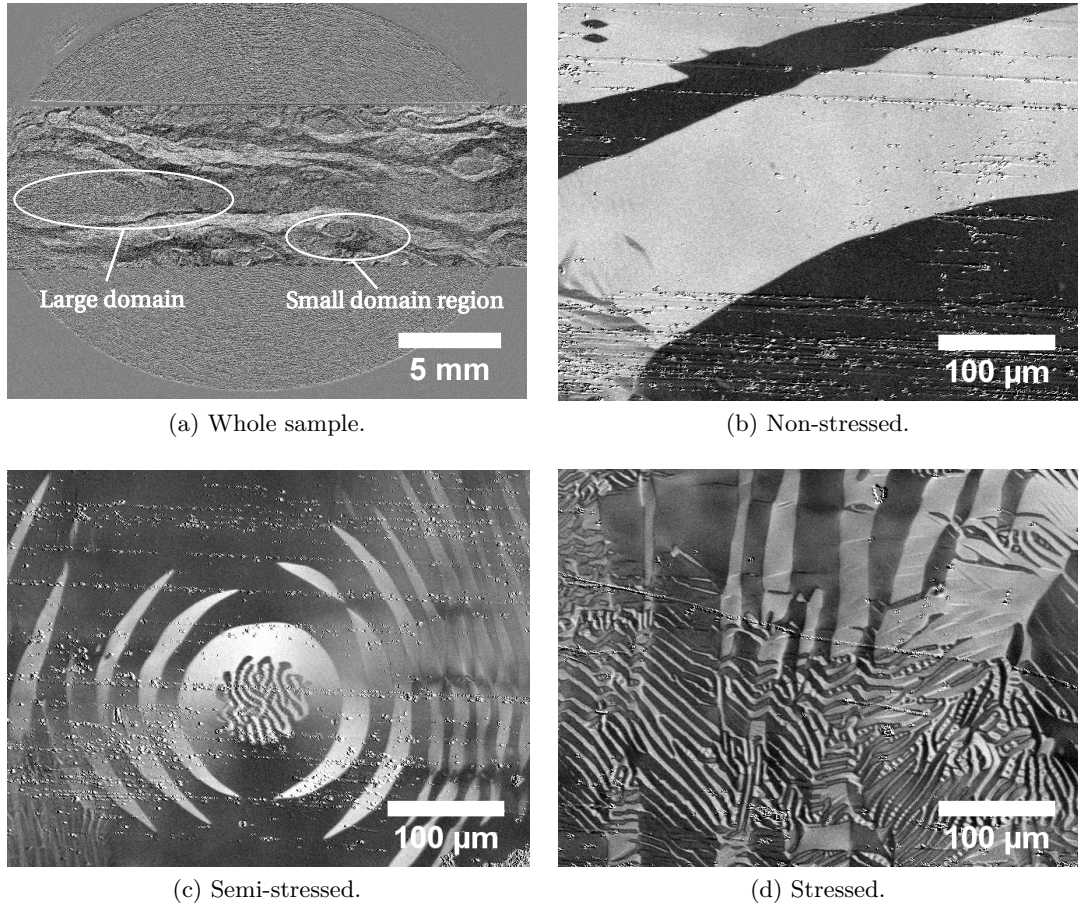
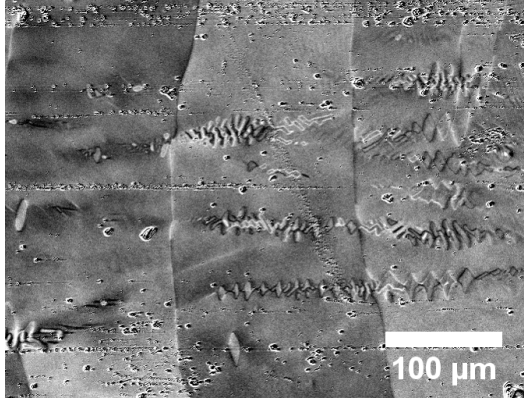


Figure 3.40 – Magnetic domain observation for sample C6: whole sample (a), non-stressed (b), semi-stressed (c) and stressed (d).

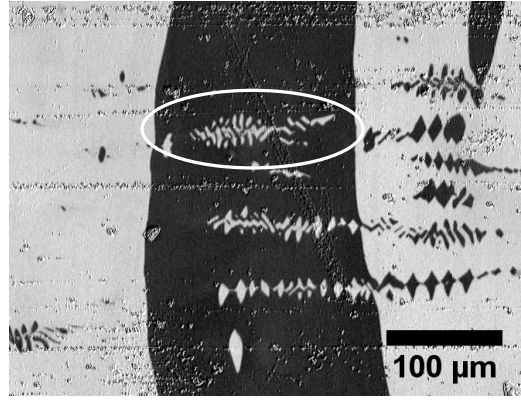
A more detailed analysis was performed on the circular-structured shaped domains. The first image of each series is done with parallel sensitivity, whilst the second with

Chapter 3. Iron-based alloys results

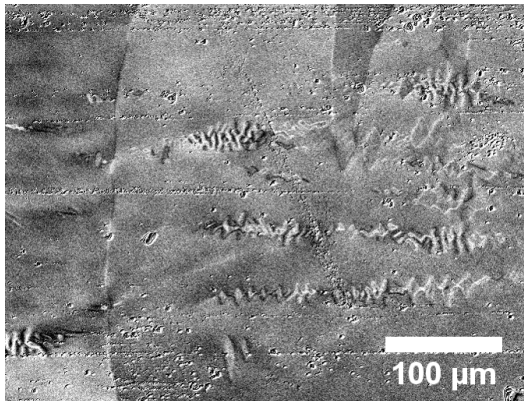
perpendicular sensitivity in order to make visible all the possible magnetic structures. Figure 3.41 shows clearly the topographical irregularities that the sample has, creating at some points smaller domains, like it is highlighted in Figure 3.41 (b).



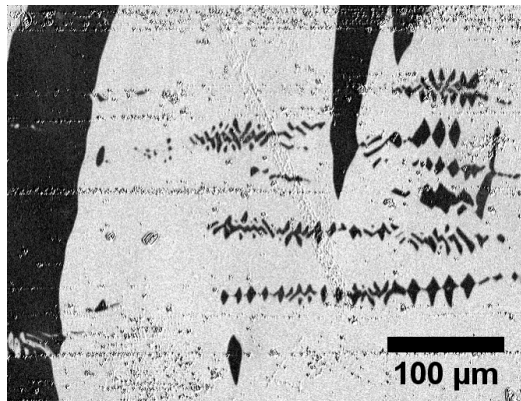
(a) Detail 1: parallel sensitivity.



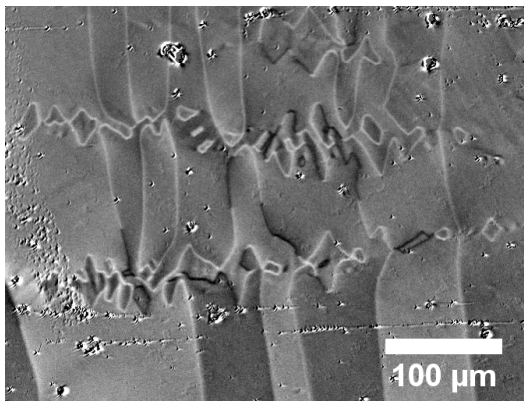
(b) Detail 1: perpendicular sensitivity. Ellipse highlights domains associated with topographic irregularities.



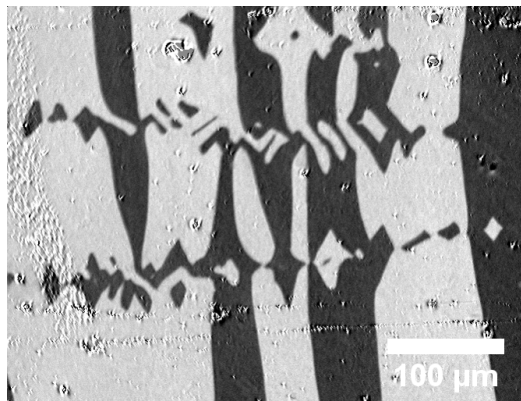
(c) Detail 2: parallel sensitivity.



(d) Detail 2: perpendicular sensitivity.



(e) Detail 3: parallel sensitivity.



(f) Detail 3: perpendicular sensitivity.

Figure 3.41 – Details of the circular-structured domains for sample C6.

Sample F

BH-curves in Figure 3.42 show that the sample presents anisotropy, the two being different from each other. The rounded shape also suggests that the sample has mainly small-sized domains, which is confirmed by the images in Figure 3.43. Stress perpendicular to the long axis was applied, creating a directional behaviour of the domains as can be seen on Figure 3.43 (d). This is confirmed in the MOKE-loop in Figure 3.42 (b), where the stress makes the BH-curve more squared-shaped.

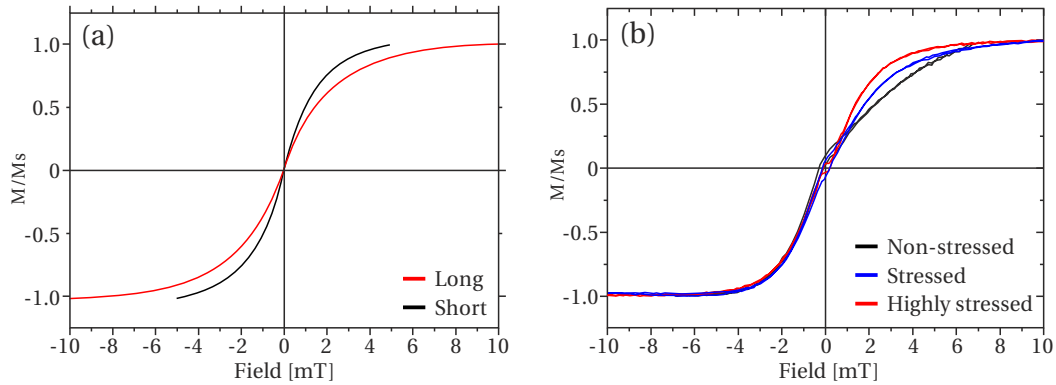


Figure 3.42 – BH-loop (a) and MOKE-loop (b) of sample F.

Images confirm that the sample presents non-directional domains to the magnetic field. More images for F domains can be found in Appendix A.

Sample MA

Sample MA could not be studied due to its fragility caused by its nanocrystallinity.

Assessment

The MOKE analysis are very important in order to study the domain structure of the sample and its magnetic response. The ability also to see how the domains are affected by stress and how this changes magnetisation is very interesting to understand the behaviour of the material. For the iron-based alloys, the BH-loops show that the three samples analysed present very similar behaviour, showing no coercivity nor remanence. MOKE-loops show how stress affects the sample's domains, C6 presenting the most sensitivity to it and F the least. This is important, as the ribbons, when wound into cores, will always be stressed and present the domain configuration visible in the stressed areas studied.

Like for the VSM magnetisation loops, the MOKE loops are done on a part of ribbon from the material, presenting few pinning sites and therefore giving as a result BH-loops with almost or no coercivity at all.

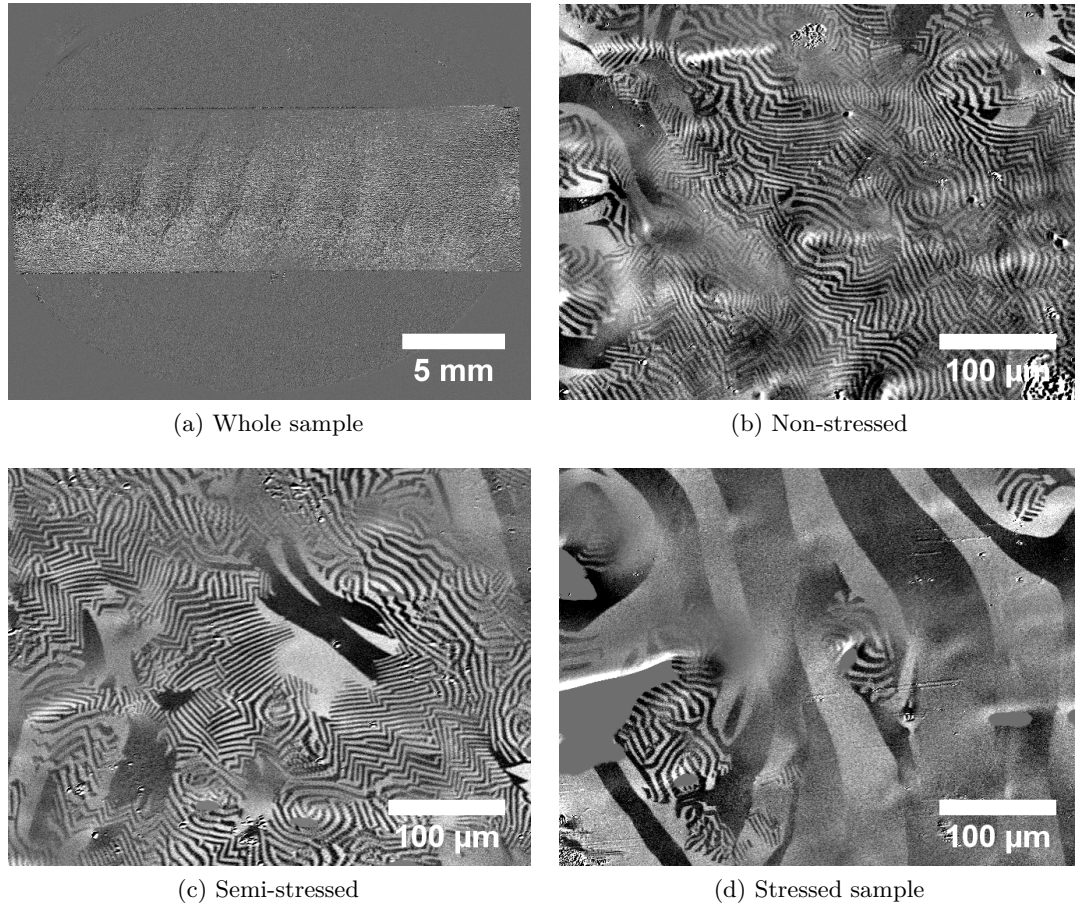


Figure 3.43 – Magnetic domain observation for sample F: whole sample (a), non-stressed (b), semi-stressed (c) and stressed (d).

3.4.6 Barkhausen Noise

Figure 3.44 shows the comparison between the as-cast iron-based materials. It can be seen that the nanocrystalline MA sample presents the highest and widest noise structure, at 0.55 AU and 0.2 s wide. Sample C1 and F are similar in width (0.1 s), but sample C1 presents a maximum noise level of 0.35 AU and F of 0.13 AU, the lowest of them all. Sample C6 is an intermediate between these two groups, with a width of approximately 0.3 s and a maximum noise level of 0.25 AU.

Assessment

The width and noise level of sample MA is caused by the nanocrystals present in the sample acting as pinning sites and creating this noise during the magnetisation process. Sample F, with the lowest and narrowest noise, matches the magnetic domain observations which show that the non-stressed sample shows a homogeneous distribution of small-sized

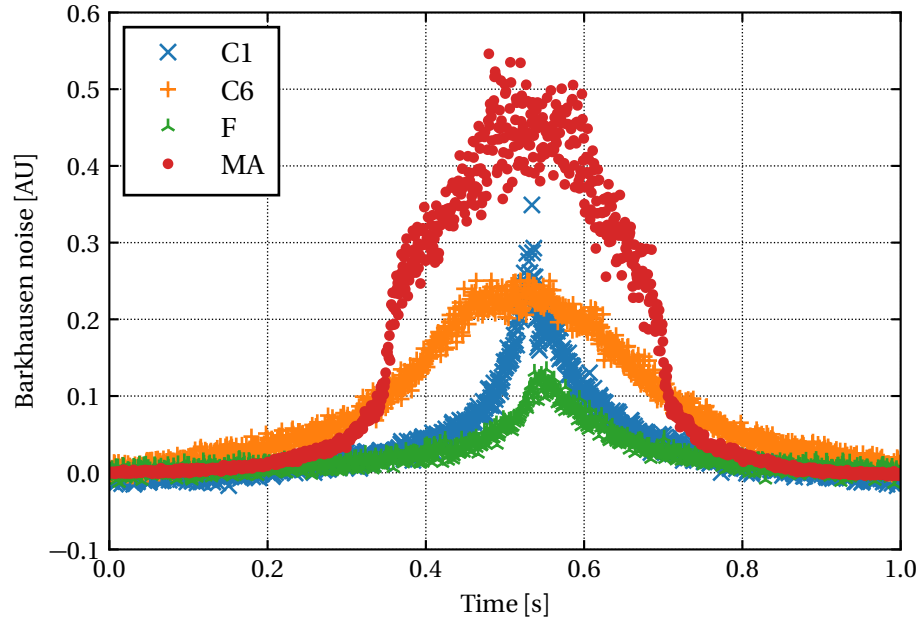


Figure 3.44 – Barkhausen Noise comparison for iron-based alloys.

domains. Sample C1 and C6 are an intermediate case, with a mix of big and small domains, with C6 having bigger domains in the non-stressed state.

3.5 Other physical properties

3.5.1 Thickness

Table 5.1 shows the thickness for all of the iron-based alloys. All the measurements are in the expected range for this kind of materials, between 20 μm and 30 μm , with C1 and C6 being the thickest, 4 μm more than F and MA.

Table 3.24 – Thickness results of iron-based alloys.

Sample	Thickness [μm]	St. Dev. [μm]
C1	27.1	0.7
C6	27.3	0.9
F	23.3	0.6
MA	23.3	0.9

3.5.2 Density

Table 3.25 shows the density, standard deviation and uncertainty for the measurement. All the values are in the expected range, around 7.5 g cm^{-3} for alloys of this kind.

Table 3.25 – Density results of iron-based alloys in g cm^{-3} .

Sample	Density	St. Dev.	Uncertainty	Literature
C1	7.39	2.3×10^{-3}	9.5×10^{-3}	
C6	7.23	2.4×10^{-3}	8.2×10^{-3}	
F	7.29	4.2×10^{-3}	9.7×10^{-3}	
MA	7.69	7.9×10^{-3}	21×10^{-3}	7.35 [61]

3.6 Results discussion

Thinking about the application for the materials, the most important parameters are the ones linked to the magnetic properties. It has been shown in the relative complex permeability graphs that C1 and F present a better frequency response, but still show too low a permeability (3000 and 1000 respectively) to be considered as good candidate materials for core fabrication. Sample C6 has an even worse permeability vs. frequency response, dropping quickly from 3000, its maximum. The coercivity measurements are also not encouraging for this type of application. The three materials have a high coercivity (above 15 A m^{-1}) and a remanence of 0.7 T or lower.

However, as has been stated before, nanocrystalline iron-based materials have very interesting magnetic properties and are widely used. Results have shown that all of the materials have a Curie temperature much lower than their crystallisation temperature. This means that thermal treatment over the Curie temperature can be done without risking a change in the crystalline properties if this is the objective. If the objective is to nanocrystallise the samples, 500°C is a reasonable temperature that can be reached by common industrial ovens.

Another critical parameter is the BN, which is closely related to the magnetic domains. It has been shown that sample MA presents the highest BN due to its nanocrystallinity, and that the other three samples have a narrower and lower noise distribution. This will be a point of reference when comparing to the annealed samples in order to see how the thermal treatment is changing the domains as well as the BN.

The composition and crystalline phase studies are useful to understand the magnetic behaviour of the sample. After a thermal treatment it is important to know what phases have been created to understand the changes in parameters like the BH-curve or permeability.

4 Cobalt-based alloy results

For this chapter, the cobalt-based alloys have been renamed as follows:

- Vacuumschmelze GmbH & Co. KG: Co-based amorphous 6025 G40 → (V)
- Nanostructured & Amorphous Materials, Inc. (Nanoamor): Co-based amorphous → (N)
- Metglas, Inc.: iron-based amorphous Finemet FT-3 and Co-based alloy 2705 M → (M)

4.1 Composition

4.1.1 XPS

As with the iron-based alloys, the surface analyses of all the cobalt samples showed a high percentage content of oxygen and carbon. Figure 4.1 shows the surface XPS results for samples V and N, the result for sample M can be seen in the Appendix B.

Table 4.1 shows a summary of the carbon and oxygen surface content (in atomic %). All samples show over 40 % of carbon content and over 25 % of oxygen content, rendering the quantification of the composition of the alloy impossible.

Table 4.1 – Carbon and oxygen surface content.

Sample	Carbon content [at. %]	Oxygen content [at. %]
V	48.05	30.88
N	56.87	25.88
M	40.62	36.44

An in-depth analysis of sample V showed that the oxygen and carbon layer are still present at a depth of 9 nm, where there is still a 9.04 % of carbon and a 7.45 % oxygen. Figure 4.2 shows how the atomic percent composition of the sample changes with depth

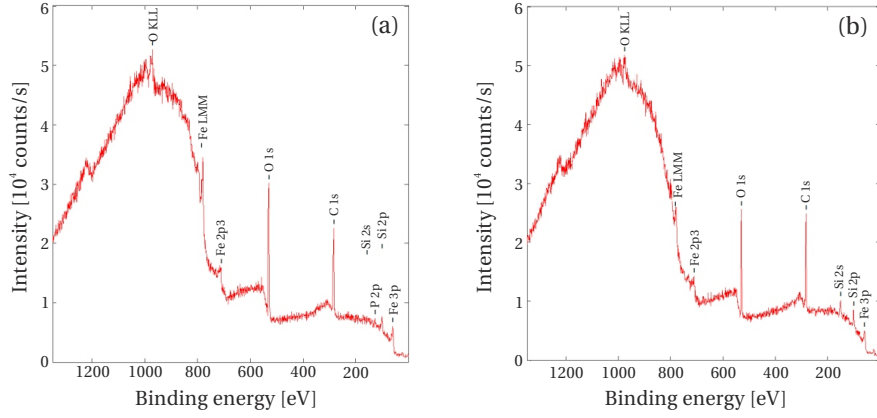


Figure 4.1 – XPS surface results for samples V (a) and N (b).

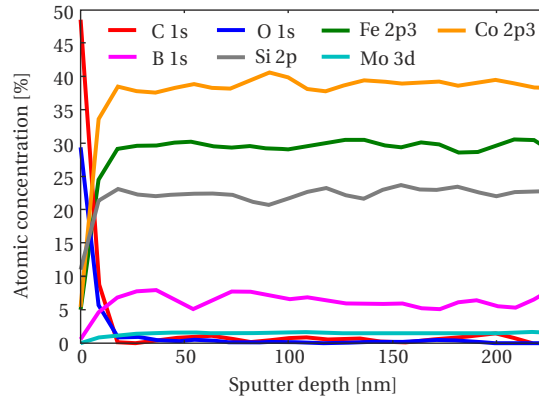


Figure 4.2 – XPS in-depth results for sample V.

(each sputtered layer was 9 nm). The same effect of preferential sputtering was observed by comparing with the other composition results, giving a composition enriched in cobalt. No more cobalt-based samples were analysed due to this.

4.1.2 SEM-EDX

The following table show the composition for the cobalt-based alloys in atomic percent.

Table 4.2 – SEM-EDX results for cobalt-based alloys.

Sample	Composition [at. %]
V	$\text{Co}_{73.6}\text{Fe}_{4.4}\text{Si}_{20.1}\text{Mo}_{1.8}$
N	$\text{Co}_{73.5}\text{Fe}_{5.5}\text{Si}_{19.3}\text{Ni}_{1.7}$
M	$\text{Co}_{76.7}\text{Fe}_{4.9}\text{Si}_{14.9}\text{Ni}_{1.7}\text{Mo}_{1.8}$

4.1.3 EMPA

Table 4.3 shows the EMPA results for the cobalt-based materials in atomic percent.

Table 4.3 – EMPA results for cobalt-based alloys.

Sample	Composition [at. %]
V	$\text{Co}_{67.6}\text{Fe}_{4.2}\text{Si}_{16}\text{B}_{10.7}\text{Mo}_{1.5}$
N	$\text{Co}_{64.9}\text{Fe}_{4.7}\text{Si}_{14.8}\text{B}_{14.2}\text{Ni}_{1.3}$
M	$\text{Co}_{68.7}\text{Fe}_{4.6}\text{Si}_{12} \cdot 0 \text{B}_{11.7}\text{Ni}_{1.4}\text{Mo}_{1.5}$

4.1.4 Assessment

The following compositions are known from literature:

- Vitrovac 6025 G40: $\text{Co}_{67}\text{Fe}_4\text{Si}_{16.5}\text{B}_{11}\text{Mo}_{1.5}$ [68]
- Metglas 2705M: $\text{Co}_{75-85}\text{Fe}_{1-5}\text{B}_{1-5}\text{Si}_{3-7}\text{Ni}_{1-5}\text{Mo}_{1-5}$ [69]

Boron cannot be detected by SEM-EDX and therefore, none of the results can be used qualitatively as they all contain it. Comparing both results by normalising the EMPA results without taking into account the boron content, the maximum difference in element composition is of 2.2 %, found in the silicon content of sample V. The results are in good agreement with the composition found in the literature for samples V and M and can therefore be taken as valid. The XPS results cannot be used because of the preferential sputtering in the in-depth results and the contamination in the surface results.

4.2 Crystallinity

4.2.1 XRD

All the samples show crystallinity compatible with α -iron as can be seen in Figure 4.3 (the α -iron peaks shown in red). Diffraction peaks are not very high with respect to the baseline noise, due to the low proportion of crystalline phase present, indicating that it is mostly the amorphous phase.

4.2.2 HE-XRD

Diffraction patterns are very similar to each other. They can all be fitted by a cobalt-based structure with space group $P6_3/mmc$, with $a \approx 2.55 \text{ \AA}$ and $c \approx 4.73 \text{ \AA}$. However, the diffraction patterns show an added unusual background, which indicates the presence of

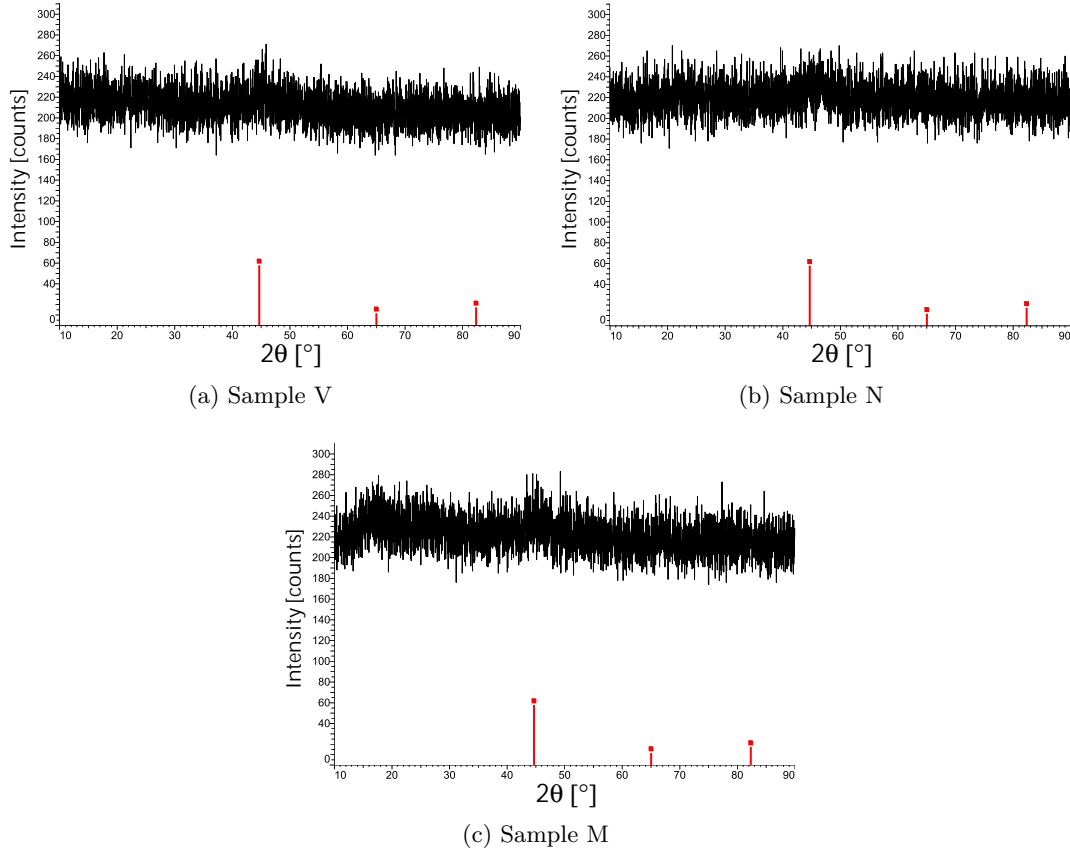


Figure 4.3 – XRD diffraction patterns for V (a), N (b), M (c).

another crystalline structure in all of the samples. The most probable one is $\text{Co}_5\text{Si}_2\text{B}$ (with a space group $I4/mcm$, $a \approx 8.5 \text{ \AA}$ and $c \approx 4.0 \text{ \AA}$). The refinement of the contributions of the phases, gives about 30 % of the pure cobalt-phase and 70 % of the $\text{Co}_5\text{Si}_2\text{B}$ for all samples. Results are shown in Table 4.4.

Table 4.4 – HE-XRD results for cobalt-based alloys.

Sample	Crystalline phase composition	Average size [nm]
V	Co: $31.1 \% \pm 0.5 \%$	2.0 ± 0.2
	$\text{Co}_5\text{Si}_2\text{B}$: $68.9 \% \pm 0.6 \%$	1.4 ± 0.2
N	Co: $33.0 \% \pm 1 \%$	2.2 ± 0.2
	$\text{Co}_5\text{Si}_2\text{B}$: $67.0 \% \pm 1 \%$	1.5 ± 0.2
M	Co: $31.0 \% \pm 0.7 \%$	1.9 ± 0.2
	$\text{Co}_5\text{Si}_2\text{B}$: $69.0 \% \pm 0.9 \%$	1.3 ± 0.2

Figure 4.4 shows the Diffraction Pattern for sample V, where the arrow at $\theta \approx 13$ indicates the contribution of the $\text{Co}_5\text{Si}_2\text{B}$ phase. The pink line is the background after subtracting the Diffraction Patterns (DPs) of both contributing phases, their peaks represented by the strips under it. Results for samples N and M are very similar and can be seen in the Appendix.

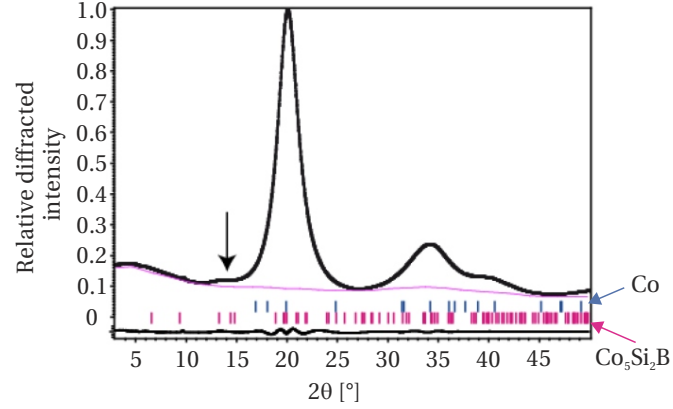


Figure 4.4 – Diffraction Pattern of sample V.

4.2.3 TEM

Sample V

The DPs of sample V show rings indicating that the sample presents crystallinity. Figure 4.5 (b) and (c) shows that the crystals present in the sample are small (around 1 nm) and distributed homogeneously in the sample. The high resolution image does not show any particular features in the sample.

Table 4.5 – V DP rings vs Co_2Si and Co DP rings.

	V	Co_2Si	Co	Difference
Radius 1 [nm^{-1}]	3.34	3.64		9.2 %
Radius 2 [nm^{-1}]	3.89	4.38		12.8 %
Radius 3 [nm^{-1}]	4.78		4.91	2.9 %
Radius 4 [nm^{-1}]	6.13	6.94		13.3 %
Radius 5 [nm^{-1}]	6.47	7.29		12.6 %
Radius 6 [nm^{-1}]	6.76		6.74	0.3 %

Looking at the DP for sample V and checking in the Crystallographic Open Database (COD), there is not a single structure that fits the DP of the sample completely. Hexagonal cobalt (with space group $P63/mmc$, COD ID 9008492) and Co_2Si (space group $P6_3mm$, COD ID 9009209) combined are a good fit for the structure's DP, with the main and most intense rings resolved by them as can be seen on Figure 4.6.

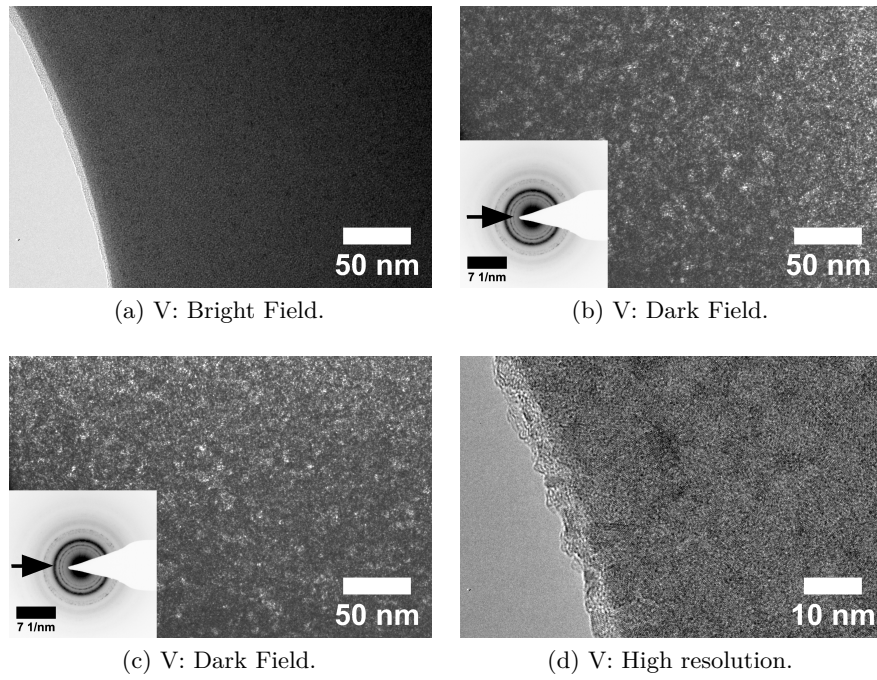


Figure 4.5 – TEM images for sample V: bright field (a), dark field (b,c), high resolution (d). The arrow in the insert shows the selected ring in the DP.

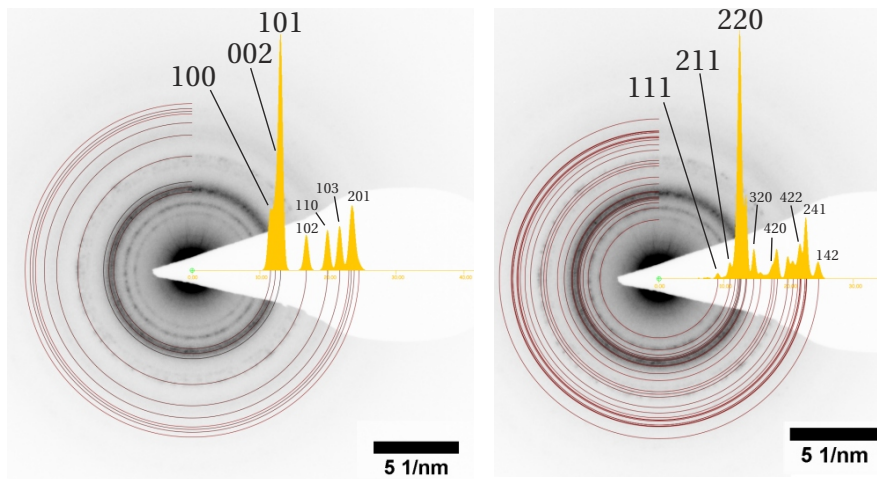


Figure 4.6 – DP of sample V with the theoretical rings of hexagonal cobalt (a) and Co_2Si (b) superimposed.

Table 4.5 shows the calculations with the most intense peaks that appear in the DP, comparing them with both structures. The combination of both gives a good fit with the DP of the sample, as the Co structure for example, does not have the most inner rings that can be seen on Figure 4.6 (a) that are present in the Co₂Si structure.

Sample N

The sample's DPs indicate that the sample presents crystallinity. The bright field in Figure 4.7 (a) and (b) shows a refined grain structure with very small grains about 2 nm in diameter.

Hexagonal cobalt (with space group P63/mmc) is a good fit with the sample's N DP. Table 4.6 shows the radii for the measured sample and for the cobalt structure found in the COD.

Table 4.6 – N DP rings vs hexagonal cobalt's DP.

	Radius 1 [nm^{-1}]	Radius 2 [nm^{-1}]
N	4.67	7.88
Co	4.61	7.98
Difference	1.4 %	1.2 %

Sample M

Sample M's Dark Field images show that the sample presents crystalline regions of approximately 5 nm, that seem to form clusters of crystalline regions as can be seen on Figure 4.9 (b) and (c).

The comparison of structures from the COD shows that there is not a single structure that fits the DP completely. Hexagonal cobalt (with space group P63/mmc) and Co₂Si (space group Pbnm) combined are a good fit for the structure's DP, with the main and most intense rings resolved by them.

Table 4.7 shows the difference between the chosen structures's DP rings and the sample's rings.

Table 4.7 – M DP rings vs Co₂Si and Co DP rings.

	Radius 1 [nm^{-1}]	Radius 2 [nm^{-1}]	Radius 3 [nm^{-1}]	Radius 4 [nm^{-1}]
M	3.46	4.07	5.03	6.95
Co ₂ Si	3.64	4.38	5.35	
Co			4.91	6.73
Difference	5.2 %	7.7 %	6.4 %, 2.3 %	3.1 %

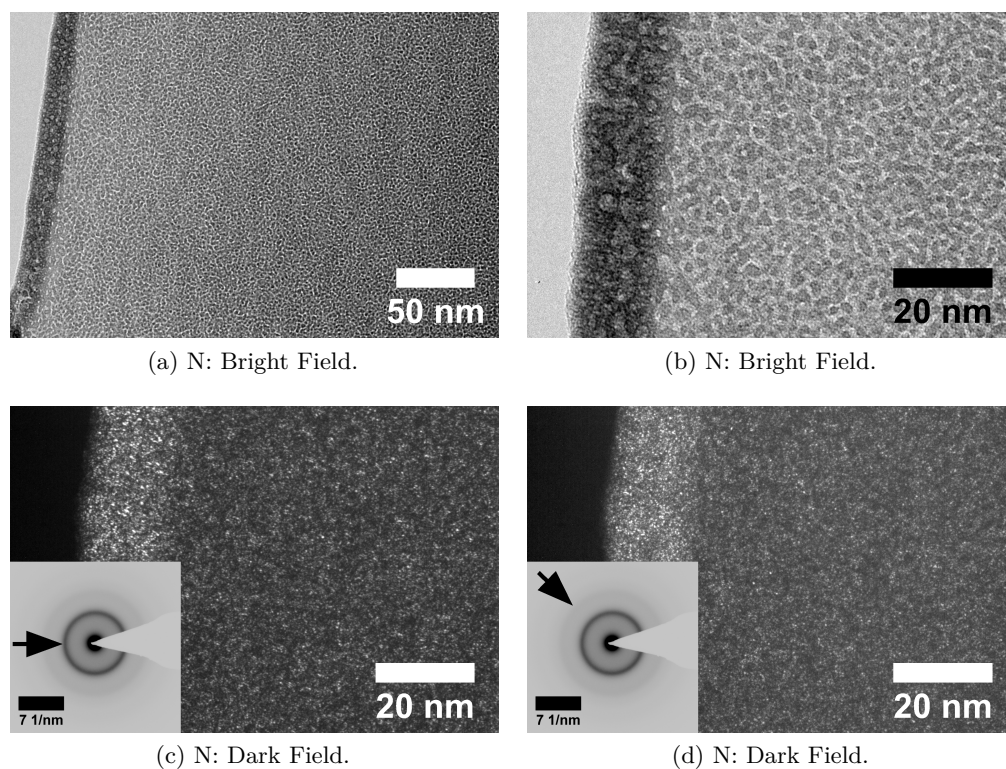


Figure 4.7 – TEM images for sample N: bright field (a,b), dark field (c,d).

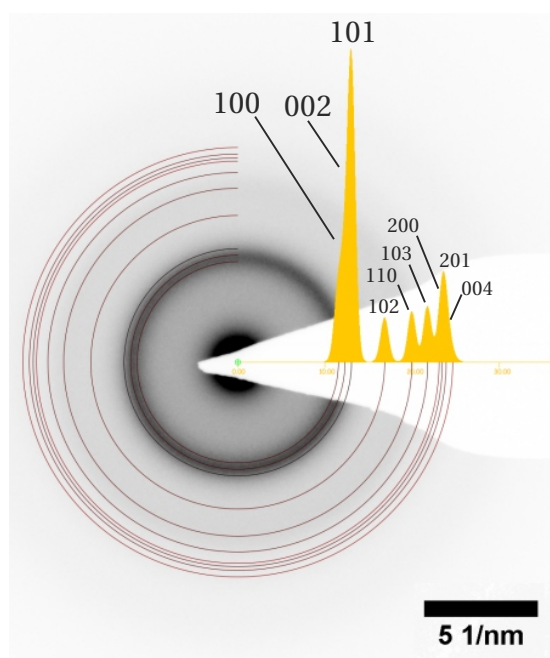


Figure 4.8 – DP of sample N with the theoretical rings of hexagonal cobalt superimposed.

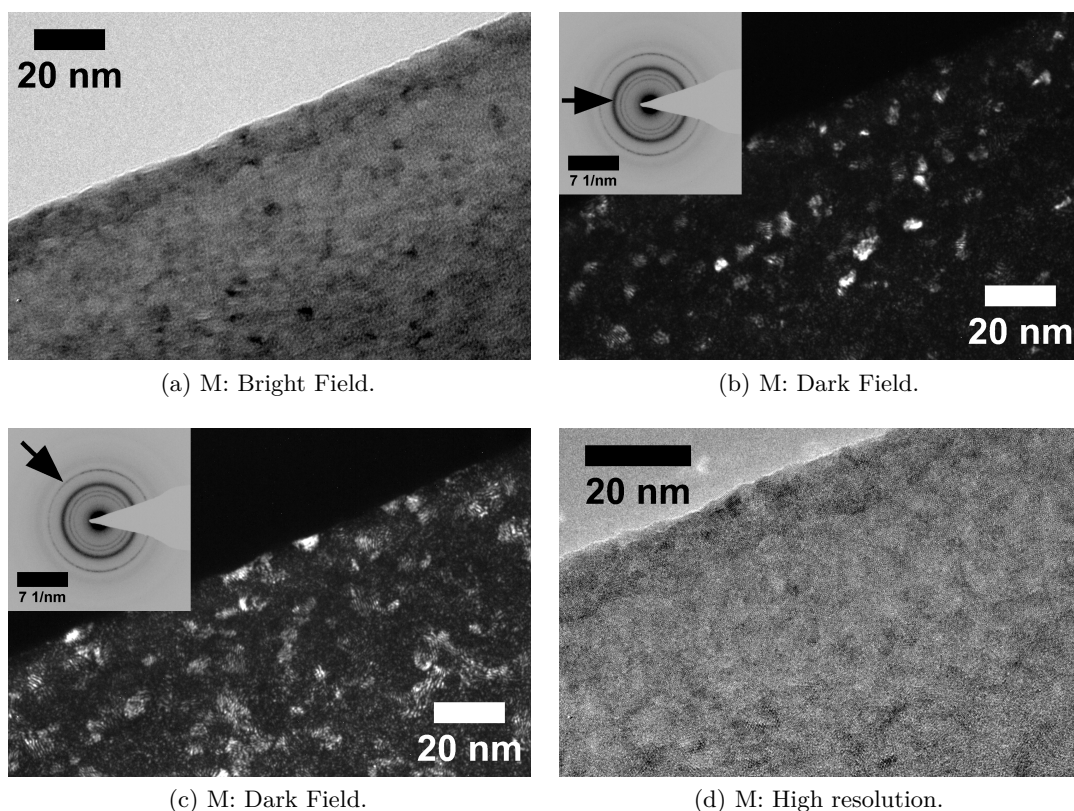


Figure 4.9 – TEM images for sample M: bright field (a), dark field (b,c), high resolution (d).

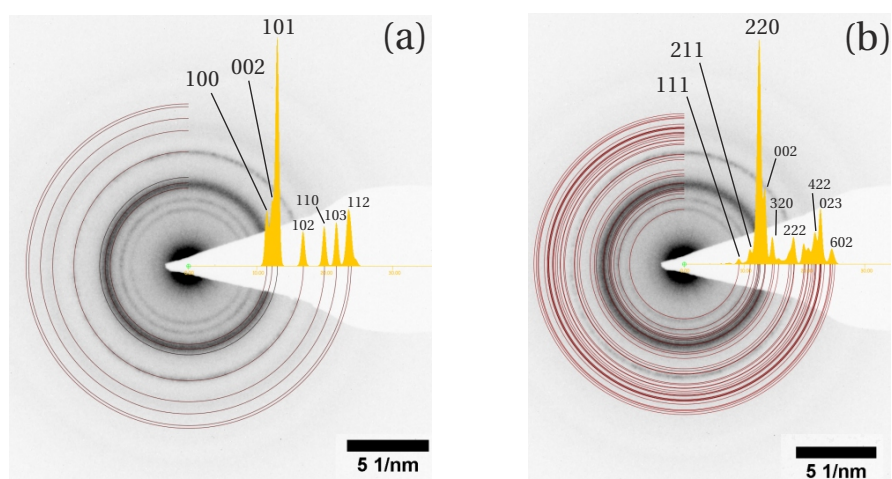


Figure 4.10 – DP of sample M with the theoretical rings of hexagonal cobalt (a) and Co_2Si (b) superimposed.

4.2.4 Assessment

All the cobalt-based alloys show very small crystallite size by conventional XRD and HE-XRD, with average sizes of about 2 nm. The TEM results show that in material M, crystallites form clusters of crystalline areas of about 5 nm.

Regarding the composition of the crystals, all HE-XRD and TEM diffraction profiles fit a cobalt-based structure with space group $P6_3/mmc$ (cell parameters $a \approx 2.55 \text{ \AA}$ and $c \approx 4.73 \text{ \AA}$). The HE-XRD analyses point towards a secondary crystalline structure with composition $\text{Co}_5\text{Si}_2\text{B}$, with a space group $I4/mcm$, $a \approx 8.5 \text{ \AA}$ and $c \approx 4.0 \text{ \AA}$ for all of the samples, but the TEM results differ. Whilst for samples V and M the same $\text{Co}_5\text{Si}_2\text{B}$ structure as the HE-XRD was found to be the best match, in sample N there seems to be no other phase present apart from the cobalt one.

4.3 Phase transformation

4.3.1 DSC

PerkinElmer DSC 8000

Table 4.8 shows the onset and peak crystallisation temperatures for the cobalt-based samples at $10^\circ\text{C min}^{-1}$, the rest of the tables with heating rates of 5°C min^{-1} , $20^\circ\text{C min}^{-1}$ and $50^\circ\text{C min}^{-1}$ can be found in Appendix B. Samples V and N presented a peak with a very similar onset at about 555°C , while M showed two peaks, one at 530.1°C and another one at 558.3°C .

Table 4.8 – PerkinElmer DSC 8000 results for cobalt-based alloys at $10^\circ\text{C min}^{-1}$.

Sample	Onset [$^\circ\text{C}$]	Peak [$^\circ\text{C}$]	Area [J g^{-1}]
V	551.0	557.2	71.3
N	551.1	554.0	85.3
M	517.9	530.1	13.3
	553.27	558.3	40.9

Figure 4.11 shows the plots with the onset and peak crystallisation temperatures for all samples and peaks (as sample M presents two). As with the iron-based samples, the temperatures measured at $20^\circ\text{C min}^{-1}$ look higher than predicted suggesting there might be a problem with the calibration at this particular heating rate.

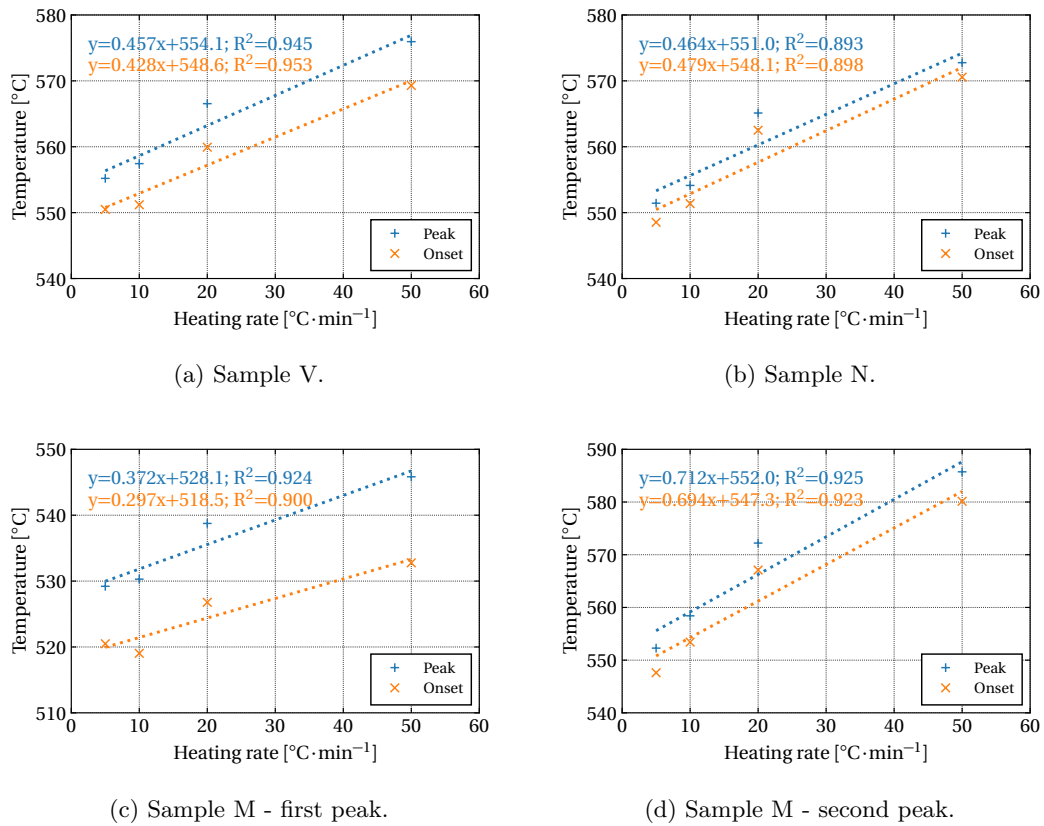


Figure 4.11 – Heating rate dependence of crystallisation onset and peak temperatures for cobalt-based samples.

Netzsch DSC 404 C

The Netzsch DSC, going up to higher temperatures, revealed that samples V and M have a second peak with onset at 613.1 °C for sample V and at 597.4 °C for sample M. With this DSC, the two M peaks that were clearly separated before, appear together with the same onset at 512.8 °C and the two peaks with values very similar to the ones seen with the PerkinElmer DSC, at approximately 530 °C and 555 °C. Compared to the iron-based alloys, the cobalt-based ones present a low difference between the onsets of crystallisation. The largest one can be found in sample V, at 66.8 °C, while in the iron-based alloys it was 210.6 °C for sample F. The lowest difference is 25.1 °C (calculated with the first two peaks of crystallisation, as they are both on the same curve).

The melting temperatures for the alloys can be seen in Table 4.10. Four scans were performed in order to calculate the average of the melting temperature. It can be seen that the three samples present a very similar result (around 1010 °C).

¹Peak temperatures, and not onset, were used for this calculation as sample M presents one single broad peak with just one onset

Table 4.9 – Netzsch DSC 404 C results for cobalt-based alloys at $10\text{ }^{\circ}\text{C min}^{-1}$.

Sample	Onset [$^{\circ}\text{C}$]	Peak [$^{\circ}\text{C}$]	Area [J g^{-1}]	$\Delta\text{Onset}(T_{x2} - T_x)$
V	546.3	552.3	65.2	66.8
	613.1	638.4	33.7	
N	548.2	549.1	73.6	49.2
	597.4	626.4	7.927	
M	512.8	529.1	72.3	25.1 ¹
	-	554.2		
	638.2	656.2	30.2	125.4

Table 4.10 – Melting temperatures for cobalt-based alloys.

Sample	Onset [$^{\circ}\text{C}$]	Std. Dev. [$^{\circ}\text{C}$]
V	1011.7	1.0
N	1007.6	1.4
M	1007.1	2.6

The cobalt-based alloys show a similar behaviour as the iron-based alloys, lacking a glass transition temperature. The same assumption can be taken for these alloys, where other reactions, such as structural relaxation, occur near the glass transition.

4.3.2 High Temperature in-situ XRD (HT-XRD)

Sample V

Figure 4.12 shows the results for the HT-XRD for sample V for heating up to $670\text{ }^{\circ}\text{C}$. It can be seen in Figure 4.12 (b) that before annealing the sample shows a broad peak in the range of 40° to 50° . Figure 4.12 (a) shows a crystallisation onset temperature of about $570\text{ }^{\circ}\text{C}$ to $580\text{ }^{\circ}\text{C}$, with new diffraction peaks appearing at $590\text{ }^{\circ}\text{C}$.

The phase analysis in Figure 4.13 shows peaks for the following phases: cubic $\text{B}_6\text{Co}_{21}\text{Mo}_2$ (21 %), hexagonal $\text{Co}_{0.9}\text{Si}_{0.1}$ (30 %), orthorhombic Co_2Si (20 %), tetragonal Fe_2B (16 %), cubic $\text{Co}_{0.85}\text{Si}_{0.15}$ (9 %), cubic CoSi (3 %) and cubic CoSi_2 (1 %).

Sample N

Figure 4.14 (a) shows the DPs of the sample at the different annealing temperatures up to $700\text{ }^{\circ}\text{C}$, while Figure 4.14 (b) shows the as-cast and final DP. The onset of the first crystallisation occurs between $550\text{ }^{\circ}\text{C}$ and $575\text{ }^{\circ}\text{C}$ and the second one between $575\text{ }^{\circ}\text{C}$ and

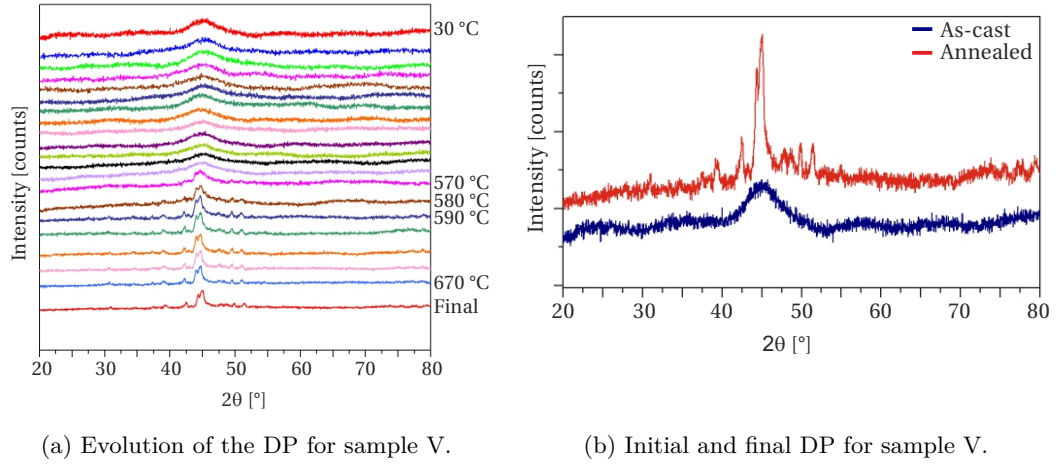


Figure 4.12 – HT-XRD analysis for sample V.

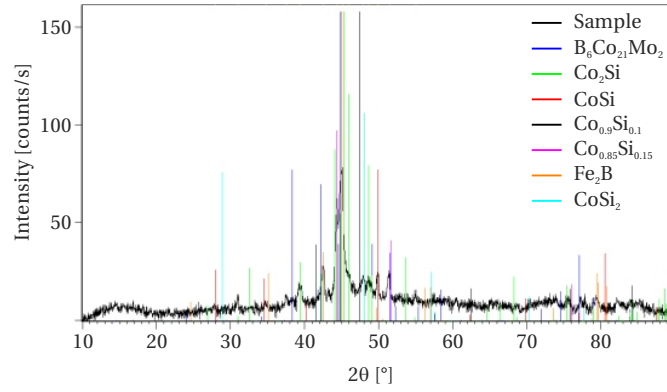


Figure 4.13 – Phase analysis for sample V after annealing.

600 °C as can be seen on Figure 4.14 (a).

The phase analysis of sample N shown in Figure 4.15 gives a crystalline structure of composition Co_2Si , the rest of the peaks cannot be identified confidently enough to suggest another possible phase.

Sample M

Sample M presents an onset crystallisation temperature between 525 °C to 550 °C and a second one between 625 °C to 650 °C as can be seen on Figure 4.16 (a). Figure 4.16 (b) shows the sample before and after annealing, where a broad peak between 40° to 50° is visible.

Figure 4.17 shows the phase analysis for the annealed sample. Two phases can be identified confidently, Co_2Si and $Co_{21}Mo_2B_6$.

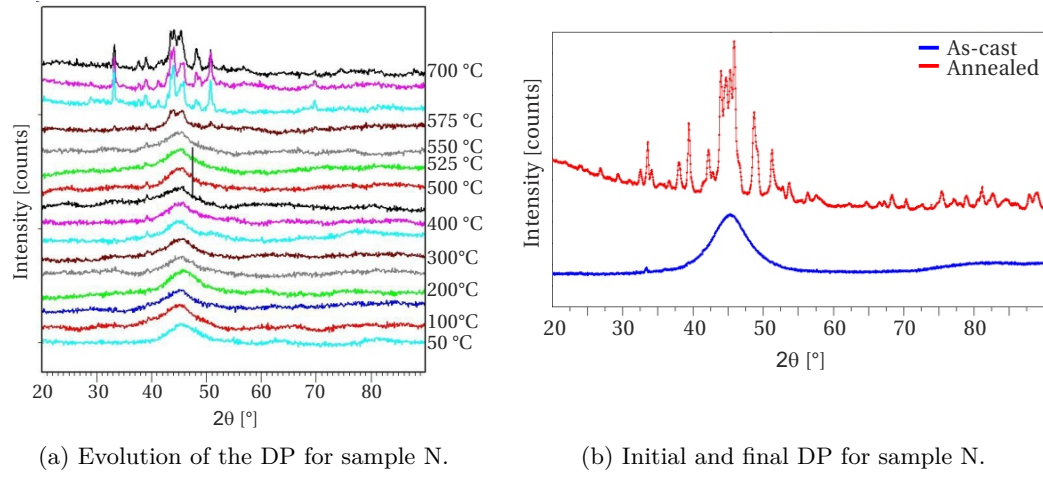


Figure 4.14 – HT-XRD analysis for sample N.

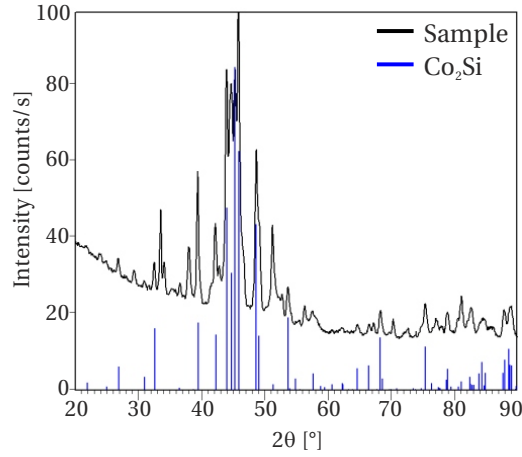


Figure 4.15 – Phase analysis for sample N after annealing.

Table 4.11 shows a summary of the HT-XRD results.

Table 4.11 – HT-XRD results for iron-based alloys.

Sample	T_x [°C]	Composition
V	570 - 580	Co_2Si , CoSi , $\text{Co}_{0.9}\text{Si}_{0.1}$, $\text{Co}_{0.85}\text{Si}_{0.15}$, Fe_2B , CoSi_2
N	550 - 575 575 - 600	Co_2Si
M	525 - 550 625 - 650	Co_2Si $\text{Co}_{21}\text{Mo}_2\text{B}_6$

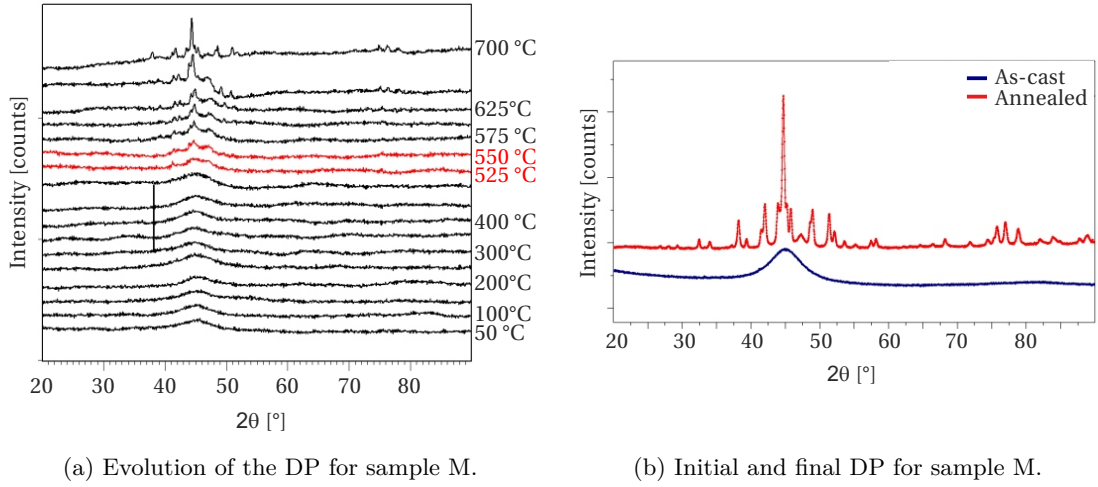


Figure 4.16 – HT-XRD analysis for sample M.

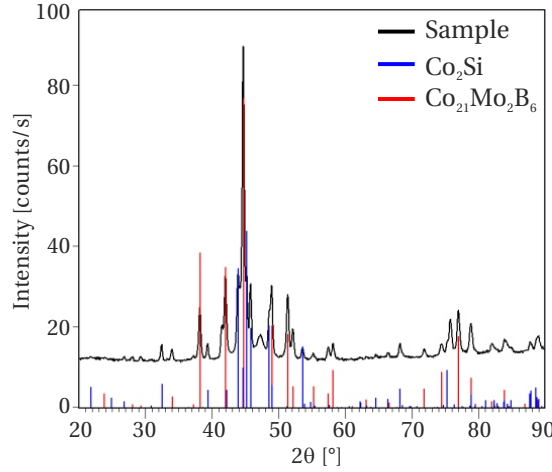


Figure 4.17 – Diffraction pattern of sample M after annealing.

4.3.3 Assessment

Comparing the three techniques and the differences between their measurements, it can be seen that:

- The relative differences between both DSCs comparing the onset and the peak crystallisation temperatures is less than 1 % for all the samples. The biggest difference is the first peak crystallisation temperature of M, with a relative difference of 0.98 %. The highest relative area difference under the curves can be also found in sample M at 19.77 %, mainly due to the difference in baseline as has been mentioned before.

Table 4.13 shows a summary of the onset crystallisation temperatures for cobalt-based alloys. The second peak of sample V was only measured by the Netzsch DSC as the

Chapter 4. Cobalt-based alloy results

Table 4.12 – Relative difference between both DSC measurements.

Sample	Onset [%]	Peak [%]	Area [%]
V	0.86	0.92	8.57
N	0.53	0.89	13.67
M	0.98	0.19	19.77
	0.66	0.74	1.90

PerkinElmer did not reach this temperature and in the HT-XRD it cannot be clearly identified as there are so many peaks already present at this temperature. The second crystallisation peak of sample N is not visible on the PerkinElmer DSC as it only reached up to 600 °C.

Table 4.13 – Onset of crystallisation temperatures comparison for cobalt-based alloys.

Sample	PE DSC [°C]	Netzsch DSC [°C]	HT-XRD [°C]	Literature [°C]
V	551	546	570 - 580	550 [8]
N	551	548	550 - 575	
	-	597	575 - 600	
M	518	513	525 - 550	520 [69]
	553	-	575 - 600	-
	-	638	625 - 650	-

Table 4.14 – Absolute relative difference between the onset crystallisation temperature measured by both DSC's and HT-XRD.

Sample	PerkinElmer vs HT-XRD [%]	Netzsch vs HT-XRD [%]
V	4.17	4.99
N	2.02	2.54
	-	1.62
M	3.65	4.60
	2.93	0.08

- Calculating the absolute relative differences between the measurements, the maximum is found between the Netzsch DSC and the HT-XRD measurement (4.99 %) for sample V. The rest of the relative differences are under this value and can be therefore considered as accurate taking into account the precision of the instruments and the different measuring techniques. The value from the HT-XRD taken to calculate this is the average of the two temperatures between which the crystallisation is detected.

- The HT-XRD analysis does not see the double crystallisation that is observed as the second crystallisation temperature is not reached.

4.4 Magnetic Properties

4.4.1 Impedance analyses

Table 4.15 shows the maximum relative complex permeability measured for each pair of cores, taking into account the uncertainty of the measurement (only values with less than 10 % uncertainty were taken into account). The differences in permeability between cores is 44.8 % for the V cores, 0.4 % for the N cores and 1.5 % for the M cores.

Table 4.15 – Impedance results for cobalt-based alloys.

Sample	Max. relative permeability	Max. Relative difference [%]
V	165 626	44.8
N	158 110	0.4
M	250 802	1.5

Figure 4.18 shows the relative permeability of three of the V cores. The difference of 44.8 % in relative permeability comes from the comparison of cores V-2 and V-3, with maximum relative permeabilities of 182 826 and 102 657. Looking more closely into the core's parameters to understand this difference, it was seen that core V-2 had 9.93 % more mass than core V-3, but only 1.1 % more of packing factor and 6.76 % more of effective area. The difference in permeability therefore comes from this difference in mass between both cores.

Figure 4.19 shows a summary of the amorphous cobalt-based cores. All of the cores present a permeability which decreases in frequency. Material N presents the best frequency response, still presenting a permeability of 1×10^3 at 1 MHz.

Assessment

It can be seen from Figure 4.19 that the three materials look like good candidates for building cores, with a high initial permeability that could be interesting for applications that require good low-frequency performance.

4.4.2 BH-curve measurements

For the cobalt-based alloys, sample N was measured with the old setup, while the rest of the samples were measured with the new one. The differences between the samples can be seen in Figure 4.20.

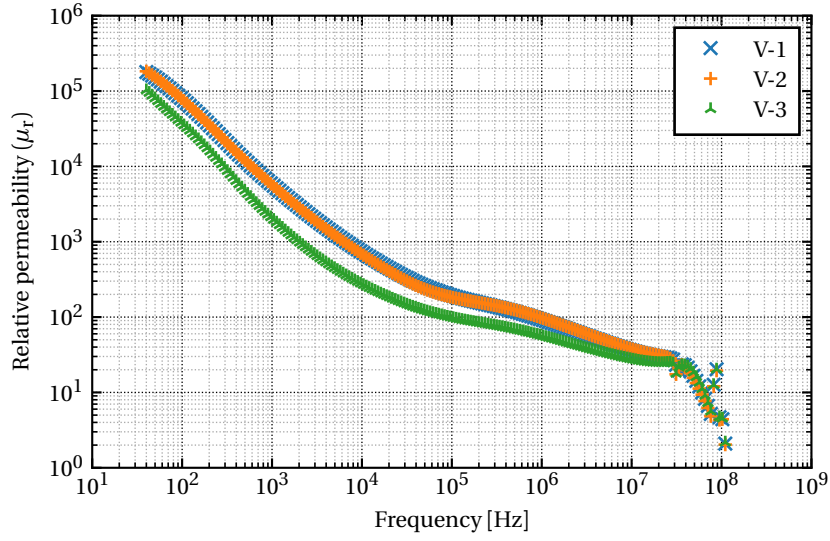


Figure 4.18 – Relative complex permeability for three V cores.

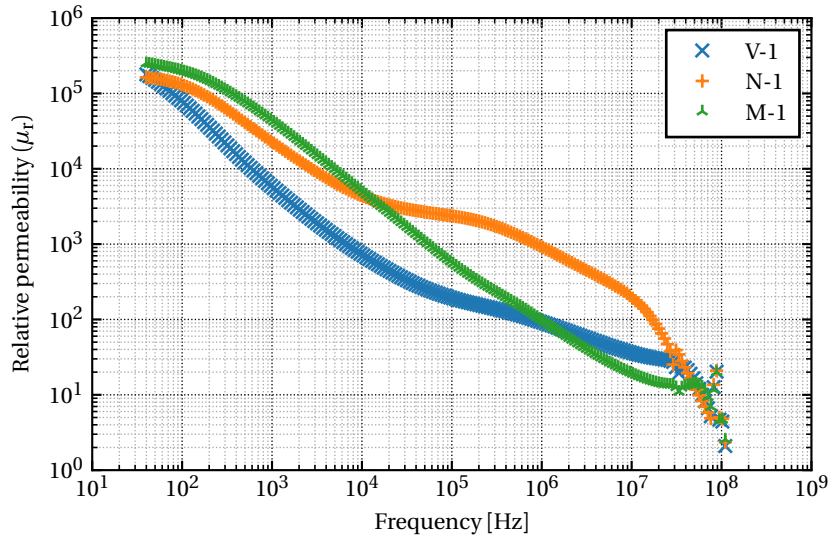


Figure 4.19 – Relative complex permeability for the cobalt-based materials.

Table 4.16 shows a comparison between all the cores made from each material. It is especially interesting to see that cores of material V, that showed a difference of 44.8 % in their permeability values, have quite similar BH-curves, with only 2.18 % between cores in their coercivity values and 0.56 % in remanence. On the other hand, M cores, with a permeability difference of 1.5 % show more differences in the BH-curve, notably an 8.22 % difference of their remanence values.

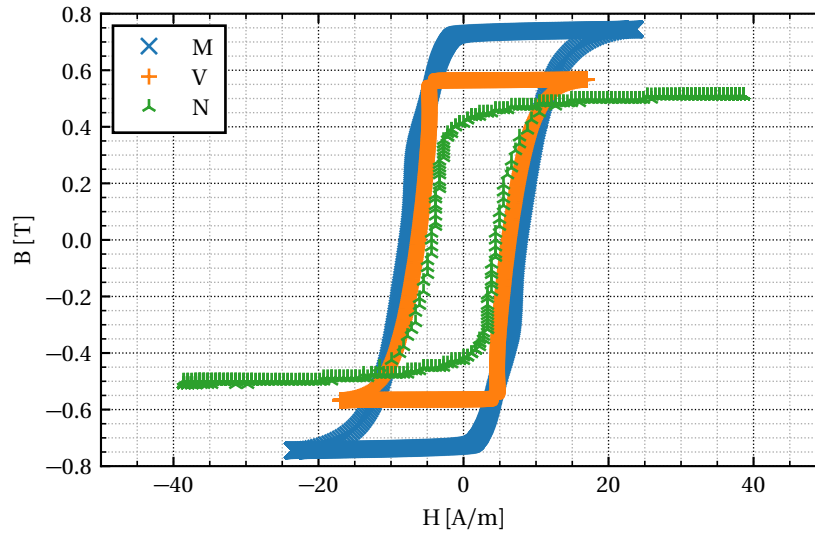


Figure 4.20 – Comparison of BH-curves for the cobalt-based alloys.

Table 4.16 – BH curve results for cobalt-based alloys.

Sample	Coercivity [A m^{-1}]	Remanence [T]	Max. relative difference (H_c , B_r)
V	7.71	0.56	2.18 %, 0.56 %
N	4.44	0.43	1.36 %, 2.33 %
M	8.91	0.69	4.11 %, 8.22 %

4.4.3 Curie temperature measurements

TGA

As for the iron-based alloys, data was recorded during the heating and cooling ramps, where thermal hysteresis was found in all alloys due to the magnetocaloric effect. Figure 4.21 is an example of a test done with material N, heating up and cooling down the sample several times. It can be seen that the first heating ramp is different from the following ones, suggesting that there is a process of stress relaxation that changes the material's properties. The rest of the ramps are similar to each other, so this structural change happens with the first heating ramp and then the material shows the same Curie temperature for the rest of the cycles.

Another study on the N material changing the final annealing times after the heating ramp (with plateaus of 10, 20, 40 and 60 minutes) showed that there was no significant difference in the Curie temperature, with differences of less than 5 % between measurements.

Table 4.17 – Curie temperature at $10^{\circ}\text{C min}^{-1}$ for cobalt-based alloys with TGA.

Sample	Curie temperature at $10^{\circ}\text{C min}^{-1}$ [$^{\circ}\text{C}$]
V	222
N	223
M	361

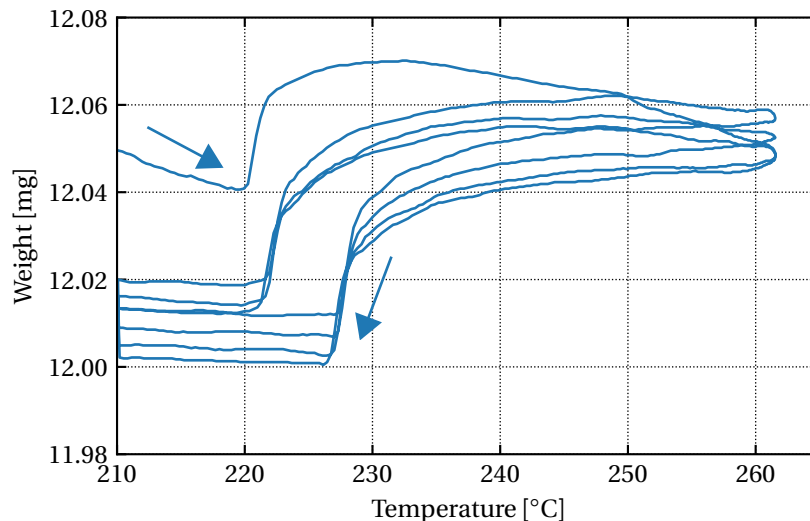


Figure 4.21 – Curie Temperature hysteresis curve for sample N at $20^{\circ}\text{C min}^{-1}$.

Kappabridge

Thermal hysteresis was also seen in all the cobalt samples. Figure 4.22 shows the measurement of sample V, where the thermal hysteresis can be seen. As with the DSC measurements, all of the Curie temperatures during cooling were higher than during heating. The rest of the measurements can be seen in Appendix B.

Table 4.18 – Curie temperature at $11^{\circ}\text{C min}^{-1}$ for cobalt-based alloys with Kappabridge.

Sample	Curie temperature at $11^{\circ}\text{C min}^{-1}$ [$^{\circ}\text{C}$]
V	227 ± 7
N	228 ± 7
M	362 ± 11

Assessment

Table 4.19 shows a comparison between all the measurements for the cobalt-based samples. It can be seen that there is a very good agreement between the results of both methods,

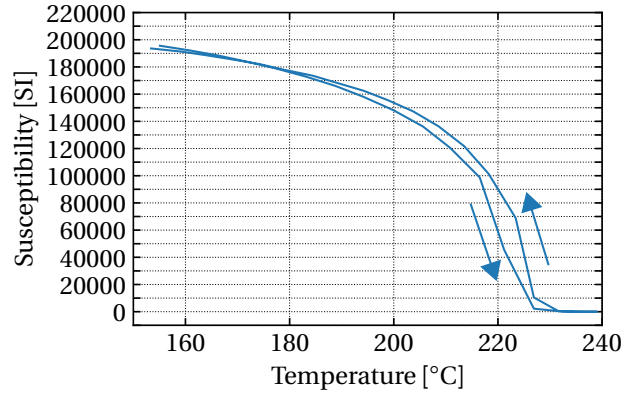


Figure 4.22 – Kappabridge measurement for sample V.

with the maximum difference being 2 % found in sample V.

Table 4.19 – T_C comparison for TGA, Kappabridge, VSM and literature values [°C].

Sample	TGA	Kappabridge	Literature
V	222 ± 2.6	227 ± 7	220 [8]
N	223 ± 2.6	228 ± 7	
M	361 ± 2.6	362 ± 11	365 [69]

Comparing both methods, the biggest difference can be seen in the V sample during the heating curve, where there is a relative difference of 5.5 % between both measurements. The biggest relative difference on the cooling curve is seen in the N sample, 3.9 %.

As mentioned for the iron-based alloys, the difference between the Curie and the first crystallisation temperature should be as big as possible to make sure that the microstructure of the alloy is not modified if only magnetic annealing is needed. In the case of the cobalt-based alloys, the smallest difference is 151 °C for sample M, then 319 °C and 320 °C for alloys V and N respectively as can be seen on Table 4.20. This difference is large enough to avoid the risk of unwanted crystallisation when annealing around T_C .

Table 4.20 – Difference between first crystallisation temperature and T_C [°C].

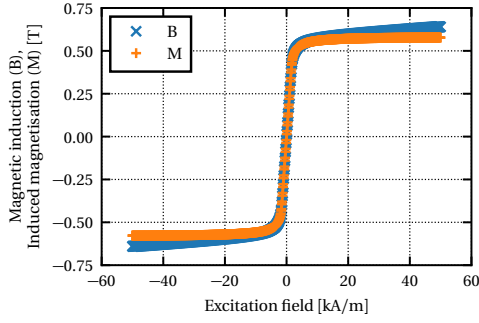
Sample	$\Delta(T_x - T_C)$
V	319
N	320
M	150

4.4.4 VSM

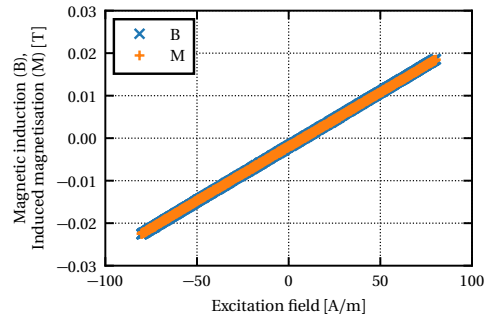
VSM measurements were taken with excitation fields up to 200 kA m^{-1} . Below, two measurements for each sample are presented, the first one showing the sample saturated

for a higher excitation field and the second one at a lower excitation field to see a close-up at coordinates (0,0).

Sample V



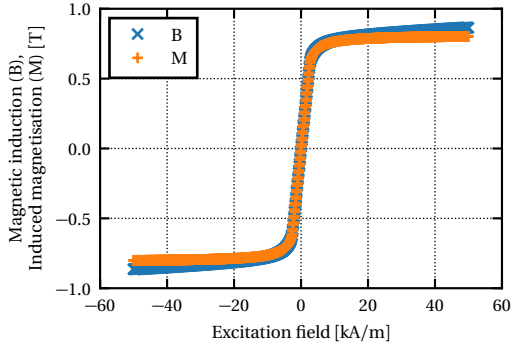
(a) V: Magnetisation curves.



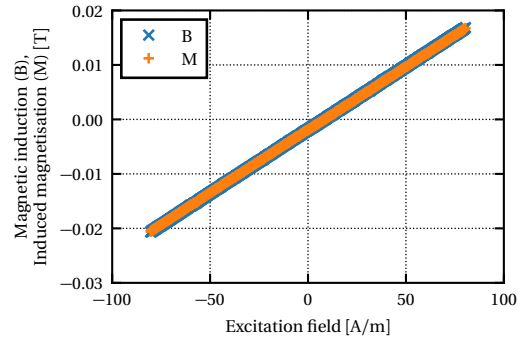
(b) V: Magnetisation curves close-up.

Figure 4.23 – VSM magnetisation curves for sample C1 (a) and a close-up of the central part (b).

Sample N



(a) N: Magnetisation curves.



(b) N: Magnetisation curves close-up.

Figure 4.24 – VSM magnetisation curves for sample N (a) and a close-up of the central part (b).

Sample M

AGM

AGM measurements were done to cross-check the VSM results, using the same conditions. The AGM analyses gave the same saturation results (extracted from the M magnetisation curve) as the VSM, the relative differences for sample V being 0.1 %, 2.2 % for N and 2.5 % for M.

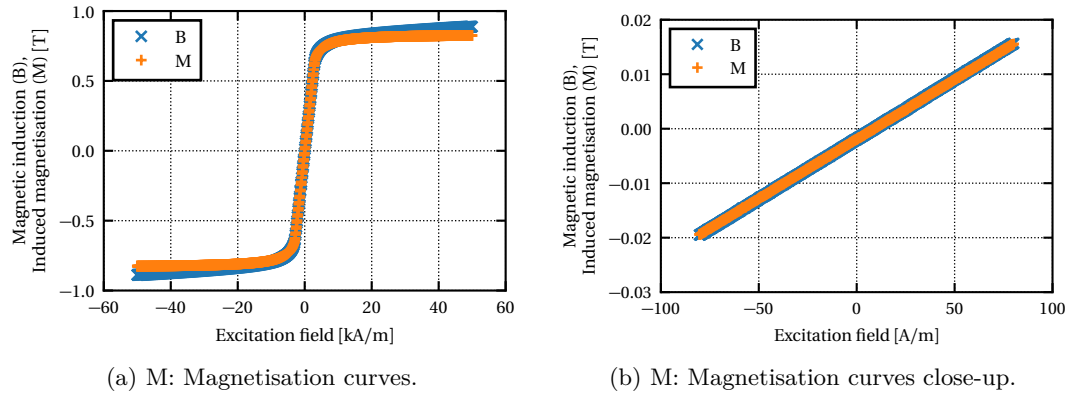


Figure 4.25 – VSM magnetisation curves for sample M (a) and a close-up of the central part (b).

Assessment

None of the samples present coercivity and remanence is practically zero. It can be seen in the close-up graphs that some samples are not centred, which is due to some residual magnetisation. Table 4.21 shows a summary of the saturation values of the induced magnetisation (M) measured.

Table 4.21 – VSM saturation summary for cobalt-based alloys.

Sample	Saturation [T]
V	0.58 ± 0.002
N	0.81 ± 0.042
M	0.83 ± 0.003

4.4.5 Magnetic domain imaging

MFIM

MFIM tests were performed on only some of the samples, as it became clear from the first results that the uneven surface was the main limitation factor in the area to visualise. In addition to this, the irregular topography interfered with the magnetic signal, made it hard to separate both in the post-processing stage. The best example of MFIM domains can be seen in Figure 4.26. Long domains can be seen horizontally in the image, with the effect of the topography clearly visible in the vertical "depressions" caused by it.

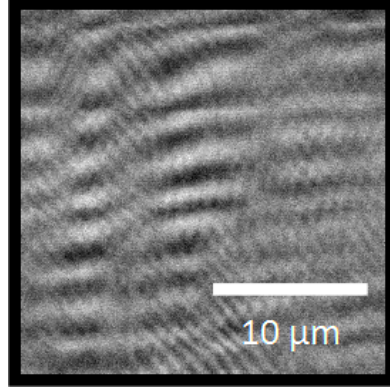


Figure 4.26 – MFM measurement for sample V.

Sample V

Sample V presents stresses at the edges and the applied stress from the attachment has no effect on the domain behaviour. The BH-loop in Figure 4.27 (a) indicates that there is a slight anisotropy in the short axis. The MOKE loops in Figure 4.27 (b) are inconclusive to determine anisotropy in the sample due to the magnetic nature of the chosen area.

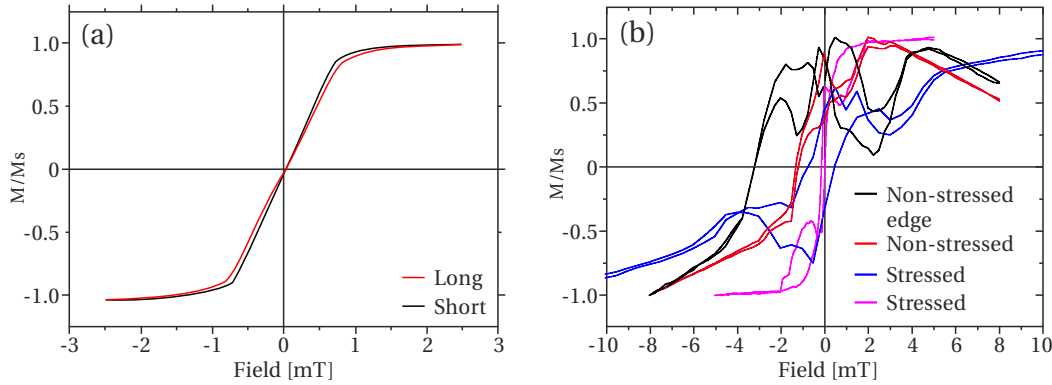


Figure 4.27 – BH-loop (a) and MOKE-loop (b) of sample V.

The domain images, however, show high anisotropy in the longitudinal direction as can be seen in Figure 4.28 (a), where the whole sample is visible. It is clear that the setup with which the BH-curve was measured was not able to measure the sample correctly and detect the high anisotropy present in the sample. Non-stressed parts of the sample like in Figure 4.28 (b) show long, homogeneously distributed domains along the whole sample. Regions with semi-induced stressed due to the edge (at the right of the image) of the sample show smaller domains present and originating from the edge, as indicated with arrows in 4.28 (c). Stressed regions show a change in the shape of the elongated domains and the domain walls become more irregular. More images can be seen in Appendix B.

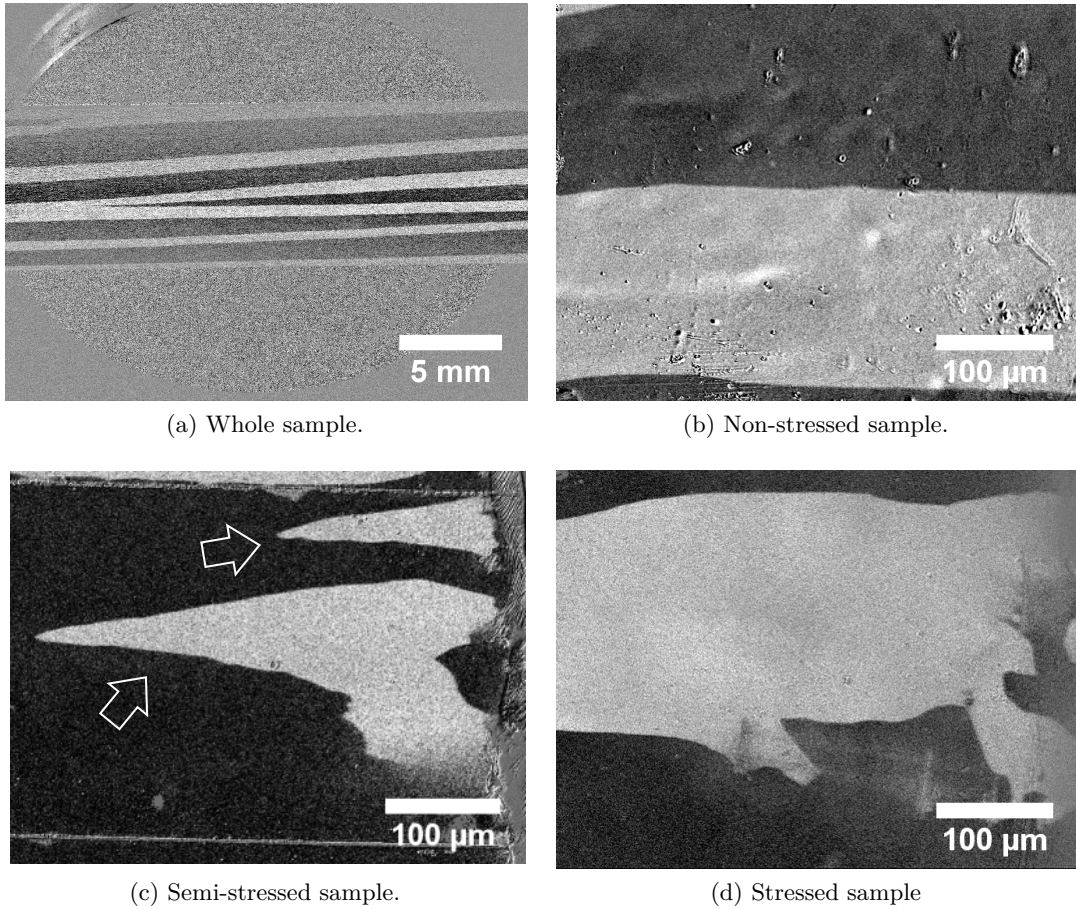


Figure 4.28 – Magnetic domain observation for sample V: whole sample (a), non-stressed (b), semi-stressed (c) and stressed (d).

Sample N

The BH-curve and MOKE-loop show that there is no apparent anisotropies in the sample (Figures 4.29 (a) and (c)), where the MOKE-loop of the whole sample is very similar to the BH-curve. Stresses present have a "rounding-effect" on the MOKE-loop as can be seen in Figure 4.29 (b). As before, the BH-curve does not seem to give a true interpretation of the reality of the domains in the sample like for sample V.

The domain images indicate that the sample presents high anisotropy in the longitudinal direction, but in patches, due to inhomogeneities marked with arrows in Figure 4.30 (a). These seem periodic and could come from the cooling wheel from the material fabrication process. Figure 4.30 (d) is from a transition region of semi induced stress with spiked-shaped domains present around the inhomogeneities pointed out before. Stress regions do not have different domain configuration from the non-stressed regions.

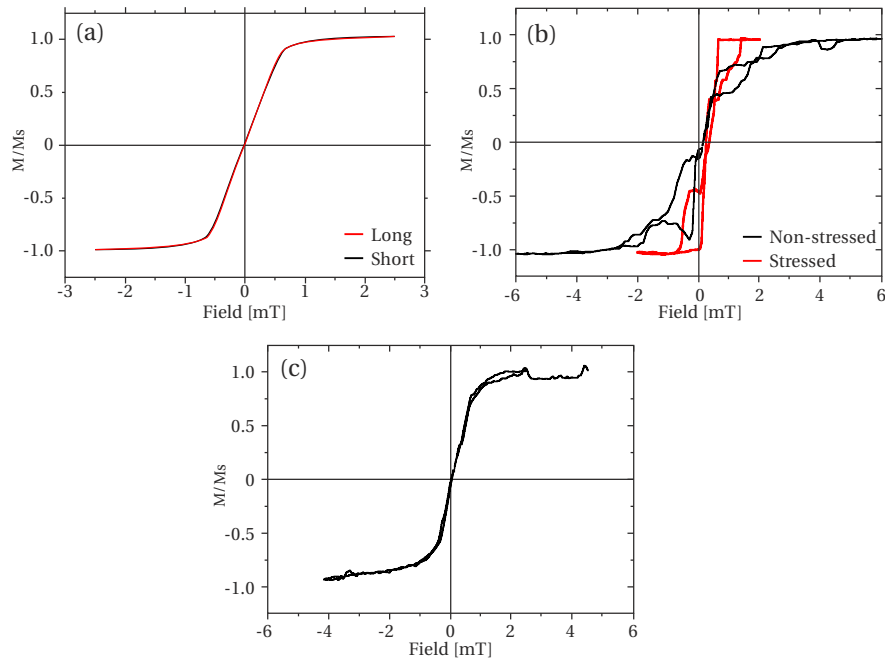


Figure 4.29 – BH-loop (a), MOKE-loop (b), and MOKE-loop of the whole sample (c) of material N.

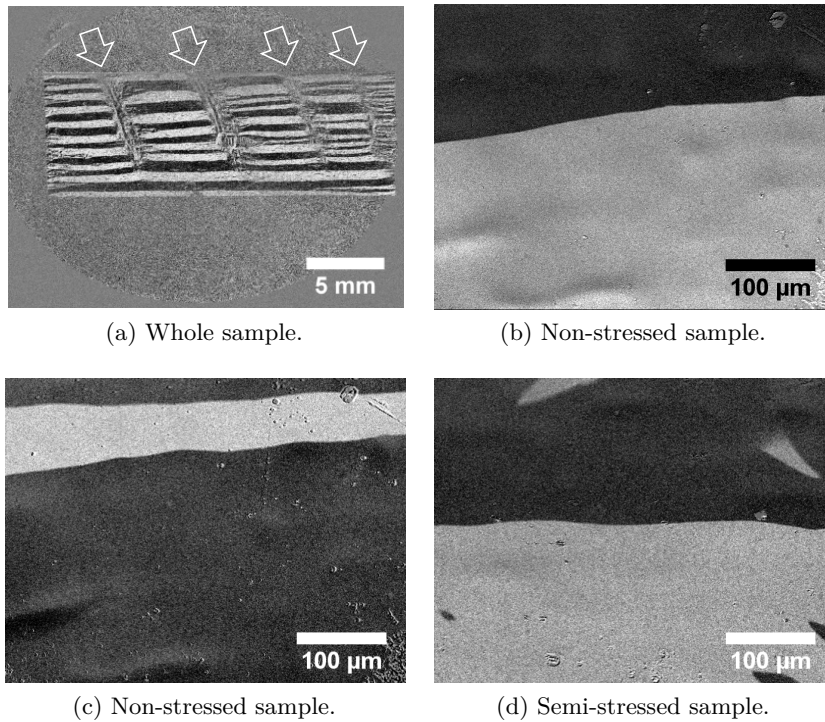


Figure 4.30 – Magnetic domain observation for sample N: whole sample (a), non-stressed (b, c) and semi-stressed (d).

Sample M

As with the previous two samples, the BH-loop does not indicate any kind of anisotropy as can be seen in Figure 4.31 (a). The MOKE-loops (Figure 4.31 (b)) are inconclusive as well, but the MOKE-loop of the whole sample (Figure 4.31 (c)) shows a similar behaviour to the BH-loop.

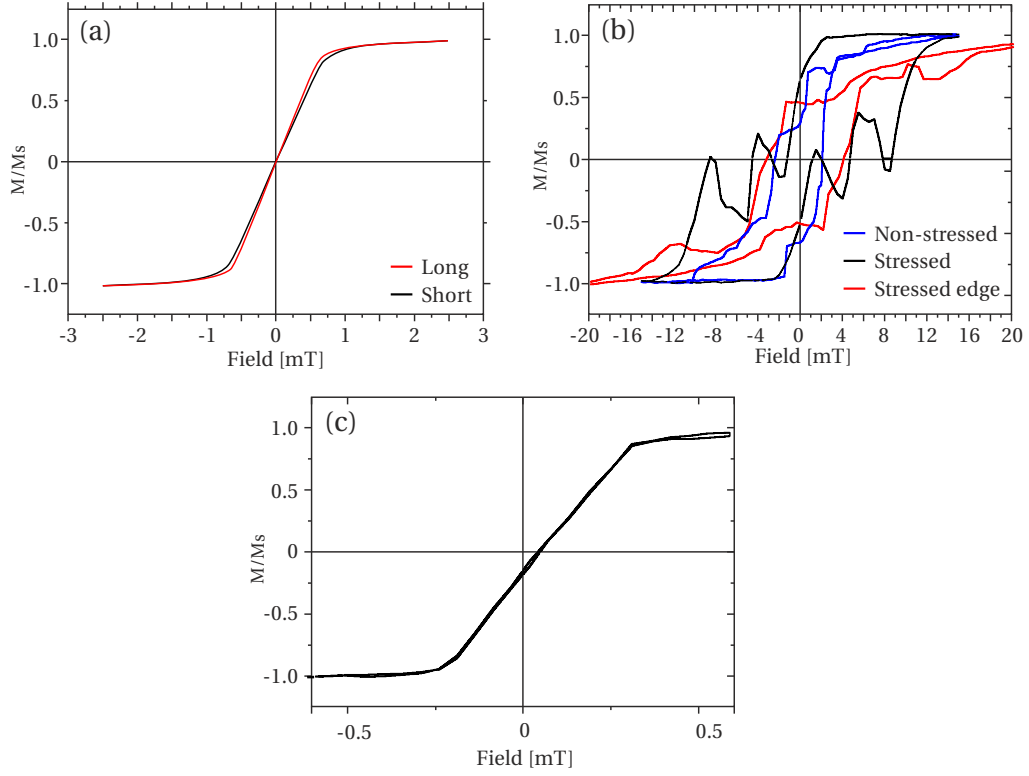


Figure 4.31 – BH-loop (a), and MOKE-loop (b) and whole-sample MOKE loop (c) of sample M.

Domains in sample M also show high anisotropy, with stress build-up seen at edges of sample (on the right on Figures 4.32 (b)-(d)), creating smaller domains in this area. Apart from this, stress regions do not have different domain configuration from the non-stressed regions.

Assessment

The cobalt-based alloys show a very similar domain pattern compared to each other. The BH-curve, due to the setup's configuration, is not able to properly measure the high anisotropy present in all of the samples in the longitudinal direction of the ribbon. Long domains of several hundreds of microns wide are present in all of the samples. Sample N has a patterned configuration due to changes in the surface topography of the sample,

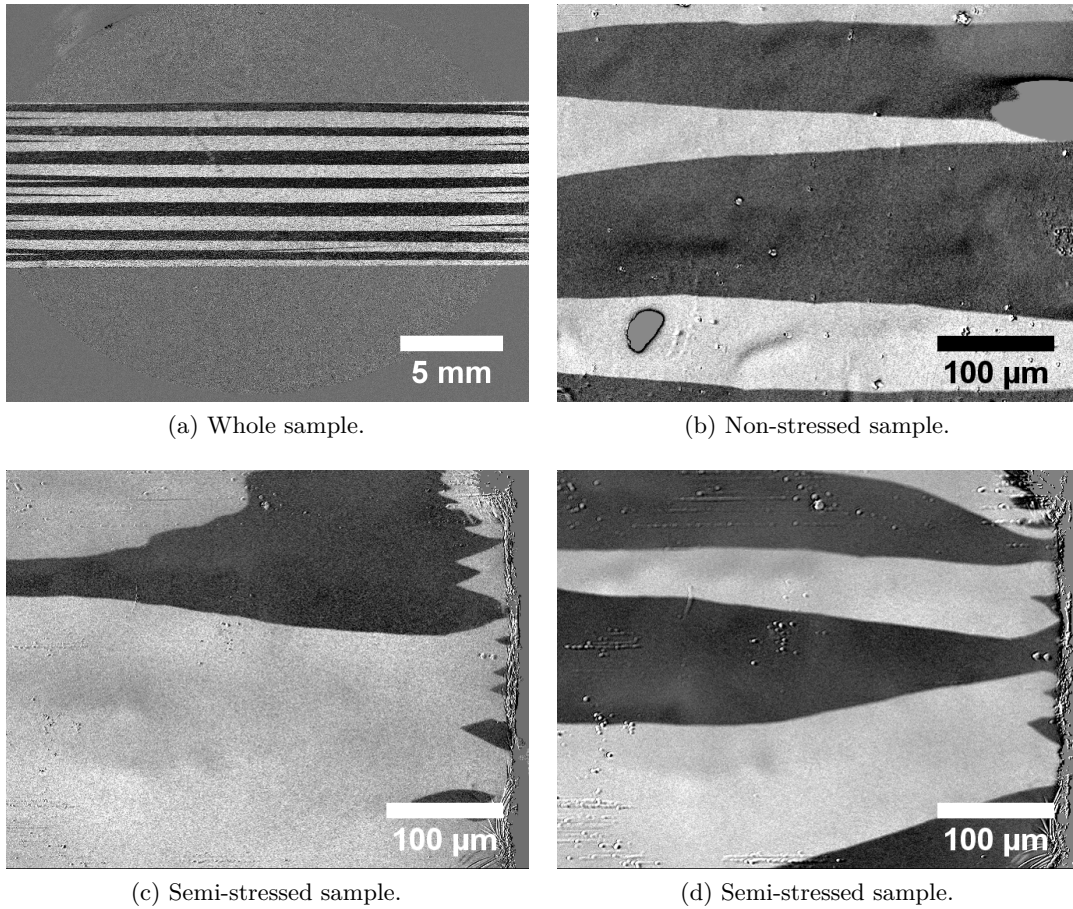


Figure 4.32 – Magnetic domain observation for sample M: whole sample (a), non-stressed (b) and semi-stressed (c, d).

due to its fabrication process.

4.4.6 Barkhausen Noise (BN)

Figure 4.33 shows the comparison of BN between the as-cast cobalt-based materials. It can be seen that all the samples present a similar width of about 0.2 s, but sample N shows the highest noise level over 0.5 AU. Samples V and M show flatter, lower noise response, with sample M being the lowest with a flat-top of around 0.3 AU.

Assessment

The BN comparison for the cobalt-based samples is very interesting, as their domain configuration is very similar. The difference in the BN indicates that the three samples have very different pinning points in the material, which would then mean that sample

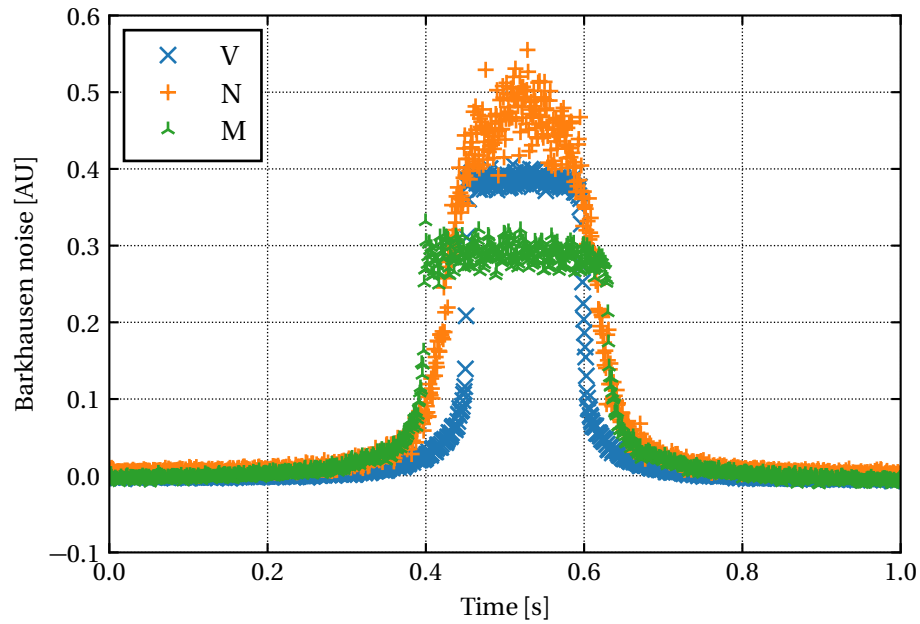


Figure 4.33 – Barkhausen Noise comparison for cobalt-based alloys.

M is the most homogeneous, having the lowest noise of them all.

4.5 Thickness

Table 4.22 shows the thickness for all of the cobalt-based alloys. All the measurements are in the expected range for this kind of materials, between $20\text{ }\mu\text{m}$ and $30\text{ }\mu\text{m}$, with N being the thickest at $28.7\text{ }\mu\text{m}$.

Table 4.22 – Thickness results of cobalt-based alloys.

Sample	Thickness [μm]	St. Dev [μm]
V	20.4	0.5
N	28.7	0.5
M	22.6	0.7

4.6 Density

Table 4.23 shows the density, standard deviation, uncertainty and bibliography values for the density of the cobalt-based alloys. All the values are in the expected range, around 7.8 g cm^{-3} for alloys of this kind.

Table 4.23 – Density results of cobalt-based alloys in g cm^{-3} .

Sample	Density	St. Dev	Uncertainty	Literature
V	7.69	1.5×10^{-3}	8.5×10^{-3}	7.80 [8]
N	7.70	1.9×10^{-3}	9.3×10^{-3}	
M	7.91	1.2×10^{-3}	9.0×10^{-3}	7.80 [69]

4.7 Results discussion

Looking at the magnetic properties but for application purposes the three cobalt samples show a very high initial permeability that decreases quickly with frequency. Samples V and N show a permeability of about 160 000, while sample M 250 000. Coercivity measurements show that all of the materials have a coercivity under 9 A m^{-1} , with sample N having the lowest at, 4.44 A m^{-1} . However, sample N also presents the lowest remanence of them all, with 0.43 T against 0.56 T for sample V and 0.69 T for sample M.

Regarding the characteristic temperatures, samples V and N show very similar crystallisation ($\approx 550^\circ\text{C}$) and Curie temperatures ($\approx 220^\circ\text{C}$) but M shows a different behaviour, with a first crystallisation 518°C at and Curie temperature at 360°C . All of the materials would be good candidates taking into account these parameters. The Curie temperature is well below the crystallisation temperature which would allow magnetic annealing under the Curie temperature without risking the crystallisation of the material. Crystallisation temperatures, like for iron-based alloys, are all over 500°C , which, as has been said before, it is a technologically reachable value if the samples are to be crystallised.

As the magnetic domains of the three samples look very similar, the BN is another indication of the magnetic behaviour of the samples. Material N presents the highest BN, while V and M are lower (the noise of material M is almost half that of sample M).

5 Results of thermal treatments

5.1 Choice of materials

After all the material analyses, the choice of the material that was to be thermally annealed was made upon the as-cast properties. The most interesting parameters for the transformer cores have already been described in Chapter 1, and are the losses and permeability. Looking at the results in Chapters 3 and 4, it can be seen that based on permeability and losses, the best alloys are the amorphous cobalt-based ones. It has been shown that the iron-based alloys do not present very interesting properties in their amorphous state, while the cobalt-based alloys do. Technologically speaking, the cobalt-based alloys with a big temperature difference between the Curie and crystallisation temperatures would be optimal to avoid changing the amorphous state of the material. For the iron-based alloys, it is more interesting to nanocrystallise them in order to improve their magnetic properties. As the results show that the V and N alloys are very similar, only one was annealed. The V alloy, being a well-known commercially available product was the one chosen for the annealing tests. Alloy M presents very good characteristics and is different enough to alloy V that its study is also of interest. In order to study the effect of crystallisation, alloy F was thermally treated above its crystallisation temperature to see how its magnetic properties change.

Table 5.1 – Summary of materials to be annealed.

Sample	Type	Number of treatments
F	iron-based	5
V	cobalt-based	4
M	cobalt-based	3

5.1.1 Thermal treatments

To thermally treat the samples, a Vide Appareillages Scientifiques oven from CERN from was used. The setup consisted of a vacuum furnace connected to a power switchgear board from San Giorgio Automazione and PLC system from Siemens. The vacuum inside the oven guaranteed that the samples did not oxidise and their composition remained intact. Figure 5.1 shows the oven with one of the samples inside.

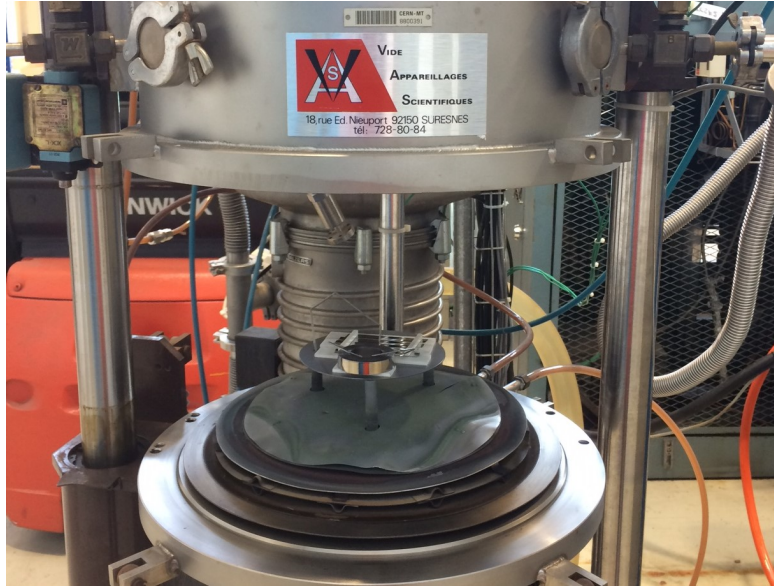


Figure 5.1 – Open oven with core and ribbons inside.

All treatments were done with a heating rate of $10^{\circ}\text{C min}^{-1}$, as this was the recommended temperature increase so that the samples would be evenly heated inside the oven. The reference Curie and crystallisation temperatures used for the thermal treatments correspond therefore to those for the mentioned heating rate. Cooling was done by venting with argon to speed up the natural convection cooling process (which took at least a couple of hours).

To see the effects of annealing, taking into account the critical temperatures of the alloys, three thermal treatments were done for each material:

- below the Curie temperature
- between the Curie and crystallisation temperatures
- above the crystallisation temperature

To simplify notation, the samples annealed below the Curie temperature (T_C) have been given the suffix "-C", the ones between T_C and the crystallisation temperature (T_x) "-S" and the ones above T_x "-X".

5.2 Annealing results

5.2.1 F samples ($T_C = 327^\circ\text{C}$, $T_x = 511^\circ\text{C}$)

Below T_C

Two tests below T_C were done with sample F. Sample F-C1 (previously F-1) was heated from room temperature up to a maximum of 283°C during a total of 1.8 hours. Sample F-C2 (previously F-2) was heated for 2.3 hours, followed by a plateau of 1.01 hours at an average temperature of 285°C and a maximum temperature of 288°C to see the effect of time on the results.

Sample F-C1 was annealed at an average pressure of 3.8×10^{-6} mbar, while F-C2 at 1.9×10^{-6} mbar.

The maximum permeability measured for F-C1 was 1816, while for F-C2 it was 1797. It can be seen that F-C2 is the core that was presented previously as being the most different to the other F-cores. The permeability analysis shows that after annealing, the differences between F-C1 and F-C2 are negligible (1 %). It can therefore be said that annealing below T_C for sample F increases the permeability up to a maximum, without changing the frequency response of the material. This change is probably due to the stress-relaxation in the material. This conclusion is supported by the fact that the difference between the as-cast samples is larger than the one between the treated samples.

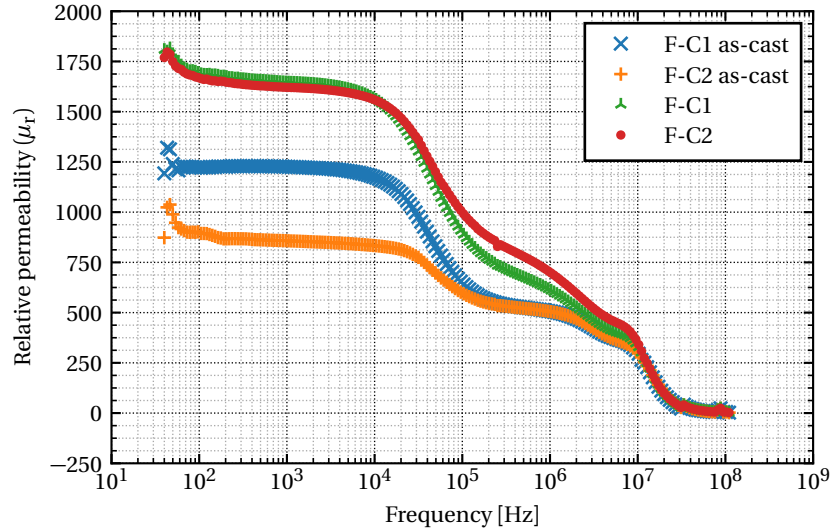


Figure 5.2 – Permeability analysis of sample F before and after annealing below T_C .

Figure 5.3 shows the comparison of the three BH-curves. F-C1 shows a coercivity of

Chapter 5. Results of thermal treatments

18.8 A m^{-1} and F-C2 18.3 A m^{-1} (3 % difference), while the remanence was 0.26 T and 0.25 T respectively (a 4 % difference). It does not seem from these results that there is a great influence in the BH-curve parameters when annealing below T_C .

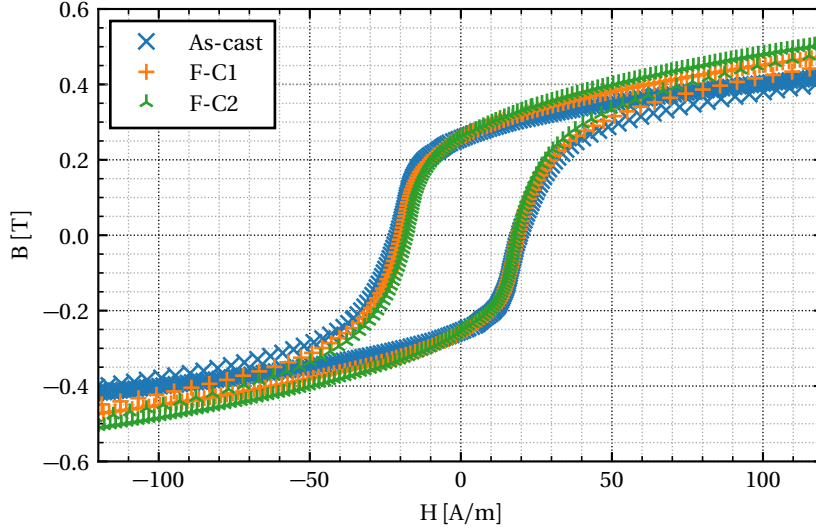


Figure 5.3 – BH-curve of sample F before and after annealing below T_C .

Figure 5.4 shows the BN for F-C1 and F-C2. It can be seen than F-C1, which had a lower annealing time, has a higher BN level than F-C2.

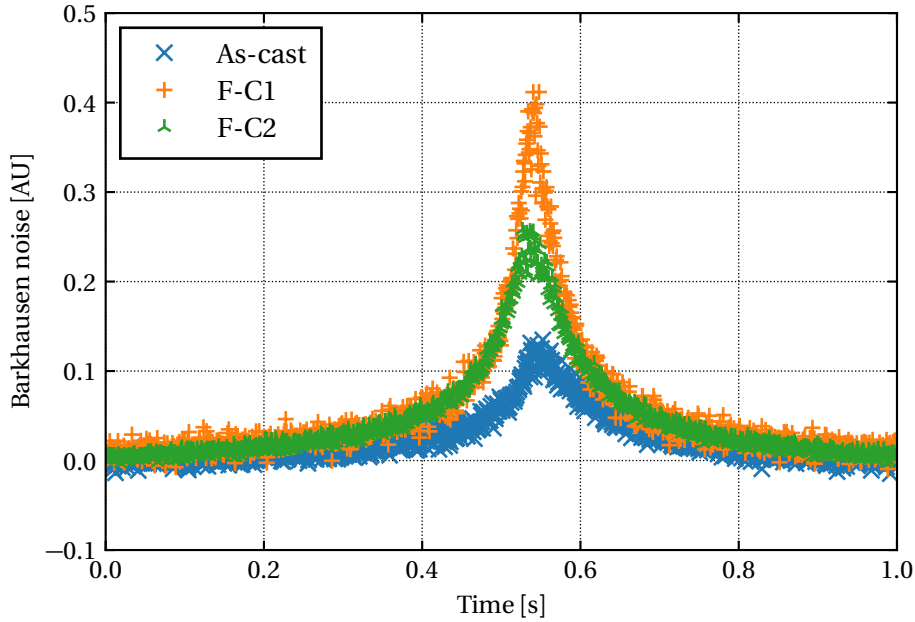


Figure 5.4 – BN of sample F before and after annealing below T_C .

Between T_C and T_x

F-S was annealed for a total of 1.9 hours, with a plateau of 1.1 hours at an average temperature of 403 °C and pressure of 3.8×10^{-6} mbar. Figure 5.5 shows a maximum permeability of 11 259, an increase of 768 % from the as-cast sample. This is a much bigger difference than the one seen in the treatments below T_C .

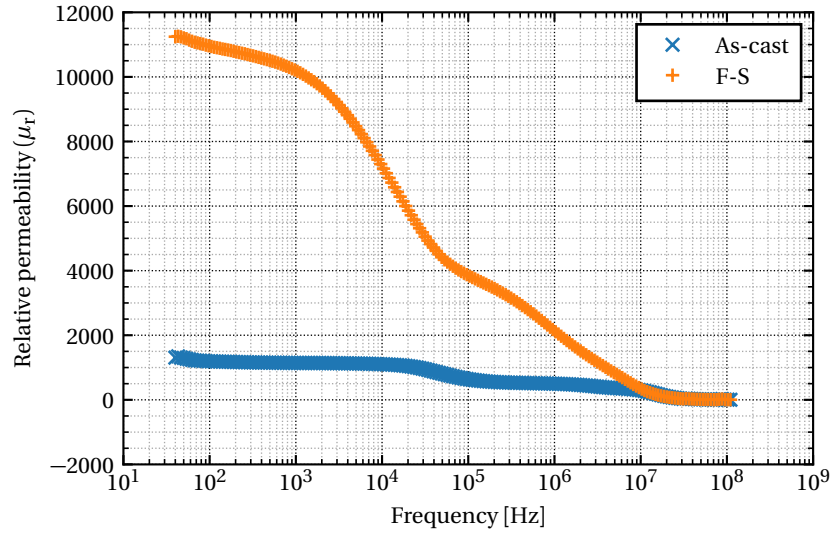


Figure 5.5 – Permeability analysis of sample F before and after annealing between T_C and T_x .

F-S shows a coercivity of 6.87 A m^{-1} , down from 14.37 A m^{-1} ; a decrease of 52.2 %. The remanence increased 150 % from 0.26 T to 0.4 T. From the permeability and the BH-curve it can be seen that the stress-relief really occurs above T_C (without crystallising the sample), improving the magnetic properties. It can also be seen that frequency response of the annealed material does not change.

The BN in the sample is increased by a factor of 3 as can be seen in Figure 5.7.

Above T_x

Two annealing tests were done above T_x , F-X1 with a total heating time of 17.5 minutes and F-X2 with a total heating time of 1.7 hours including an isothermal plateau of 32.5 minutes at an average temperature of 552 °C and pressure of 4.8×10^{-6} mbar.

Figure 5.8 shows the permeability for the as-cast cores and their annealed state. F-X1 shows a maximum permeability of 150 971 and F-X2 151 399, an increment of 11 117 % and 11 149 % respectively, a factor of over 112 for both.

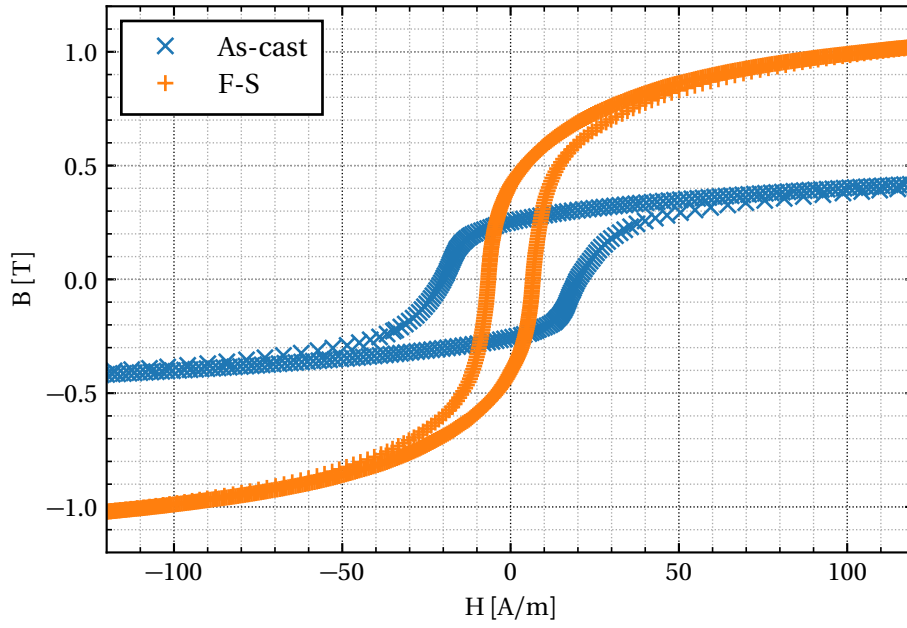


Figure 5.6 – BH-curve of sample F before and after annealing between T_C and T_x .

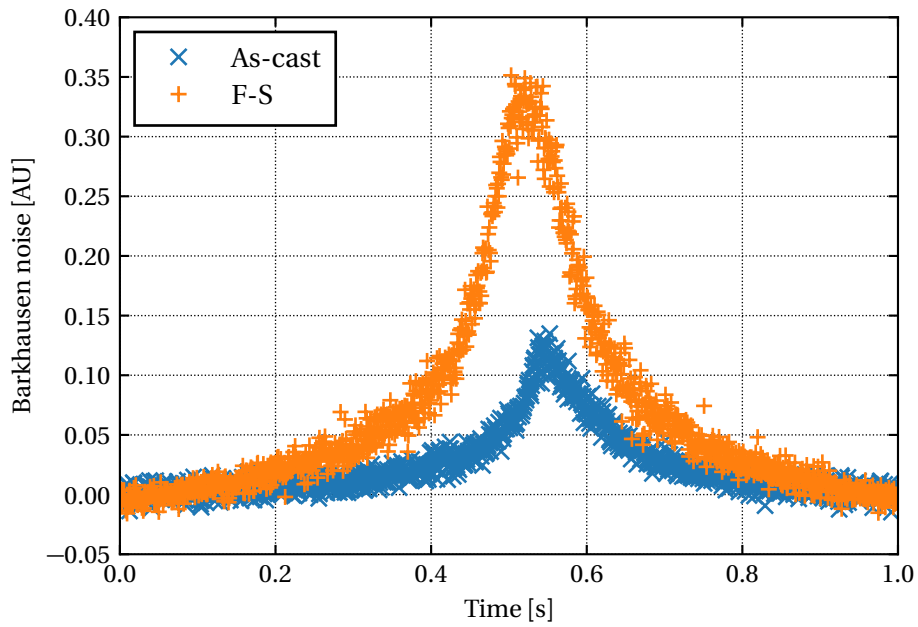


Figure 5.7 – BN of sample F before and after annealing between T_C and T_x .

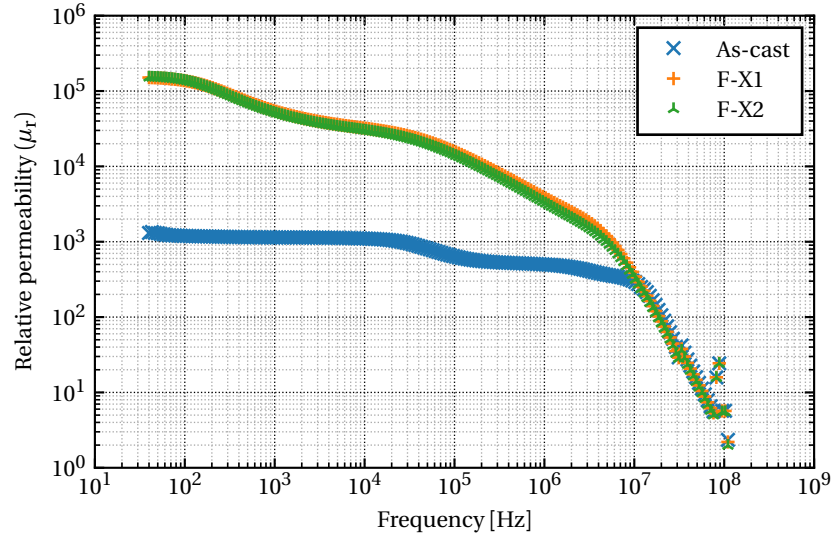


Figure 5.8 – Permeability analysis of sample F before and after annealing above T_x .

The BH-curve shows that both treatments give a much narrower BH curve, with a decrease in coercivity in F-X1 of 84.2 % and of 81.7 % in F-X2, down to 3.44 A m^{-1} and 3.53 A m^{-1} respectively. The remanence increased by over 100 % in both cases, to 0.55 T and 0.54 T.

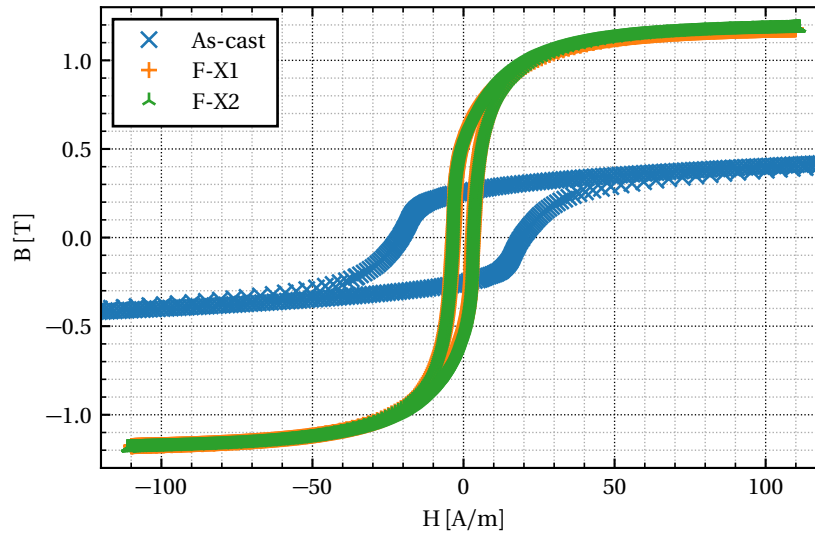


Figure 5.9 – BH-curve of sample F before and above T_x .

The BN for both samples increased after the thermal treatment, also widening the noise region that was originally a peak as can be seen in Figure 5.10. It is interesting to see how the permeability and the BH-curve look very similar for both samples, but the BN

shows a significant difference between them. This effect might originate from the size of the crystals that should be bigger in F-X2 due to the much higher annealing time (1.7 hours compared to 17.5 minutes for F-X1).

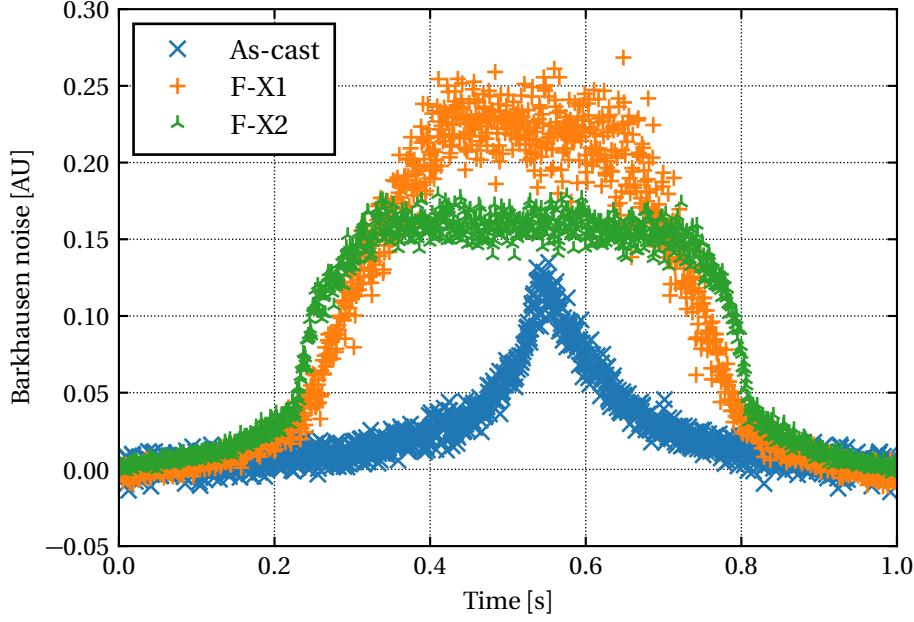


Figure 5.10 – BN of sample F before and after annealing above T_x .

5.2.2 V samples ($T_C = 222^\circ\text{C}$, $T_x = 550^\circ\text{C}$)

Below T_C

The sample was annealed for a total of 2.2 hours, heating up from room temperature and reaching a maximum temperature of 169.6°C , with a pressure of 2.6×10^{-6} mbar. Figure 5.11 shows a slight decrease in maximum permeability of 8.8 %, while the frequency response improves in the annealed core.

Figure 5.12 shows the BH-curve of the sample before and after annealing. Coercivity decreased by 39.3 %, down to 3.8 A m^{-1} , while remanence stayed almost the same, decreasing by 7.1 % from 0.56 T to 0.52 T.

The BN is shown in Figure 5.15 to compare with the sample annealed between T_C and T_x .

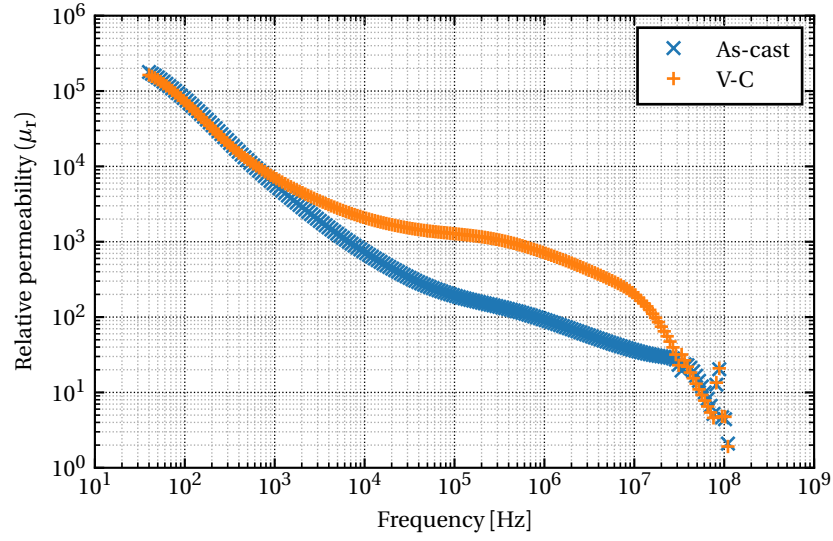


Figure 5.11 – Permeability analysis of sample V before and after annealing below T_C .

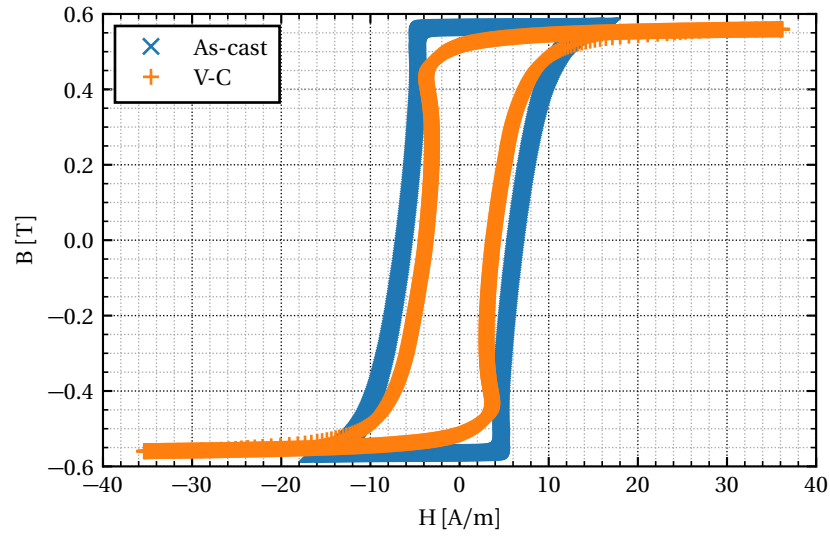


Figure 5.12 – BH-curve of sample V before and after annealing below T_x .

Between T_C and T_x

Sample V-S was annealed for a total of 2.1 hours with a plateau of 58.5 minutes and an average temperature of 450.1°C . The maximum temperature reached was 457.4°C and the average pressure during the treatment was 5.5×10^{-6} mbar. Figure 5.13 shows that the annealed core has a maximum permeability of 381 526, up by 108.7 %.

The BH-curve shows a very steep decrease in coercivity of 86.6 %, down to 0.84 A m^{-1} ,

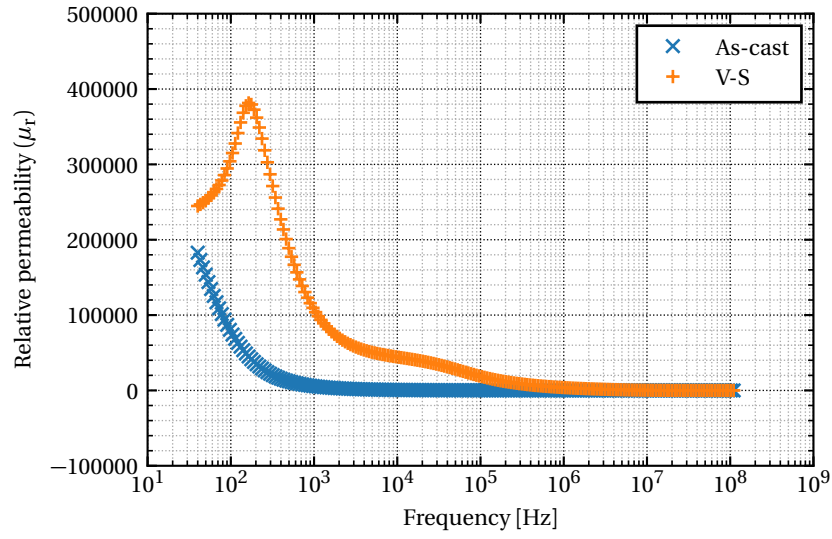


Figure 5.13 – Permeability analysis of sample V before and after annealing between T_C and T_x .

while the remanence decreased by 23.2 % to 0.43 T.

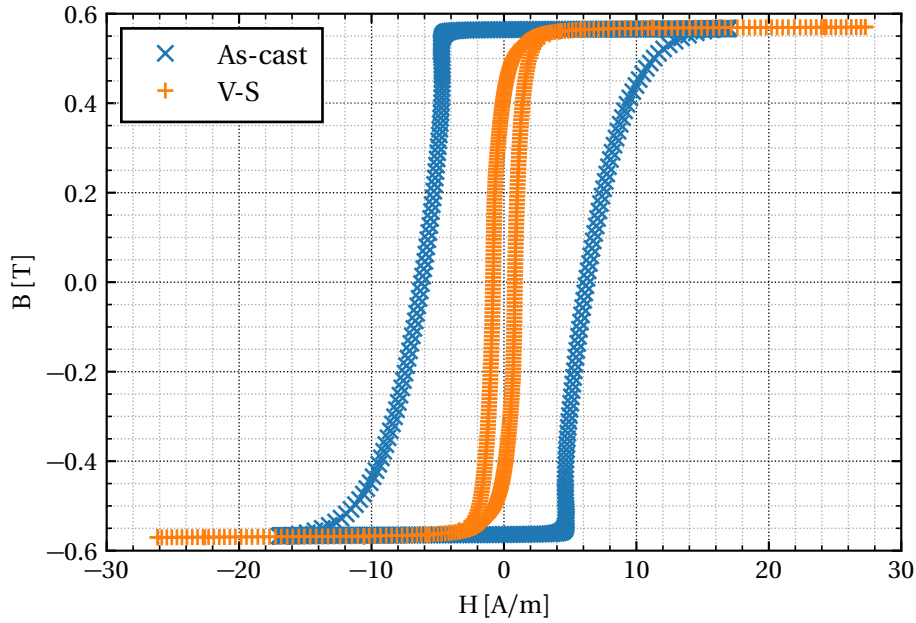


Figure 5.14 – BH curve of sample V before and after annealing between T_C and T_x .

Figure 5.15 shows the BN noise for V-C and V-S. It can be seen that the noise becomes narrower after the treatment but it increases slightly in intensity for both cases.

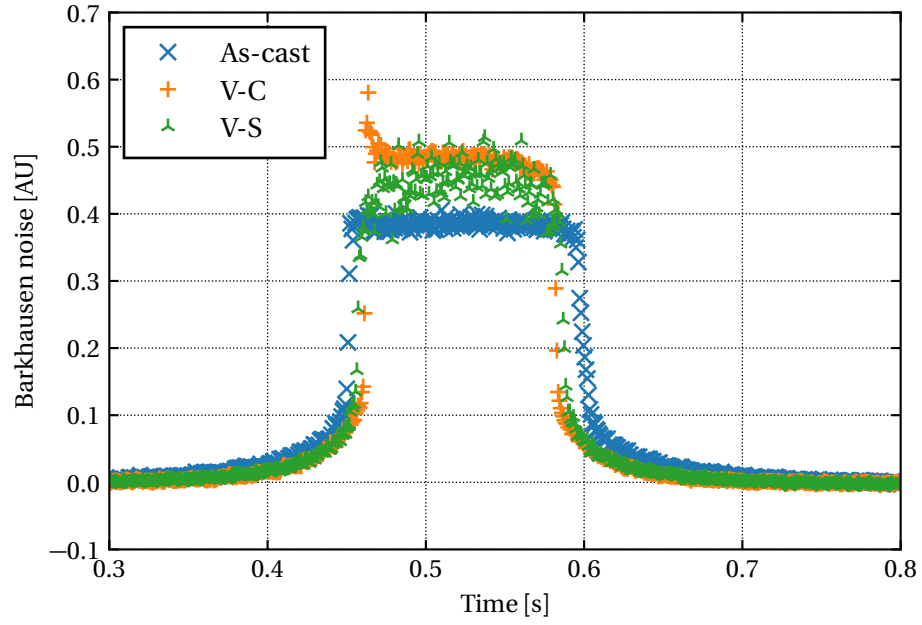


Figure 5.15 – BN of sample V before and after annealing below T_C (V-C) and between T_C and T_x (V-S).

Above T_x

Two tests were done above T_x , one with a time of 15 minutes above the crystallisation temperature and the other one with 30 minutes. However, both samples lose all of their magnetic properties and show practically no permeability, a flat BH-curve and no BN.

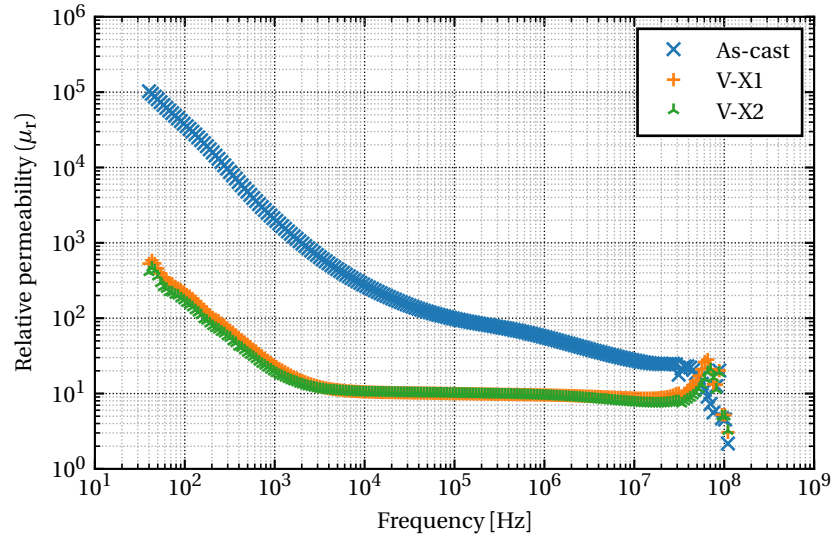


Figure 5.16 – Permeability of samples V-X1 and V-X2 annealed above T_x .

Figure 5.16 shows the permeability of both samples. This could be explained by the formation the boride phase (Fe_2B) that was seen in the HT-XRD results.

5.2.3 M samples ($T_C = 361^\circ\text{C}$, $T_x = 513^\circ\text{C}$)

Below T_C

Sample M-C was annealed for a total of 1.7 hours, the maximum temperature being 319.9°C and the average pressure 4.3×10^{-6} mbar. Figure 5.17 shows that the permeability decreased by 96.1 % to 9776.

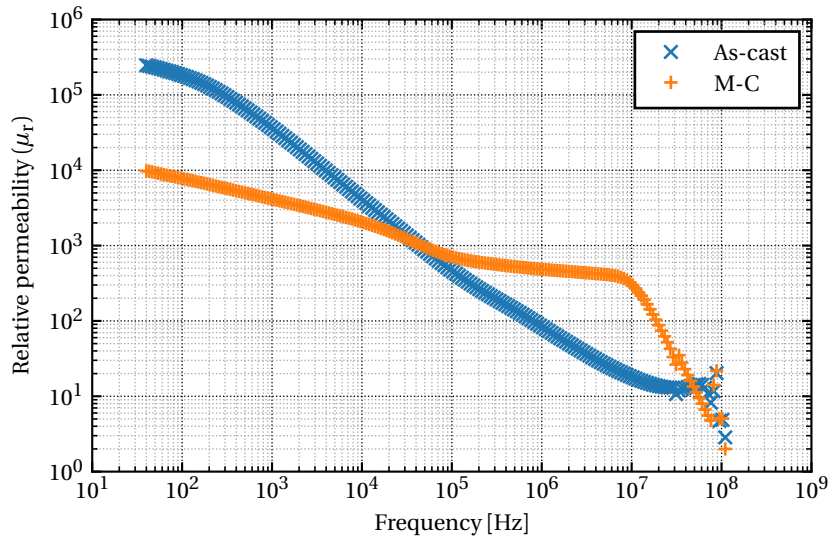


Figure 5.17 – Permeability analysis of sample M before and after annealing below T_C .

The BH-curve of the annealed sample shows an increase in coercivity of 104.5 %, up to 15.6 A m^{-1} and a decrease in remanence of 11.9 % to 0.59 T. It can be seen that the sample presents a so-called "constricted" curve. These kinds of loops were first seen in Perminvar material, an alloy of 25 % cobalt, 45 % nickel and 30 % iron, and they are called "Perminvar loops" [12]. The name is based the fact that the material has a constant permeability and almost zero hysteresis losses at low fields. If the excitation field increases gradually, the BH-curve opens up but having this characteristic shape. This magnetic behaviour could be explained by two different mechanisms:

- the presence of domains at 90° and 180° in a complex network, such that one kind cannot move independently from the other. At low fields, none of the walls get to move irreversibly [2].
- the fixing of magnetic domains in their as-cast state after the annealing without a magnetic field, due to the induced local anisotropy along the axis of local magnetisation.

This "wall pinning" means that a small non-zero field is needed to de-pin the walls, that, when exceeded, will make the walls snap into a new position with a sharp change of permeability [12]. Figure 5.18 (a) shows a typical Perminvar loop and Figure 5.18 (b) shows a schematic of a BH-curve of a pinned wall.

Both of these mechanisms create the same kind of BH-curve, where the pinning of the walls creates the characteristic shape. Further MOKE analysis of the annealed sample could give more insight into exactly which mechanism is creating the Perminvar loop-like curve in sample M, but seeing the magnetic domain configuration of sample M in the as-cast state (longitudinal domains in the casting direction), the second mechanism seems more plausible.

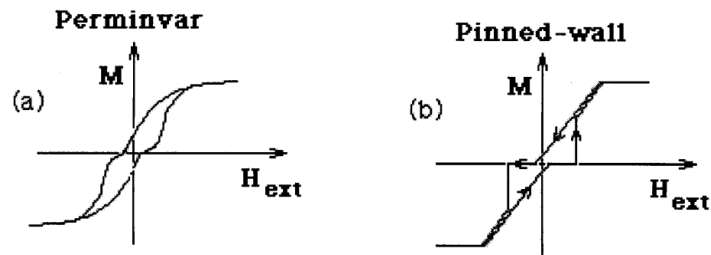


Figure 5.18 – Explanation of the Perminvar-type loop, adapted from [12].

The BN for the sample is shown together with that for M-S in Figure 5.22.

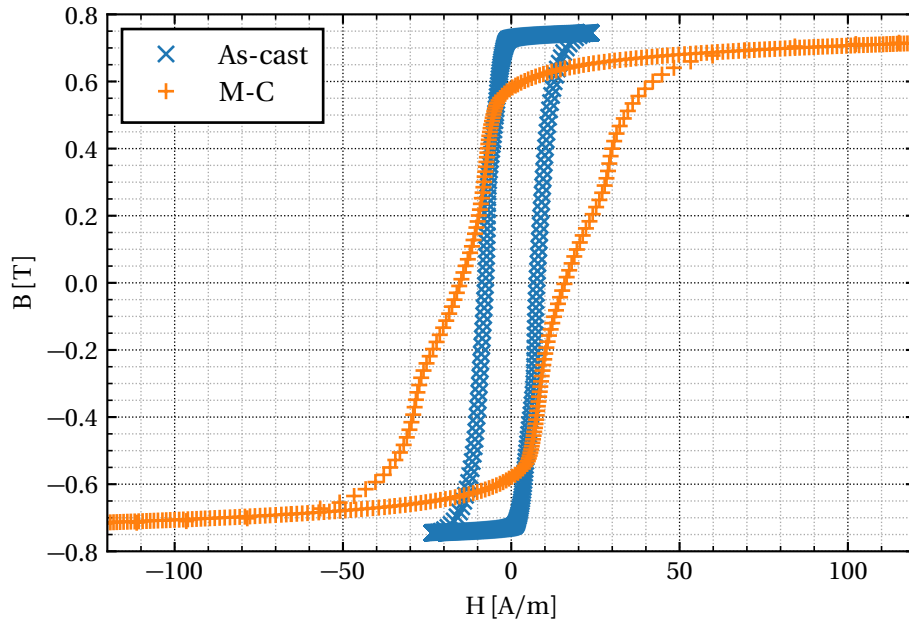


Figure 5.19 – BH curve of sample M before and after annealing below T_C .

Between T_C and T_x

Sample M-S was annealed for 2 hours with a plateau of 54.5 minutes at an average temperature of 450.3 °C and a pressure of 4.4×10^{-6} mbar. The maximum temperature reached was 454.7 °C. Figure 5.20 shows the same tendency as M-C, although the frequency response is flatter in this case. Permeability drops by 99.2 % to 2049 but remains constant up to almost 10 MHz.

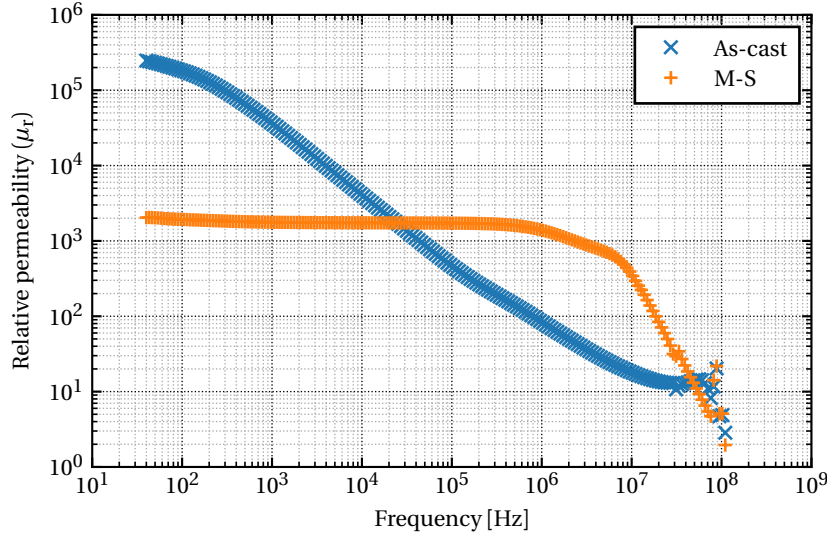


Figure 5.20 – Permeability analysis of sample M before and after annealing between T_C and T_x .

The BH-curve shows the same Perminvar loop shape as M-C but more pronounced. It is clear that the increase in temperature makes the effect more pronounced. As with sample M-C, a MOKE study would show the mechanism behind the characteristic loop. Coercivity decreased by 11.3 % to 6.78 A m^{-1} , while remanence dropped by 82.1 % to 0.12 T.

BN also increases slightly as in all other samples, but the width remains similar. Both samples have a comparable BN structure after annealing.

Above T_x

A core was annealed for 1.9 hours with a plateau of 27.5 minutes, an average temperature of 558.9 °C and a pressure of 3.0×10^{-6} mbar. The maximum temperature reached was 561.3 °C. As with material V, the samples above T_x show practically no permeability, a flat BH-curve and no BN. Figure 5.23 shows the permeability of both samples. This could be explained by the formation the phase with composition $\text{Co}_{21}\text{Mo}_2\text{B}_6$ that was seen in the HT-XRD results..

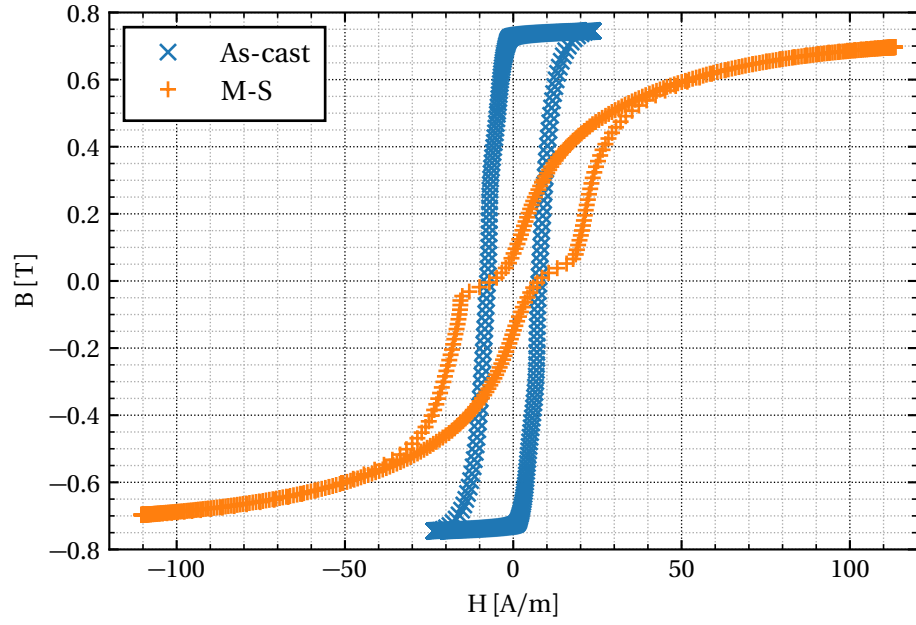


Figure 5.21 – BH curve of sample M before and after annealing between T_C and T_x .

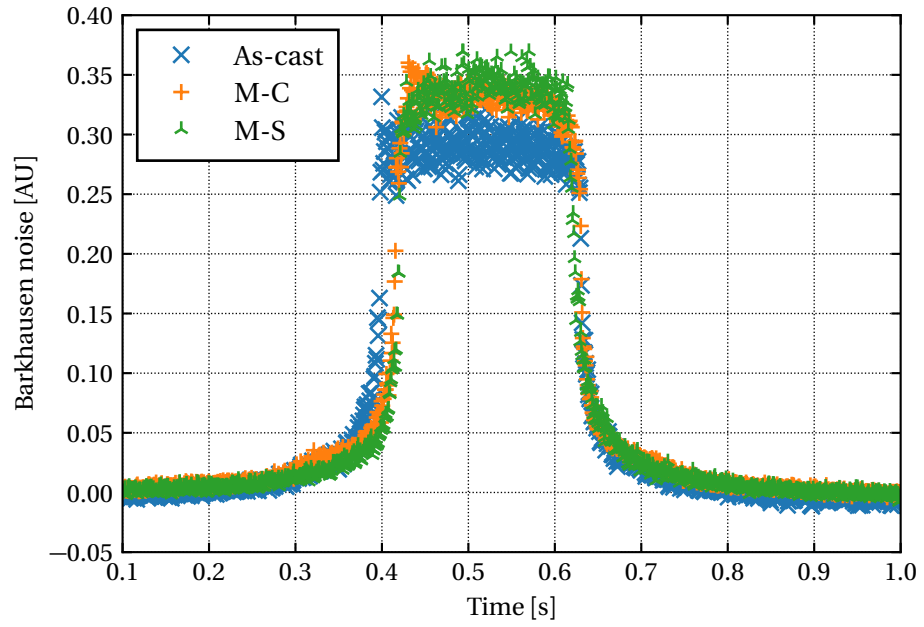


Figure 5.22 – BN of sample M before and after annealing below T_C (M-C) and between T_C and T_x (M-S).

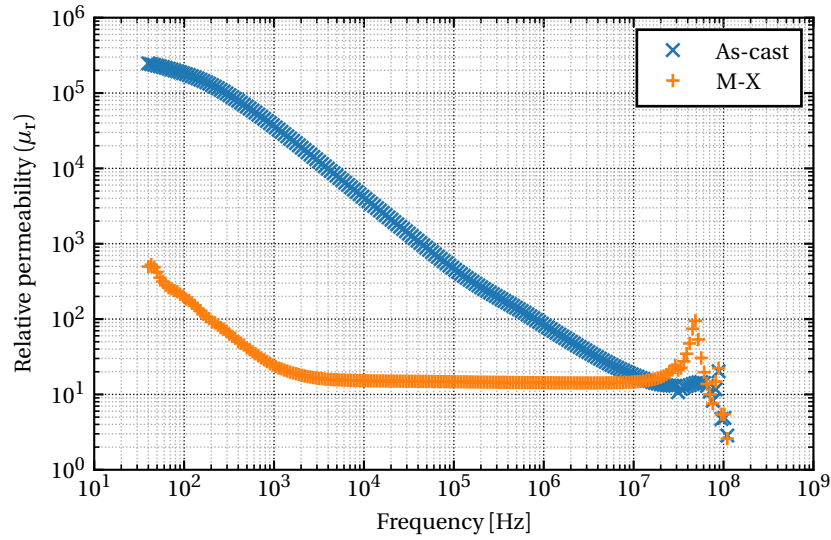


Figure 5.23 – Permeability analysis of sample M after annealing above T_x .

5.2.4 Summary of results

Table 5.2 shows a comparison of the changes in the parameters before and after annealing.

Table 5.2 – Comparison of parameters before and after annealing.

Sample	Time [h]	$\Delta\mu_{max}$ [%]	ΔH_c [%]	ΔB_r [%]	ΔBN_{max} [%]
F-C1	1.8	37.5	2.3	8.3	205.4
F-C2	2.3 + 1.1	73.2	-0.7	4.2	91.0
F-S	0.8 + 1.1	768.0	-52.2	150.0	160.5
F-X1	0.3	11117.2	-84.2	111.5	99.0
F-X2	1.1 + 0.5	11148.9	-81.7	107.7	33.0
V-C	2.2	-8.8	39.3	-7.1	43.1
V-S	1.0 + 1.1	108.7	-86.6	-23.2	26.7
V-X1	1.4	-99.4	-	-	-
V-X2	1.7	-99.5	-	-	-
M-C	1.7	-96.1	104.5	-11.9	8.6
M-S	0.9 + 1.1	-99.2	-11.3	-82.1	11.5
M-X	1.4 + 0.5	-99.8	-	-	-

General observations for iron-based alloy F

- All of the thermal treatments increase permeability (the biggest one being found in the treatments above T_x) and BN.

- The annealing below T_C has almost no effect on the BH-curve parameters, but the permeability and BN increase.
- Annealing above T_C without crystallising improves the magnetic properties significantly, increasing permeability and remanence, and decreasing coercivity.

General observations for cobalt-based alloys

- Annealing below T_C worsens the magnetic properties, decreasing permeability and remanence, and increasing coercivity.
- Annealing above T_C without crystallising has a different effect for alloy V and M. Sample V-S shows improved magnetic properties after the treatment, with higher permeability and a better frequency response, lower coercivity and slightly lower remanence, due to the rounding of the BH-curve, but not affecting saturation. On the other hand, sample M presents a different response after the thermal treatment. Permeability is lower but has a much flatter response (more similar to a ferrite), with a very high cut-off frequency, and the BH-curve is significantly more rounded, with a lower coercivity and remanence.
- It is worth mentioning that sample M shows an unusual BH-curve after the annealing. This can be explained by the growth of the nanocrystalline regions present in the sample, making the BH-curve a sum of the magnetisation of the amorphous phase and the newly formed crystals.
- Crystallisation of cobalt-based alloys completely destroys the magnetic properties of the material. As mentioned in [40], this must be caused by the crystallisation of the undesired boride-phases after the thermal treatment. The HT-XRD analyses indeed showed that sample V presented Fe_2B and M $\text{Co}_{21}\text{Mo}_2\text{B}_6$ after the annealing treatment.

Table 5.3 shows a comparison of the parameter values before and after annealing.

Table 5.3 – Comparison of parameters before and after annealing.

Sample	$\frac{\mu_{max} \text{ before}}{\mu_{max} \text{ after}}$	$\frac{H_c \text{ before}}{H_c \text{ after}}$	$\frac{B_r \text{ before}}{B_r \text{ after}}$	$\frac{BN \text{ before}}{BN \text{ after}}$
F-C1	$\frac{1321}{1816}$	$\frac{18.4}{18.8}$	$\frac{0.24}{0.26}$	$\frac{0.13}{0.41}$
F-C2	$\frac{1038}{1797}$	$\frac{18.4}{18.8}$	$\frac{0.24}{0.26}$	$\frac{0.13}{0.26}$
F-S	$\frac{1297}{11259}$	$\frac{14.4}{6.9}$	$\frac{0.16}{0.4}$	$\frac{0.13}{0.35}$
F-X1	$\frac{1346}{150971}$	$\frac{21.8}{3.4}$	$\frac{0.26}{0.55}$	$\frac{0.13}{0.27}$
F-X2	$\frac{1346}{151399}$	$\frac{21.8}{3.4}$	$\frac{0.26}{0.55}$	$\frac{0.13}{0.27}$
V-C	$\frac{178896}{163240}$	$\frac{6.3}{3.8}$	$\frac{0.56}{0.52}$	$\frac{0.41}{0.58}$
V-S	$\frac{182826}{381526}$	$\frac{6.3}{0.8}$	$\frac{0.56}{0.43}$	$\frac{0.41}{0.51}$
V-X1	$\frac{102657}{585}$	$\frac{6.3}{-}$	$\frac{0.56}{-}$	$\frac{0.41}{-}$
V-X2	$\frac{102657}{466}$	$\frac{6.3}{-}$	$\frac{0.56}{-}$	$\frac{0.41}{-}$
M-C	$\frac{251106}{9776}$	$\frac{7.6}{15.6}$	$\frac{0.67}{0.59}$	$\frac{0.33}{0.36}$
M-S	$\frac{250927}{2049}$	$\frac{7.6}{6.8}$	$\frac{0.67}{0.12}$	$\frac{0.33}{0.37}$
M-X	$\frac{247488}{527}$	$\frac{7.6}{-}$	$\frac{0.67}{-}$	$\frac{0.33}{-}$

6 Conclusions and outlook

6.1 Conclusions

The main objective of the thesis, which was to build test cores and anneal them from previously selected amorphous iron-based and cobalt-based materials, was achieved. This was done after identifying the key parameters of the materials for this application, contacting suppliers and studying the available materials to find the most suitable ones looking at their as-cast properties. The materials were then characterised to find the most suitable parameters for their thermal treatment as well as to establish which of them would be good candidates to continue the study. This characterisation also allowed one to determine what causes the changes to the properties before and after the thermal treatment. All available materials were wound into small sample cores with an outer diameter of 40 mm to measure the properties of cores. After this, three alloys were selected: the amorphous iron-based alloy Finemet FT-3 from Metglas with composition $\text{Fe}_{79.6}\text{Si}_{16.1}\text{Nb}_3\text{Cu}_1\text{Co}_{0.1}$ (named sample F), the Vacuumschmelze amorphous cobalt-based Vitrovac 6025 G40 alloy with composition $\text{Co}_{67.6}\text{Si}_{16}\text{B}_{10.7}\text{Fe}_{4.2}\text{Mo}_{1.5}$ (named V) and the Metglas amorphous cobalt-based alloy 2705 M with composition $\text{Co}_{68.7}\text{Si}_{12}\text{B}_{11.7}\text{Fe}_{4.6}\text{Mo}_{1.5}\text{Ni}_{1.4}$ (named M). Both cores and ribbons of the selected materials were annealed at different temperatures and durations to study the effect of the treatment in both. Measurements of the samples were taken after the thermal treatment and compared to the results of the as-cast materials to see the effects of the annealing.

6.1.1 Iron-based alloys

All the iron-based alloy compositions were studied by EMPA, and were shown to have a composition of $\text{Fe}_{73.5}\text{Cu}_1\text{Nb}_3\text{Si}_{13.5}\text{B}_9$, similar to the well known Finemet alloy. Qinhuangdao Yanqin Nano Science & Technology iron-based amorphous alloy (named C1) and alloy F also showed as well traces of cobalt in their composition, while Qinhuangdao Yanqin Nano Science & Technology iron-based nanocrystalline alloy (named C6) lacked

niobium and sample F lacked boron. The composition analysis of the samples is key to facilitate the remaining sample characterisation. The phase identifications of crystalline regions in the sample is simplified if the sample's composition is characterised confidently.

The crystallinity studies were done at room temperature on as-cast samples and gave differing results. All of them showed that, with the exception of the nanocrystalline iron-based alloy from Magnetec (MA), the alloys present very small crystallites (about 1.5 nm) and are mainly amorphous. Sample MA, as expected, presented bigger crystalline regions of 14.3 nm embedded in an amorphous matrix when measured by HE-XRD. Conventional XRD determined all crystalline phases to be bcc (α -iron). HE-XRD concluded the same for samples C1 and C6, but determined that for the nanocrystalline sample, MA, the crystalline composition was $\text{Fe}_{75}\text{CuNb}_{3.3}\text{Si}_{16.7}\text{B}_7$. It was not possible to verify this result by conventional XRD nor HT-XRD as the sample was too brittle to be analysed. Structure refinement of this crystalline structure determined that the structure is compatible with a structure type Fe_3Si : a cubic structure with a space group type Fm-3m and cell parameter $a = 5.66 \text{ \AA}$. TEM, on the other hand, pointed towards a bcc $\text{Fe}_{0.91}\text{Si}_{0.09}$ structure in all samples, which is known to be one of the possible final phases after the crystallisation mechanism of Finemet materials [41]. This means that there are already small clusters in the sample that correspond to the composition of the final nanocrystals that would be found in the material after crystallisation.

Phase transformation analysis measured by DSC determined that all samples had two crystallisation peaks. The temperature difference between them is very important as a greater difference makes the second crystallisation temperature (T_{x2}) less likely to be reached when crystallising the samples over the first one (T_x). Indeed, the HT-XRD analysis of sample C6 (the only sample analysed over T_{x2}) indicates the crystallisation of Fe_2B , which is known to degrade the magnetic properties of these materials. The same technique revealed that samples C1 and F crystallise into cubic Fe_3Si and sample C6 into cubic $\text{Fe}_{1.9}\text{Si}_{0.1}$, which correspond well to the expected phases described in literature. The lowest difference between crystallisation peaks of the amorphous materials is 42.2°C in sample C6 and the maximum 210°C in sample F. Special care should be taken during heating when crystallising to ensure that the samples do not reach the second crystallisation temperature. All iron-based crystallisation temperatures are below 550°C , which can easily be achieved by industrial ovens.

The maximum relative permeabilities were measured on the 40 mm sample cores. The amorphous iron-based materials (C1, C6 and F) show very low values, the highest one being 3057 for sample C6. It was seen that the core production step is critical, with differences in permeability of up to 30 % caused by manipulation and therefore induced stresses. For the intended application, change of permeability with frequency is one of the most crucial core parameters. Materials C1 and F present plateaus in their permeability vs frequency behaviour as opposed to sample C6, where the permeability decreases quickly with the increase in frequency.

The BH-curve is another key factor influencing the choice of material for the application in beam instrumentation. Besides the magnetic characteristics associated with the curve (remanence, coercivity and shape), reproducibility is also important for accurate pairing of two identical cores if required by the specific application. In the course of laboratory measurements, a new improved setup for BH-curve measurements was developed. Most importantly, the analogue integrators of the original setup were replaced by digital integration conducted off-line on the raw data. Furthermore, the cabling and individual components of the setup were also improved. The iron-based cores presented high coercivities over 14 A m^{-1} , with a maximum of 19.8 A m^{-1} in sample F. Typically, high losses are not desirable for materials used in transformer cores, as they may lead to damage due to material heating. Temperature affects the performance of the materials and should always be kept lower than their recommended service temperature, which varies for each alloy. Losses can be decreased by using insulation between the ribbon layers and therefore a material with interesting properties but relatively high losses could be considered as a suitable candidate if the insulation option can be implemented during the core fabrication process. The remanence of the material should not be very high in case the core needs demagnetisation during operation. Remanence for iron-based alloys vary from 0.25 T (for F) to 0.7 T (for C6).

The Curie temperature (T_C) was determined by several methods that presented a good agreement (TGA, Kappabridge and VSM). T_C is an important reference point if the material is to be thermally treated in a magnetic field to induce anisotropy. This is done just below T_C . In order to ensure that during this process the microstructure of the sample is not altered, T_C should be well below the crystallisation temperature. In the case of the iron-based alloys, this difference is more than enough, the smallest one being 91°C for sample C6 and the largest one, 182°C for sample C1. All of the samples presented thermal hysteresis caused by the magnetocaloric effect of the samples.

VSM and AGM measurements were done on the samples and both yielded the same results. All samples presented curves with no coercivity nor remanence. The highest saturation was observed in sample C6 (2.04 T), followed by C1 with 1.53 T and MA with 0.79 T. These measurements only take into account a very small fraction of the material and do not represent the final BH-curve of an actual core. These measurements are therefore useful to study the intrinsic magnetic behaviour of the alloy, but they are not indicative of how it will behave when wound into a large core.

A first test with TEM was done to observe the magnetic domains in sample MA. However, the sample preparation to make it transparent to electrons as well as the reduced visible area that the technique gives, makes TEM an unsuitable technique for this particular application. MFM was also tested for this purpose, but the topography of the samples made it very difficult to observe domain without introducing considerable stresses by holding down the sample. Magnetic domains observation of the whole sample was successfully achieved by Magneto-Optical Kerr Effect (MOKE) measurements. Domain

observation is important to understand the magnetisation effects that appear in the BH-curve of the sample and magnetic (Barkhausen) noise. The three samples measured (C1, C6 and F) presented patches of small domains mixed with larger, longer domains up to a hundred micrometres wide. The magnetisation curve of sample C1 is affected by the stresses present in the sample, increasing its coercivity. C6 shows an even bigger effect of stress on magnetisation, while sample F shows almost no effect. This fact should be taken into account, as during the winding process stresses are introduced as the material is bent to form the core.

Barkhausen Noise (BN) is a parameter that is hypothesised to affect the absolute limit of sensitivity of DC Current Transformers. It is therefore an interesting parameter to measure and compare when making cores for this application. For the as-cast materials, the highest BN was seen in MA, which would be expected from the presence of the nanocrystals acting as possible pinning points during magnetisation. This gives a BN almost twice as large as the one of the amorphous materials. MA also shows a wider noise structure than the rest, which is not a desirable attribute for the intended application.

The thickness and densities of the samples were in range of the expected values, between 20 μm to 30 μm for thickness and $\approx 7.5 \text{ g cm}^{-3}$. Density is a parameter that should be taken into account when calculating the packing factor of the core in order to obtain the effective area, which will have an influence in the calculation of the BH-curve results.

6.1.2 Cobalt-based alloys

The composition of cobalt-based alloys was also determined by EMPA. All of them have a $(\text{CoFe})_{70-90}(\text{SiB})_{10-30}$ base with additions of molybdenum and nickel: sample V presents molybdenum, amorphous cobalt-based alloy from Nanoamor (named N) presents nickel and sample M presents both elements. This composition is typical of cobalt-based amorphous alloys, with boron and silicon to stabilise the amorphous phase and at least one transition metal to help with the Glass Forming Ability and to inhibit diffusion.

The crystallinity studies were done at room temperature on as-cast samples. Conventional XRD showed the samples are mainly amorphous with small bcc (α -iron) crystallites. HE-XRD identified the crystallites present in the sample as a mix of pure hexagonal cobalt (space group $P6_3/mmc$, with $a \approx 2.55 \text{ \AA}$ and $c \approx 4.73 \text{ \AA}$) and $\text{Co}_5\text{Si}_2\text{B}$ crystallites (with a space group $I4/mcm$, $a \approx 8.5 \text{ \AA}$ and $c \approx 4.0 \text{ \AA}$) in a 30:70 ratio for the three samples. TEM confirmed the presence of the pure cobalt crystallites but showed that Co_2Si crystallites were a better match for the secondary phase present in samples V and M, while sample N presented only the cobalt structure.

Phase transformation analyses measured by DSC determined that all samples had two crystallisation peaks. HT-XRD analysis of sample V gave a complex Diffraction Pattern where several cobalt silicides and Fe_2B were found. Samples N and M both showed Co_2Si

crystallites and sample M also presented $\text{Co}_{21}\text{Mo}_2\text{B}_6$ crystals at a higher crystallisation temperature over 600°C . Samples V and M present very similar crystallisation temperature onsets at about 550°C and 600°C , while alloy M has a first crystallisation with two peaks (529°C and 554°C) and a third one with onset at 538°C . Cobalt-based alloys and iron-based alloys therefore have a similar first crystallisation temperature, making them suitable for crystallisation treatments. The difference between the first and second crystallisation peaks is lower than found in iron-based materials, with sample M having only a 25°C difference between the two peaks.

Cobalt-based materials have a much higher permeability than iron-based materials with even that of sample N, 158 110, over 50 times the maximum value of that for iron-based. The highest permeability is found in sample M, 250 802. Unlike the iron-based alloys, cobalt-based do not present any plateaus and permeability decreases with the increase in frequency, with sample V presenting the fastest decrease. Due to their very high initial permeability, the three materials still have permeabilities between 1×10^3 and 1×10^4 at 10 kHz.

Compared to iron-based alloys, cobalt-based alloys have a smaller coercivity, the maximum being 8.91 A m^{-1} for sample M, compared to the minimum of 15.05 A m^{-1} of sample C1. Remanence is comparable, with sample N showing the minimum, 0.43 T and M the maximum, 0.69 T. The small coercivity of sample N (4.44 A m^{-1}) is within the desired range for transformer cores.

The Curie temperature (T_C) was measured by TGA and Kappabridge. Both methods are in good agreement and with the theoretical temperatures found in literature. Samples V and N have a Curie temperature of about 225°C and sample M shows a higher one at 360°C . The differences between T_C and the first crystallisation temperature for these alloys is quite high, 151°C for sample M, and 319°C for samples V and N, giving more than enough margin to avoid unwanted crystallisation during thermal treatment.

VSM and AGM measurements also gave the same results for cobalt-based. All samples presented zero-coercivity magnetisation curves with small remanence. The highest saturation was observed in sample M (0.83 T), very far away from the iron-based maximum of 2 T for sample C6. Sample V has the lowest saturation at 0.58 T.

As opposed to iron-based alloys, cobalt-based alloys show almost identical domain configuration. The three samples show high anisotropy with long domains in the longitudinal direction of the ribbon. Only sample N presents some discontinuity in the surface characteristic of the sample. Sample N is least affected by stresses induced in the sample, while V and M suffer to a greater extent, increasing their losses considerably with applied stress. This effect of stress can be compared to the one sustained by the iron-based sample C6, as the other two (C1 and F) showed a similar behaviour to sample N.

Regarding the BN, cobalt-based samples present a flat-top shaped response, different to the peak-shaped response seen for iron-based materials. This is caused by the size and shape of the domains, as in the cobalt-based materials, long longitudinal domains will grow encountering pinning points until they reach saturation. The magnetisation process will have almost no rotation of domains. This gives the characteristic shape to the BN. Iron-based alloys, presenting a mixture of small and big domains, can have less noise as some of the magnetisation of the sample occurs by domain rotation.

6.1.3 Thermally treated cores

Test cores were produced with iron-based material F and cobalt-based materials V and M as their as-cast properties seemed most-suitable for building transformer cores. Primarily, permeability and losses were taken into account to make this choice. Despite its far from ideal as-cast properties in its amorphous state, material F was also chosen as nanocrystalline iron-based alloys have excellent soft magnetic properties. Permeability, BH-curve and BN were measured after the treatments to compare to the as-cast properties.

Three types of thermal treatments were performed on all samples: below T_C , between T_C and T_x , and over T_x . All treatments were done under vacuum with a heating rate of $10\text{ }^{\circ}\text{C min}^{-1}$.

F alloy

Two thermal treatments were done below T_C ($319\text{ }^{\circ}\text{C}$) to the F alloy, one with a total heating time of 1.8 h and the other with a heating time of 2.3 h followed by an isothermal plateau of 1 h. Despite the differences in the cores due to the induced stresses caused by manipulation during the core fabrication, after the thermal treatment both cores were practically identical. The final, maximum permeability between both of them differed by less than 1 %, but the increase was not very big, from about 1000 in its as-cast state to under 1750 after the annealing. The comparison of the BH-curves showed little change from the as-cast state, except for a slight increase in the slope of the saturated region of the BH-curve. This indicates that the magnetic domains of the sample have not changed significantly during the thermal treatment. The sample annealed for a longer time presented lower BN than the other sample, but both showed higher noise (by a factor of almost 2 and 4 respectively) than the sample before annealing. This could be due to the increase of pinning sites in the material, the effect of stress-relief and changes in the domain size and distribution of the sample. In order to exactly see the contributions of both factors to the changes, MOKE analysis and XRD should be done on the annealed samples.

The sample annealed between T_C and T_x ($508\text{ }^{\circ}\text{C}$) showed more changes, due to the higher temperature of the treatment ($403\text{ }^{\circ}\text{C}$). Permeability showed an increase of 768 %, and

the BH curve became more elongated, increasing the remanence by 150 % and decreasing the coercivity by 52.2 %. BN after annealing had the same shape as the as-cast sample, but the noise increased by more than a factor of 2. It is clear that a higher temperature has a direct effect on the magnetisation characteristics. If stress-relief was occurring in the previous case at a lower temperature, it is also happening, but in greater measure, at higher temperatures. During this treatment, the BH-curve is clearly changing, suggesting that there is a change in the magnetic domain distribution of the sample. This would also explain the changes in the BN.

Two tests were done over the crystallisation temperature, one with a total treatment time of 17.5 min and the other with a total heating time of 1.7 h which included a plateau of 32.5 min at 552 °C. Both samples showed an increase in permeability of over 11 110 %, with no differences between them. The BH-curves of the two annealed cores were very similar, becoming more elongated and narrower than the as-cast curves, with a decrease in coercivity of just over 80 % down to 3.5 A m^{-1} and an increase of remanence of 100 % up to 0.55 T. The BN is the only parameter that is clearly different for both samples. Although both of them present an increase in the noise level, the sample annealed for a shorter time has a higher and wider BN response. Taking into account the difference in the treatment times, this has to be due to the presence of small crystalline domains that would act as pinning points during magnetisation. A higher annealing time could yield larger crystalline areas, reducing these pinning points.

V alloy

Material V was annealed for a total of 2.2 h up to a maximum temperature of 169.6 °C, under its T_C of 222 °C. This gave a better permeability vs. frequency response, with the appearance of a plateau from 1 kHz up to 1 MHz. The BH-curve showed a decrease in coercivity of 39.3 %, with almost no changes in remanence nor saturation. BN has a similar response before and after annealing, with a width of 0.2 s, but the annealed ribbon shows a higher noise level. Further analysis of the domain configuration and the crystalline state of the sample is needed in order to conclude which exact mechanism is in play.

The sample annealed between T_C and T_x (546 °C) at an average temperature of 450.1 °C showed a different permeability curve, with a peak just over 100 Hz. This might be caused by resonances in the core and/or in the magnetic domains. Further study would be needed around this peak in order to determine its origin. This peak in permeability is 108.7 % higher than the as-cast value. The BH-curve becomes very narrow, showing a decrease in coercivity of 86.6 %, down to 0.84 A m^{-1} and a decrease in remanence of 23.2 %, making the annealed curve rounder. The BN shows a similar structure and noise level as the material annealed just under the Curie temperature.

Two test were done over T_x at different annealing times, 15 min and 30 min. Both samples showed no BH-curve and no BN after thermal treatment. The permeability was measurable but diminished to a maximum value of under 1000 that decreases quickly, reaching zero at about 1 kHz. The cause for the degradation in the magnetic properties is related to the crystalline phases and crystal size after the thermal treatment. The HT-XRD analysis showed that the sample presented a boride phase (Fe_2B) that could explain this effect. Further studies of the crystallised material should be done to fully understand this result.

M alloy

Alloy M was annealed below T_C (361°C) for 1.7 h at an average temperature of 319.9°C . Permeability decreased by 96.1 %, but showed a flatter frequency response with a plateau up to 10 MHz, low permeability of 100. The BH-curve showed a "constricted" shape typical of Perminvar alloys, that is caused by either the presence of domains at 90° and 180° or the fixing of the magnetic domains due to their induced local anisotropy. MOKE studies of the annealed samples would give the definite response for the causes of this effect.

The annealing between T_C and T_x (513°C) showed the same, but more pronounced effect in the permeability and BH-curve as the previous treatment. This is certainly due to the higher temperature. Again, further studies would be needed to determine the cause behind this change. Both samples, the one annealed under T_C and the one annealed between T_C and T_x have a similar BN comparable to the as-cast BN, but with higher noise values.

The material annealed above T_x showed the same behaviour as sample V, where no BH-curve nor BN could be measured and permeability was reduced to a minimum. HT-XRD studies in this case also showed the presence of another boride, $\text{Co}_{21}\text{Mo}_2\text{B}_6$ that should be further studied by XRD and MOKE to see if it is the cause for this result.

Comparison of cobalt based and iron based alloys

Comparing iron-based alloys and cobalt-based alloys, it is clear that they are very different in their as-cast properties. Iron-based materials are not suitable for any application discussed in this thesis due to their very low permeability and high losses. On the other hand, cobalt-based alloys show excellent as-cast properties and could be used in this form to make good quality transformer cores. Once thermally treated, the iron-based alloys studied transform into better quality materials. The nanocrystallisation of these alloys gives excellent results, with increase in permeability, remanence and saturation and a decrease in losses. Cobalt-based alloys behave differently. Annealing over the crystallisation temperature renders the material unusable, with a very low final

permeability. Sample V, when annealed under T_x shows an increase in permeability and a decrease in coercivity. Sample M however, shows a "Perminvar-like"-loop when annealed under T_x , making it unusable for this specific application.

Another important factor to take into account is the BN. All of the thermal treatments increase the noise in the materials. If the magnetic noise is finally determined to be the limiting cause of the sensitivity for the beam monitors, then the as-cast materials will be the most interesting to use in this case.

6.1.4 Proposed materials for transformer cores

Based on the results presented in this thesis, one can suggest that the best material to build DCCT cores would be the nanocrystallised Finemet FT-3 material (F). It shows a high permeability up to 10 kHz and a low coercivity of about 3.5 A m^{-1} , with a rounded BH-curve and saturation over 1 T.

Regarding FBCTs, the cores need a very flat BH-curve with high permeability and no coercivity. From all the materials presented, Vacuumschmelze's cobalt-based Vitrovac 6025 G40 (V) is the material that would be the most suitable. It has the lowest coercivity (0.84 A m^{-1}) and saturation of 0.5 T. However, the perfect material would need magnetic thermal annealing to create a high magnetic anisotropy in the material to achieve a flat curve.

6.2 Outlook

The topic of soft magnetic materials for beam instrumentation is very specific and the application requires some particular characteristics. Moreover, in order to reach the ultimate performance, different instruments pose different requirements the magnetic materials used. Further research along the lines of this thesis would be required for future in-house development of instruments.

Current problems related to the specificity of the CERN's requirements and the core-fabrication industry include their reluctance to manufacture large cores (of external diameters of 200 mm or more) and high prices, which are a limiting factor when trying to conduct R&D in this field. Ideally, a wide range of different cores with different magnetic properties would be bought for testing the influence of these properties on the instrument's performance, but this is currently not feasible.

Another factor which is very specific to a particle accelerator environment is the presence of ionising radiation. The cores installed in beam instrumentation devices are constantly exposed to radiation which can lead to activation or material damage. The inevitable degradation of a core's magnetic properties due to radiation may eventually render

the instrument dysfunctional. This scenario would normally entail replacement of the magnetic cores. Ideally, if a mechanism for manufacturing cores with predefined parameters is mastered, obtaining replacement cores would be a relatively easy procedure.

The in-house fabrication of magnetic cores is not an intricate process but it has some key aspects that should be carefully taken into account. Ribbons of soft magnetic materials are exceptionally sensitive to stresses, hence the handling and storing of the material should be done with great care. This is especially true when the material needs to be un-boxed, mounted and dismounted for core winding. Introduction of additional stresses during the core winding procedure might create a stress gradient between the core's innermost and outermost layers leading to a significant change of the magnetic properties. In order to minimise differences between manufactured cores, the winding mechanism must feature a ribbon tension control mechanism as well as a counter of wound ribbon layers. If insulation became necessary for a certain application, the first and technologically most accessible approach would be to introduce Kapton tape between the ribbon layers while winding the core. This tape should be as thin as possible to maintain the cross-section of the core without losing too much effective area and therefore decreasing the packing factor. Another solution would be to use a sol-gel that would become a ceramic during thermal treatment in the oven. The sol-gel should be carefully chosen not only to penetrate by capillarity between the ribbon layers, but also to ensure (if the treatment is going to be done under vacuum), that none of the components can damage any of the vacuum equipment connected to the oven.

Regarding the choice of materials, it is clear that the quality of the as-cast alloys has a great influence on the final properties of the cores. The cobalt based Metglas 2705 M (with composition $\text{Co}_{76.7}\text{Fe}_{4.9}\text{Si}_{14.9}\text{Mo}_{1.8}\text{Ni}_{1.7}$) and Vacuumschmelze 6025 G40 ($\text{Co}_{73.6}\text{Fe}_{4.4}\text{Si}_{20.1}\text{Mo}_{1.8}$) materials are the base of many of the industrial transformer cores used nowadays and show excellent magnetic properties as has been presented in the results of this thesis. However, if the kind of material needed is known, with the base properties defined for their transformation into cores (with low Curie temperature well below the crystallisation temperature for magnetic annealing for example), it is possible, as has been proven with the Nanoamor material (with composition $\text{Co}_{73.5}\text{Fe}_{5.5}\text{Si}_{19.3}\text{Ni}_{1.7}$), to buy a very similar material from other companies specifying these parameters. Smaller companies offer more flexibility in quantities for purchase, which also means that for producing test cores, less material needs to be purchased, lowering the costs.

With the work presented in this thesis, there is now a catalogue of materials to choose from for building magnetic cores. The most important steps for characterising potential new materials have been established, and the assessment of whether a new material could be a potential new candidate for building cores can be now done efficiently.

A Iron-based alloys results

A.1 Composition: XPS

Figure A.1 shows the surface analyses for sample C6 and F.

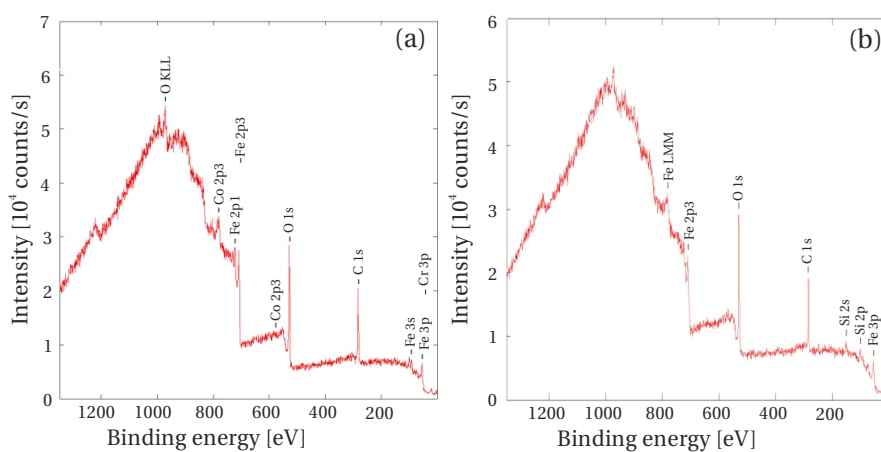
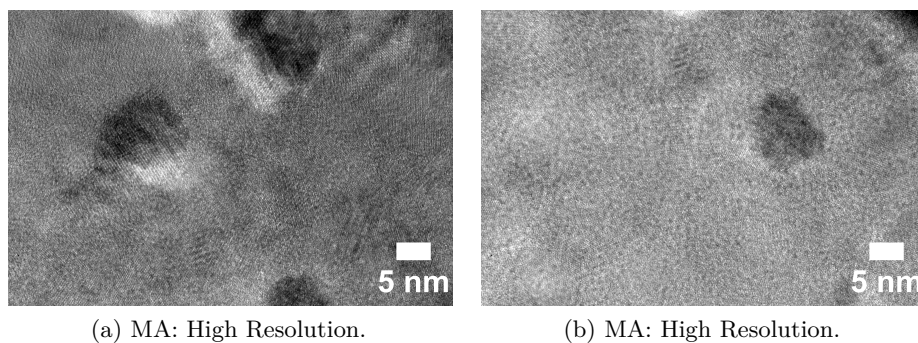


Figure A.1 – XPS surface results for samples C6 (a) and F (b).

A.2 Crystallinity: TEM of sample MA

Figure A.2 shows additional high resolution TEM images of sample MA.



(a) MA: High Resolution.

(b) MA: High Resolution.

Figure A.2 – High resolution TEM images for sample MA.

A.3 Phase transformation: DSC

PerkinElmer DSC 8000 results at $5^{\circ}\text{C min}^{-1}$

Table A.1 – Iron-based alloys results at $5^{\circ}\text{C min}^{-1}$

Sample	Onset [$^{\circ}\text{C}$]	Peak [$^{\circ}\text{C}$]	Area [J g^{-1}]
C1	507.77	525.45	69.70
C6	496.88	505.44	52.84
	538.04	543.96	76.53
F	507.04	527.71	71.10

PerkinElmer DSC 8000 results at $20^{\circ}\text{C min}^{-1}$

Table A.2 – Iron-based alloys results at $20^{\circ}\text{C min}^{-1}$

Sample	Onset [$^{\circ}\text{C}$]	Peak [$^{\circ}\text{C}$]	Area [J g^{-1}]
C1	521.29	543.71	75.73
C6	512.65	521.11	41.55
	557.36	563.43	67.98
F	525.08	544.42	57.20

PerkinElmer DSC 8000 results at $50^{\circ}\text{C min}^{-1}$

Table A.3 – Iron-based alloys results at $50^{\circ}\text{C min}^{-1}$

Sample	Onset [$^{\circ}\text{C}$]	Peak [$^{\circ}\text{C}$]	Area [J g^{-1}]
V	569.30	575.84	40.76
N	570.57	572.76	67.11
M	531.74	545.38	17.36
	580.25	585.73	32.99

A.4 Magnetic properties: Magnetic domain imaging

A.4.1 Sample C1

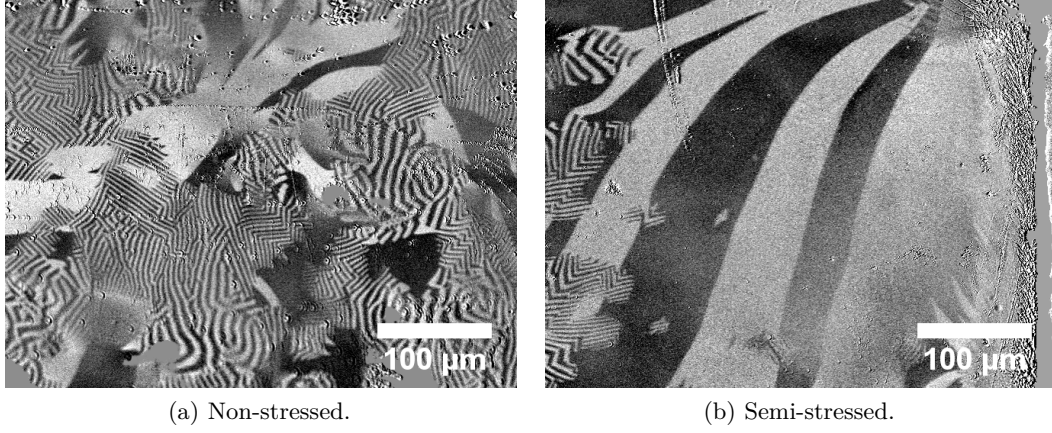


Figure A.3 – Magnetic domains of sample C1.

A.4.2 Sample C6

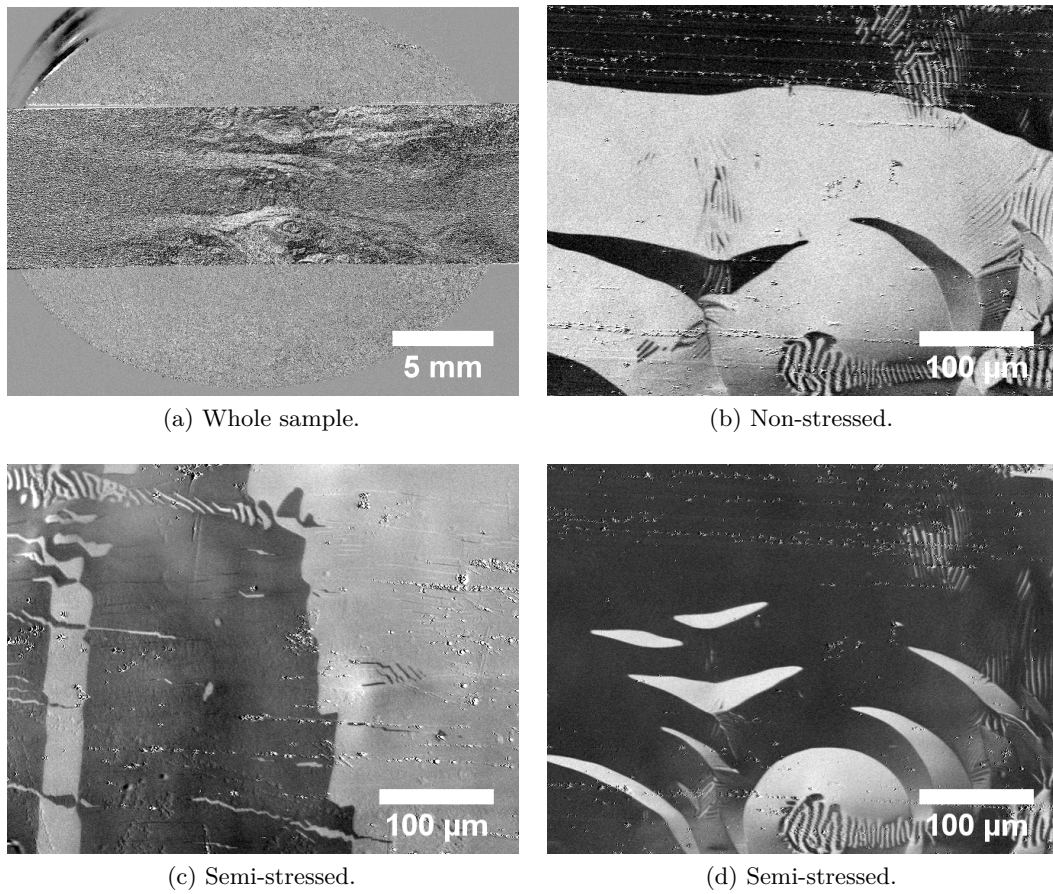
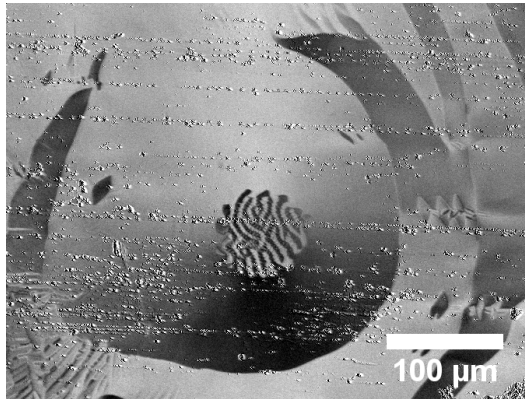


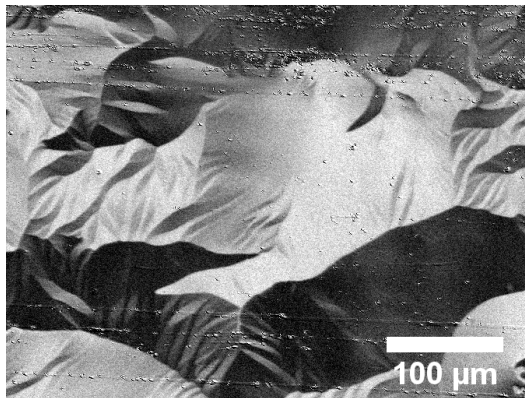
Figure A.4 – Magnetic domains of sample C6.



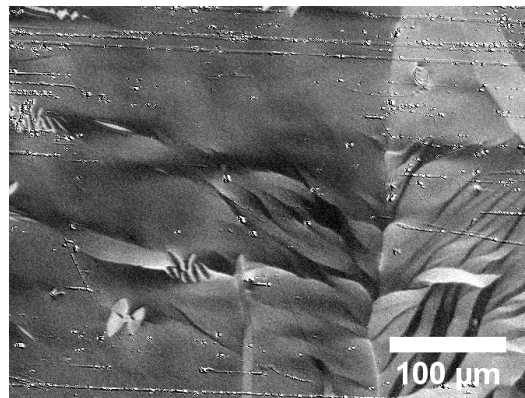
(a) Semi-stressed.



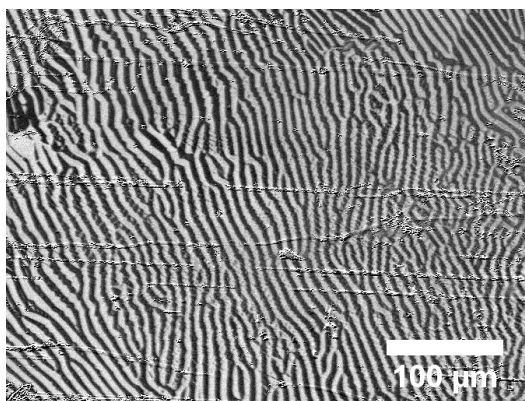
(b) Semi-stressed.



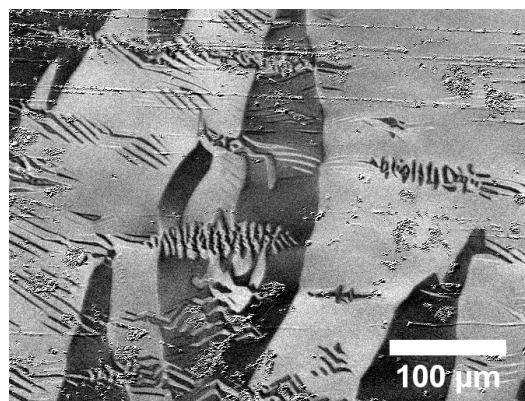
(c) Stressed.



(d) Stressed4.



(e) Stressed.



(f) Stressed.

Figure A.5 – Magnetic domains of sample C6.

A.4. Magnetic properties: Magnetic domain imaging

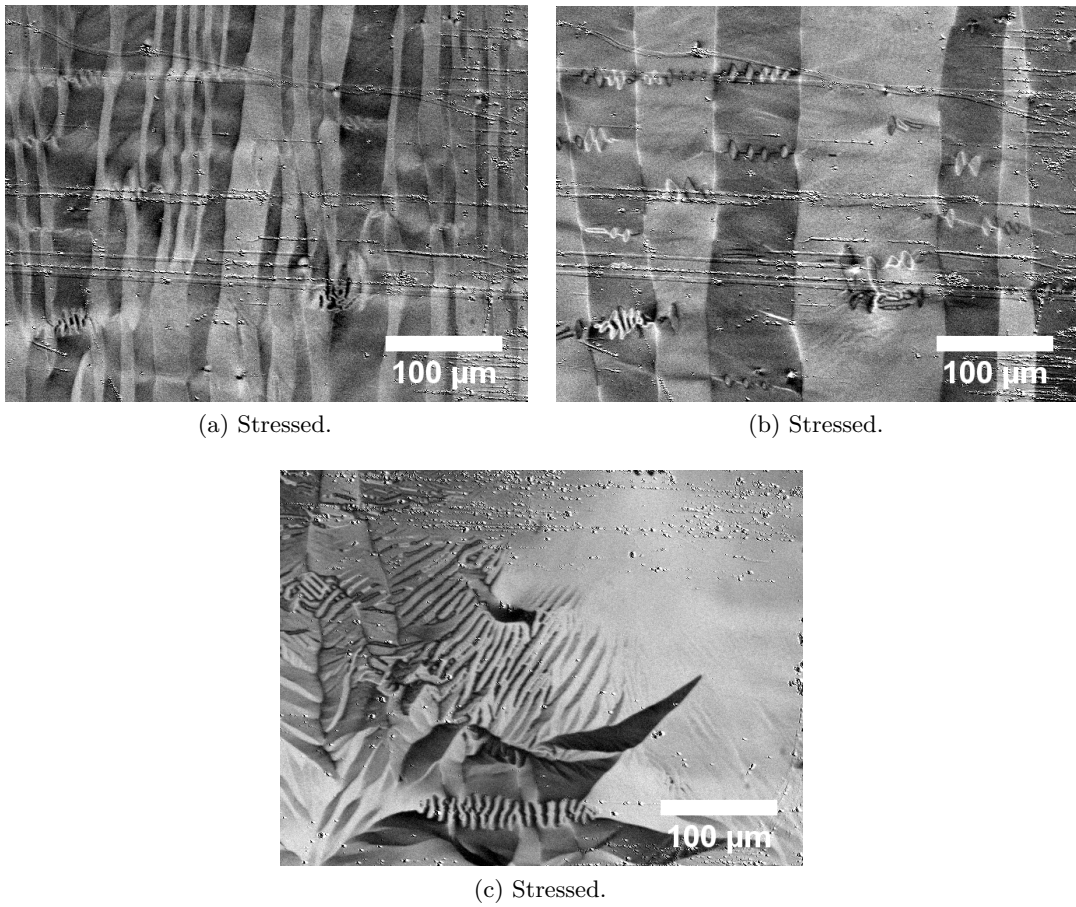


Figure A.6 – Magnetic domains of sample C6.

Sample F

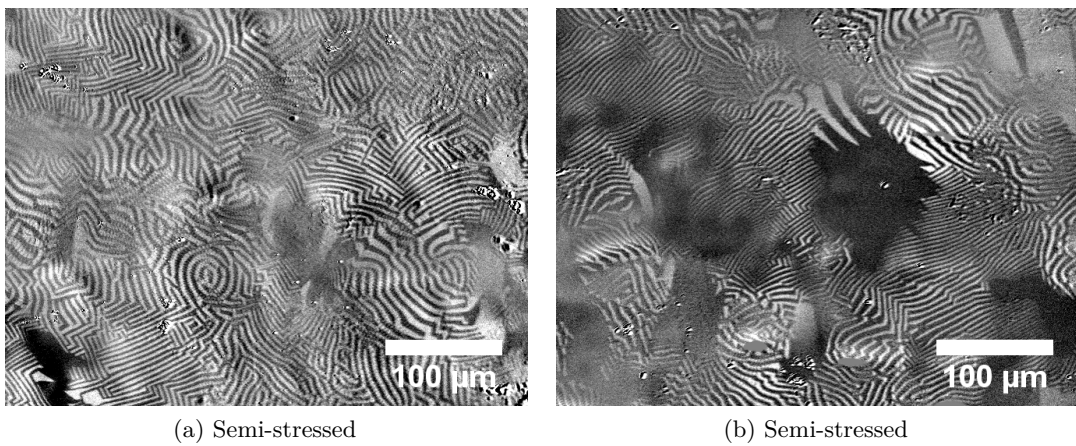


Figure A.7 – Magnetic domains of sample F.

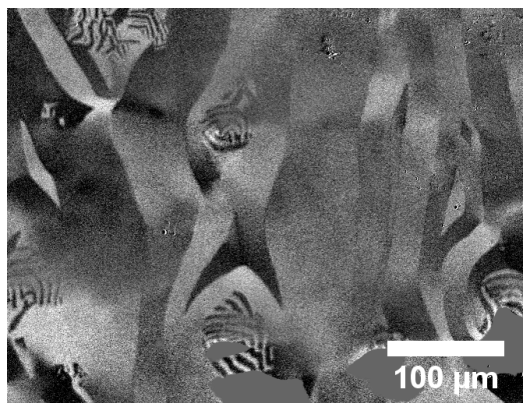


Figure A.8 – Magnetic domains of sample F in the stressed area.

B Cobalt-based alloy results

B.1 Composition: XPS

Figure B.1 shows the surface analyses for sample M.

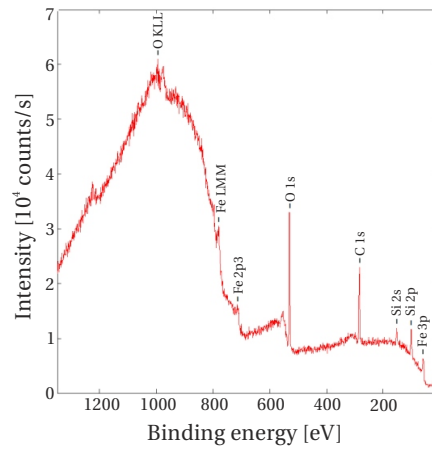


Figure B.1 – XPS surface results for sample M.

B.2 Crystallinity: HE-XRD

Figure B.2 shows the Diffraction Patterns (DP) of samples N and M.

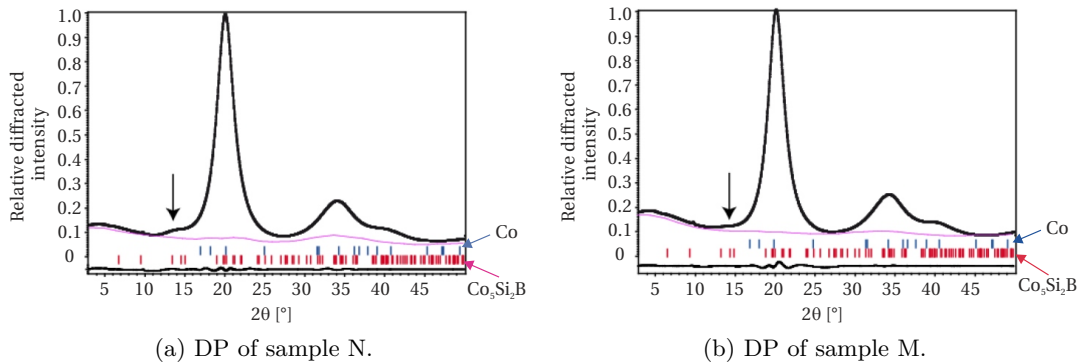


Figure B.2 – HE-XRD Diffraction Patterns of sample N (a) and sample M (b).

B.3 Phase transformation

B.3.1 DSC

PerkinElmer DSC results at $5^{\circ}\text{C min}^{-1}$

Table B.1 – Cobalt-based alloy results at $5^{\circ}\text{C min}^{-1}$

Sample	Onset [$^{\circ}\text{C}$]	Peak [$^{\circ}\text{C}$]	Area [J g^{-1}]
V	550.29	555.21	75.51
N	548.46	551.41	85.50
M	518.13	528.32	7.65
	547.38	552.37	43.33

PerkinElmer DSC results at $20^{\circ}\text{C min}^{-1}$

Table B.2 – Cobalt-based alloy results at $20^{\circ}\text{C min}^{-1}$

Sample	Onset [$^{\circ}\text{C}$]	Peak [$^{\circ}\text{C}$]	Area [J g^{-1}]
V	559.97	566.79	71.16
N	562.22	565.10	85.11
M	524.83	538.04	14.72
	566.92	572.23	43.97

PerkinElmer DSC results at $50^{\circ}\text{C min}^{-1}$

Table B.3 – Cobalt-based alloy results at $50^{\circ}\text{C min}^{-1}$

Sample	Onset [$^{\circ}\text{C}$]	Peak [$^{\circ}\text{C}$]	Area [J g^{-1}]
V	569.30	575.84	40.76
N	570.57	572.76	67.11
M	531.74	545.38	17.36
	580.25	585.73	32.99

B.3.2 TEM

Sample M

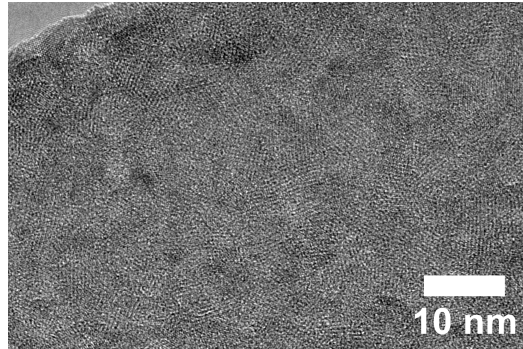
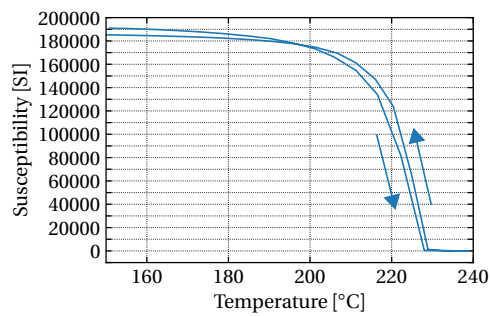


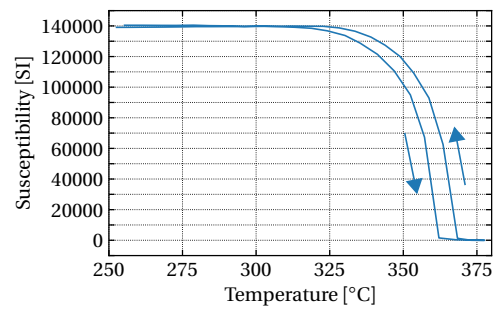
Figure B.3 – High-Resolution TEM of sample M

B.4 Magnetic properties

B.4.1 Curie Temperature: Kappabridge



(a) T_C measurement of V.



(b) T_C measurement of N.

B.4.2 Magnetic domain imaging: MOKE

Sample V

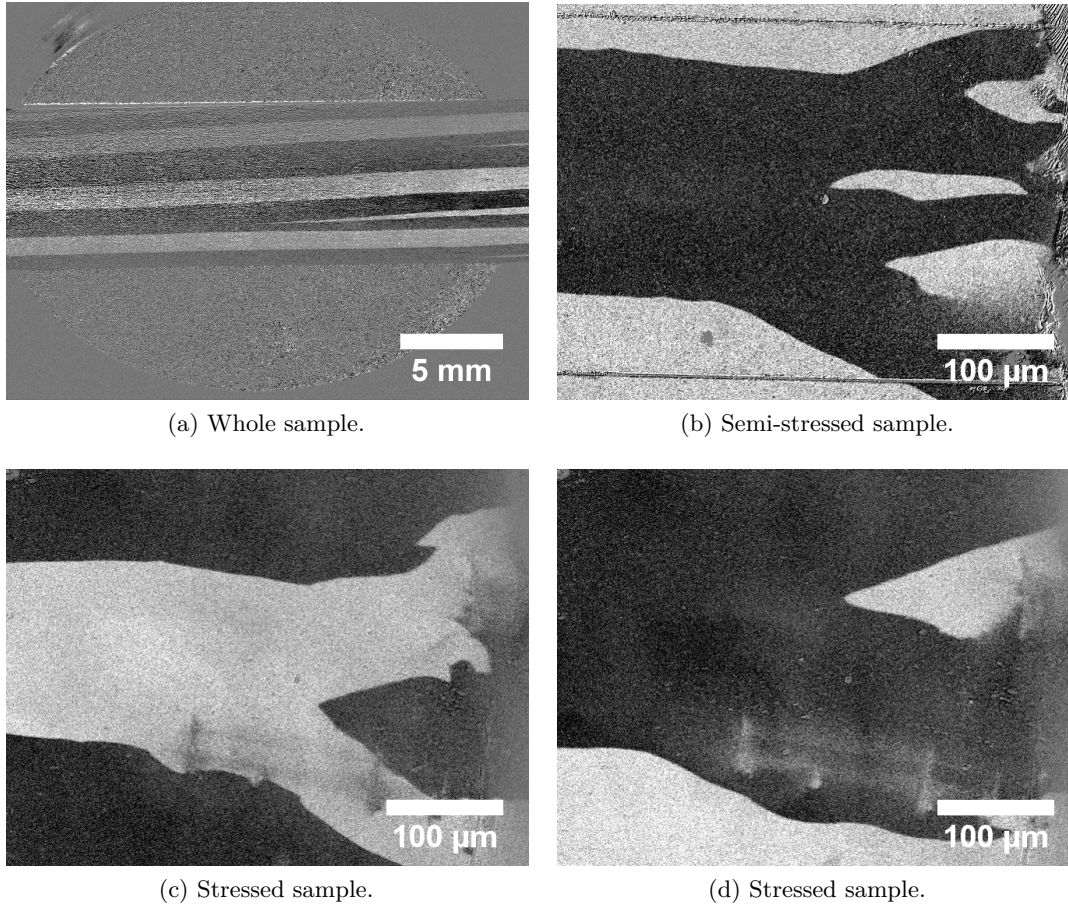


Figure B.4 – Magnetic domains of sample V.

Sample N

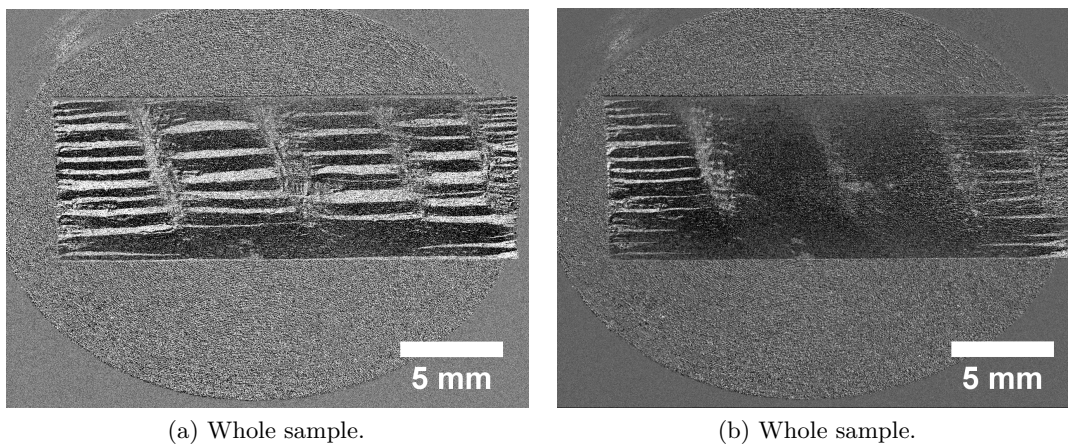


Figure B.5 – Magnetic domains of sample N.

C Magnetism basics [1], [2]

When looking at the relationship between magnetic field and magnetisation, the simplest example is a coil of N turns (commonly called solenoid), length L metres and a passing current of I amperes. The magnetic field produced will be:

$$H = \frac{N \cdot I}{L} \quad (\text{C.1})$$

The units of H are therefore A turn m^{-1} or just A m^{-1} . If this magnetic field is applied in vacuum, a magnetic induction (B) is created, as can be see in Figure C.1.

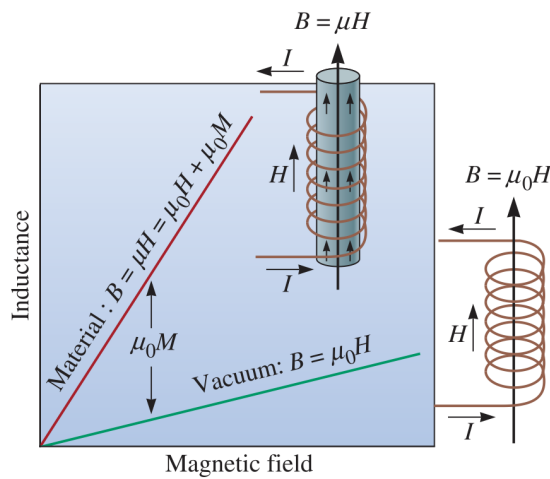


Figure C.1 – Relationship between magnetic field (H) and inductance (B) [1].

B is related to H by the magnetic permeability of vacuum constant (μ_0), which has a

Appendix C. Magnetism basics [1], [2]

value of $4\pi 10^{-7} \text{ Wb A}^{-1} \text{ m}^{-1}$ (also H m^{-1}):

$$B = \mu_0 \cdot H \quad (\text{C.2})$$

When a material is placed inside the coil, the magnetic induction is determined by how the material interacts with the field, which is determined by its permeability (μ). μ magnifies or decreases the magnetic field, so the total magnetic induction can be described by Eq. C.3:

$$B = \mu \cdot H \quad (\text{C.3})$$

We can rewrite this equation taking into account that this total magnetic induction is actually the sum of the effect of the applied magnetic field and the effect of the magnetic material:

$$B = \mu_0 \cdot H + \mu_0 \cdot M \quad (\text{C.4})$$

It should be taken into account that B , H and M are vectors, but as they are usually parallel, Eq. C.4 is written in its scalar form.

Magnetic susceptibility (χ) is defined as the ratio between the induced magnetisation (M) and the applied field (H). Since M and H both have units of A m^{-1} , susceptibility is dimensionless:

$$\chi = \frac{M}{H} \quad (\text{C.5})$$

Eq. C.5 shows that the susceptibility is also a measurement of the degree to which a material affects the magnetic field. Permeability is also an indication of this, and it is normally given as a relative value to vacuum:

$$\mu_r = \frac{\mu}{\mu_0} \quad (\text{C.6})$$

Susceptibility and permeability are therefore related, as Eq. C.7 shows:

$$\mu_r = 1 + \chi \quad (\text{C.7})$$

For ferromagnetic and ferrimagnetic materials, the term $\mu_0 M$ is much greater than $\mu_0 H$ and thus, for these materials, the magnetic induction is:

$$B \approx \mu_0 \cdot M \quad (\text{C.8})$$

However, sometimes both terms (induced magnetisation and magnetic induction) are used interchangeably, as the goal is normally to have a high value of both.

C.0.1 Types of magnetic materials

Taking the previous section into account, one can classify the different types of magnetic behaviour into the following categories:

- diamagnetic: where the material has "negative" magnetism, i.e. the induced magnetisation (M) is in the opposite direction to the applied field H . Copper, silver, silicon and gold are diamagnetic at room temperature. Diamagnetic substances have a small and negative χ and μ just below one.
- antiferromagnetic: these materials have a zero net magnetization, as dipoles inside the material align in an anti-parallel manner and cancel each other. They have very small positive χ at all temperatures, but χ varies with it. Most (but not all) are ionic compounds like oxides, sulphides, chlorides, etc.
- paramagnetic: where very large magnetic fields are required to create induced magnetisation. They have a small positive χ and μ just above one. Aluminium and titanium are paramagnetic at room temperature.
- ferromagnetic: small magnetic fields can induce large magnetisation. The susceptibility depends on the intensity of the applied field. Above the Curie temperature, ferromagnetic materials become paramagnetic. Some examples include iron, nickel, cobalt and gadolinium.
- ferrimagnetism: in the same way as ferromagnets, these can be largely magnetised by application of small magnetic fields. The difference with ferromagnets lies in the mechanism for this magnetisation. In ceramic materials, different ions have different

magnetic moments that in presence of a magnetic field, some align with the field, while some remain antiparallel. However, there is a net magnetization due to different strength or number of these ions. Examples include some ferrites (double oxides of iron and another metal)

- superparamagnetism: when the grain size of ferromagnetic or ferrimagnetic material is below a critical size, they behave as paramagnetic. The magnetic dipole inside the particle becomes comparable to the thermal energy and as a result, energy fluctuations can become anisotropy forces and spontaneously reverse the magnetisation direction randomly behaving like if it did not have a net magnetic moment.

List of Symbols

A Effective cross-sectional area [m^2].

B_s Saturation induction [T].

B Magnetic induction [T].

D Grain size [mm].

H_{ext} External magnetic field [A m^{-1}].

H_c Coercivity [A m^{-1}].

H Applied magnetic field [A m^{-1}].

I' Current of primary winding [A].

L_{eff} Inductance of toroidal coil [H].

N_1 Number of turns on primary winding.

N Number of turns.

R_{eff} Equivalent resistance of magnetic core including wire resistance [Ω].

R_w Resistance of wire [Ω].

T_{C2} Second Curie Temperature [$^{\circ}\text{C}$].

T_C Curie Temperature [$^{\circ}\text{C}$].

T_{x2} Second crystallization temperature [$^{\circ}\text{C}$].

T_x Crystallization temperature [$^{\circ}\text{C}$].

V_{sec} Voltage across secondary winding [V].

β width at the Full Width Half Maximum (FWHM) [rad].

β Bragg diffraction angle [rad] or [$^{\circ}$].

List of Symbols

κ Crystallite shape factor.

λ X-ray wavelength [nm].

μ'' Imaginary part component of relative complex permeability.

μ' Real part component of relative complex permeability.

μ_0 Permeability of free space.

μ Relative complex permeability.

ω Angular frequency.

τ Mean size of crystals [nm].

l Average magnetic path length of toroidal core [m].

Acronyms

AC Alternating Current.

AD Antiproton Decelerator.

AGM Alternating Gradient Magnetometry.

ALICE A Large Ion Collider Experiment.

ATLAS A Toroidal LHC ApparatuS.

BCT Beam Current Transformer.

BN Barkhausen Noise.

CERN European Organization for Nuclear Research.

CMS Compact Muon Solenoid.

COD Crystallographic Open Database.

DC Direct Current.

DCCT DC Current Transformer.

DP Diffraction Pattern.

DSC Differential Scanning Calorimetry.

EMPA Electron Micro Probe Analyser.

FWHM Full Width at Half Maximum.

GFA Glass-Forming Ability.

HE-XRD High Energy X-ray Diffraction.

HT-XRD High Temperature in-situ XRD.

Acronyms

ICP-OES Inductive Coupled Plasma - Optical Emission Spectrometry.

ICT Integrating Current Transformer.

ISOLDE Online Isotope Mass Separator.

ISR Intersecting Storage Rings.

LHC Large Hadron Collider.

LHCb Large Hadron Collider beauty.

MFM Magnetic Force Microscopy.

MOKE Magneto-Optical Kerr Effect.

nTOF neutron Time-Of-Flight.

PCB Printed Circuit Board.

PS Proton Synchrotron.

SEM-EDX Scanning Electron Microscopy- Energy-Dispersive X-ray spectroscopy.

STM Scanning Transmission Microscopy.

TEM Transmission Electron Microscopy.

TGA Thermogravimetric Analysis.

TIE Transport-of-Intensity Equation.

VSM Vibrating Sample Magnetometry.

WCT Wall Current Transformer.

XPS X-ray Photoelectron Spectroscopy.

XRD X-ray Diffraction.

Bibliography

- [1] D. R. Askeland, P. P. Fulay, and W. J. Wright, *The Science and Engineering of Materials*. Stamford: Cengage Learning, 6th ed., 2010.
- [2] B. D. Cullity and C. D. Graham, *Introduction to Magnetic Materials*. Hoboken, New Jersey: John Wiley & Sons, Inc., second ed., 2008.
- [3] E. Mobs, “The CERN accelerator complex,” 2016.
- [4] P. Odier, “DCCT technology review,” in *Proceedings of Workshop on “DC Current Transformers and Beam-Lifetime Evaluations”* (A.-J. Peters, H.-J. Schmickler, and K. Wittenburg, eds.), (Lyon), pp. 3–5, 2004.
- [5] B. Wolf, ed., *Handbook of Ion Sources*. CRC Press, 1995.
- [6] G. Gelato, “Beam Transformers,” in *Beam Instrumentation* (J. Bosser, ed.), ch. 7, p. 293, Geneva: CERN, second ed., 1994.
- [7] G. Herzer, “Nanocrystalline soft magnetic alloys,” in *Handbook of Magnetic Materials* (K. Buschow, ed.), vol. 10, ch. 3, pp. 415–462, Hanau: VACUUMSCHMELZE GmbH & Co., 1997.
- [8] R. Hilzinger and W. Roderwald, *Magnetic Materials*. Hanau: VACUUMSCHMELZE GmbH & Co., 2013.
- [9] M. A. Willard and V. G. Harris, “Soft magnetic materials: Nanocrystalline alloys from amorphous precursors,” *JOM*, vol. 54, pp. 44–46, mar 2002.
- [10] Metglas, “Metglas 2826MB Iron-Nickel Base Alloy Technical Bulletin,” 2011.
- [11] A. Hubert and R. Schaefer, eds., *Magnetic Domains: The Analysis of Magnetic Microstructures*. Berlin, Heidelberg: Springer Berlin Heidelberg, 1998.
- [12] C. K. Kim, I. H. Lee, Y. C. Chung, and R. C. O’Handley, “Design of amorphous magnetic materials for high frequency sensors based upon permalloy characteristics,” *Materials Science and Engineering B: Solid-State Materials for Advanced Technology*, vol. B76, no. 3, pp. 211–216, 2000.

Bibliography

- [13] R. Vajtai, ed., *Springer Handbook of Nanomaterials*. Berlin, Heidelberg: Springer Berlin Heidelberg, 2013.
- [14] R. C. Webber, “Tutorial on Beam Current Monitoring,” 2000.
- [15] P. Odier, D. Belohrad, J.-J. Gras, and M. Ludwig, “Operational Experience and Improvements of the LHC Beam Current Transformers,” in *Proceedings of DIPAC11*, (Hamburg, Germany), pp. 467–469, 2011.
- [16] J. Sharp, “The Induction Type Beam Monitor for the PS,” 1962.
- [17] I. K. Harvey, “A precise low temperature dc ratio transformer,” *Review of Scientific Instruments*, vol. 43, no. 11, pp. 1626–1629, 1972.
- [18] R. Geithner, R. Neubert, W. Vodel, M. Schwickert, H. Reeg, R. Von Hahn, and P. Seidel, “A non-destructive beam monitoring system based on an LTS-SQUID,” *IEEE Transactions on Applied Superconductivity*, vol. 21, no. 3, pp. 444–447, 2011.
- [19] Bergoz Instrumentation, “FCT Datasheet version 4.3.1,” 2015.
- [20] D. Belohrad, M. Krupa, L. Soby, J. Bergoz, and F. Stulle, “A new Integrating Current Transformer for the LHC,” in *International Beam Instrumentation Conference (IBIC)*, (Monterey), 2014.
- [21] M. Krupa and L. Soby, “Beam Intensity Measurements in the Large Hadron Collider,” in *International Conference "Mixed Design of Integrated Circuits and Systems"*, (Gdynia), pp. 592–597, 2013.
- [22] K. B. Unser, “Design and preliminary tests of a beam intensity monitor for LEP,” *Proceedings of the 1989 IEEE Particle Accelerator Conference. Accelerator Science and Technology*, 1989.
- [23] K. Unser, “The circulating beam current monitor.” 1968.
- [24] K. B. Unser, “Beam Current Transformer with D. C. to 200 MHz Range,” *IEEE Transactions on Nuclear Science*, vol. 16, no. 3, 1969.
- [25] K. B. Unser, “A Toroidal DC Beam Current Transformer with High Resolution,” 1981.
- [26] P. Kottman, “Theoretical and experimental investigation of magnetic materials for DC beam current transformers,” 1998.
- [27] R. Hilzinger and W. Roderwald, “Basic material properties,” in *Magnetic Materials*, p. 608, Hanau: VACUUMSCHMELZE GmbH & Co., 2013.
- [28] R. Groessinger, “Soft and Hard Magnets,” in *Alloy Physics: A Comprehensive Reference* (W. Pfeiler, ed.), ch. 14, pp. 861–885, Weinheim: Wiley-VCH Verlag GmbH & Co. KGaA., 2007.

-
- [29] M. Willard, J. Claassen, and V. Harris, "Magnetic and structural properties of amorphous and nanocrystalline FeNi-based alloys," *Proceedings of the IEEE Conference on Nanotechnology*, pp. 51–55, 2001.
- [30] G. Herzer, "Amorphous and nanocrystalline soft magnets," in *Proceedings of the NATO Advanced Study Institute on Magnetic Hysteresis in Novel Materials* (G. C. Hadjipanayis, ed.), vol. 338, (Mykonos, Greece), pp. 1–12, Kluwer Academic Publishers, 1997.
- [31] Y. Liu, D. Sellmyer, and D. Shindo, eds., *Handbook of Advanced Magnetic Materials*. Springer US, 2006.
- [32] M. A. Willard and M. Daniil, *Nanocrystalline Soft Magnetic Alloys: Two Decades of Progress*, vol. 21. Elsevier B.V., 1 ed., 2013.
- [33] A. Brenner, D. Couch, and E. Williams, "Electrodeposition of alloys of phosphorus with nickel or cobalt," *Journal of Research of the National Bureau of Standards*, vol. 44, no. 1, p. 109, 1950.
- [34] R. Kiessling, J. Charles, H. Suzuki, A. G. Evans, I. Tamura, M. C. Flemings, R. I. Jaffee, and G. Thomas, *Amorphous Metallic Alloys*. London: Butterworth & Co (Publishers) Ltd., 1983.
- [35] G. Herzer, "Modern soft magnets: Amorphous and nanocrystalline materials," *Acta Materialia*, vol. 61, no. 3, pp. 718–734, 2013.
- [36] A. Inoue and K. Hashimoto, eds., *Amorphous and Nanocrystalline Materials*, vol. 3 of *Advances in Materials Research*. Berlin, Heidelberg: Springer Berlin Heidelberg, 2001.
- [37] A. Takeuchi and A. Inoue, "Classification of Bulk Metallic Glasses by Atomic Size Difference, Heat of Mixing and Period of Constituent Elements and Its Application to Characterization of the Main Alloying Element," *Materials Transactions*, vol. 46, no. 12, pp. 2817–2829, 2005.
- [38] Y. Yoshizawa, S. Oguma, and K. Yamauchi, "New Fe-based soft magnetic alloys composed of ultrafine grain structure," *Journal of Applied Physics*, vol. 64, pp. 6044–6046, 1988.
- [39] M. E. McHenry, M. A. Willard, and D. E. Laughlin, "Amorphous and nanocrystalline materials for applications as soft magnets," *Progress in Materials Science*, vol. 44, pp. 291–433, oct 1999.
- [40] Y. Yoshizawa, "Nanocrystalline Soft Magnetic Materials and Their Applications," in *Handbook of Advanced Magnetic Materials* (Y. Liu, D. J. Sellmyer, and D. Shindo, eds.), no. 3, pp. 1452–1486, Boston, MA: Springer US, 1991.

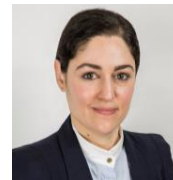
Bibliography

- [41] J. Ayers, V. Harris, J. Sprague, W. Elam, and H. Jones, “A model for nucleation of nanocrystals in the soft magnetic alloy Fe_{73.5}Nb₃Cu₁Si_{13.5}B₉,” *Nanostructured Materials*, vol. 9, pp. 391–396, jan 1997.
- [42] K. Suzuki, A. Makino, N. Kataoka, A. Inoue, and T. Masumoto, “High Saturation Magnetization and soft Magnetic Properties of bcc Fe-Zr-B Alloys with Ultrafine Grain Structure,” *Materials Transactions JIM*, vol. 31, no. 8, pp. 743–746, 1990.
- [43] M. A. Willard, M.-Q. Huang, D. E. Laughlin, M. E. McHenry, J. O. Cross, V. G. Harris, and C. Franchetti, “Magnetic properties of HITPERM (Fe, Co)₈₈Zr₇B₄Cu₁ magnets,” *Journal of Applied Physics*, vol. 85, no. 1999, p. 4421, 1999.
- [44] J. T. S. Irvine and R. Valenzuela, “Effects of thermal annealing amorphous ribbons,” vol. 1486, no. 1992, pp. 1486–1490, 1992.
- [45] H. Fujimori, H. Yoshimoto, T. Masumoto, and T. Mitera, “Anomalous eddy current loss and amorphous magnetic materials with low core loss (invited),” *Journal of Applied Physics*, vol. 52, no. 3, pp. 1893–1898, 1981.
- [46] R. Hasegawa and T. Yoshida, “Magnetic materials for particle accelerators,” in *Proceedings of International workshop on recent progress in induction accelerators*, (Tsukuba, Ibaraki (Japan)), pp. 66–69, 2007.
- [47] D. Spasojević, S. Bukvić, S. Milošević, and H. Stanley, “Barkhausen noise: Elementary signals, power laws, and scaling relations,” *Physical Review E*, vol. 54, no. 3, pp. 2531–2546, 1996.
- [48] F. Bitter, “Experiments on the nature of ferromagnetism,” *Physical Review*, vol. 41, no. 4, pp. 507–515, 1932.
- [49] ESRF, “Characteristics of the Swiss-Norwegian Beamline A-station,” 2016.
- [50] ESRF, “What is synchrotron light?,” 2016.
- [51] PerkinElmer Inc., “Technical Specifications Thermal Analysis for the DSC 8000/8500 Differential Scanning Calorimeters,” 2009.
- [52] Agilent Technologies Japan, “Agilent 4294A Precision Impedance Analyzer Operation Manual,” 2003.
- [53] Advanced Geoscience Instruments Co., “MFK1-FA/CS4/CSL User Guide,” 2009.
- [54] L. Tauxe, *Paleomagnetic Principles and Practice*, vol. 17 of *Modern Approaches in Geophysics*. Dordrecht: Kluwer Academic Publishers, 2003.
- [55] J. McCord, “Progress in magnetic domain observation by advanced magneto-optical microscopy,” *Journal of Physics D: Applied Physics*, vol. 48, no. 33, p. 333001, 2015.

-
- [56] TESA SA, “TESAMASTER High Precision Micrometers with Digital Counter reading to 0.1 mm.”
- [57] Association Française de Normalisation (AFNOR), “ISO 3650:1999: Spécification géométrique des produits (GPS) Étalons de longueurs,” 1999.
- [58] Mettler-Toledo AG, “Operating Instructions: Mettler Toledo Classic Balance Line AB-S,” 2007.
- [59] Micromeritics Instrument Corporation, “AccuPyc 1330 Pycnometer Operator’s Manual,” 2001.
- [60] M. Drosch, *Dealing with Uncertainties*. Heidelberg, Germany: Springer Berlin Heidelberg, second ed. ed., 2009.
- [61] Magnetec, “Magnetec Nanoperm technical data,” 2016.
- [62] Hitachi Metals America, “Amorphous & Nanocrystalline Materials,” 2016.
- [63] W. Yu, H. Zeng, Y. Sun, Y. Sun, and Z. Hua, “Effect of heating rates on the crystallization process of Fe₆₄Co₁₆Zr₁₀B₁₀ amorphous alloy,” *Physics Letters a*, vol. 381, no. 18, pp. 1573–1576, 2017.
- [64] H. W. Jin, Y. J. Kim, and C. G. Park, “The effect of Fe on the crystallization behavior of Al-Mm-Ni-Fe amorphous alloys,” *Journal of Materials Science*, vol. 36, no. 8, pp. 2089–2094, 2001.
- [65] V. Franco, C. F. Conde, A. Conde, and L. F. Kiss, “Superparamagnetic behaviour in an Fe 76 Cu 1 Nb 3 Si 10.5 B 9.5 alloy,” *Journal of magnetism and . . .*, vol. 216, pp. 400–403, 2000.
- [66] V. Franco, J. Blázquez, B. Ingale, and A. Conde, “The Magnetocaloric Effect and Magnetic Refrigeration Near Room Temperature: Materials and Models,” *Annual Review of Materials Research*, vol. 42, no. 1, pp. 305–342, 2012.
- [67] P. Kollár, Z. Birčáková, J. Füzer, and M. Kuźmiński, “DC Magnetic Properties of Amorphous Vitrovac Ribbon,” *Acta Physica Polonica A*, vol. 131, no. 4, pp. 675–677, 2017.
- [68] S. Flohrer, R. Schäfer, and G. Herzer, “Magnetic microstructure of nanocrystalline FeCuNbSiB soft magnets,” *Journal of Non-Crystalline Solids*, vol. 354, no. 47-51, pp. 5097–5100, 2008.
- [69] Metglas, “Metglas 2705M Cobalt Base Magnetic Alloy Material Safety Data Sheet,” pp. 1–7, 2013.

Silvia Aguilera

+41 78 672 78 90
05 - March - 83
silvia.aguilera@gmail.com



EDUCATION

- 2014 - current:** École Polytechnique Fédérale de Lausanne (EPFL), Switzerland **PhD Student**
Thesis title: Study and Characterization of Magnetic Materials for Beam Intensity Monitors at CERN
- 2001 - 2010:** Ramon Llull University (URL), IQS Technical School, Barcelona, Spain **M. Sc. in Industrial Engineering**
(Specialisation in Materials Science)
- 2006 - 2010:** URL, IQS Technical School, Barcelona, Spain **M. Sc. in Chemical Engineering**

PROFESSIONAL EXPERIENCE

- 8/2011 - 2/2014:** CERN, Geneva, Switzerland **Fellow**
Development and thermal treatment of metallic materials for building transformer cores
- 8/2010 - 7/2011:** Inprocess Technology and Consulting, Barcelona, Spain **Junior Flow Assurance Engineer**
Simulations with OLGA (SPT Group) for the Oil and Gas industry
- 9/2008 - 5/2010:** URL, IQS Technical School, Barcelona, Spain **Teaching Assistant**
2/2010 - 5/2010: Materials Technology - 4th year Industrial Engineering
9/2009 - 2/2010: Materials Science - 3rd year Industrial Engineering
2/2009 - 6/2009: Materials Technology
9/2008 - 2/2009: Ceramic and Polymeric Materials - 4th year Industrial Engineering, Materials Science specialisation
- 7/2005 - 6/2009:** URL, IQS Technical School, Barcelona, Spain **Assistant to the Materials Engineering Group**
10/2007 - 6/2009:
• Development of Educational Resources on New Platforms: Podcasts and wikis for e-learning
• Support of Online Educational Resources (Blackboard Academic Suite™) for five courses of Industrial and Chemical Engineering, Bachelor in Chemistry and Master in Bioengineering
• Preparation of contents for the Materials Engineering Group webpage (<http://gemat.iqs.url.edu>)
10/2006 - 6/2007:
• Programming of the Materials Engineering Group's Database in Microsoft Access: management of staff, stock and equipment for three separate labs in the Group
7/2005 - 6/2006:
• Technical support to Chemical Industry (including among others, paints, fertilizers, adhesives...)

LANGUAGES

Spanish: mother tongue **English:** level C2 (CEF) **French:** level B2 (CEF)

COMPUTER SKILLS

- **Good level:** Office, Catia V5, ANSYS, AutoCAD, GRANTA CES Selector, Visual Basic, LaTeX
- **Fair level:** Solidworks, COMSOL

PUBLICATIONS

S. Aguilera, H Hofmann, P. Odier "Study and Characterization of Soft Magnetic Materials for Beam Intensity Monitors at CERN". 8th Joint European Magnetics Symposia. Glasgow, (**8/2016**). Journal of Physics Conference Series 903(1):012035 (**10/2017**)

S. Aguilera, H Hofmann, P. Odier "Magnetic Materials for Current Transformers". International Beam Instrumentation Conference (IBIC), Barcelona, Spain, (**11/2016**)

S. Aguilera, H Hofmann, P. Odier "Study and Characterization of Magnetic Materials for Beam Intensity Monitors". International Conference on Accelerator Optimization, Seville, Spain (**10/2015**)

S. Aguilera, P. Odier, R. Ruffieux, "Magnetic Materials for Current Transformers". International Beam Instrumentation Conference (IBIC), Oxford, UK, (**9/2013**)

COURSES

3/2016: Magnetic materials in modern technologies (2 credits), EPFL

1/2016: Effects of radiation on materials (2 credits), Paul Scherrer Institut (PSI), Switzerland

9/2015: CCMX summer school: characterisation of materials (1 credit), EPFL

9/2015: Design and analysis of experiments in materials science and engineering (2 credits), EPFL

2/2015: Transmission electron microscopy and diffraction (1 credit), EPFL

9/2014 - 2/2015: Seminar series on advances in materials (2 credits), EPFL

12/2014: Scanning electron microscopy techniques (1 credit), EPFL

10/2014: CERN Accelerator School 2014: Introduction to Accelerator Physics (2 credits), CERN

2/2013 - 7/2013: "8.02x: Physics II (Electricity and Magnetism)", MITx (The Massachusetts Institute of Technology), Cambridge, US

INTERESTS

Level 1 diving instructor, 3 star CMAS diver

Aerobics instructor (The Dance Aerobics Company)